LOCALIZED SCOUR AROUND STRUCTURES UNDER TRANSIENT FLOW CONDITIONS

RAZIEH MEHRZAD

Thesis submitted to the University of Ottawa
in partial fulfillment of the requirements for the
Ph.D. degree in Civil Engineering

Academic advisors:
Dr. Ioan Nistor and Dr. Colin D. Rennie

Department of Civil Engineering
Faculty of Engineering
University of Ottawa

Ottawa, Canada, 2021

ABSTRACT

In recent years, extreme natural phenomena such as tsunamis or storm surges have affected populated coastal regions around many coastal regions around the world and with particular impact for countries bordering the Indian, Pacific and Atlantic Oceans. Such extreme events caused significant loss of life and extensive damage to coastal communities. Field surveys conducted from the 1992 Nicaragua Tsunami to the relatively recent 2011 Tohoku Japan Tsunami have recorded lots of evidence of scour around damaged buildings and bridge foundations. It is documented that scouring is one of the significant causes of coastal structural damages. In post-tsunami forensic engineering surveys of India and Thailand following the 2004 Great Sumatra Andaman tsunami, researchers were able to document local scour occurrences not only at buildings located close to shore, but also hundreds of meters inland. (Yeh and Li 2008, Nistor et al. 2012 and Li et al. 2012). The most damaging 2011 Tohoku Tsunami provided an outstanding opportunity to document (Chock et al., 2013) a variety of failure modes of infrastructure including coastal and onshore structures.

This research program encompassed a comprehensive experimental and numerical investigation and analysis for the scour mechanism and vortex structures due to inland-propagating tsunami-like bores on a dry or flooded horizontal mobile bed, representing comprehensive tsunami-induced scour study. The primary objective of this thesis was to investigate the influence of different parameters on the bore propagation characteristics and how they affect the scouring process. To achieve this objective, a series of hydraulic bores consistent with the dam-break wave theory were generated. Extensive experiments were conducted to perform parametric analysis on both bore propagation and local scour (e.g., influence of structure size, bore height, bed initial condition, bed material size and second tsunami wave). The secondary objective involved development of a numerical model to simulate local scour and predict the three-dimensional (3D) flow pattern around a structure induced by tsunami–like bore. The open source Telemac-Mascaret numerical model was used to determine flow characteristics adjacent to the structure and the associated bed evolution and resulting local scour. The 3D hydrodynamic Telemac model couples internally with the sediment transport module SISYPHE to solve bed evolution equations. The efficiency of the numerical model was assessed and compared quantitatively and qualitatively with the results of the physical experiments.

The studies show a longer duration of a turbulent bore induced more scour depth compared to that generated by solitary or long waves. The short duration and very turbulent nature of the bores induced rapid scour. It was shown that the location of maximum scour depth and sediment deposition pattern downstream of the structure are well captured by the numerical model, however; magnitude of scour depth is underpredicted compared to that of the experimental work.

It was found that the ASCE (2016) prescriptions on estimating scour underpredicts the maximum scour depth and thus, the use of the ASCE (2016) provisions, may lead to undesirable underestimations of maximum scour depth. The results of this study have contributed to the American Society of Civil Engineers (ASCE) 7 Chapter 6, which is the first standard written in mandatory language in the world, which specifically prescribes guidance for the design of tsunami resilient critical infrastructure using also a probabilistic framework for the determination of the extent of coastal inundation.

ACKNOWLEDGEMENTS

First, I would like to express my deepest thanks to my academic advisors, Prof. Ioan Nistor and Prof. Colin Rennie throughout my time at the University of Ottawa, they provided me with countless opportunities during my Ph.D. studies. Their patience, motivation, and immense knowledge helped me all the time of research and writing of this thesis. Their kind help and consultation paved the jagged research path for me and shed light on the dark and obscure research areas which led to real meaningful academic and industrial contributions.

I would like to acknowledge the support of several sources of funding which facilitated the realization of this project: The University of Ottawa PhD International Scholarship and the NSERC Discovery grants of Prof. Nistor and Prof. Rennie. I acknowledge the support of Mr. Mark Lapointe, Hydraulic Laboratory Technician at the University of Ottawa, as well as of Lea Palmeri, Marion Naude, Camille Coupau, research interns from France at the University of Ottawa, for their assistance with conducting this experimental work.

This thesis work is dedicated to my husband (Mehran) who has been a constant source of support and encouragement during the challenges of graduate school and life. I am truly thankful for having him in my life. Without him, none of the work I have done to this point would have been possible. This work is also dedicated to my parents who have always loved me unconditionally and for giving me the opportunities and experiences that have made me who I am.

Razieh Mehrzad
December 2020

TABLE OF CONTENTS

ABSTRACT ii
ACKNOWLEDGEMENTS iii
TABLE OF CONTENTS iv
LIST OF FIGURES viii
LIST OF TABLES xiii
LIST OF ACRONYMS xiv
LIST OF SYMBOLS xv
Chapter 1 . INTRODUCTION 1
- 1.1 Background 1
- 1.2 Thesis objective 4
  - 1.2.1 Primary objective 4
  - 1.2.2 Secondary objective 5
- 1.3 Scope 6
- 1.4 Novelty of the study 7
- 1.5 Publications 9
  - 1.5.1 Journal articles 9
  - 1.5.2 Conference papers and other refereed contributions 9
- 1.6 Outline of the thesis 9

Chapter 2 . LITERATURE REVIEW 12
- 2.1 Local scour 12
  - 2.1.1 Time phases of the scour process 13
  - 2.1.2 Scour depth prediction model 15
- 2.2 Tsunami induced scour 17
- 2.3 Physical modelling of tsunami flow conditions 20
- 2.4 Physical studies on tsunami induced scour 23
- 2.5 Numerical modeling of scour in supercritical flows 31
- 2.6 Estimation of local scour in current design guidelines 35
- 2.7 Sediment transport 38
  - 2.7.1 Sediment physical properties 39
  - 2.7.2 The forces on a sediment particle 41

2.7.3 Effective roughness 42
2.7.4 The initiation of sediment movement 43
2.8 Discussion 46
Chapter 3 : THE NUMERICAL METHOD 47
3.1 TELEMAC 3D 47
3.1.1 Turbulence models 50
3.1.2 Computational mesh 51
3.1.3 Bottom friction 52
3.2 SISYPHE 53
3.2.1 Coupling between bedload and suspended load 55
3.2.2 Shields parameter 57
3.2.3 Settling velocities 57
3.2.4 Transport rate 58
3.2.5 Bedload transport 58
3.2.6 Sediment transport formula 59
3.3 Coupling between sediment transport and hydrodynamic modules 62
Chapter 4 . SCOUR MECHANICS OF A TSUNAMI-LIKE BORE AROUND A SQUARE STRUCTURE. 63
Abstract 63
4.1 Introduction 63
4.2 Research objectives 68
4.3 Experimental setup and test procedure 68
4.3.1 Flume and instrumentation 68
4.3.2 Experimental procedure 71
4.3.3 Geotechnical characteristics of the sediment 73
4.3.4 Scale effects 73
4.3.5 Dam break wave hydrodynamics 74
4.4 Results 75
4.4.1 Scour processes – qualitative observations 75
4.4.2 Bore-scour and stream-wise velocity 81
4.4.3 Run-up and scour depth time history 83
4.4.4 Stream-wise velocity 85

4.4.5 Characteristics of flow field around the structure 86
4.4.6 Bore front velocity 87
4.4.7 Froude number 89
4.4.8 Scour evolution 90
4.4.9 Infiltration and scour rate 92
4.4.10 Final scour topography 93
4.5 Discussion 95
4.6 Conclusions 99
Chapter 5 . EFFECT OF BED CONDITION (WET VERSUS DRY) ON LOCAL SCOUR DUE TO TSUNAMI-LIKE BORE 101
Abstract 101
5.1 Introduction 101
5.2 Research objectives 105
5.3 Experimental setup 106
5.4 Experimental test program 109
5.5 Test repeatability 111
5.6 Results 112
5.6.1 Effect of bed condition on bore characteristics 112
5.6.2 Effect of bed condition on local scour 123
5.6.3 Effect of second tsunami wave 126
5.7 Discussion 129
5.8 Conclusions 132
Chapter 6 . STRUCTURE WIDTH EFFECT ON LOCAL SCOUR INDUCED BY TURBULENT BORE 134
Abstract 134
6.1 Introduction 134
6.2 Research objectives 137
6.3 Experimental setup 137
6.4 Results 140
6.4.1 Distribution of flow field around the structure 140
6.4.2 Run-up depth and scour depth time history 142
6.4.3 Scour depth 142

6.4.4 Scour profile 143
6.4.5 Final scour topography 145
6.4.6 Scour evolution around the structure 147
6.4.7 Structure width effect on scour depth and bore depth 149
6.5 Discussion 151
6.6 Conclusion 154
Chapter 7 . EXPERIMENTAL AND NUMERICAL MODELLING OF SCOUR AND EROSION INDUCED BY TURBULENT BORE 156
Abstract 156
7.1 Introduction 156
7.2 Research objectives 158
7.3 Laboratory experiment 158
7.4 3D numerical model 161
7.5 Results and discussion 163
7.5.1 Time-history of water surface 163
7.5.2 Velocity time history 164
7.5.3 Time history of scour depth 165
7.5.4 Bathymetry 166
7.5.5 Flow field induced by turbulent horseshoe vortex 169
7.6 Conclusions 170
Chapter 8 . CONCLUSIONS AND RECOMMENDATION FOR FUTURE WORK 172
8.1 Conclusion 172
8.2 Recommendations for future work 175
REFERENCES 177
APPENDIX A - HYDRODYNAMIC AND SEDIMENT TRANSPORT NUMERICAL PARAMETERS 192
APPENDIX B – PUBLISHED CONFERENCE PAPERS 203
APPENDIX C- SENSITIVITY ANALYSIS 230

LIST OF FIGURES

Figure 1-1: Surge created from the first tsunami wave arriving at Rikuzentakata (roughly 1.5 km inland from the bayfront) in the Iwate Prefecture, Japan during the 2011 Tohoku tsunami (Hagen, 2014). 1
Figure 1-2: Typical tsunami-induced scour holes at building foundations: a) approximately 1.5 m deep in India, from the 2004 Indian Ocean tsunami (Yeh and Li 2008); b) Koh Khao, Thailand. Case SS-4 (Francis 2006) c) Foundation failure of a breakwater, from the 1993 Okushiri Japan tsunami, (Yeh and Li 2008). 3
Figure 2-1*: Main feature of flow field around the pier in steady flow (Arneson et al. 2012)* 12
Figure 2-2(a,b): variation of local scour depth with flow velocity and time 13
Figure 2-3: Schematization of sediment transport along upstream scour slope (initial phase), (Hoftmans, 1993) 14
Figure 2-4: Schematization of sediment transport along upstream scour slope (development phase), (Hoftmans, 1993) 14
Figure 2-5: Schematization of sediment transport along upstream scour slope (stabilization phase), (Hoftmans, 1993) 15
Figure 2-6: Schematization of sediment transport along upstream scour slope (equilibrium phase), (Hoftmans, 1993) 15
Figure 2-7: Local scour, Koh Khao, Thailand. Case SS-4. Tonkin et al. (2013) 20
Figure 2-8: Overtopping scour, Taito Port, Japan. Case TO-1. Tonkin et al. (2013) 20
Figure 2-9: Channelized scour. Great Nicobar Case RS-3. Tonkin et al. (2013) 20
Figure 2-10: General scour. Yamamoto-cho, Japan. Case TN-12. Tonkin et al. (2013) 20
Figure 2-11: Potential tsunami inundation profiles (adopted from Takahashi et al. (2011)). 21
Figure 2-12: State from which the scour by a back-flow started 24
Figure 2-13: State to which the scour by a back-flow fully progressed 25
Figure 2-14: Example of images recorded from inside the cylinder, Tonkin et al. (2003) 26
Figure 2-15: Time development of scour around a cylinder on a sand bed (crosses: front, squares: sides, circles: back), Tonkin et al. (2003) 27
Figure 2-16: Wave height (blue) and pore pressures (all other colors) at the back of the cylinder on a sandbed, Tonkin et al. (2003) 27
Figure 2-17: Video images showing b) undermining of the corner of the structure and d) scour hole pattern, Nakamura et al. (2008) 29
Figure 2-18: Temporal Formation of Local Scour Hole in Sand at 5 second Intervals 30
Figure 2-19 : Experimental versus Numerical Results of Tsunami Wave Propagation, Nakamura et al. (2008) 33
Figure 2-20: Topography changes in and around the harbor area. (a) numerical results of Fuji et al. (2009), (b) experimental data of Fuji et al. (2009), (c) numerical results predicted by the vertically averaged model 34
Figure 2-21: Computed longitudinal surface profiles of tsunami wave propagation, breaking, and run-up 35
Figure 2-22: Tsunami velocity vs. scour depth (FEMA 2000) 37

Figure 2-23 : observed local scour depth and estimated flow depth for different sediment types, with bounding plausible design envelopes, Tonkin et al. (2013) 37
Figure 2-24: Local Scour depth due to sustained flow and pore pressure softening (ASCE 7-16) 38
Figure 2-25: Forces on a sediment particle (inclined bed), (Kabir, 2005)................................... 41
Figure 2-26: Forces on a sediment particle by Van Rijn (1993).. 44
Figure 2-27: Forces on a sediment particle by Yang, (1996) 45
Figure 2-28: Shields parameter with respect to particle Reynolds number (Raudkivi, 1998)...... 46
Figure 3-1: Bottom elevation profile 54
Figure 4-1: Typical tsunami-induced scour holes at building foundations: a) approximately 1.5 m deep in India, from the 2004 Indian Ocean tsunami (Yeh and Li 2008); b) Koh Khao, Thailand. Case SS-4 (Francis 2006).. 64
Figure 4-2: Experimental setup, a) side view (not to scale), b) plan view (not to scale)............. 69
Figure 4-3: a) Experimental setup to monitor the scour process; b) Reflected (looking down from the top of the structure to the mirror placed inside) view of the structure’s front face 71
Figure 4-4.Comparison between Chanson’s (2009) dam-break analytical solution and the experimentally obtained bore profile for Test 1 at h_u = 2.48 s. 75
Figure 4-5. Incoming bore propagation and associated flow and scour pattern: a) top view of the incoming bore, b) side view of the incoming bore. Scour profiles around the structure; c) front face, d) side face, and e) back face, at t = 0.2 s for Test 1 (h_u = 0.25 m)..................................... 76
Figure 4-6. Incoming bore propagation and associated flow and scour: a) top view of the incoming bore, b) side view of the incoming bore. Scour profiles around the structure; c) front face, d) side face, and e) back face, at t = 1 s for Test 1 (h_u = 0.25 m).. 77
Figure 4-7. Incoming bore propagation and associated flow and scour: a) top view of the incoming bore, b) side view of the incoming bore. Scour profiles around the structure; c) front face, d) side face, and e) back face, at t = 3.25 s for Test 1 (h_u = 0.25 m).................................... 78
Figure 4-8.Incoming bore propagation and associated flow and scour: a) top view of the incoming bore, b) side view of the incoming bore. Scour profiles around the structure; c) front face, d) side face, and e) back face, at t =16.1 s for Test 1 (h_u = 0.25 m).................................... 79
Figure 4-9.a) Suspended sediment movement from outer slope to inner slope at t = 6.41 s, b) Suspended sediment moving back to the upstream of scour hole and the oscillation of the boundary between two slopes at t = 7.06 s, c) Final scour hole geometry with outer and inner slopes at t = 24 s, for Test 1(h_u = 0.25 m)... 80
Figure 4-10.Incoming bore propagation and associated flow and scour: a) top view of the incoming bore, b) side view of the incoming bore. Scour profiles around the structure; c) front face, d) side face, and e) back face, at t = 24 s for Test 1 (h_u = 0.25 m)...................................... 81
Figure 4-11.Time-history of the water surface elevations measured by the wave gauges located at the front (red line), side (light blue) and back (pink line) face of the structure, and scour depth measured at the front (red line with triangle pattern), side (light blue line with cross pattern) and back (pink line with star pattern) face of the structure, and horizontal velocity (black line) measured 50cm upstream of the structure for an impoundment depth, h_u = 0.25 m (Test 1)....... 82
Figure 4-12. a) Run-up depth time history; b) Scour depth time history..................................... 84

Figure 4-13. Comparison of the stream-wise velocity for Tests 1, 2 and 3 86
Figure 4-14. Distribution of the flow field around structures for a) Test 1, b) Test 2 and c) Test 3 86
Figure 4-15. Video snapshot of the bore front tracking a) over the false floor and b) over the sediment section 88
Figure 4-16. a) Bore front velocity along the flume; b) Relationship between maximum bore depth and bore front velocity 89
Figure 4-17. a) Scour measurements location, Scour depth time history for b) Test1, c) Test 2 and d) Test 3... 91
Figure 4-18. Video snapshots for tracking the infiltration and scour 92
Figure 4-19. Scour rate (red line) and infiltration rate (black line) for: a) Test 1, b) Test 2 and c) Test 3.. 93
Figure 4-20. Plan view of the bed scour depth for a) test 1, b) test 2 and C) test 3...................... 94
Figure 4-21. Relationship between scour depth and flow depth.. 96
Figure 5-1: Local scour due to tsunami bore around building foundations. a) Japan (courtesy of Dr. Ioan Nistor, 2012); b) 1.4 m deep in India, from the 2004 Indian Ocean tsunami (Yeh and Li 2008) 102
Figure 5-2: Surge created from the first tsunami wave arriving at Rikuzentakata (roughly 1.5 km inland from the bayfront) in Iwate Prefecture, Japan during the 2011 Tohoku tsunami (Hagen 2014). 104
Figure 5-3: Experimental setup, a) side view (not to scale), b) plan view (not to scale)) 107
Figure 5-4: (a) Dam-break flume in the Hydraulics Laboratory at the University of Ottawa, Canada, b) Experiment setup for measuring the scour depths, velocity and water surface elevation and (c) View of the front and side faces from inside the structure shot with the GoPro video-camera 108
Figure 5-5: Dam-break wave propagation over the horizontal bed with a wet bed condition.... 110
Figure 5-6: Repeated tests conducted for Test #1, a) water surface elevation, b) scour depth and c) stream wise velocity.. 112
Figure 5-7: Image of the Styrofoam particle, circled in red, taken by the high-speed video camera 113
Figure 5-8: Comparison between the measured average sustained flow velocity (V2) with the value calculated using Chanson's equation (2004) for Test # 4 to Test #14 114
Figure 5-9: V2gd2 and d2/d1 as a function of the d_1/h) for Test # 4 to Test #14 114
Figure 5-10: Average bore front velocity as a function of the water depth ratio (r=d1/h) for Test # 1 to Test #14.. 115
Figure 5-11: Bore-front velocity along the flume for Tests # 1,4,5,6 with h = 0.25 m and various downstream still water depths d_1. 115
Figure 5-12: Free surface profile measured at X= 5.6 m prior to the bore's impact with the structure a) Test #1 (h = 0.25 m, d_1= 0 m), b) Test# 5 (h = 0.25 m, d_1 = 0.05 m) and c) Test #6 (h = 0.25 m, d_1 = 0.125 m) 117
Figure 5-13: Comparison of bore front profiles for Test #1 (h = 0.25 m, d_1= 0 m; purple), Test# 5 (h = 0.25 m, d_1 = 0.05 m; blue) and Test #6 (h = 0.25 m, d_1 = 0.125 m; red).......................... 117

Figure 5-14: Air-entrained bore front in the a) dry bed (Test#1) and b) wet bed (Test#5) 118
Figure 5-15: Top views of bore front for: a) dry bed, Test#1 ; b) 0.025 m deep wet bed, Test#4; c) 0.05 m deep wet bed, Test#5; and d) 0.125 m deep wet bed conditions, Test#6. Flow from left to right. 119
Figure 5-16: Top views of bore-front for: a) dry bed, Test#1, b) 0.025 m deep wet bed, Test#4 c) 0.05 m deep wet bed, Test#5 and d) 0.125 m deep wet bed conditions, Test#6. Flow from left to right. 119
Figure 5-17: Measured water surface elevation (black line) and measured streamwise velocity (red line) for: 121
Figure 5-18: Time-history of the scour depth for dry bed (Test#1), 0.025 m deep wet bed (Test#4), 0.05 m deep wet bed (Test#5) and 0.125 m deep wet bed (Test#6) 123
Figure 5-19: Final scour topography for a) dry bed (Test#1), b) 0.025 m deep wet bed (Test#4), c) 0.05 m deep wet bed (Test#5) and d) 0.125 m deep wet bed (Test#6) 125
Figure 5-20: Scour depth time history for a) Test #25 and b) Test #27 127
Figure 5-21: Increased maximum scour depth due to the second bore, a) Test #25-first run, b) Test #25 – second run, ... 128
Figure 5-22: Final scour topography of Test #25 after: a) first run, b) second run 129
Figure 5-23: Scour depth (ds), for various structure shapes and sizes and bed sediment particle size and condition, as a function of the flow Froude number. Results for circular structures are from LaVictoire et al. (2014). The field data are described in Chock et al. (2013) 130
Figure 5-24: main features of the flow field around the structure a) no initial water depth b) with initial water depth 131
Figure 5-25: Second bore advancing on a previously eroded bed 132
Figure 6-1: Local scour depth variation with flow shallowness in steady flow (Melville 2008) 136
Figure 6-2: Experiment setup, side view, (not to scale) 138
Figure 6-3: (a) Experimental setup to monitor the scour process; (b) Reflected (looking from above-mirror inside) view of the structure’s front face 139
Figure 6-4: Three different square structure sizes 140
Figure 6-5: flow field around structures, (left column: flow direction from left to right, run up over the front face), (middle and right columns: surface roller and wake development region) for a) Test 2 (B = 0.2 m, h = 0.25 m) and b) Test 3 (B = 0.1 m, h = 0.25 m) 141
Figure 6-6: Bore depth measured for Test 1 (B = 0.3 m, h = 0.25 m), Test 2 (B = 0.2 m, h = 0.25 m) and Test 3 (B = 0.1 m, h = 0.25 m) at a) the front face and b) the side face 142
Figure 6-7: Scour development around the upstream corners of the structures for Test 1 (B = 0.3 m, h = 0.25 m), Test 2 (B = 0.2 m, h = 0.25 m) and Test 3 (B = 0.1 m, h = 0.25 m) 143
Figure 6-8: Final scour profile indicated by dash lines for Test 1 (B = 0.3 m, h = 0.25 m), Test 2 (B = 0.2 m, h = 0.25 m) and Test 3 (B = 0.1 m, h = 0.25 m), left columns: front face, middle columns: side face and right columns: back face 144
Figure 6-9: left: final scour topography with black squares and arrows from left to right showing structures and flow direction, right: images of the final scour holes with arrows and dash lines showing flow direction and boundary of the final scour hole for a)Test 1 (B = 0.3 m, h = 0.25 m), b)Test 2 (B = 0.2 m, h = 0.25 m) and c) Test 3 (B = 0.1 m, h = 0.25 m) 147

Figure 6-10: Scour evolution around the structures for b) Test 1 (B = 0.3 m, h = 0.25 m), c) Test 2 (B = 0.2 m, h = 0.25 m) and d) Test 3 (B = 0.1 m, h = 0.25 m). The different locations around each structure are shown in a. 148
Figure 6-11: Structure width effect on a) run-up depth and b) scour depth 150
Figure 6-12: a) h/ B variation with H_{max}/B, b) local scour depth variation with flow shallowness 151
Figure 6-13:comparison of temporal development of scour depth for Test 1, Test 2, Test 3 with the empirical equation of Gumgum and Guney (2019) for live-bed scour under flood waves .. 152
Figure 7-1: Experimental setup side view (not to scale)........ 159
Figure 7-2: Sediment section: Left: Sand bed, Right: Gravel bed........ 160
Figure 7-3: a) 3D mesh isometric view (not to scale), b) 2D mesh over the sediment section and around the structure........ 162
Figure 7-4: Measured and computed run up depth: a) sand - dry bed, b) gravel - dry bed, c) sand – wet bed, d) gravel- wet bed........ 164
Figure 7-5: measured streamwise velocity at 2cm depth above the bed........ 165
Figure 7-6: Computed depth average velocity: a) sand, b) gravel........ 165
Figure 7-7: Measured and computed scour depth time history: a) sand - dry bed, b) gravel - dry bed, c) sand – wet bed, d) gravel- wet bed........ 166
Figure 7-8: Measured final bathymetry a) sand-dry, b) gravel-dry 167
Figure 7-9: Final scour profile from the inside video camera a) sand - dry condition, b) gravel – dry condition........ 168
Figure 7-10: Computed final bathymetry a) sand-dry, b) gravel-dry 168
Figure 7-11: contours of instantaneous streamwise velocity and streamtracers in the plane of Y = 0.75 m 170

LIST OF TABLES

Table 1-1: Generalized Observed Tsunami Inundation for the 2004 Indian Ocean Tsunami (Peterson et al. 2006) 2
Table 2-1: Different scour depth prediction models 16
Table 2-2: Design Guidelines for Scour Depth, Dames and Moore (1980) 35
Table 2-3: Tsunami Design Criteria (Hwang et. al., 2006; adapted from FEMA (2000) 36
Table 2-4: Design local scour depth due to sustained flow and pore pressure softening (ASCE 7 - 2016) 38
Table 4-1**.** Experimental test program 72
Table 4-2. Calculated bore Froude numbers 90
Table 5-1: Experimental test program 110
Table 5-2: Description of tests 111
Table 6-1: Experimental test program 140
Table 7-1: Summary of experimental tests 161

LIST OF ACRONYMS

ADV	Acoustic Doppler Velocimeter
ASCE	American Society of Civil Engineering
ASM	Algebraic Stress Model
CCD	Charge-coupled device
CFD	Computational fluid dynamics
CSCE	Canadian Society of Civil Engineering
DNS	Direct Numerical Simulation
DTM	dynamic two-parameter mixed model
EDF	Electricite de France
FEM	Finite Element Model
FEMA	Federal Emergency Management Agency
ITST	International Tsunami Survey Team
k-£	A two-equation turbulence model
k-*w*	A two-equation turbulence model
LES	large eddy simulation
NS	Navier Stokes
RANS	Reynolds-averaged Navier–Stokes equations
RSM	Reynolds Stress Model
SPH	Smoothed-particle hydrodynamic
VLES	Very Large Eddy Simulation
VOF	volume of fluid
WG	Wave Gauge
2D	Two-dimensional
3D	Three-dimensional

LIST OF SYMBOLS

α	Interface between suspended-load layer and bed-load layer(m)
a_1, a_2, a_3	Distance used by Van Rijn (1993) to describe force on particles (m)
α_p	Projected area where lift and drag force acts (m^2)
B	Flume width, structure size (m)
b_1, b_2, b_3	Distance used by Van Rijn (1993) to describe force on particles (m)
C	depth-averaged sediment concentration (kg/m^3| m^3/m^3)
C_c	coefficient of curvature
C_D	drag coefficient
C_h	Chezy coefficient ($m^{1/2}/s$)
C_h'	grain related Chezy coefficient
C_{eq}	the near-bed concentration
C_f	dimensionless friction coefficient
c_f	quadratic friction coefficient
C_L	lift coefficient
C_s	Volumetric sediment concentration m^3/m^3
C_u	coefficient of uniformity
c_v	consolidation coefficient of the soil
d	Diameter of a sediment particle (m)
D	Structure size (m)
d_{ch}	the characteristic sand grain diameter (m)
D_d	Deposition flux
d_1	Down stream water depth (m)
d_2	flow depth immediately behind the positive surge (m)
d_*	the dimensionless characteristic sediment diameter (m)
D_*	non-dimensional grain diameter
(d_{50} or d_i)	median diameter (m)
d_S	Scour depth (m)
e_{min}	minimum void ratio
e_{max}	maximum void ratio
E_e	Erosion flux
ε_s	sediment diffusivity coefficient
f	a function of' read in an equation
f	Darcy-Weisbach friction factor
F_D	Drag force (N)
F_L	Lift force (N)
F_G	Force due to gravity (N)
Fr	Froude number
F_R	Resisting force due to particle movement (N)
F_x , F_y	source terms (m/s^2)
g	acceleration due to gravity (m/s^2)

h	water depth (m), upstream water depth (m)
h_u	Upstream water depth (m)
H_{max}	Maximum run up depth (m)
$I, I_1 \text{ and } I_2$	Einstein integrals
K	von Karman constant
k_i	coefficient (k_i) which accounts for the angle of flow and for live or clear flow condition
K_s	permeability coefficient
k_s	effective roughness height (m)
k_{sf}	form roughness (m)
k_{sg}	grain roughness (m)
M_0	Overturning moment due to FD and FR (N-m)
M_R	Resisting moment due to FL and FG (N-m)
μ	coefficient of viscosity related to shear flow (Ns/m^2)
μ_b	bed form factor or efficiency factor
$\mu_{xy(t)}$	coefficient of viscosity related to the turbulent flow (Ns/m^2)
n_p	Bed porosity (%)
P_i	percentage by mass of that fraction (%)
p	Pressure (N/m^2)
Q	(tracer unit) tracer source of sink
Q_b	Bed load
q_b	Volumetric bed-load transport (m^2/s)
q_s	The suspended sediment transport rate (m^2/s)
Q_s	suspended load
q_t	Volumetric total sediment load transport (m^2/s)
Q_t	total sediment load
Q_s	sediment transport (volume) vector per unit width
p_{atm}	atmospheric pressure (N/m^2)
ρ_s	Density of fluid (kg/m^3)
ρ	Density of the sediment (kg/m^3)
ρ_0	Reference density (kg/m^3)
$\Delta\rho$	variation of density around the reference density (kg/m^3)
R_p	Rouse number
R^2	correlation coefficient
Re_*	Particle Reynolds number
Re_s	roughness Reynolds number
r	is the ratio of d_1/h
s	specific gravity
t	Time (s)
t_1	characteristic time (s)
T(°C, *g/L*)	passive or active (acting on density) tracer
T_0	the non-dimensional gate opening time
τ_0	bed shear stress

τ_{ij}	Shear stress component acts in the i-direction on a surface with a normal in the j-direction (N/m^2)
τ_c	Critical bed shear stress (N/m^2)
$T*$	excess shear stress parameter
U	Velocity component in X direction (m/s)
U	Bore front velocity (m/s)
u_0	Effective particle velocity near bed (m/s)
u_*	Shear velocity (m/s)
u	Flow velocity (m/s)
u'	Component of fluctuating velocity vector along x-direction (m/s)
V	Velocity component in Y direction (m/s)
ν	cinematic viscosity and tracer diffusion coefficients (m^2/s)
V_0	initial reservoir velocity (m/s)
V_c	critical velocity (m/s)
V_2	Sustained flow velocity (m/s)
v'	Component of fluctuating velocity vector along y-direction (m/s)
v_{ss}	settling velocity (m/s)
v_T	Turbulent kinematic viscosity (m^2/s)
W	natural water content in dry
W	Velocity component in Z direction (m/s)
w'	Component of fluctuating velocity vector along z-direction (m/s)
W_r	The work required elevating the sediment load over a height equal to the bed-form height (J/s/m)
W_d	The work done by the fluid on moving the particles over a length *J/s/m* equal to the bed form length (J/s/m)
x	horizontal space components (m)
y	horizontal space components (m)
y_m	maximum scour depth (m)
$y_{m,e}$	equilibrium scour depth (m)
y_{se}	equilibrium scour depth (m)
y_1	water depth (m)
z	vertical space component (m)
Z_f	bottom elevation (m)
Z_S	free surface elevation (m)
Z_{ref}	The interface between the bedload and suspended load (m)
σ	standard deviation
σ_g	geometric standard deviation
Δ	relative submerged density
ϕ_r , φ	critical angle of repose
θ	Deposition flux
θ_c	Critical Shield's parameter
Φ_b	dimensionless bed sediment load function

Φ_s	Non-dimensionnel sand transport rate
Φ_t	dimensionless total sediment transport load function
γ_b	buoyant unit weight of soil
Λ_T	pore pressure ratio
λ	characteristic length scale (m)

Chapter 1. INTRODUCTION

1.1 Background

Rapid displacement of a large volume of water in an ocean or large lakes generates a series of long waves which are called tsunami. These displacements are usually generated by the impulsive disturbances above or below the water surface such as the uplift or subsidence of the seafloor during submarine earthquakes, aerial or submerged landslides, underwater explosions, volcanic eruptions, or asteroid impacts. The energy of such extreme events is transmitted to the entire water column. The resulting waves propagate outward in different directions from the source. The wavelength, amplitude and period vary, depending on the size of the source generating mechanism. According to the Federal Emergency Management Agency (FEMA) P-646 design guideline 2012, upon reaching shallow coastal areas, tsunamis break, further form, depending on the nearshore bathymetry and coastal topography, a bore or a surge which propagate inland. A tsunami bore is characterized by a turbulent and steep foaming front. The breaking is predominant for leading elevation waves and occurs as a result of wave shoaling and non-linear transformations over the continental shelf (Yeh, 2009). The tsunami bore propagates onshore due to its momentum, as shown in Figure 1-1.

Figure 1-1: Surge created from the first tsunami wave arriving at Rikuzentakata (roughly 1.5 km inland from the bayfront) in the Iwate Prefecture, Japan during the 2011 Tohoku tsunami (Hagen, 2014).

Generally, the first tsunami bore propagates over dry land (dry bed condition) while the subsequent bores, which in some cases could be larger than the first one, inundate the already flooded coastline (wet bed condition) before full recession of the first bore. Therefore, it is important to define the design guideline based on two hydrodynamic conditions, tsunami bores propagating over a wet bed and tsunami bores traveling over dry bed.

Reconnaissance surveys of inundated sites have provided measurements of runup heights, overland flow depths and inundation extent across a broad geographic region, including India, Thailand, and Andaman/Nicobar (2004 Indian Ocean Tsunami). Table 1-1 shows different tsunami run up height and overland flow depth for a range of inundation conditions (Peterson et al. 2006). From Table 1-1, it can be concluded that a tsunami wave is capable of reaching the coastal zone while maintaining significant depth. As a result, it can cause widespread destruction not only close to shoreline, but also kilometers inland from the shoreline.

Table 1-1: Generalized Observed Tsunami Inundation for the 2004 Indian Ocean Tsunami (Peterson et al. 2006)

Location	India	Andaman/Nicobar	Thailand	Sumatra
Runup height (m)	2-5	3-15	5-10	5-20
Overland flow depths (m)	0.2-2	Not available	2-5	2-15
Inland inundation distance (m)	Up to 800	Not available	Up to 5,000	Up to 10,000

Canada is surrounded by three oceans (Pacific, Arctic, and Atlantic Oceans), and its coastline is the longest in the world and its shorelines have been affected by tsunamis in the past. More specifically, Canada’s West Coast located in the western-most province of the country (British Columbia), which borders the Pacific Ocean, is at a significantly higher risk of being hit by earthquake-induced tsunamis compared to Canadian coastlines facing the Arctic and Atlantic Oceans (Clague et al. 2003). Leonard et al. (2014) conducted a preliminary probabilistic tsunami hazard assessment along the Canadian coastlines and showed that the probability for tsunami run-ups reaching elevations over 1.5 m and 3 m for the Pacific coast are much higher than those for the Atlantic and Arctic coasts. The coast of British Columbia has historically experienced major tsunamis, both seismic and landslide generated, although most of them did not cause significant damage to infrastructure (Clague et al. 2003) either due to the low population density at their time of occurrence or due to the fact that some hit sparsely inhabited coastal areas.

Based on damage surveys of historic tsunami events, the 2004 Indian Ocean Tsunami, the 2011 Tohoku Japan Tsunami, and the storm surge associated with Hurricane Katrina in 2005, or Typhoon Haiyan in Philippines (2014), structural damage from such extreme events can be due to: (1) direct hydrostatic and hydrodynamic loading from water inundation; (2) impact forces from water-borne debris; (3) fire spread by floating debris and combustible liquids; (4) scour and slope/foundation failure (FEMA- P646)

Over the last few decades, the estimation of flooding hazards has mostly focused on the hydraulic conditions (i.e., hydraulic loading and floodplain mapping,). However, field investigations of flood-stricken communities have indicated the necessity for considering secondary effects, such as erosion and debris (Ghobarah et al. 2006, Robertson et al. 2007, Palermo et al. 2013, Chock et al. 2013). This thesis will address tsunami-induced scour and erosion.

Yeh and Li (2008) observed local scour at the seaward corner of a schoolhouse in Kalapakkom, India (Figure 1-2a). The inundation depth was 0.95 m above the building's floor and the run-up height was estimated at 4.1 m. Francis (2006) also reported local scour around the corner of the two-story pile supported hotel foundation in the Koh Khao Jomtien, Phangaa, Thailand (Figure 1-2b). The estimated run-up depth at that location was 10 m. The scour depth was approximately 1.5 m with a horizontal span of 5 m. During the 1993 Okushiri Tsunami attack, at the entrance of Okushiri Port, Japan, a scour depth of 4 m occurred between breakwaters, causing them to overturn as a result of foundation failure (Figure 1-2c), (Yeh and Li 2008).

a) b) c)

Figure 1-2: Typical tsunami-induced scour holes at building foundations: a) approximately 1.5 m deep in India, from the 2004 Indian Ocean tsunami (Yeh and Li 2008); b) Koh Khao, Thailand. Case SS-4 (Francis 2006) c) Foundation failure of a breakwater, from the 1993 Okushiri Japan tsunami, (Yeh and Li 2008).

1.2 Thesis objective

Based on these recent findings, a concerted international research effort has been made to create guidelines and standards to properly design critical infrastructure (such as vertical evacuation structures, bridges, and hospitals) to withstand tsunamis loads and effects. The Federal Emergency Management Agency (FEMA) in the United States has developed two sets of guidelines related to tsunamis: FEMA P55 (Fourth Edition, 2011) provides instruction on the design and construction of coastal structures to damage from natural disasters (such as hurricanes, earthquakes, and floods), and FEMA P646 (Second Edition, 2012) which provides formulations for specifically calculating tsunami loads on vertical evacuation structures. The Building Center of Japan has developed a code for the formulation of loads to inland structures as a result of tsunami flooding (Okada et al. 2005). The American Society of Civil Engineers (ASCE/SEI7) has also developed a design standard for incorporating tsunami-resistant design for structures in at-risk states (Alaska, Washington, Oregon, California, and Hawaii). The ASCE/SEI 7 Chapter 6 - Tsunami Loads and Effects (ASCE, 2016) is the world’s only design standard written in mandatory language. Section 6.12 provides conservative design guidance to assist with the estimation of tsunami-induced scour. These prescriptions are based on post-tsunami field surveys of scour observed around structures conducted by Tonkin et al. 2011.

This research encompasses a comprehensive experimental and numerical investigation and analysis for the scour mechanism and vortex structures due to inland-propagating tsunami-like bores on a dry or flooded horizontal mobile bed.

1.2.1 Primary objective

The key objective of this study is to simulate the unique features of the scouring process of a tsunami-like bore and observe the formation of local scour around a square structure. This study aims to improve the understanding of scour mechanisms due to inland propagating tsunami-like bore using experimental modeling. The main goal of the experimental work was to find the relation between the local scour depth and bore characteristics.

The overall objectives of the experimental work consist of investigating different parameters that might affect the bore characteristics and scour process.

1- Effect of bore height on the characteristics of a bore and scour process
2- Effect of bed condition on the characteristics of a bore and scour process

3- Effect of structure size on the flow field around the structure and scour process
4- Effect of bed material size on the flow field around the structure and scour process
5- Effect of subsequent cyclical tsunami waves, which may create significant scour around coastal structures

To achieve these primary objectives a series of hydraulic bores consistent with the dam-break wave theory were generated. A dam-break wave was generated by the release of water impounded behind a rapidly opening swing gate. A novel video-recording system was used to monitor the evolution of the scour and vortex structure. Image processing enabled tracking the time and spatial evolution of the scour and observations of sediment movement around the structure.

Specific research objectives related to the mechanics of local scour included analysis of the scouring process, sediment movement, flow field around the structures, infiltration rate, scour profile and time history of scour depths. Further specific research objectives related to analysis of bore characteristics included assessment of the bore profile, run up height, bore front velocity, the sustained flow velocity and stream-wise velocity. The quantification of these results and comparison with theory ensured that perfect hydraulic bores were being generated

1.2.2 Secondary objective

Ultimately, a numerical model was developed to replicate the physical experiments. Physical models provide the best replication of the scouring process under turbulent flows, although they require extensive preparation and are time consuming. Numerical simulations as an alternative method are less common in this field of study. Given the flow complexities, numerical models are difficult to develop, and especially when supercritical flows are also being simulated

In this study, an open source Telemac-Mascaret modeling system was used to simulate local scour due to a turbulent bore. Telemac is developed by Electricite de France (EDF) and has initially been created at Laboratoire National d'Hydraulique et Environment, (LNHE) of EDF R&D Department. TELEMAC is a set of modelling tools capable of simulating several aspects of natural free surface hydraulics: currents, waves, transport of tracers and sedimentology. The 3D hydrodynamics module (Telemac-3D) is based on the solution of the 3D continuity and Reynolds Averaged Navier-Stokes (RANS) equations with non-hydrostatic pressure approximation. 3D RANS equations are solved using a finite element discretization. The 3D hydrodynamic model is coupled internally with the sediment transport module SISYPHE.

The experimental data were used for the validation of the numerical models and for the assessment of their capabilities to predict tsunami- induced bore erosion and deposition. The efficiency of the numerical model was assessed quantitatively and qualitatively by comparison with the experimental results. Comparisons were made based on the scour evolution, final bed topography after the passage of the wave, as well as the run up recorded at the front of structure. Sensitivity analysis of the numerical results to several parameters was conducted, such as the turbulence model [including RANS (k-e, constant viscosity and mixing length) and LES (Smagorinsky) approaches], mesh refinement, bed roughness, critical shear stress as well as the sediment transport formula.

1.3 Scope

The objective of this thesis is to provide a comprehensive investigation and analysis for the scour mechanism and vortex structures due to inland-propagating tsunami-like bores on a dry or flooded horizontal mobile bed through experimental and numerical modeling. Due to time constraints and physical constraints of the laboratory environment, this study has some inherent limitations in the evaluation of the scour mechanism.

- The experiments were performed at a relatively small-scale (1:40 geometric scale or smaller). Due to limitation of the available laboratory facilities, this scale was chosen to be as large as possible while maintaining reasonable prototype scale flow conditions.
- Because of flume geometry limitations and in order to avoid sidewall effects and to minimize the channel blockage, only three structural sizes were investigated.
- Because of time restriction only square configurations with different cross section dimensions were investigated.
- Due to the lack of field investigation data regarding scour, the physical modelling experiments could not be directly validated using field data. However, the candidate did validate the prescriptions of ASCE7 Chapter 6 and a few limited field data.
- The physical modelling experiments employed an idealized topography. The influence of complex topographies with mixed or layer sediments was not investigated within this thesis.

- Due to both the limited volume of the impounding reservoir and the sediment bed thickness constraint, the duration of the sustained flow was limited when compared to actual tsunami-induced bores. However, the duration of sustained flow attained in this experimental program was sufficient to adequately quantify the quasi-steady hydrodynamic flow.
- The study considered flow propagation over a flat bed. Neither flow advancing over a sloped bed nor the reverse drawdown flow were considered.
- The experimental work was conducted using only two types of non-cohesive sediments, and scour induced by turbulent bore in a cohesive sediment bed was not studied.
- Sediment size could not completely be scaled geometrically using Froude scaling as per the flow and structure's characteristics.

1.4 Novelty of the study

Many aspects of this study are novel to this field of research. Scouring mechanisms associated with tsunami surge in a transient flow with duration of less than an hour differs from that of a steady current and a consistent short-wave field (river scour and seabed scour, respectively). There is lack of information and documentation about tsunami-induced scour across the international scientific community. Previous studies have mostly investigated the impacts of tsunami-induced forces on structures. Current design codes and guidelines provide only minimal information and recommendations for tsunami-induced scour around structures and they are mostly based on a limited amount of field observations and few lab tests. Studies focusing on tsunami-induced scour are less frequent, although it is documented that scouring is the primary cause of damage to coastal structures (Chen et al. 2016). Studies such as this one provides highly detailed measurements of local scour, leading to a better understanding of this unique scouring process. The research results will help improve methods of estimating local scour for future application in design codes. These findings can be used in improving and expending the existing design guidelines for tsunami loading or as a preliminary design recommendation for infrastructure in tsunami-prone areas.

Few studies in any context have investigated tsunami-induced scouring around coastal and offshore structures. Two studies that are the most related to this research are by Tonkin et al. in 2003 and Nakamura et al. in 2008 and McGovern et al. in 2019. The tsunami waves employed in these studies were solitary and long waves, respectively. At present, general scientific consensus indicates that solitary waves tend to be less representative of actual tsunamis (Madsen et al. 2008, Stolle et al. 2017). The use of hydraulic bores generated from dam break waves have been shown to replicate better the features of tsunami-induced flooding (Chanson, 2006).

Furthermore, the current study focuses on inland structures located on a dry or wet horizontal bed, rather than structures located close to shore on sloped wet beaches. Also, previous studies mostly observed final scour depth; however, in this study an innovative video-analysis system was used to record the evolution of the scour and vortex structure. Image processing provides highly detailed information of the scouring process, yielding temporal and spatial evolution of the scour around the structure.

Due to the complex nature of scouring in such a turbulent flow, different parameters should be considered in the tsunami scour estimation method. However, there is no research that performed parametric analysis of tsunami scour. In this study various parameters that might affect local scour were examined using experimental and numerical methods. These parameters include structure size, bore height, bed initial conditions (wet vs dry), median sediment size (d_{50}), and presence of a second tsunami wave.

Moreover, in this study numerical simulations as an alternative method for scour assessment has been used. Numerical models are used less commonly in this field of study, especially when supercritical flows are being simulated. The efficiency of the numerical model was assessed quantitatively and qualitatively by comparison with the experimental results.

In summary, the novelty of this study are as follows:

- Providing detailed measurements of tsunami-induced local scour
- Better understand this unique scouring process
- Improve methods to estimate tsunami-induced local scour for future application in design codes.
- Focus on inland structures located on a dry or wet horizontal bed, rather than structures located close to shore on sloped wet beaches.
- Detailed video-analysis system to record the evolution of the scour and vortex structure.
- Use of the dam break waves instead of solitary and long waves (Tonkin et al. 2003, Nakamura et al. 2008 and McGovern et al. 2019)

1.5 Publications

1.5.1 Journal articles

1- Scour mechanics of a tsunami-like bore around a square structure. *Journal of Waterway, Port, Ocean, and Coastal Engineering (ASCE),* Under second review. The manuscript can be found in Chapter 4.

2- Effect of bed condition (wet versus dry) on local scour due to tsunami like bore. *Coastal Engineering Journal,* under second review. The manuscript can be found in Chapter 5.

3- Structure width effect on local scour induced by turbulent bore . *Canadian Journal of Civil Engineering (CSCE),* under review. The manuscript can be found in Chapter 6

1.5.2 Conference papers and other refereed contributions

1- Experimental and numerical modelling of scour and erosion induced by turbulent bore. *The Canadian Society of Civil Engineering Conference (CSCE, 2020).*
The manuscript can be found in Chapter 7.

2- Experimental modeling of supercritical flows-induced erosion around structures, *the 6th International Conference on the Application of Physical Modelling in Coastal and Port Engineering and Science (Coastlab16), Ottawa, Canada, (2016).*
The manuscript can be found in Appendix B.

3- Modelling supercritical flow-induced scour around structures, *Proceeding of the Annual Conference of Civil Engineering, CSCE 2017, Vancouver, Canada, (2017).*
The manuscript can be found in Appendix B.

4- Scour mechanism around structures due to turbulent bores" *Young Coastal Scientists and Engineers - North America-2015,* University of Delaware, Delaware, USA, oral presentation, July 2015.

1.6 Outline of the thesis

- **Chapter 1.** provides an introduction to the study outlining the objectives, scope, contributions and publications from this research.
- **Chapter 2.** is a literature review in five divisions describing sediment transport, local scour, physical studies on scour, numerical modeling of scour in supercritical flows and

estimation of local scour in current design guidelines and standards. Also, discussions on the importance of further research on this subject are presented at the end of this section.

- **Chapter 3.** provides an introduction to the hydrodynamic and morphodynamic models used in this study along with brief descriptions of the discretization process and solution procedure.
- **Chapter 4.** presents a highly detailed analysis of the mechanics of scour around a square structure due to an inland-propagating tsunami-like bore using physical modelling. The article is in second review in Journal of Waterway, Port, Ocean, and Coastal Engineering (ASCE), and is titled “Scour mechanics of a tsunami-like bore around a square structure”. Different characteristics of a generated bore, final scour topography, and the relationship between scour depth and bore characteristics are assessed.
- **Chapter 5.** presents the effect of bed condition on bore characteristics such as bore free surface profile, bore front velocity, sustained flow velocity, runup, stream wise velocity of bore propagation and resulting local scour. Moreover, the effect of second tsunami wave was discussed. The article is under review in Coastal Engineering Journal, titled “Effect of bed condition (wet versus dry) on local scour due to tsunami like bore”.
- **Chapter 6**. aims to investigate the effect of structure size on local scour induced by the impact of rapidly advancing tsunami-like hydraulic bores on a freestanding square cross-sectional structure. The article is under review in Canadian Journal of Civil Engineering (CSCE), titled “Effect of bed structure size on bore propagation and resulting local scour”. Flow shallowness represents the effects of the depth of flow in relation to the pier width. The relationships between the flow shallowness and non-dimensional scour depth were discussed.
- **Chapter 7.** presents experimental and numerical results of bore-induced local scour around a square structure. The article was published in the proceedings of the Annual Conference of the Canadian Society for Civil Engineering (CSCE, 2020), titled “Experimental and numerical modelling of scour and erosion induced by turbulent bore”. The accuracy of the numerical model was assessed quantitatively and qualitatively by comparing its results with those obtained from the physical experiments. Comparisons are made based on the

scour evolution, final bed topography after the passage of the wave, as well as the run up recorded at the front of the structure.

- **Chapter 8.** outlines the conclusions of this study and provides recommendations for future work.
- **The Appendices** provide the hydrodynamic and sediment transport numerical parameters as well as modified Fortran codes developed for the numerical work (Appendix A), the published conference papers that were also part of the development of the thesis are included in Appendix B. Moreover, sensitivity analysis of the numerical results is also provided in Appendix C.

Chapter 2. LITERATURE REVIEW

This literature review consists of five main parts which presents current state-of-the-art research on scour under supercritical flows and an overview of the sediment transport. The first and second part provides various engineering aspects related to the local scour and tsunami induced scour. The third part presents different methods to physically model tsunami flow conditions. The fourth and fifth parts deal with experimental/field and numerical studies on scour. The sixth part provides some information about the current methods of estimating local scour in design guidelines.

2.1 Local scour

The formation of vortices at the base of piers or abutments causes local scour around them. Figure 2-1 shows a schematic of the flow field around a cylindrical pier. The downward flow on the upstream surface of the obstruction generates the horseshoe vortex at a bridge pier and causes acceleration of the flow around the nose of the pier. The horseshoe vortex causes removal of the bed material around the base of the pier. A scour hole develops as the amount of sediment moving away from the base region is greater than that transporting into the hole. The strength of the horseshoe vortex is reduced, as the depth of scour increases. Moreover, there are some vertical vortices called the wake vortex downstream of the pier, which also cause removal of bed material. Further downstream of the pier the intensity of wake vortices decreases which causes deposition of bed material (Arneson et al. 2012).

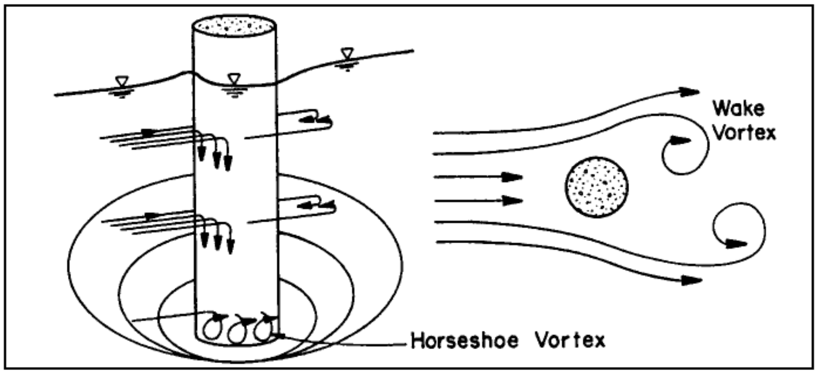

Figure 2-1*: Main feature of flow field around the pier in steady flow (Arneson et al. 2012)*

There are two conditions for scour in a steady flow: clear-water and live-bed scour (Kothyari et al. 1992). Clear-water scour is the condition where there is no transport of the bed material from the upstream of the pier. The obstruction of flow at the pier or abutment accelerates flow around the structure causing the bed material to move. In contrast, live-bed scour occurs when there is transport of bed material from the upstream reach into the crossing. The scour hole cyclically deepens during the rising stage of a flood and refills during the falling stages.

Clear-water scour reaches its maximum magnitude over a longer period of time compared to live-bed scour, (Figure 2-2a, Kothyari et al. 1992). This is because clear-water scour occurs mainly in coarse-bed material streams and it may reach a maximum depth after several floods. Maximum local clear-water pier scour is about 10 percent greater than the equilibrium local live-bed pier scour. If the mean velocity (V) in the upstream flow is equal to or less than the critical velocity (V_c) of the median diameter (D_{50}) of the bed material, local scour will be clear-water scour. Conversely, if the mean velocity is greater than the critical velocity of the median bed material size, live-bed scour will occur, (Figure 2-2b, Bruce et al. 1999).

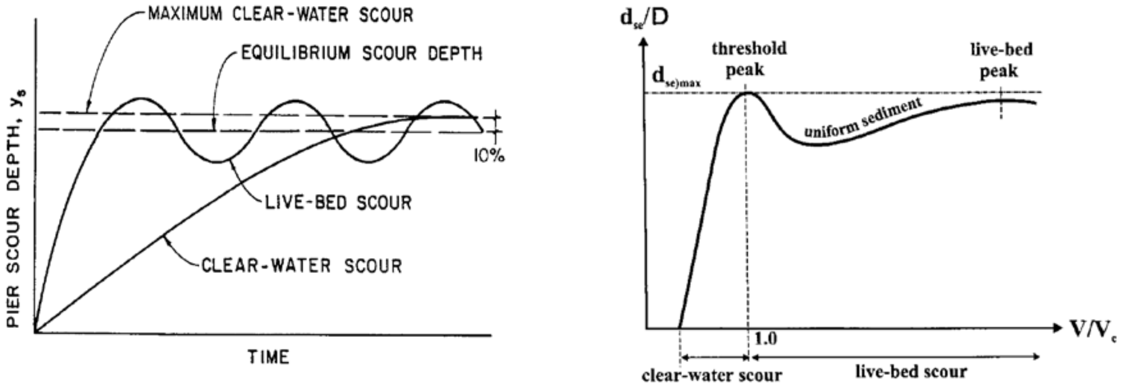

a) Pier scour depth in a sand-bed stream as a function of time, Kothyari, et al. (1992)

b) Influence of Flow Intensity, Bruce et al. (1999)

Figure 2-2(a,b): variation of local scour depth with flow velocity and time

2.1.1 Time phases of the scour process

Hoftmans (1993) described several phases in the scour process behind hydraulic structures. The flow pattern and the sediment transport along the upstream slope of the scour hole have been investigated by these authors and four phases in the evolution of a scour hole were identified as: 1- initial phase, 2- development phase, 3- stabilization phase and 4- equilibrium phase.

Initial phase: The flow in the scour hole is almost uniform in the stream-wise direction in the early stage. In this phase of the scour process, the erosion capacity is most intense compared to the erosion capacity observed in the other phases of the scour process. Also, Breusers (1966) showed that in the initial stage a certain amount of bed material near the upstream scour slope goes into suspension. Most of these suspended sediments are transferred with the main flow and stay in suspension due to the internal balance between the upwards diffusive flux and the convective (downwards) flux, Figure 2-3. Some of these particles will deposit and go into suspension again due to the large bursts of the turbulent flow near the bed. Some particles with a jump height smaller than a reference height are transported as bed load (Hoftmans, 1993).

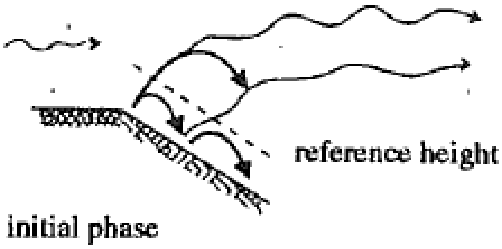

Figure 2-3: Schematization of sediment transport along upstream scour slope (initial phase), (Hoftmans, 1993)

Development phase: In the development stage the scour depth increases significantly, but the form of the scour hole does not change. Measurements of Hoffmans (1990) showed that the upper part of the upstream scour slope is in equilibrium, while the lower section is still in motion. The amount of suspended load close to the bed is reduced compared to the initial phase due to the decrease in flow velocities near the bed over time. Bed particles are picked up and moved by the flow, but the time-averaged amount of the sediment transport in the upper part of the upstream scour slope is small. This is due to recirculation within the scour hole: sediment transport rate due to the instantaneous reverse flow velocities are almost equal to the rate of sediment transport due to the instantaneous streamwise flow velocities (Figure 2-4).

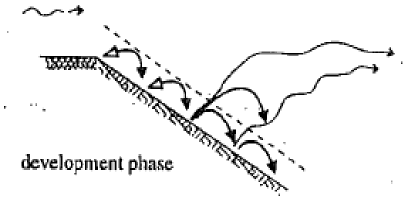

Figure 2-4: Schematization of sediment transport along upstream scour slope (development phase), (Hoftmans, 1993)

Stabilization phase: In the stabilization stage the development of the maximum scour depth decreases. In the deepest part of the scour hole, the erosion capacity is lower than the erosion capacity downstream from the point of reattachment. As such, the dimensions of the scour hole increase more in the streamwise direction than in the vertical direction. The more the scour process continues, the more the flow velocities above the lower part of the upstream scour slope decrease. In this phase the equilibrium condition for scour slope at the upstream part and the maximum scour depth are almost reached (Figure 2-5).

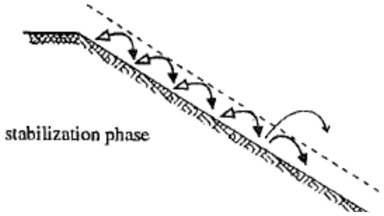

Figure 2-5: Schematization of sediment transport along upstream scour slope (stabilization phase), (Hoftmans, 1993)

Equilibrium phase: In the equilibrium phase the dimensions of the scour hole no longer change significantly. Generally, in this phase of the scour process, the bed particles at the upstream scour slope are only rolling and sliding beneath a saltation height (Figure 2-6).

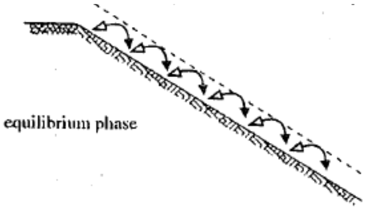

Figure 2-6: Schematization of sediment transport along upstream scour slope (equilibrium phase), (Hoftmans, 1993)

2.1.2 Scour depth prediction model

Numerous studies have been conducted to understand the mechanism of the scour process around a structure in steady flow. Due to the complex nature of scouring, different parameters should be considered in the scour estimation method. Therefore, it is challenging to formulate a mathematical model to achieve a general theory for predicting the scour. Table 2-1 shows some of these equations found in literature that consider various parameters such as: structure size (a), flow velocity (u), median sediment size (d_{50}), Froude number (Fr), water depth (y_1), and coefficient (k_i) which accounts for the angle of flow and for live-bed or clear-water flow condition.

Table 2-1: Different scour depth prediction models

Scour depth equations	**Proposed by:**
y_{se}=0.946 $\left(\mathrm{Q}/1.76\sqrt{d_{50}}\right)^{1/3}$: $d_{50}\ in\ mm$	Lacey and inglis (1959)
y_{se}/y_1=2.15$\left(u/\sqrt{gy_1}\right)^{0.33}(a/y_1)^{0.4}$	Liu et al. (1961)
y_{se}/y_1=6.65$Fr-0.51-5.49{Fr_1}^2$	Chitale (1962)
y_{se}=2.278$\left(q^2/1.76\sqrt{d_{50}}\right)^{1/3}+2.5a$: $d_{50}\ in\ mm$	Chitale (1988)
$y_{se}=1.4a$	Bresusers (1965)
$y_{se}/y_1=1.95(a/y_1)^{1/6}-1$	Arunachlam (1965)
$y_{se}/y_1=2.43(a/y_1)^{1/4}$	Blench (1966)
$y_{se}/a=3.3(d_{50}/a)^{0.2}(y_1/a)^{0.13}$	Hancu (1971)
$y_{se}/a=2.42\left(2\frac{u}{u_c}-1\right)\left(\frac{u^2}{ga}\right)^{1/3}$	Hancu (1971)
$y_{se}=1.5a$	Neil, (1973)
$y_{se}=538(u_r r)^{1.28},\ d_{50}\leq 0.5\ mm$ $u_r=0.092a^{-0.5}u^{0.83}, r=0.1a$	Qadar (1981)
${}^{y_{se}}/_{a}=1.41\left({}^{y_1}/_{a}\right)^{0.3}\left({}^{u_c}/_{\sqrt{gy_1}}\right)^{0.25}$	Jain (1981)
${}^{y_{se}}/_{y_1}=2.02{Fr_1}^{0.21}{\sigma_g}^{-0.24}\left({}^{a}/_{y_1}\right)^{0.98}$	Johnson (1992)
$y_{se}=1.35a^{0.7}y_1^{0.3}$	Breusers (1977)
$y_{se}=2.2K_i y_0 F_r^{0.43}\left(\frac{a}{y_1}\right)^{0.65}$	CSU :Colorado state university
$y_{se}=2.3a$	Raudkivi (1986)
$y_{se}=0.000223R_b^{0.619}$	Shen (1969)
$y_{se}=k_{ya}k_I k_d k_s k_t k_\theta$	Melville (2000)

It should be noted that all these equations do not consider time (*t(s)*), and thus consider only equilibrium scour. However, a few researchers have considered the time evolution of scour toward the equilibrium condition. For example, Pilarczyk (1998) proposed a method for prediction of scour depth as a function of time and the equilibrium scour depth for clear water scour.

$$\frac{y_m}{y_{m,e}}=1-\,e^{\ln\left(1-\frac{\lambda}{y_{m,e}}\right)\left(\frac{t}{t_1}\right)^{\gamma}} \qquad 2\text{-}1$$

in which: t_1 = characteristic time at which y_m = λ(s), y_m= maximum scour depth at t (m), $y_{m,e}$= equilibrium scour depth (m), γ = coefficient (-) and λ = characteristic length scale (m). In the development phase, when t << t_1, equation (2-17) converts to the equation (2-2) originally proposed by Breusers (1966):

$$\frac{y_m}{\lambda} = (\frac{t}{t_1})^{\gamma} \qquad 2\text{-}2$$

Values of γ range from 0.2 to 0.4 for two-dimensional flow. The turbulent length scale has many definitions in literature; it represents the size of turbulent eddies. In shallow water conditions the size of the largest eddies is of order of the water depth, which thus can be used as the characteristic length scale. On the other hand, in deep water conditions the dimensions of the hydraulic structure can be used as λ.

Moreover, Gumgum and Guney (2020) derived the following equation for time dependent live bed scour under flood waves.

$$\frac{d(t)}{b} = 1.43 \left[\frac{V}{V_c} - I_w\right]^{0.37} \left[\frac{y}{b}\right]^{0.36} (1 - e^{-0.007T}) \qquad 2\text{-}3$$

Various regression analyses were performed by using a large amount of data. In order to derive an equation to predict the temporal live bed scour depth, the flow intensity (V/V_c), the dimensionless flow depth (y/b) and the dimensionless time (T) were taken as effective parameters. $d(t)$ is the time dependent scour depth; y is the approach flow depth: b is the pier width; I_w is the threshold value of the flow intensity that causes the incipient sediment entrainment, this value was suggested as 0.5 by Breusers (1977). T is obtained from the following equation for each time step of the flood, where ρ and ρ_f are the densities of the sediment and water, respectively.

$$T = \frac{\sqrt{g\ (\rho/\rho_f - 1) d_{50}}}{b} t \qquad 2\text{-}4$$

2.2 Tsunami induced scour

The tsunami scour mechanism is the result of the physical interaction between water, soil and structures. While it is similar to other scour events, it differs greatly in time, space, and magnitude (Francis, 2006). Post-tsunami field survey evidence indicates that destructive tsunamis cause substantial coastal sediment mobilization (Chen et al. 2016). Measurements collected from several tsunami events, such as the 1992 Nicaragua Tsunami and the 2004 Indian Ocean Tsunami, have recorded substantial evidence of scour around damaged buildings and bridge foundations (Yeh and Li (2008), Ghobarah et al. 2006, Saatcioglu et al. 2006a, Saatcioglu et al. 2006b, Chock et al. 2013). These field surveys noted that scouring was one of the primary causes of coastal structural damage (Chen et al. 2016). Tsunami waves with inundation depths of 5–25 m have been measured following several major recent tsunami events (2004 Indian Ocean and 2011 Tohoku Tsunami). Coastal inundation is inevitably accompanied by high flow velocities both during the inland flow as well as during the drawdown phase. These high flow velocities produce high bed shear stresses and large amounts of sediment movement over large areas, resulting in substantial beach erosion and scouring around a large number of structures (Ghobarah et al. 2006, Saatcioglu et al. 2006a, Saatcioglu et al. 2006b, Chock et al. 2013 and Li et al. 2012).

The scour formation mechanisms under tsunami loading are similar to those generated by storm waves: however, some differences do exit between the two. Storm waves have a period of seconds and act over durations of hours. Tsunamis have only a few waves, however, each with a period of minutes to tens of minutes. Moreover, depending on the coastal topography, the typical tsunami inundation distance can be of a few tens of meters to several kilometers, much greater than the inland storm wave penetration.

The presence of live bed behavior with maximum scour depth greater than the end of event scour depth was observed during tsunami experimental modeling (Yeh & Tonkin, 2004). Complex tsunami inundation flow patterns likely include both live bed and clear-water conditions. Perhaps more clear-water conditions are prevalent during runup of the first wave, transitioning to live bed conditions during drawdown and the inflow of subsequent tsunami waves. This complicates the effort to explain field observations, since observed scour depths may not represent the maximum depth, or conditions producing observed levels of damage (FEMA 2000).

Based on the geometry of the scour feature and the type of flow that caused the scour, observed tsunami inundation scour characteristics are divided as four significant mechanisms (Tonkin et al. 2013), as follows.

Local Scour is a deep scour hole around or under a structure. “Local scour” is loss of material resulting from sustained shear flow around a structure. An example of this type of scour hole is shown in Figure 2-7.

Overtopping Scour occurs when inundation flow overtops a structure (often a tsunami barrier or seawall) and plunges onto the landward toe surface with concentrated jetting action (Figure 2-8).

Channelized Scour is where massive flow is diverted to a small area; vertical scour lines often form alongside a barrier to flow. This type of scour is associated with large-scale hydrodynamics in which the incident or (more often) return flow is forced into a channel over a relatively long distance. Channelized scour can occur in the free field, in pre-existing channels, or as long-shore flow adjacent to a road (Figure 2-9).

General Scour is represented by loss of land surface over a considerable portion of the inundation area, where high flow velocity and high shear stresses at the soil water create vast zones of erosion. This type of scour may also be increased through pore pressure softening leading to full liquefaction, residual soil strengths, or high pore-water gradient shear erosion (Yeh and Li 2008). General scour specifically excludes local scour actions (Figure 2-10). The available observational data does not include sufficient channelized or general scour data to validate predictive methods specific to those types. Flow duration likely affects scour depth for channelized scour, such as for return flows sustained over a significant event period. General scour typically has not been observed to damage structures (other than pavement), though it may contribute to failures by other scour mechanisms in cases where they interact.

Figure 2-7: Local scour, Koh Khao, Thailand. Case SS-4. Tonkin et al. (2013)

Figure 2-8: Overtopping scour, Taito Port, Japan. Case TO-1. Tonkin et al. (2013)

Figure 2-9: Channelized scour. Great Nicobar Case RS-3. Tonkin et al. (2013)

Figure 2-10: General scour. Yamamoto-cho, Japan. Case TN-12. Tonkin et al. (2013)

2.3 Physical modelling of tsunami flow conditions

Tsunamis propagate over a wide variety of bed and coastal topography, which makes modelling of tsunami flow conditions the most complicated aspect of tsunami modeling. The variation in the environmental conditions result in a large variation in the wave period and wave shapes (Sriram et al. 2016). As shown in Figure 2-11, Takahashi et al. (2011) identified differences in tsunami inland inundation from the 2011 Tohoku tsunami based on coastline configurations:

a) Breaking wave type: tsunami wave breaks near the shoreline of a mild-sloping beach, runs up the sand dune and propagates over the low-lying land behind the dunes.

b) High runup type: tsunami wave breaks on a relatively steep slope and rapidly reaches high runup heights.

c) Slowly varying type: Steep cliffs facing relatively deep-sea fronts resulting in the tsunami wave not breaking and moving relatively smoothly up and down.

d) Overtopping type: Relatively deep-sea fronts with relatively flat land results in the tsunami wave rapid overtopping and inundation.

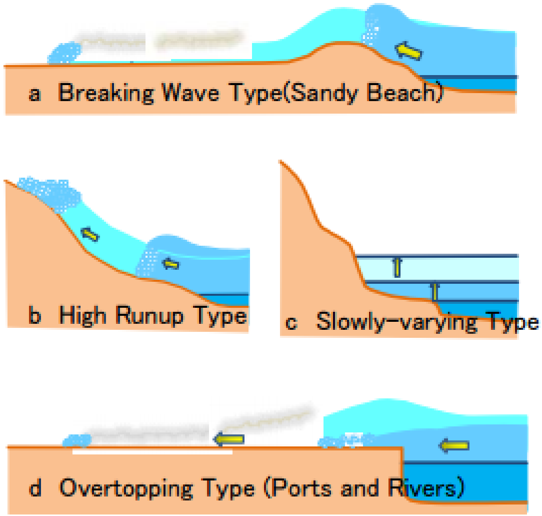

Figure 2-11: Potential tsunami inundation profiles (adopted from Takahashi et al. (2011)).

Different approaches have been used in the past for experimentally generating a tsunami flow condition. As a result of research attempts to model asymmetry of the long waves in the shoaling process and the large space- and time-scales associated with the tsunami wave, modelling of tsunami flow conditions has developed through many studies (Madsen, 2010). Carrier and Greenspan (1958) derived an analytical solution of fully non-linear non-breaking waves on a uniformly sloping beach and later used the solution to model maximum tsunami inundation (Carrier et al. 2003). Based on the Carrier and Greenspan (1958) solution, conoidal waves (Synolakis et al. 1988) and N-waves (Tadepalli and Synolakis, 1994) have been used in the modelling of tsunami waves for maximum wave runup (Synolakis et al. 1988, Tadepalli and Synolakis, 1994, Madsen and Schaeffer, 2010).

Solitary waves and long waves generated in an experimental flume or wave basin have been used previously to simulate tsunami waves. However, such waves generated in the laboratory have a major limitation related to their period as it is difficult to ensure the proper time scale for the duration of such solitary waves. Solitary waves may be too short in duration compared to real tsunamis, and long waves may have insufficient initial velocity. While the use of solitary waves is still acceptable for investigating initial wave impacts, in order to investigate scour occurring during a tsunami event, one needs more realistic scaling of the duration of the tsunami—induced bore. Madsen et al. (2008) noted that many of the solitary wave studies failed to establish any correlation to geophysical tsunamis and showed that the traditional solitary wave had relative time- and space-scales on the order of several orders of magnitudes smaller than field surveys of the 2004 Indian Ocean tsunami.

Recently, elongated solitary waves have been successfully generated in laboratory conditions and have shown more reasonable length and time-scales (Goseberg et al. 2013). Combining the solitary wave front, that has been extensively used as a reasonable estimation of the hydrodynamic loads for near-shore and debris motion studies for near-shore and debris motion studies (Arikawa, 2011, Chinnarasri et al. 2013, Seiffert et al. 2014, Yao et al. 2014, Wutrich et al. 2018, Stolle et al. 2019, Wutrich et al, 2019) with the elongated tail give a much better representation of near-shore tsunami flow conditions. Sriram et al. (2016) showed that the runup time-series of the elongated solitary wave had a similar profile to forensic engineering results from the 2009 Samoa tsunami. However, the elongated solitary waves tend to require large-scale facilities, which can often be limiting.

Moreover, lately, a combination of steady flows and waves have been combined numerically by Larsen et al. (2017) and, later, experimentally by Larsen et al. (2018) for tsunami-induced scour around offshore wind turbine monopiles. Foster et al. (2017) noted that, over shorter time scales, tsunamis are cyclic over their defined period T and can be assumed to exhibit quasi-steady currents. McGovern et al. (2019) also conducted a series of experiments using a Pneumatic Long Wave Generator to create tsunami-like oscillatory flows with wave periods of 25–147 s equivalent to 3–17.3 minutes at a 1:50 Froude scale.

Over the past decade, a new approach for experimentally reproducing tsunami-induced hydraulic bores is to generate a dam-break wave by rapidly releasing water impounded behind a gate into a straight channel. Chanson (2006) analyzed visual images of an actual tsunami bore from the 2004 Indian Ocean Tsunami and concluded that the flow characteristics of tsunami-induced bores are similar to those of a dam-break wave. Chanson (2006) reported the following equations for the free surface profile.

$$\frac{1}{9}\left(2-\frac{x}{t}\right)^2 \qquad -t \le x \le \left(\frac{3}{2}U-1\right)t \qquad \text{2-5}$$

$$d = \sqrt{\frac{f}{4}U^2(x_s - x)} \qquad \left(\frac{3}{2}U-1\right)t \le x \le x_s \qquad \text{2-6}$$

wherein:

d = Dimensionless flow depth measured normal to the invert: $d = \frac{d^{'}}{d_0^{'}}$

$d^{'}$ = Flow depth (m) measured normal to the invert

$d_0^{'}$ = Initial reservoir height (m) measured normal to the chute invert

x = Dimensionless longitudinal distance measured from the dam wall:

x_s= Dimensionless wave front position

U = Dimensionless wave front celerity:

For turbulent motion, the flow resistance may be approximated by the Altsul formula:

$$f = 0.1\left(1.46\,\frac{k_s'}{D_H'} + \frac{100}{\mathrm{Re}}\right)^{1/4} \qquad \text{2-8}$$

where k_s' is the equivalent sand roughness height, D_H' is the hydraulic diameter, and Re is the flow Reynolds number (Idelchik, 1969, 1994; Chanson, 2004a).

Imamura et al. (2008) used a dam break wave to model the motion of entrained boulders, Arnason et al. (2009) examined the interaction of bores with free-standing structures, and Al-Faesly et al. (2012) evaluated mitigation walls and their effectiveness at limiting tsunami impacts forces. Dam break waves have been particularly prevalent in numerical modelling due to the relative simplicity of developing the wave as opposed to the generation of other wave maker mechanisms (Canelas et al. 2013, Amicarelli et al. 2015). In the present study, the dam break approach has been utilized to generate hydraulic bores to simulate tsunamis in the laboratory.

2.4 Physical studies on tsunami induced scour

Several studies have stressed that scour was the main failure mechanism for many coastal structures during the 2011 Tohoku tsunami (Jayaratne et al. 2016). Numerous experimental studies over the past several decades have investigated the scour mechanisms around vertical cylinders and breakwaters, including Van et al. (2007), Mazumder and Ojha (2007), Zhao et al. (2010), Yeh (2010), Kato et al. (2006, 2012), Yeganeh-Bakhtiary et al. (2012), Arikawa et al. (2012), Arya and

Shingan (2012), Larsen et al. (2016) and McGovern et al. (2019). Post-tsunami investigations of scour include Wilson et al. (2012) in harbours, Bricker et al. (2012) at coastal defences, and Chen et al. (2013) at coastal roadways. Bricker et al. (2012) conducted a field study of scour depths measured on the landward side of seawalls and floodwalls, as well as beside a building foundation footing, from the 2011 Tohoku tsunami.

Vu Thanh Ca et al. (2012) proposed prediction methods on the maximum scour depth and its position at the beach in front of a seawall. They reported that in the case that the crown height of a seawall is fairly high compared with the thickness of a back-flow on the crown, the back-flow separates from the crown and draws a parabolic curve. They made a beach of slope 1/15 using sand (0.2 mm) or gravel (10mm) as well as two seawall models in a water channel (50 cm wide, 80cm height and 22m length) in which a large tank was installed for generating back-flow. They then conducted scour experiments, and measured the velocities on the seawall crown with a disc-shaped electromagnetic current meter and read the thicknesses of backflow on the seawall crown and the scour depths in video photographs as seen in Figure 2-12 and Figure 2-13.

Figure 2-12: State from which the scour by a back-flow started

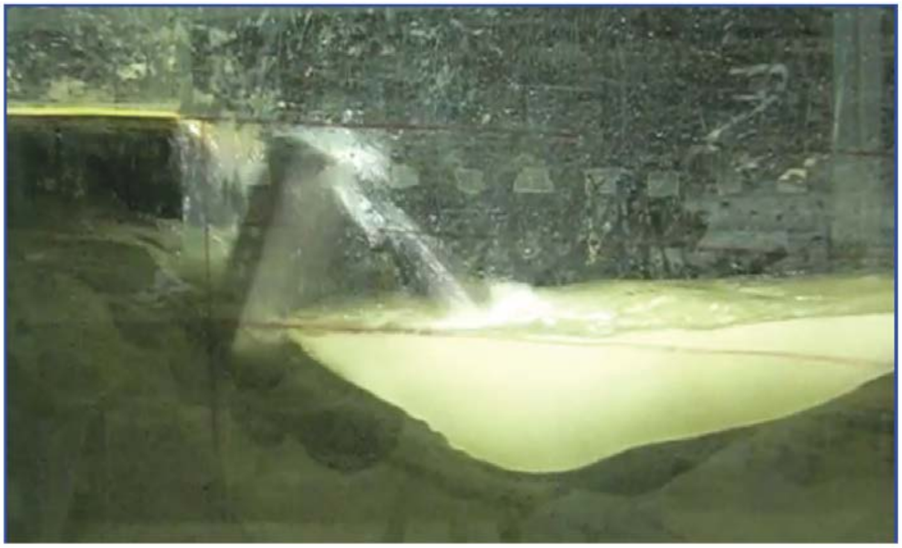

Figure 2-13: State to which the scour by a back-flow fully progressed

However, experiments related to scour around structures caused by tsunamis are limited to few studies. Two studies that are the most related to the research at hand will be reviewed in detail in this section. The first, by Tonkin et al. (2003), examined scour around a cylindrical structure located on a sloped sandy beach, whereas the other study by Nakamura et al. (2008), focused on scour around a square structure located on a horizontal sand bed.

Tonkin et al. (2003) used a pier-like cylindrical structure made of Plexiglas for their physical scour experiments. The structure had a diameter of 50 cm and was located near the crest of a 1:20 sloped sand beach, with a median grain size of 0.35 mm. For certain tests, a gravel collar (D_{50}=3.6 mm) surrounded the base of the cylinder. The tsunami waves were simulated by generating solitary waves using a piston type wave maker at a location offshore from the sand slope. Based on runup heights, the scale of the waves was approximately 1:10 of a realistic tsunami wave.

Measurements were taken using capacitance type wave gauges, pressure transducers, electromagnetic flow meters and miniature CCD cameras. The pressure transducers were placed in the sand below the initial level of the bed and the cameras were located inside the cylinder. The parameters varied in the different test runs were the still water depth, the incident wave height, the embedded depth of the cylinder and the presence or not of the gravel collar. Most observations made by Tonkin et al. (2003) were taken from the video footage of the cameras located within the cylinder (Figure 2-14).

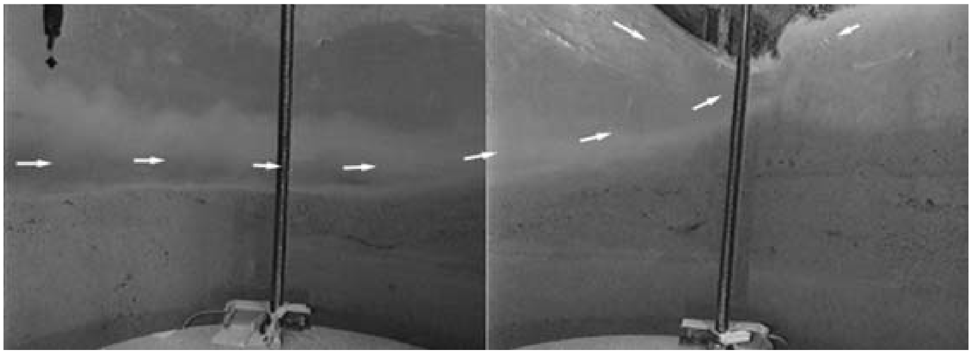

Figure 2-14: Example of images recorded from inside the cylinder, Tonkin et al. (2003)

The cameras were able to record the temporal formation of the scour hole and covered the entire contour of the cylinder at the level of the water/sand interaction (Figure 2-15). Tonkin et al. (2003) observed that the runup of the waves caused a rapid flow along the sides of the structure and scour holes were created at both offshore corners of the structure. Along the sides of the structure, the flow was strong and sediment was brought into suspension and transported onshore. Once the flow velocities decreased and the scour hole had reached its maximum depth, deposition of the suspended sediment occurred. The sediment scoured on the sides of the structure also rolled down the steep slope formed during the uprush and slowly filled the scour hole at the corner of the structure. The final maximum scour depth was therefore observed to be only 75% to 90% that of the actual maximum scour depth. The observations of the scour mechanism in both sand and gravel beds during each phase are summarized as follows:

- *Wave impact and immediate breaking*:

Horseshoe type vortex forms at the front of the cylinder, due to the overturning breaking motion of the wave. Scour hole forms, which is much deeper for the gravel substrate than for the sand

- *Runup period*:

Sand: scour at the front and sides of the cylinder causes the particles to become suspended and the sand is transported onshore, away from the cylinder

Gravel: scour at the front and sides of the cylinder causes the particles to move as bedload towards the back of the cylinder, where they settle into a uniform slope

- *Early drawdown period*:

Sand: very little scour at the back

Gravel: particles are entrained down the slope and are transported offshore by the force of a vortex sheet formed on the sides of the cylinder

- *Final drawdown period*:

Sand: a very turbulent horseshoe vortex forms at the back of the cylinder, which scours an important quantity of sand

Gravel: the scour hole formed in the previous stages is filled by gravel particles that were earlier transported onshore.

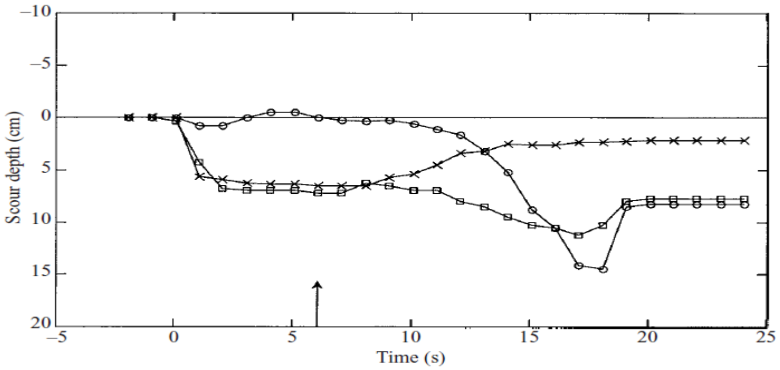

:

Figure 2-15: Time development of scour around a cylinder on a sand bed (crosses: front, squares: sides, circles: back), Tonkin et al. (2003)

In addition to this general scour mechanism, Tonkin et al. (2003) also observed scouring effects caused by pore pressure gradients. The pressure transducers measured a significant drop in pore pressure during the rapid drawdown period of the tests (Figure 2-16). Pore pressure drops were mostly measured for the tests with a sand bed. The drawdown period also coincided with the maximum scour depths at the back of the cylinder.

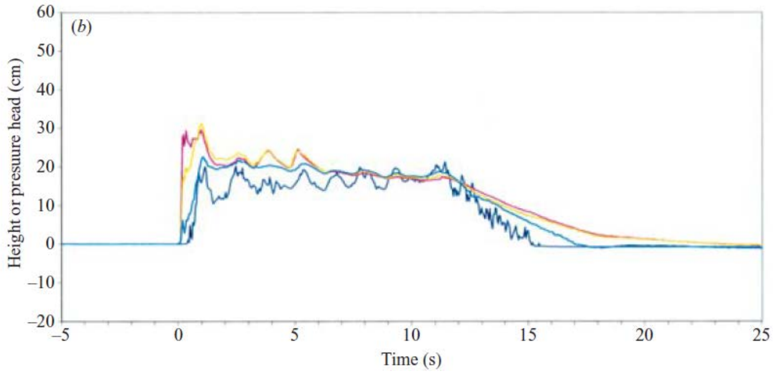

Figure 2-16: Wave height (blue) and pore pressures (all other colors) at the back of the cylinder on a sandbed, Tonkin et al. (2003)

The measured pore pressures indicated gradients and reached up to half of that required for liquefaction. Tonkin et al. (2003) therefore concluded that the loss of sediment cohesion due to the pore pressure gradients caused the sand to be scoured more easily during drawdown and were the main factor in the formation of the large scour hole behind the cylinder. Tonkin et al. (2003)'s methodology is cited in the ASCE (2016) Chapter 6: 'Tsunami Loads and Effects' design standards.

The study undertaken by Nakamura et al. (2008) has both similarities and differences with the one by Tonkin et al. (2003). Nakamura et al. (2008) also chose to study the local scour around piers induced by tsunami waves focused on land-based structures. The setup used for the physical experiments consisted of a long-sloped beach leading to a steep revetment. On the onshore side of the revetment, a horizontal sand bed was used as the foundation backfill for a 0.14 m wide wooden structure.

The test runs were performed using solitary and long-period waves. Both types of waves were generated using a piston-type wave maker. The duration of the long-period waves was approximately double that of the solitary waves. The parameters modified in the different runs included the still water depth, the incident wave height, the embedded depth of the structure, the wave period of the long waves, the widths of the structure (0.10 m and 0.14 m) and the median grain size of the sand particles (0.2 mm and 0.45 mm). Measurements were taken using capacitance type wave gauges, pore water pressure gauges and video cameras. For the 0.14 m wide structure, an alternate acrylic material was used, and thus a camera was placed inside the structure to record the scour formation at the offshore corner. The scouring mechanisms observed by Nakamura et al. (2008) was similar to that observed by Tonkin et al. (2003), but differed in some details because of the different geometry of the structure and the lack of drawdown in the experiments. Nakamura, et al. (2008) determined that the duration of the solitary waves was too short to properly simulate tsunami scour. In the case of the long-period waves, the duration of the flow was long enough that the sand located behind the structure was also scoured (Figure 2-17a, b).

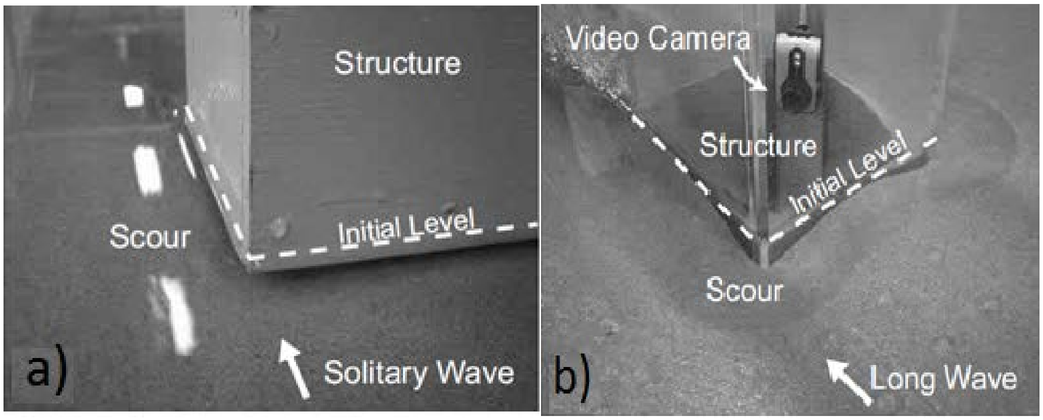

Figure 2-17: Video images showing b) undermining of the corner of the structure and d) scour hole pattern, Nakamura et al. (2008)

In cases where the embedded depth of the structure was small, the scouring was even able to undermine the offshore corner of the structure. The main conclusions of the study were that the final scour depth increases as the overtopping height increases, and that the maximum scour depth does not coincide with the final scour depth.

Moreover, lately, McGovern et al. (2019) also conducted a series of experiments using a Pneumatic Long Wave Generator to create tsunami-like oscillatory flows with wave periods of 25–147 s equivalent to 3–17.3 minutes at a 1:50 Froude scale. In their study, waves propagate over a slope before impinging over a flat wet sediment pit in which a square structure was placed. They used the Keulegan-Carpenter (KC) number which includes the period of the flow and its velocity which are the two key parameters in wave and current scour studies. McGovern et al. (2019) concluded that the instantaneous scour development is similar to that generated by a current or even a tidal current, due to the long period of the inundation by comparing the long wave scour with current and tidal current scour.

McGovern et al. (2019) concluded that the rate of onshore scour development varies with time due to the changes in flow velocity and depth and that the scour depths is more dependent upon inundation duration than velocity for their particular experimental conditions. They also reported that KC influence is not necessarily the same as observed for wind wave and current scour due to transition of tsunami from wave-like to current-like flows during inundation.

A few experiments have investigated tsunami bore induced scour around coastal structures, such as those by Triatmadja et al. (2011), Shafiei et al. (2015) and Lavictoire et al. (2014). Triatmadja et al. (2011) investigated the scour around cylindrical and 0.045 m X 0.045 m square prism structures located on a sloped sand bed using a flume 20.4 m long and 0.60 m wide. They reported that, the ratio of the maximum scour depth around the structure to the flow depth was from 0.2 to 0.3, and that the maximum scour depth around the square prism structure was slightly larger than that around the cylindrical structure. However, no dynamic scouring process was measured in their experiment. Lavictoire et al. (2014) used dam-break waves to investigate tsunami-like bore-induced local scour around a cylindrical structure (as shown in Figure 2-18) and found that the short duration and very turbulent nature of the bore resulted in a rapid scour process.

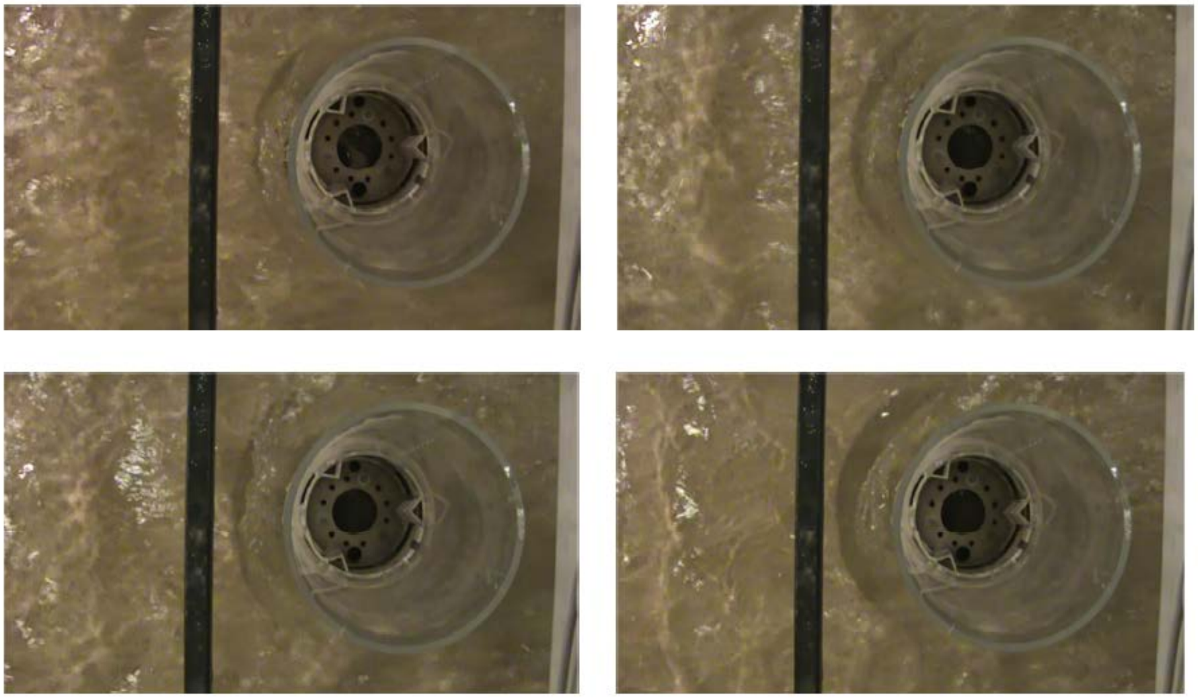

Figure 2-18: Temporal Formation of Local Scour Hole in Sand at 5 second Intervals

Lavictoire et al. (2014) found that the ratio of scour depth to flow depth ranged between 0.6 and 1.8. This ratio is significantly larger than that reported by Triatmadja et al. (2011). In addition, Lavictoire et al. (2014) reported that the scour depth was highly dependent on the bore velocity. Similar to Triatmadja et al. (2011), they only measured the final scour depth. Shafiei et al. (2015) investigated the tsunami-like bore induced scour around inland structures placed on a wet sandy foundation using three model structures: a square prism, a diamond prism, and a cylinder. They observed that maximum scour depth during and after the bore impact increased with increasing bore strength and that the structure’s shape had a significant influence on the maximum scour depth.

2.5 Numerical modeling of scour in supercritical flows

Although most research and literature in the study of scour in supercritical flows is based on physical experimental work, some authors have combined these physical tests with simulations in numerical models. The following section will provide an overview of certain numerical models created for different scenarios of scour in supercritical flows

Most numerical models for water wave transformations fall into one of the following three categories according to the assumptions (Lin and Liu, 2000): depth-averaged models, potential flow models, and Navier Stokes (NS) equation-based models, arranged in the order of increasing flexibility, complexity, and computational cost. Potential flow models are not suitable for simulating breaking waves since the irrotational flow assumption is not valid during wave breaking. NS based models (including Reynolds averaged NS simulations, large eddy simulations, and direction numerical simulations), on the other hand, are computationally expensive, and surface tracking or interface capturing methods are needed to locate the moving free surface.

Tsunami sediment motion and scour were discussed by Yeh and Li (2008) using a hypothetical analytic solution of typical tsunami condition. They demonstrated that a tsunami is capable of causing sediment motion even far offshore in both the runup and drawdown phases, and that the drawdown process is slightly stronger than the runup. They concluded that significant sediment motion in the form of bed load and suspension occur nearshore close to the maximum runup penetration. Approximately 80% of the total inundation distance from the initial shoreline can be subject to significant bed-load transport, and 65% of the inundation area is subject to fully suspended flows.

In the offshore area, significant sediment motions are anticipated up to the location of the maximum drawdown. Their model also demonstrated that momentary liquefaction may result during the drawdown phase. They also discussed about the condition that causes flow separation at the wave (bore) front. The backwash flow against the approaching wave (bore) plays a crucial role in triggering separation of the flow at the bed. This implies that a leading depression wave followed by a large height wave can effectively induce sediment suspension. On the other hand, flow attachment likely takes place during flow reversal near the maximum inundation area, which promotes sediment deposition. Yeh and Mason (2014) performed a similar analysis and compared results to laboratory and field data.

Another numerical model was developed by Nakamura et al. (2008) to simulate the scour around a square structure induced by the passing of a tsunami wave. The development of the numerical model was based on a principle introduced by Hur et al. (2007), in which two numerical sub models are coupled in order to better simulate the wave-seabed interactions. Nakamura et al. (2008) therefore decided to use a volume of fluid (VOF) sub model to simulate the wave field coupled with a finite element model (FEM) to simulate the sand foundation. They added surface tension effects based on the CSF (Continuum Surface Force) model and then introduced the large eddy simulation (LES) based on the dynamic two-parameter mixed model (DTM) for modeling eddy viscosity effects. In their simulation a continuity equation, modified Navier-Stokes equation and an advection equation of the VOF function were employed. The VOF model was able to compute velocity and pressure fields within the liquid flow. In conjunction with this, the wave-induced soil-water coupled FEM was used to calculate sand displacements and pore pressures within the sand bed. Although this type of coupled model had been previously used in other studies, Nakamura et al. (2008) attempted to improve the simulations of the model for the purposes of their own research. The results of the numerical model were in agreement with those of the experimental portion of the research. Figure 2-19 shows an example of a comparison between their numerical and experimental model results. Nakamura et al. (2008) observed and concluded that the numerical model computed a propagation speed of the wave that was slightly higher than that experimentally measured. There was also a small phase lag between the experimental and numerical results. It was also observed that in some cases, the numerical model underestimated wave runup, and in turn pore pressures, at the front of the structure. However, at other points, the excess pore water pressures were very well simulated by the numerical model for both solitary and long waves.

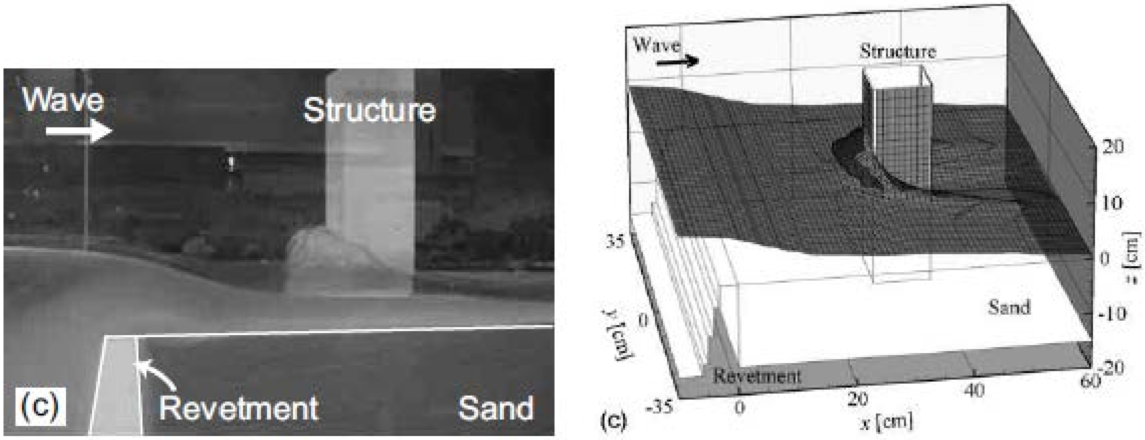

Figure 2-19 : Experimental versus Numerical Results of Tsunami Wave Propagation, Nakamura et al. (2008)

Fuji et al. (2009) carried out an experiment using a wide flume in order to clarify characteristic flow patterns and topography changes in harbors due to a tsunami. In their experiment, topography changes near an idealized harbor due to an isolated long wave were investigated. They also carried out numerical simulations on the tsunami induced topography changes using a vertically averaged model. Their model encountered difficulties in predicting deposition areas in the harbor. Although a significant local deposition area was observed at the center of the harbor in their experiment, a widespread deposition area was predicted by their numerical model. This inconsistency may have originated from the three-dimensional sediment transport in the deposition processes, which cannot be calculated by the vertically-averaged model. In the numerical simulation, to simultaneously calculate tsunami propagation in the long flume and the tsunami-induced sediment transport in the harbor in detail, a nested grid system with four domains of different resolutions was used. The velocity, the water depth, the suspended sediment concentration and the topography at lateral boundaries were exchanged among each domain. Topography changes predicted in Fuji et al. (2009) are shown in Figure 2-20. The topography changes measured by the laboratory experiments and predicted by the vertically averaged model by Fuji et al. (2009) are also shown.

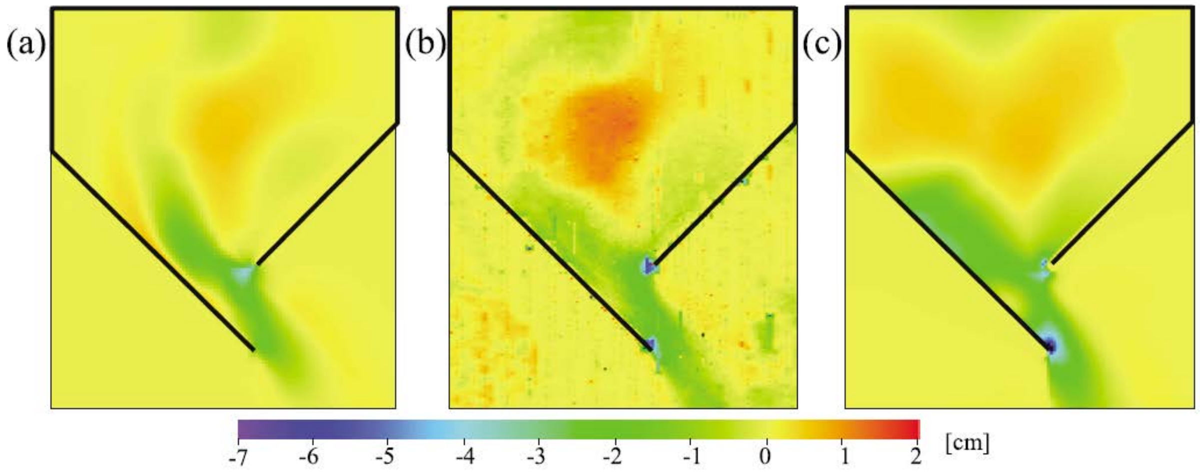

Figure 2-20: Topography changes in and around the harbor area. (a) numerical results of Fuji et al. (2009), (b) experimental data of Fuji et al. (2009), (c) numerical results predicted by the vertically averaged model

The velocity, water level and topography changes in the harbor predicted by their numerical model agreed with experimental data. The deposition at the center of the harbor could be predicted by their numerical model, although it could not be well predicted by the vertically averaged numerical model. This is because a secondary flow of the first kind, which was generated near the vortex and developed in the harbor, plays the role of transporting suspended sediment to the vortex center, which is located near the center of the harbor. Thus, to predict deposition areas with high accuracy, the secondary flow effects should be incorporated in numerical models.

Pan and Huang, (2012) developed a 2D vertical hydrodynamic and sediment-scour model to simulate tsunami wave run-up on a sloping beach to determine its effects on sediment scour around a cylinder pier located in the wave breaking and run-up zone. To resolve the steep wave front of the tsunami bore, the kinetic flux vector splitting scheme was adopted to solve the hydrodynamic model equations in the unstructured triangular mesh. A large-scale laboratory experiment of tsunami wave run-up and the effects on sediment scour around a cylinder pier, given in Tonkin et al. (2003), was used in this study to validate the numerical model. The model simulations adequately characterized the tsunami wave propagations and transformations as the wave approaches the beach from offshore, especially for the sharp tsunami front before it breaks and the tsunami bore runs up the beach slope. The model simulations also reasonably described the dynamics of the sediment scour around a cylinder pier, showing the sediment scour during wave run-up and sediment deposition during wave rundown. The model predictions of the final scour depths after the wave impact at three measurement stations reasonably matched the experimental measurements. Figure 2-21 shows computed water-surface profile propagations and transformations of the tsunami wave.

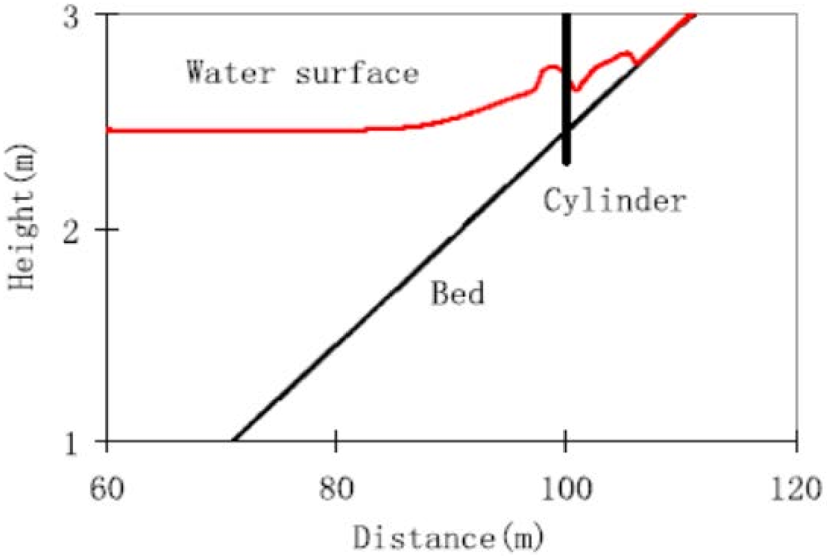

Figure 2-21: Computed longitudinal surface profiles of tsunami wave propagation, breaking, and run-up

2.6 Estimation of local scour in current design guidelines

The method for estimation of local scour for tsunami conditions was first formalized in Honolulu Building Code in 1980 by Dames and Moore. Dames and Moore (1980) suggested that scour depth is related to distance from the shoreline and soil type. As indicated in Table 2-2, scour depth is estimated as a percentage of the maximum tsunami flow depth, d.

Table 2-2: Design Guidelines for Scour Depth, Dames and Moore (1980)

Approximate Scour Depth as a Percentage of Flow Depth, d (Dames and Moore, 1980)		
Soil type	Scour depth (% of d) (Shoreline Distance < 300 feet	Scour depth (% of d) (Shoreline Distance > 300 feet
Loose sand	80	60
Dense sand	50	35
Soft silt	50	25
Stiff silt	25	15
Soft clay	25	15
Stiff clay	10	5

Observations after the 2004 Indian Ocean Tsunami indicated that scour can occur significantly farther inland than 300 feet from the shoreline. Conservative engineering judgment should be exercised in categorizing the soil type at the site into the broad categories listed above (FEMA P646 2012).

Also, the US Army Corps of Engineers used a simplified procedure associated with design criteria for the FEMA Flood Insurance Rate Map (FIRM) program. The current Coastal Construction Manual (ref. FEMA (2000) adopted the Honolulu method as summarized in Table 2-3. This method provides provisions for tsunami scour in relation to the tsunami design criteria

Table 2-3: Tsunami Design Criteria (Hwang et. al., 2006; adapted from FEMA (2000)

Standard	Explanations (scour issues in bold)
Scour depth	**Fraction of water height (5-80%) by soil type (soft to stiff clay/loose to dense sand and proximity to shoreline.**
Floodwater velocity	**Simple equations plotted as function of water height: roughly equal to the inundation depth for non-breaking waves (ft-s units); 3-5 times greater for breaking waves**
Flood Elevation	Flood elevations on FIRM map, based upon tsunami runup modeling (100 and 500 yr).
Flow Conditions	Assumes non-bore conditions except at historic bore sites
Foundation type	**Piles required within 100 m of shoreline and any location where scour depth is greater than 1 m**. An alternative is to provide shore protection (bulkhead) on all sides with final elevations above flood level.

In addition, FEMA (2000) reported that inundation velocity strongly affects scour depth, and proposed a correlation of velocity to water depth, as shown in Figure 2-22. FEMA (2000, cited by Francis, 2006) proposed a graphical relationship between inundation flow velocity and the depth of scour without consideration of the tsunami flow and the soil characteristics. There are other load components that affect subsurface pressure gradients and resulting scour and this is not accounted for in the FEMA (2000) scour method. Rather, the FEMA (2000) method works based on experience and judgment required in combining design loads.

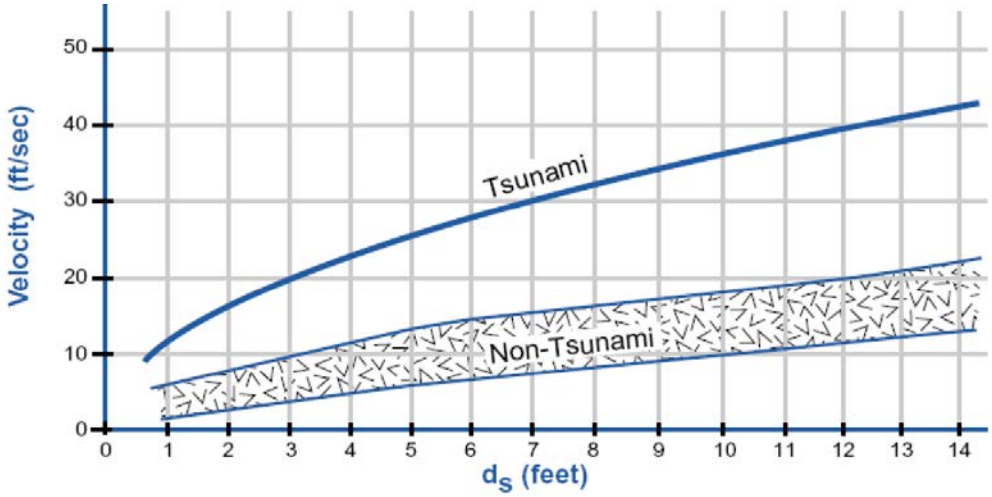

Figure 2-22: Tsunami velocity vs. scour depth (FEMA 2000)

The ASCE/SEI 7 Chapter 6 - Tsunami Loads and Effects (ASCE, 2016) is the world's only design standard written in mandatory language. Section 6.12 provides conservative design guidance to assist with the estimation of tsunami-induced scour. These prescriptions are based on post-tsunami field surveys of scour observed around structures conducted by Tonkin et al. (2011).

Tonkin et al. (2013) presented a tsunami scour evaluation procedure which includes flow and soil characteristics more precisely than the FEMA method. The upper envelope of local scour measurements was considered to be 1.2 times the flow depth, up to a maximum scour depth of 4 meters, as shown in Figure 2-23. However, they suggested a limiting scour depth of 3 meters as a reasonable alternative.

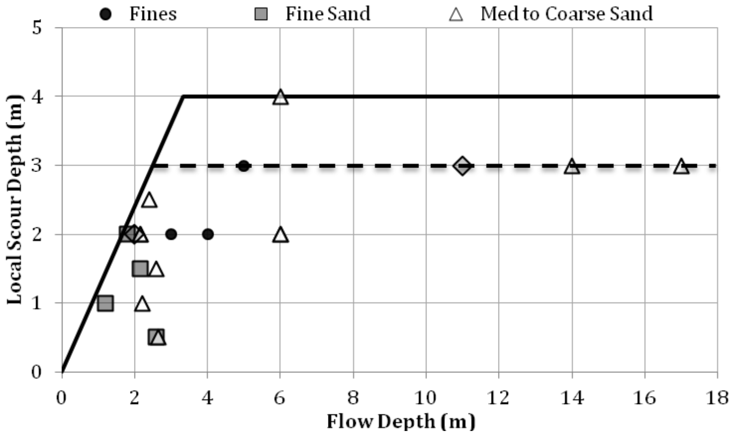

Figure 2-23 : observed local scour depth and estimated flow depth for different sediment types, with bounding plausible design envelopes, Tonkin et al. (2013)

According to the American Society of Civil Engineering (ASCE 7-16) Standards (2016), local scour design shall consider the effects of sustained flow around structures. It could be calculated using dynamic numerical or physical modeling or empirical methods in the recognized literature. In the absence of other methods, sustained flow scour and associated pore pressure softening is provided by Table 2-4 and Figure 2-24. The assumed area limits shall be considered to encompass the exposed building perimeter and to extend either side of the foundation perimeter a distance equal to the scour depth for consolidated or cohesive soils, or a distance equal to three times the scour depth for non-consolidated or non-cohesive soils.

Table 2-4: Design local scour depth due to sustained flow and pore pressure softening (ASCE 7 - 2016)

Inundation depth h	**Scour depth D^***
<10 ft (3.05 m)	1.2h
>10 ft (3.05 m)	12 ft (3.66 m)

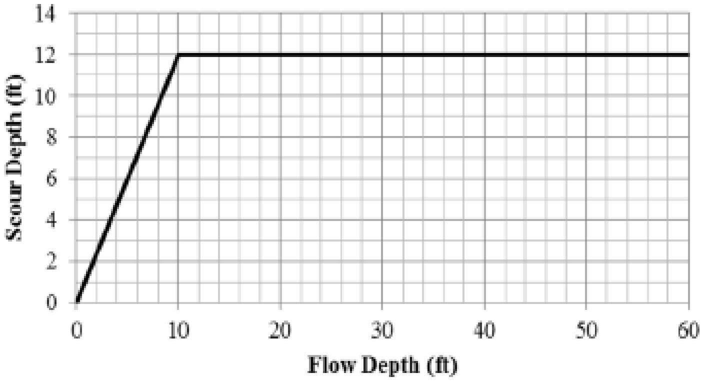

Figure 2-24: Local Scour depth due to sustained flow and pore pressure softening (ASCE 7-16)

2.7 Sediment transport

Sediment transport around a structure or bridge pier is a complex process and involves the deformation of the bed in response to scour, deposition and bed forms (in the case of live-bed scour), which strongly affect the bed roughness, energy loss and velocity gradient (Van Rijn, 1993; Yang, 1996; Raudkivi. 1998; Chien & Wan, 1999).

At a bridge site, sediment can be transported in three different modes; bed load, suspended load and wash load (Van Rijn, 1993; Yang, 1996: Raudkivi, 1998). A large number of experiments have been conducted, resulting in development of several empirical or semi-empirical formulae for local scour, as well as for the initiation of sediment particle movement and determination of the potential sediment transport. These sediment transport formulae have been used to calculate local scour in open channel computational fluid dynamics (CFD) models. Therefore, to inform the development of the CFD model, basic knowledge of sediment transport is important. This section summarises various engineering aspects related to sediment transport and local scour (Kabir, 2005).

2.7.1 Sediment physical properties

The sediment particles can be characterised based on their size, shape, uniformity, cohesiveness, settling velocity and angle of repose. Sediment dimensions cover a large "size" range, which in turn is used to classify the sediments (Yang, 1996). Sediment size is commonly categorized using sieve analysis. The most common sediment size classification is the American Geophysical Union classification, which is based on the approximate diameter of the sediment particles (Armitage & McGahey, 2003). Van Rijn (1993) and Yang (1996) present a so-called "shape factor" to take into account the deviation from spherical to differentiate a wide variety of sediment shapes that are observed in river and coastal environments. Naturally worn quartz particles typically have a shape factor of 0.7. Sieve analysis is commonly used to determine the size of sediments. Sediment uniformity is calculated from frequency histograms. The frequency histograms depict the percentage of material by mass passing from one sieve diameter but retained on one smaller. Statistical parameters such as the mean, standard deviation, skewness and kurtosis can be determined from sieve analysis (Van Rijn, 1993: Yang, 1996).

The "median diameter" (d_{50} or d_i) is the diameter representing the 50% cumulative percentile value (50% by mass of the particles in the sediment sample are finer than the d_{50} grain size)

$$d_{50}\ (or\ d_i) = \frac{d_{15.9} + d_{84.1}}{2} \qquad 2\text{-}5$$

The "mean diameter" $\overline{d}$ is the arithmetic mean of the particle size and can be expressed in terms of the median diameter d_i of any particle size fraction and the percentage by mass of that fraction p_i as follows:

$$\overline{d} = \frac{\sum p_i d_i}{100} \qquad 2\text{-}6$$

The "'standard deviation" σ is determined using the mean diameter (Equation 2-7). The "'geometric standard deviation" σ_g, (Equation 2-8) represents the uniformity of the distribution of the sediment.

If σ_g <1.3 the sediment is considered to be uniform. Moreover, if σ_g >1.3. the sediment is considered to be non-uniform (Melville, 1997).

$$\sigma^2 = \frac{\{\sum p_i(d_i - \overline{d})^2\}}{100} \qquad 2\text{-}7$$

$$\sigma_g = \sqrt{\frac{d_{84.1}}{d_{15.9}}} = \frac{d_{84.1}}{d_{50}} = \frac{d_{50}}{d_{15.9}} = \frac{1}{2}\left[\frac{d_{50}}{d_{15.9}} + \frac{d_{84.1}}{d_{50}}\right] \qquad 2\text{-}8$$

The "settling velocity or fall velocity " of a particle is defined as the terminal velocity of that fluid particle in an unbounded quiescent volume of water. In general. it depends on the size, shape, surface-roughness and density of the particle, and on the density and viscosity of the fluid. The particle concentration, fluid turbulence and the presence of boundaries can also influence the settling velocity.

According to Van Rijn (1993), the settling velocity *(v_{ss})* of non-spherical natural sediment particles of sieve diameter *d*, specific gravity *s*, kinematic viscosity *v* and acceleration of gravity *g* can be estimated using equation 2-9, 2-10 and 2-11:

$$v_{ss} = \frac{(s-1)gd^2}{18v} \quad if\ 1 \le d \le 100\ \mu m \qquad 2\text{-}9$$

$$v_{ss} = \frac{10v}{d}\left[\sqrt{\left(1 + \frac{0.01(s-1)gd^3}{18v^2}\right)} - 1\right] \quad if\ 100 < d \le 1000\ \mu m \qquad 2\text{-}10$$

$$v_{ss} = 1.1[(s-1)gd]^{0.5} \quad if\ d > 1000\ \mu m \qquad 2\text{-}11$$

Cheng (1997) also calculated the settling velocity of natural sand particles by defining the "relative submerged density" *(Δ)* and the "dimensionless particle diameter" *(d_*)* as:

$$v_{ss} = \frac{v\left(\sqrt{25 + 1.2d_*^2} - 5\right)^{1.5}}{d} \qquad 2\text{-}3$$

$$d_* = \left(\frac{\Delta g}{v^2}\right)^{1/3} d_{50} \qquad 2\text{-}4$$

$$\Delta = \frac{\rho_s - \rho}{\rho} \qquad 2\text{-}5$$

Sediments can be divided mainly into two groups: "cohesive" (i.e. clay, silt) and "non- cohesive" (i.e. sand and coarser particles). The weight of the particles is the dominant force in determining the transportability of non-cohesive sediments. For the cohesive sediments, the physicochemical forces are an important factor. The cohesive materials affect the soil properties such that the particle tends to behave as one large coherent mass (Vanoni, 1975). This study will focus only on non-cohesive sediment types. The angle of repose or critical angle of repose *(ϕ_r)* of a granular material is the steepest angle of descent or dip relative to the horizontal plane to which a material can be piled without slumping. Van Rijn (1993) lists the angle of repose of quartzitic sand sediment. However, ϕ_r has to be estimated experimentally for material other than quartztic sand.

2.7.2 The forces on a sediment particle

There are three main forces acting on an exposed particle; drag, lift and gravity. depicts the different forces act on a sediment particle (inclined bed), (Kabir, 2005).

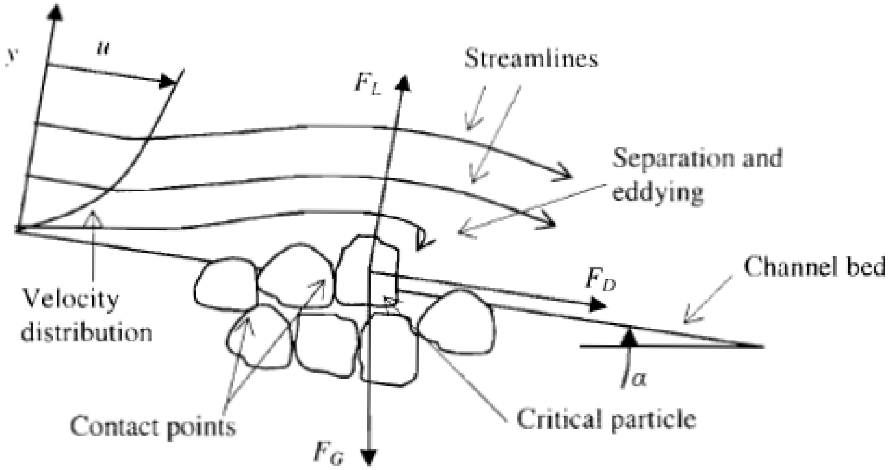

Figure 2-25: Forces on a sediment particle (inclined bed), (Kabir, 2005)

The gravitational force F_G is related to the submerged weight of the critical particle. Even in the absence of fluid motion, there is a net force on the particle and its direction depends on the "buoyancy" effect. The gravitational force acts vertically down if the particle is denser than water and vertically upward if it is not. Van Rijn (1993) describes the gravitational force F_G on a critical particle with a particle diameter d, particle density ρ_s, and water density ρ as:

$$F_G = \frac{1}{6}\pi(\rho_s - \rho)gd^3 \qquad 2\text{-}6$$

The drag F_D and lift F_L forces are the horizontal and vertical components due to the integrated shear stress and pressure forces acting on the particle. The shear stress at any point on the particle surface acts tangentially to the direction of flow and depends on the local velocity gradient or one of its three-dimensional variants (Equation 2-16), (Kabir, 2005).

$$\tau_{xy} = \left(\mu + \mu_{xy(t)}\right)\left(\frac{\partial u}{\partial y} + \frac{\partial v}{\partial x}\right) \quad 2\text{-}7$$

In Equation 2-16, μ and $\mu_{xy(t)}$ are the coefficient of viscosity related to shear flow and the turbulent flow. The pressure force on the particle surface is normal to the surface and depends on the depth and local velocity in accordance with the Bernoulli Equation. If Z is the height above some arbitrary datum, the Bernoulli equation can be written as in Equation 2-17. The pressure p can be set equal to $\rho g y$ at water depth y assuming hydrostatic conditions (Kabir, 2005).

$$\frac{p}{\rho g} + \frac{u^2}{2g} + z = Constant\ along\ the\ streamline \qquad 2\text{-}8$$

Equation 2-17 indicates that, for a constant datum, increases in velocity lead to a corresponding decrease in the local pressure. This situation leads to the flow separation, which ultimately results in the formation of eddies. These eddies redistribute the pressure more uniformly over the separated surfaces, Armitage & McGahey (2003). Van Rijn (1993) shows that the integration of pressure forces over the entire surface of the particle indicates the resultant drag force.

Chien & Wan (1999) describe the drag force F_D and the lift force F_L using the projected area a_p (which is defined differently for drag and lift), drag coefficient C_D, lift coefficient C_L, density of water and effective velocity near the bed particle u_o as:

$$F_D = C_D a_P \frac{\rho u_0^2}{2} \qquad 2\text{-}9$$

$$F_L = C_L a_P \frac{\rho u_0^2}{2} \qquad 2\text{-}10$$

2.7.3 Effective roughness

The effective roughness height k_s is the sum of the "grain roughness" k_{sg} generated by the skin friction and the "form roughness" k_{sf} " generated by the pressure forces acting on the bed.

$$k_s = k_{sg} + k_{sf} \qquad 2\text{-}20$$

According to Van Rijn (1993), two approaches can be used to estimate the bed roughness; bed form and grain related parameters (e.g., bed form length, height, steepness and bed material size) or integral parameters (e.g. mean depth, mean velocity). According to Young et al. (1997), the particle at the boundary could form part of a laminar boundary (Re_s, < 5), a transitional boundary (5 < Re_s, < 70) or a turbulent boundary (Re_s, > 70), where Re_s, is roughness Reynolds number defined as:

$$Re_s = \frac{u_* k_s}{v} \qquad 2\text{-}21$$

where v is the kinematic viscosity and u_* is the shear velocity, which is defined using the bed shear stress τ_0 and the density of fluid ρ as:

$$u_* = \sqrt{\frac{\tau_0}{\rho}} \qquad 2\text{-}11$$

Colebrook & White (1937) show when Re_s, increases beyond 3.5, separation commences behind the top of the particle and a wake is formed. According to Chien & Wan (1999), the form drag becomes then the dominant force. Other definitions of k_s, are k_s, = d_{65} (Einstein, 1950), k_s, = d_{90} (Meyer-Peter & Muller, 1948), k_s, = d_{85} (Simons & Richardson, 1966) and k_s, = $3d_{50}$ (SISYPHE, 2014).

2.7.4 The initiation of sediment movement

Van Rijn (1993) describes the initiation of sediment movement using forces acting on the spherical sediment particle on flat bed shown in the Figure 2-26.

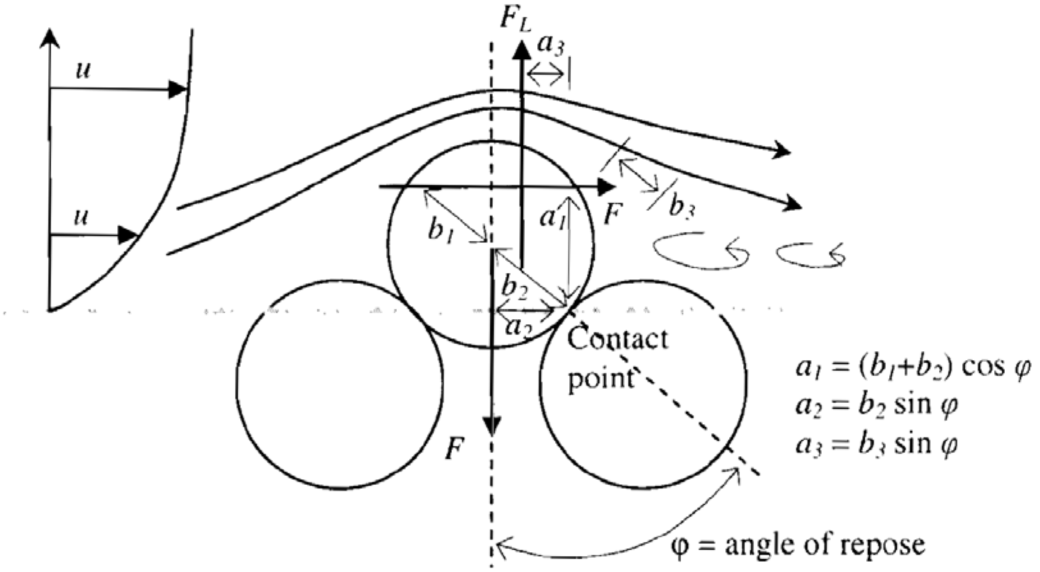

Figure 2-26: Forces on a sediment particle by Van Rijn (1993)

In the derivation, Van Rijn (1993) neglects the ratio of the lift force and the submerged particle weight ($F_L/F_G = 0$). He introduces the empirical coefficient α_1 by which the effects of lift force have been taken into account. The condition of sediment movement therefore yields as:

$$F_D \geq \alpha_1 F_G \tan \varphi \, , where \; \alpha_1 = \frac{b_2}{b_1+b_2} \qquad \text{2-12}$$

The value of the empirical coefficient α_1 depends on the local turbulence and hence the Reynolds number (Van Rijn, 1993). Yang (1996) adds further simplifications and shows the incipient motion of sediment particles satisfies one or more of the three conditions indicated in Equations 2-24 to 2-26 .

$$F_L = F_G \qquad \text{2-13}$$

$$F_D = F_R \qquad \text{2-14}$$

$$M_O = M_R \qquad \text{2-15}$$

where F_L is the lift force, F_G is the gravitational force, F_D is the drag force, F_R is the resistance force, M_O is the overturning moment due to F_D and F_R and M_R is the resisting moment due to F_L and F_G .

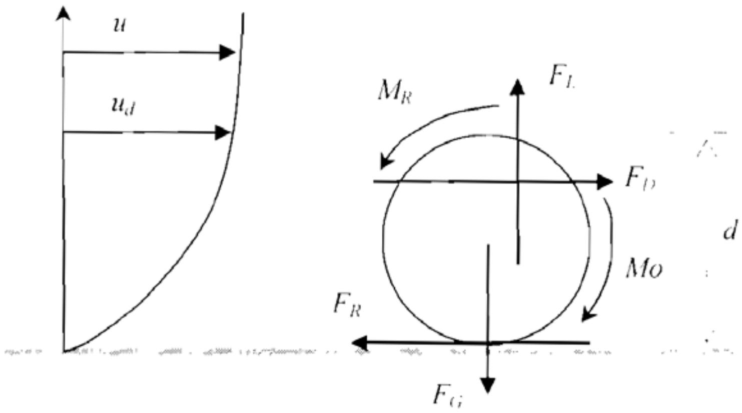

Figure 2-27: Forces on a sediment particle by Yang, (1996)

Many researchers define the sediment incipient movement criteria using shear stress (Shields, 1936), velocity (Yang, 1973). stream power (Bagnold, 1966) or probability (Gessler, 1970). All of these approaches are reported in Van Rijn (1993). Shields (1936) used dimensional analysis to establish his well-known "Shields diagram" for an incipient motion of a particle using the dimensionless parameters, i.e., the particle Reynolds number Re_* (Equation 2-27) and the Shields parameter θ (Equation 2-28).

$$Re_* = \frac{u_* d}{v} \qquad 2\text{-}16$$

$$\theta = \frac{\tau_0}{(\rho_s - \rho) g d} = \frac{\rho u_*^2}{(\rho_s - \rho) g d} \qquad 2\text{-}17$$

where u_* is the shear velocity (Equation 2-22). d is the particle diameter, v is the kinematic viscosity, τ_0 is the bed shear stress, ρ_s is the density of sediment, ρ is the density of water and g is the acceleration of gravity. τ_c, is the critical bed shear stress for incipient motion and critical Shields parameter θ_c, is given by (Equation 2-29):

$$\theta_c = \frac{\tau_c}{(\rho_s - \rho) g d_{50}} \qquad 2\text{-}18$$

shows the Shields parameter as a function of the particle Reynolds number. The solid line band presents the spread of data by Shields, however, most of the published data lie within the dashed lines (Raudkivi, 1998).

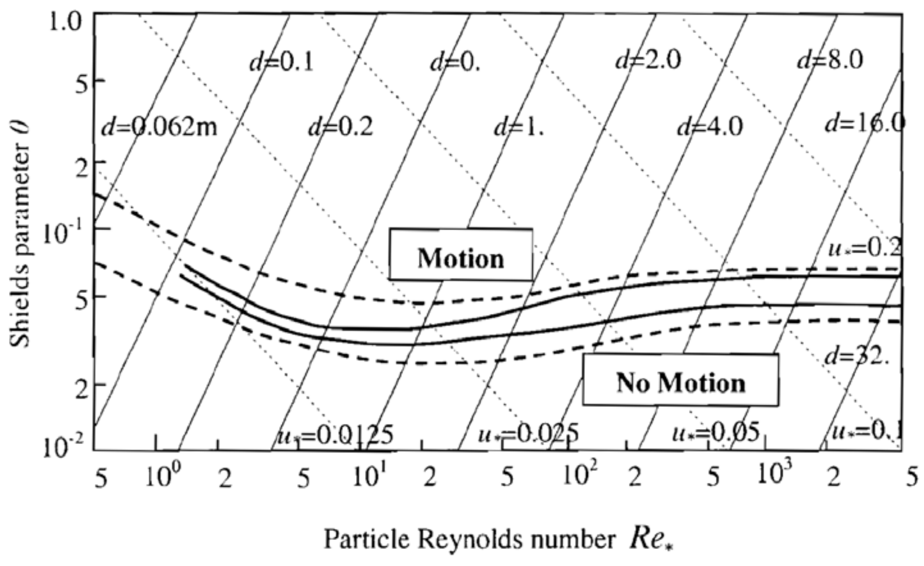

Figure 2-28: Shields parameter with respect to particle Reynolds number (Raudkivi, 1998)

2.8 Discussion

In conclusion, the literature review has highlighted the following deficiencies: This literature review has shed light on the current state of research and design guidelines on scour due to supercritical flow and/or tsunami and dam-break waves. With regards to tsunami-induced scour, this literature review has underlined the importance and acute need for further research on the subject. Studies such as this one provide highly detailed measurements of local scour, leading to a better understanding of this unique scouring process. The few attempts at simulating, describing and quantifying tsunami scour are clearly insufficient in comparison to the requirements for such knowledge. Hopefully, advancements in both physical and numerical modelling allow for a better understanding of the physics of the scour failure mechanisms, of interest to researchers, engineers and coastal communities around the world. These advancements should lead to the development of new methodologies much needed to strengthen structures against tsunami-induced scour and improving building codes to upgrade the standards of safety.

Chapter 3: THE NUMERICAL METHOD

3.1 TELEMAC 3D

The TELEMAC-3D code solves such three-dimensional equations as the free surface flow equations (with or without the hydrostatic pressure hypothesis) and the transport-diffusion equations of intrinsic quantities (temperature, salinity, concentration). Its main results, at each point in the resolution mesh in 3D, are the velocity in all three directions and the concentrations of transported quantities. Water depth is the major result as regards the 2D surface mesh. The TELEMAC-3D's prominent applications can be found in free surface flow, in both seas and rivers; the software can take the following processes into account (Telemac user manual, 2018):

_ Influence of temperature and/or salinity on density,
_ Bottom friction,
_ Influence of the Coriolis force,
_ Influence of weather elements: air pressure, rain or evaporation and wind,
_ Consideration of the thermal exchanges with the atmosphere,
_ Sources and sinks for fluid moment within the flow domain,
_ Dry areas in the computational domain: tidal flats,
_ Current drift and diffusion of a tracer, with generation or disappearance terms,

The code is applicable to many fields. The main ones are related to the marine environment through the investigations of currents being induced either by tides or density gradients, with or without the influence of such an external force as the wind or the air pressure. It can be applied either to large extent areas (on a sea scale) or to smaller domains (coasts and estuaries) for the impact of sewer effluents, the study of thermal plumes or even sedimentary transport. As regards the continental waters, the study of thermal plumes in rivers, the hydrodynamic behaviour or natural or man-made lakes can be mentioned as well. TELEMAC-3D is developed by the LNHE (Laboratoire National d'Hydraulique et Environnement) of the Research and Development Division of EDF (EDF-R&D), (Telemac user manual, 2018).

The TELEMAC-3D code solves the three-dimensional hydrodynamic equations with the following assumptions:

_ Three-dimensional Navier-Stokes equations with a free surface changing in time,

_ Negligible variation of density in the conservation of mass equation (incompressible fluid),

_ Hydrostatic pressure hypothesis (that hypothesis results in that the pressure at a given depth is the sum of the air pressure at the fluid surface plus the weight of the overlying water body),

_ Boussinesq approximation for the momentum.

Due to these assumptions, the three-dimensional equations being solved are:

$$\frac{\partial U}{\partial x}+\frac{\partial V}{\partial y}+\frac{\partial W}{\partial z}=0 \qquad 3\text{-}1$$

$$\frac{\partial U}{\partial t}+U\frac{\partial V}{\partial x}+V\frac{\partial U}{\partial y}+W\frac{\partial U}{\partial z}= -g\frac{\partial Zs}{\partial x}+v\,\Delta(U)+F_x \qquad 3\text{-}2$$

$$\frac{\partial V}{\partial t}+U\frac{\partial V}{\partial x}+V\frac{\partial V}{\partial y}+W\frac{\partial V}{\partial z}= -g\frac{\partial Zs}{\partial y}+v\,\Delta(V)+F_y \qquad 3\text{-}3$$

$$P=P_{atm}+\rho_0 g(Z_s-z)+\ \rho_0 g\int_z^{Z_s}\frac{\Delta\rho}{\rho_0}\,dz \qquad 3\text{-}4$$

$$\frac{\partial T}{\partial t}+U\frac{\partial T}{\partial x}+V\frac{\partial T}{\partial y}+W\frac{\partial T}{\partial z}= Div\left(v\ Grad\ (T)\right)+Q \qquad 3\text{-}5$$

wherein:

- h (m) water depth,
- Z_S (m) free surface elevation
- U, V, W (m/s) three-dimensional components of velocity,
- T (℃, g/L . . .) passive or active (acting on density) tracer,
- p (X) pressure
- p_{atm} (X) atmospheric pressure,
- g (m/s^2) acceleration due to gravity
- ν (m^2/s) cinematic viscosity and tracer diffusion coefficients
- Z_f (m) bottom depth
- ρ_0 (X) reference density
- $\Delta\rho$ (X) variation of density around the reference density
- t (s) time
- x, y (m) horizontal space components

- *z (m)* vertical space component
- F_x, F_y *(m/s²)* source terms
- Q (tracer unit) tracer source of sink
- *h, U, V, W* and *T* are the unknown quantities, also known as computational variables.

F_x and F_y are source terms denoting the wind, the Coriolis force and the bottom friction. Several tracers can be taken into account simultaneously. They can be of two different kinds, either active, i.e. influencing the flow by changing the density, or passive, without any effect on density and then on flow.

The TELEMAC-3D basic algorithm can be divided in three computational steps (three fractional steps), (Telemac user manual, 2018):

1- The first step consists in finding out the advected velocity components by only solving the advection terms in the momentum equations.
2- The second step computes, from the advected velocities, the new velocity components taking into account the diffusion terms and the source terms in the momentum equations. These two solutions enable to obtain an intermediate velocity field.
3- The third step is provided for computing the water depth from the vertical integration of the continuity equation and the momentum equations only including the pressure-continuity terms (all the other terms have already been taken into account in the earlier two steps).

The resulting two-dimensional equations (analogous to the Saint-Venant equations without diffusion, advection and source terms) are written as:

$$\frac{\partial h}{\partial t}+\frac{\partial (uh)}{\partial x}+\frac{\partial (vh)}{\partial y}=0 \qquad 3\text{-}6$$

$$\frac{\partial U}{\partial t}=-g\frac{\partial Zs}{\partial x} \qquad 3\text{-}7$$

$$\frac{\partial V}{\partial t}=-g\frac{\partial Zs}{\partial y} \qquad 3\text{-}8$$

The non hydrostatic pressure is split up into a hydrostatic pressure and a “dynamic” pressure term.. In the first phase the hydrostatic pressure is taken into account as before, but an equation for W is added: In the next step the hydrodynamic pressure is taken into account to ensure the continuity equation and yield a divergence free velocity field, this is a classical projection algorithm for Navier-Stokes equations. Finally, the free surface is updated again with the help of the depth-averaged continuity equation, where the velocity is known.

For the three-dimensional equations without the hydrostatic pressure hypothesis, the following system with an equation for W which is similar to those for U and V is then to be solved.

$$\frac{\partial U}{\partial x}+\frac{\partial V}{\partial y}+\frac{\partial W}{\partial z}=0 \qquad \text{3-9}$$

$$\frac{\partial U}{\partial t}+U\frac{\partial V}{\partial x}+V\frac{\partial U}{\partial y}+W\frac{\partial U}{\partial z}= -\frac{1}{\rho}\frac{\partial p}{\partial x}+\nu\,\Delta(U)+F_x \qquad \text{3-10}$$

$$\frac{\partial V}{\partial t}+U\frac{\partial V}{\partial x}+V\frac{\partial V}{\partial y}+W\frac{\partial V}{\partial z}= -\frac{1}{\rho}\frac{\partial p}{\partial y}+\nu\,\Delta(V)+F_y \qquad \text{3-11}$$

$$\frac{\partial W}{\partial t}+U\frac{\partial W}{\partial x}+V\frac{\partial W}{\partial y}+W\frac{\partial W}{\partial z}= -\frac{1}{\rho}\frac{\partial p}{\partial z}-g+\nu\,\Delta(W)+F_z \qquad \text{3-12}$$

The pressure is divided into a hydrostatic pressure and a "dynamic" pressure term.

$$P=P_{atm}+\rho_0 g(Z_s-z)+\ \rho_0 g\int_z^{Z_s}\frac{\Delta\rho}{\rho_0}\,dz+Pd \qquad \text{3-13}$$

As Boussinesq approximation for the momentum (the density variations are only taken into account as buoyant forces), TELEMAC-3D non hydrostatic mode is not fully NON – HYDROSTATIC.

3.1.1 Turbulence models

TELEMAC-3D generally use different turbulence model algorithms -

1- Constant viscosity
2- Mixing length (TELEMAC-3D)
3- Standard *k*-£ (TELEMAC-3D)
4- *k*-*w* (TELEMAC-3D)
5- Smagorinski model

Turbulence model is the numerical techniques to calculate the impact of turbulence on the Navier-Stokes equations or the Reynolds equations (Equation 3-14). The Reynolds equations consider the influence of turbulent fluctuations on the mean flow U (with U, V and W are the components along x-, y- and z-directions).

$$\frac{\partial U}{\partial t}+div(UU)=-\frac{1}{\rho}\frac{\partial p}{\partial x}+\nu divgradU+\left[-\frac{\partial\overline{u'^2}}{\partial x}-\frac{\partial\overline{u'v'}}{\partial y}-\frac{\partial\overline{u'w'}}{\partial z}\right]$$

$$\frac{\partial V}{\partial t}+div(VU)=-\frac{1}{\rho}\frac{\partial p}{\partial y}+\nu divgradV+\left[-\frac{\partial\overline{u'v'}}{\partial x}-\frac{\partial\overline{v'^2}}{\partial y}-\frac{\partial\overline{v'w'}}{\partial z}\right]$$

$$\frac{\partial W}{\partial t}+div(WU)=-\frac{1}{\rho}\frac{\partial p}{\partial z}+\nu divgradW+\left[-\frac{\partial\overline{u'w'}}{\partial x}-\frac{\partial\overline{v'w'}}{\partial y}-\frac{\partial\overline{w'^2}}{\partial z}\right] \qquad \text{3-14}$$

The main difficulties with turbulence models arise from the non-linear convective term in the Navier-Stokes equations, and much more so from the pressure-gradient term (Pope, 2000).

The close set of Navier-Stokes equations with mass conservation cannot be solved in a foreseeable way economically, Versteeg & Malalasekera (1995). Further introduction of the fluctuation terms in the Navier-Stokes equations further complicates the scenario, which is resolved by introducing additional "Reynolds stress" terms given in Equation 3-15.

$$\tau_{xx}=-\rho\overline{u'^2} \qquad \tau_{yy}=-\rho\overline{v'^2} \qquad \tau_{zz}=-\rho\overline{w'^2}$$

$$\tau_{xy}=\tau_{yx}=-\rho\overline{u'v'} \qquad \tau_{xz}=\tau_{zx}=-\rho\overline{u'w'} \qquad \tau_{yz}=\tau_{zy}=-\rho\overline{v'w'} \qquad \text{3-15}$$

Various techniques have been developed over the past decades to develop computational procedure of sufficient accuracy for engineers to predict the Reynolds stresses. Based on accuracy and computation costs those can be read in order as:

Direct Numerical Simulation (DNS), Large or Very Large Eddy Simulation (LES or VLES), Reynolds Stress Model (RSM), Algebraic Stress Model (ASM), k-w Model, k-£ Model, Mixing Length Model and Constant Viscosity model. Details of those can be found in Versteeg & Malalasekera (1995), Wilcox (2000), Pope (2000) and Hoffman & Johnson (2003).

3.1.2 Computational mesh

The TELEMAC-3D mesh structure is made of prisms (possibly split in tetrahedrons). In order to prepare that mesh of the 3D flow domain, a two-dimensional mesh comprising triangles which covers the computational domain (the bottom) in a plane is first constructed, as for TELEMAC-

2D. The second step consists in duplicating that mesh along the vertical direction in a number of curved surfaces known as "planes". Between two such planes, the links between the meshed triangles make up prisms (Telemac user manual, 2018).

3.1.3 Bottom friction

The friction law used for the bottom friction modelling are as follows (Telemac user manual, 2018):

0: No friction,
1: Haaland law,
2: Chézy law,
3: Strickler law,
4: Manning law,
5: Nikuradse law.

The computation of turbulent constraint at the bottom depends on the velocity profile above the bottom (within the boundary layer). The profile depends on the ratio of the wall asperity size to the viscous sub-layer thickness for further details, refer to the TELEMAC Theoretical Manual. When the asperities are larger than the viscous sub-layer thickness, the latter cannot be established, and the friction regime is rough. On the other hand, when there is a viscous sub-layer, the friction regime is smooth.

The computation of the turbulent constraint depends on the keyword TURBULENCE REGIME FOR THE BOTTOM. The available options are:

1. smooth regime,
2. rough (default value).

In smooth friction regime conditions, the friction law is not used and the constraint is computed from Reichard law of velocity profile (a law giving the friction velocity value. In rough friction regime conditions and for the bottom friction laws 2, 3 and 4, the constraint is computed from the friction velocity and its relation to the dimensionless friction coefficient. When the roughness size is known, Law 1 and Law 5 can be used. For law 5, the friction velocity is computed from the velocity profile within the logarithmic layer and from the roughness size (Telemac user manual, 2018).

3.2 SISYPHE

SISYPHE is a sediment transport and morphodynamic model which is part of the hydro informatics finite element and finite volume system Telemac - Mascaret. In SISYPHE, sediment transport rates, split into bedload and suspended load, are calculated at each node as a function of various flow (velocity, water depth, wave height, etc.) and sediment (grain diameter, relative density, settling velocity, etc.) parameters. The bedload is calculated by using a classical sediment transport formula from the literature. The suspended load is determined by solving an additional transport equation for the depth-averaged suspended sediment concentration. The bed evolution equation (Exner equation) can be solved by using either a finite element or a finite volume formulation (Villaret and Tassi, 2014); (SISYPHE v6p3 user manual, 2014).

SISYPHE is applicable to non-cohesive sediments (uniform or graded), cohesive sediments as well as sand-mud mixtures. The sediment composition is represented by a finite number of classes, each characterized by its mean diameter, grain density and settling velocity. Sediment transport processes can also include the effect of bottom slope, rigid beds, secondary currents and slope failure. For cohesive sediments, the effect of bed consolidation can be accounted for. SISYPHE can be applied to a large variety of hydrodynamic flow conditions including rivers, estuaries and coastal applications. For the later, the effects of waves superimposed to a tidal current can be included. The bed shear stress, decomposed into skin friction and form drag, can be calculated either by imposing a friction coefficient (Strickler, Nikuradse, Manning, Chezy or user defined) or by a bed-roughness predictor (Villaret and Tassi, 2014).

The bottom evolution equation is then solved using either a Finite Element or Finite Volume Method. This module cannot calculate the flow field independently. therefore, the hydrodynamic variables are either imposed in the model using FORTRAN programming or exchanging result files (hydrodynamic and sediment transport) by coupling TELEMAC-2D, TELEMAC-3D and SISYPHE. The following bottom evolution equation (Equation 3-16) is solved at each node point in order to calculate the change of sediment thickness using mass balance:

$$\left(1-n_p\right)\frac{\partial Z_f}{\partial t}+div(Q_s)=0 \qquad 3-16$$

Where n_p is the bed porosity. Z_f is the bottom elevation () and Q_s, is the sediment transport (volume) vector per unit width (Villaret and Tassi, 2014).

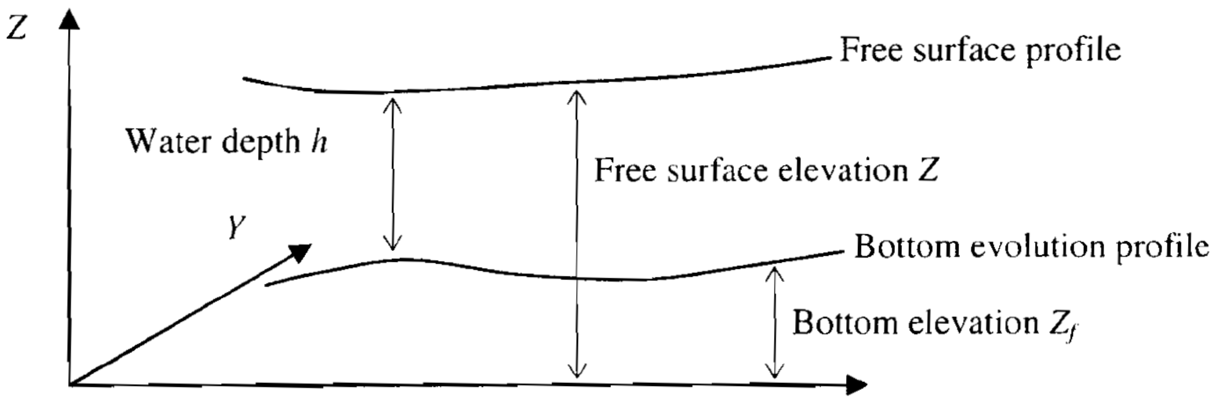

Figure 3-1: Bottom elevation profile

The following sediment transport formulae are programmed in SISYPHE for the calculation of sediment transport (volume) vector per unit width Q_s (Villaret and Tassi, 2014).

- Meyer-Peter & Muller (1948)
- Einstein & Brown (1950)
- Engelund & Hansen (1967)
- Bijker (1968)
- Bailard (1981)
- Van Rijn (1984a)
- Dibajnia & Watanabe (1992)
- Hunziker (1995)
- Soulsby & Van Rijn (1997)

Description of these formulae can be found in relevant references mentioned above or Van Rijn (1993) and Yang (1996). For simplicity, SISYPHE considers all of these formulae in terms of the Shields parameter. This study used the Meyer-Peter & Muller (1948). Einstein & Brown (1950), Engelun & Hansen (1967) and Van Rijn (1984) formulae. Details are provided in section 3.2.6

3.2.1 Coupling between bedload and suspended load

The bed evolution Equation 3-16 is only considered the bed-load transport assuming local equilibrium. Equation 3-16 is coupled with a transport-diffusion equation (Equation 3-17) in order to consider the suspended sand concentration in non-equilibrium conditions (SISYPHE, 2014).

$$\frac{\partial C}{\partial t}+U\frac{\partial C}{\partial x}+V\frac{\partial C}{\partial y}=-\frac{1}{h}\left[\frac{\partial}{\partial x}\left(h\varepsilon_s\frac{\partial C}{\partial x}\right)+\frac{\partial}{\partial y}\left(h\varepsilon_s\frac{\partial C}{\partial y}\right)+\frac{(E_e-D_d)_{z=a}}{h}\right] \qquad 3\text{-}17$$

where h is the water depth, U and V are the depth-averaged flow velocities in the x- and v directions. *C* is the depth-averaged sediment concentration. ε_s is the sediment diffusivity coefficient. E_e - D_d is the net erosion minus the deposition flux of the sediment. which was calculated at the interface between the suspended-load layer and the bed-load layer ($z = a$). The erosion (E_e) and deposition (D_d) fluxes between the suspended load and their effect on the bed evolution are calculated using various semi-empirical expressions (Villaret and Tassi, 2014).

For uniform flat beds, the bed-load layer thickness is assumed to be proportional to the grain size d_{50} • For the rippled beds, it is proportional to the bed roughness k_s. The interface layer thickness between the bedload and the suspended load i.e. $z = a$ is therefore determined as (SISYPHE, 2014):

$$a=\max(2d_{50},k_s) \qquad 3\text{-}18$$

The bottom evolution Equation 3-16 is modified in order to take into account the erosion and the deposition flux calculated from Equation 6-19 (SISYPHE, 2014).

$$\left(1-n_p\right)\frac{\partial Z_f}{\partial t}+div(Q_s)+(E_e-D_d)_{z=a}=0 \qquad 3\text{-}19$$

The erosion and deposition term $(E_e - D_d)_{z=a}$ in Equations 3-17 and 3-19 is further approximated according to Celik & Rodi (1988), which is relevant for non-cohesive sediments. They considered the equilibrium volume concentration, the near bed concentration and the settling velocity to express the mathematical relationship for the prediction of the erosion and deposition fluxes (SISYPHE, 2014):

$$(E_e - D_d)_{z=a} = v_{ss}\left(C_{eq} - C_{z=a}\right) \qquad 3\text{-}20$$

where ν_{ss} is the settling velocity, C_{eq} is the near-bed concentration and $C_{z=a}$ is the near bed concentration calculated at $z=a$. The Zyserman & Fredsoe (1994) formulation is used to calculate the near-bed concentration C_{eq}, which is expressed in terms of the critical Shields parameter θ_c, and the Shields parameter θ taking account the bottom friction (SISYPHE, 2014):

$$C_{eq} = \frac{0.331(\theta - \theta_c)^{1.75}}{1 + 0.72(\theta - \theta_c)^{1.75}} \qquad 3\text{-}21$$

The near bed concentration is calculated as a function of the mean velocity U and the depth averaged concentration C as (SISYPHE, 2014).:

$$C_{eq} = \frac{UC}{u_*}\frac{K}{I}\left[\frac{1 - a/h}{a/h}\right]^{R_P} \qquad 3\text{-}22$$

$$I = I_1 \log\left(\frac{30h}{k_s}\right) + I_2 \quad 3\text{-}23$$

$$I_1 = \int_{ah}^{1}\left(\frac{1-u}{u}\right)^{R_P} du \; and \; I_2 = \int_{ah}^{1}\left(\frac{1-u}{u}\right)^{R_P} \log(u)\, du \qquad 3\text{-}24$$

$$R_P = \frac{v_{ss}}{Ku_*} \qquad 3\text{-}25$$

where K is the von Karman constant, u_* is the shear velocity. a is the interface layer between bed load and suspended load. h is the water depth. u is the velocity in the leading direction, $k_s = 2d_{50}$ is the bed roughness height, R_p is the Rouse number and I, I_1 and I_2 are the so-called Einstein integrals (SISYPHE, 2014). The suspended sediment transport rate (q_s) is calculated by integrating the product of the Rouse concentration profile *c(z)* and the logarithmic velocity profile *u(z)*, (SISYPHE, 2014):

$$q_s = \int_{a}^{z_1} u(z)c(z)\, dz \qquad 3\text{-}26$$

3.2.2 Shear Stress

When Sisyphe is coupled with Telemac-3d, the bed shear stress is aligned with the near bed velocity in order to account for possible flow deviations. The magnitude of the bed shear stress is still related to the depth-averaged velocity, except if the Nikuradse friction law is applied. In this case, the friction velocity is related to the near bed flow velocity U^* by assuming a logarithmic velocity profile near the bed:

$$U^* = \frac{u_*}{k}\ln(\frac{z_1}{z_0}) \qquad \text{3-27}$$

where z_0 is expressed as a function of the Nikuradse bed roughness ($z_0 = k_s/30$), with k_s the grain roughness height, z_1 is the distance of the first vertical plane from the bed level; and k = 0.4 is the von Karman constant. For flat beds, the roughness height has been shown to be approximately k_s is $3d_{50}$, with d_{50} the grain size with 50% of the material finer by weight. The bed shear stress is calculated with this shear velocity, in order to account for deviations: $\tau_b = \rho\ U^*2$

The critical Shields number or dimensionless critical shear stress θ_c is defined by:

$$\theta_c = \frac{\tau_c}{(\rho_s - \rho)gd_{50}} \qquad \text{3-27}$$

where τ_c is the critical shear stress for sediment incipient motion. Values of θ_c can be either specified in the SISYPHE steering file by use of keyword SHIELDS PARAMETERS or calculated by the model as a function of non-dimensional grain diameter D_*:

$$D_* = d[\frac{\left(\frac{\rho_s}{\rho} - 1\right)g}{\nu^2}]^{1/3} \qquad \text{3-28}$$

The critical Shields number is implemented in the subroutine as follows (SISYPHE, 2014).:

$$\theta_c = \begin{cases} 0.24{D_*}^{-1}, & D_* \leq 4 \\ 0.14{D_*}^{-0.64}, & 4 < D_* \leq 10 \\ 0.04{D_*}^{-0.10}, & 10 < D_* \leq 20 \\ 0.013{D_*}^{0.29}, & 20 < D_* \leq 150 \\ 0.045, & 150 \leq D_* \end{cases} \qquad \text{3-30}$$

3.2.3 Settling velocities

The settling velocity is an important parameter for suspended sediment transport. It can be either specified or calculated by the model as a function of the grain diameter. The van Rijn formula (van Rijn, 1987 and van Rijn, 1993) which is valid for non-cohesive spherical particles and dilute suspensions, has been implemented in SISYPHE as provided in section 2.7.1, equation 2-9, 2-10 and 2-11.

3.2.4 Transport rate

When the bed shear stress exceeds the critical threshold value coarse sediment particles start to move as bedload, while the finer particles are transported in suspension. The total sediment load Q_t includes a bedload Q_b and suspended load Q_s components:

$$Q_t = Q_b + Q_s \qquad 3\text{-}29$$

Bedload occurs in a very thin high concentrated near-bed layer, where inter-particle interactions develop. The interface between the bedload and suspended load is located at $z = Z_{ref}$:

– In the thin high-concentrated bedload layer ($z < Z_{ref}$) inter-particle interactions and flow turbulent interactions strongly modify the flow structure. Equilibrium conditions are however a reliable assumption to relate the bed-load to the bed shear stress.

– In the upper part of the flow ($z > Z_{ref}$), for dilute suspension clear flow concepts still apply, and the sediment grains can be regarded as a passive scalar which follows the mean and turbulent flow velocity, with an additional settling velocity term (SISYPHE, 2014).

3.2.5 Bedload transport

A large number of semi-empirical formulae can be found in the literature to calculate the bedload transport rate bedload formulae including the Meyer-Peter and Muller, Engelund-Hansen and Einstein-Brown formulae. Most sediment transport formulae assume threshold conditions for the onset of erosion (e.g. Meyer-Peter and Muller, van Rijn and Hunziker). Other formulae are based on similar energy concept (e.g. Engelund-Hansen) or can be derived from a statistical approach (e.g. Einstein-Brown, Bijker, etc.). The non-dimensional sand transport rate Fs, is expressed as:

$$\Phi_s = \frac{Q_b}{\sqrt{g(s-1)d_{ch}^3}} \qquad 3\text{-}30$$

with $\rho_s$the sediment density, s = ρ_s / ρ the relative density, d the characteristic sand grain diameter

(d_{ch} for uniform grains), and g the gravity. The characteristic sand grain diameter can be chosen as d_{50} initially. As presented next, the non-dimensional sand transport rate Φ_s is, in general, expressed as a function of the non-dimensional skin friction or Shields parameter θ' , defined by:

$$\theta_c = \frac{\mu\tau_0}{(\rho_s - \rho)gd_{ch}} \qquad 3\text{-}31$$

with the correction factor for skin friction μ and the bottom shear stress τ_0 (SISYPHE, 2014).

3.2.6 Sediment transport formula

A large number of semi-empirical formulae have been developed to calculate the solid transport rate as a function of various hydrodynamic (e.g. water depth. Flow velocity. bottom friction. waves, etc.) and sediment (e.g. d_{50}, d_{90}. relative density. etc.) parameters (Van Rijn, 1993: Przedwojski et al. 1995: Yang, 1996: Chien & Wan, 1999: Raudkivi, 1998: SISYPHE, 2014). The transport formula can estimate only the bed load, suspended load and total load (bed and suspended load). The formulae used in this study are discussed below.

- **Meyer-Peter and Muller (1948)**

The Meyer-Peter and Muller (1948) formula is based on the energy slope approach and is limited to "bed load" transport only. According to Meyer-Peter and Muller (1948). the bed load transport (q_b can be expressed as (Van Rijn, 1993):

$$\Phi_b = \frac{q_b}{\sqrt{g(s-1)d_{50}^3}} = 8(\mu_b\theta - 0.047)^{1.5} \qquad 3\text{-}32$$

$$\mu_b = \left[\frac{C_h}{C_h'}\right]^{1.5} = \left[\frac{\log(12h/k_s)}{\log(12h/d_{90})}\right]^{1.5} \qquad 3\text{-}33$$

where Φ_b is the dimensionless bed sediment load function. θ is the Shields parameter; μ_b is the bed form factor or efficiency factor; C_h is the Chezy coefficient C_h' is the grain related Chezy coefficient. k_s is the effective bed roughness and h is the water depth. Based on the model validity tests SISYPHE (2004) recommends using the Meyer-Peter and Muller (1948) formula for the fine to coarse sediments in the range $0.4 < d_{50} < 29.0$ mm.

- **Einstein and Brown (1950)**

Einstein (1950) was one of the first researchers to estimate the sediment transport using the concept of probability. Two particular concepts drove him to do so; the difficulties in defining the critical incipient criterion and the need to take into account the turbulent flow fluctuations on sediment transport instead of the forces acting on the sediment particles. As a result, he expressed the probability for the beginning and ceasing of the sediment motion. His experiments highlighted the following points (Yang, 1996):

- There is a steady and intensive exchange of particles between bed material and bed load.
- The movement of bed load is in a series of steps and average of step length is about 100 times the particle diameter.
- The rate of erosion depends on the number and properties of particles in unit area and the probability that the instantaneous hydrodynamic lift force on the particle is large enough to move it.

Einstein (1950) method is based on a stable bed condition when the rate of deposition must be equal to the rate of erosion. The number of particles of size d eroded per unit time and unit bed area is calculated using the probability that any given particle will be eroded. At the same time the number of particles deposited per unit area and unit time are calculated using the relationship with bed load discharge. He therefore correlates this erosion and deposition taking account into the lift force and submerged weight of the particles in order to get the bed load transport. Einstein (1950) used three different graphical figures to compute the bed load. Brown (1950) further developed the Einstein (1950) approach taking account into the Shields parameter and the dimensionless characteristic sediment diameter d_* (Equation 2-13) (Yang, 1996; SISYPHE, 2004). Einstein & Brown (1950) thus proposed the following equations for bed load (Equation 3-35):

$$\Phi_b = \frac{q_b}{\sqrt{g(s-1)d_{50}^3}} = f_1(d_*)f_2(\theta) \qquad 3\text{-}34$$

$$f_1(\theta) = \left(\frac{2}{3} + \frac{36}{d_*}\right)^{0.5} - \left(\frac{36}{d_*}\right)^{0.5} \qquad 3\text{-}35$$

$$f_2(\theta) = 2.15\exp\left(-\frac{0.391}{f_1(\theta)}\right) \quad \theta \leq 0.2 \qquad 3\text{-}36$$

$$f_2(\theta) = 40\theta^3 \quad \theta > 0.2 \qquad 3\text{-}37$$

SISYPHE (2014) recommends using the Einstein & Brown (1950) formula for fine to relatively coarse sediments in the range $0.2 < d_{50} < 32.0$ mm.

- **Engelund and Hansen (1967)**

Bagnold (1966) was one of the first researchers to develop a sediment transport function from the stream power concept. Engelund & Hansen (1967) then applied Bagnold's approach and used the similarity principle to obtain their dimensionless total sediment transport load function (Φ_t). The energy-balance concept ($W_r = W_d$) is also considered taking account into the bedform height and bed-form length. W_r is the work per unit time and width required to elevate the sediment load over a height equal to the bed-form height. W_d is the work per unit time and width done by the fluid on moving the particles over a length equal to the bed form length. Engelund & Hansen (1967) formula calculates the "total load" q_t, and can be expressed as:

$$q_t = \frac{0.05U^5}{(s-1)^2 g^{0.5} d_{50} C_h^3} \qquad 3\text{-}40$$

where U is the depth averaged velocity, s is the specific density. C_h is the Chezy-coefficient. g is the acceleration of gravity. Equation 3-39 is the original sediment transport formulation as given by Engelund & Hansen (1967).

In order to achieve consistency with model formulations and bottom friction calculation. SISYPHE (2004) simplifies the original Engelund & Hansen (1967) formula in terms of nondimensionalize transport rate Φ_t as:

$$\Phi_t = \frac{q_t}{\sqrt{g(s-1)d_{50}^3}} = 0.05\frac{\theta^{2.5}}{c_f} \qquad 3\text{-}38$$

where the quadratic friction coefficient c_f can be computed using various coefficients given in SISYPHE (2004). Based on the model validity tests. SISYPHE (2004) recommends using the Engelund & Hansen (1967) formula for fine sediments in the range 0.2 < d_{50} < 1.0 mm

- **Van Rijn (1984a)**

Van Rijn (1984a) used the dimensionless characteristics particle diameter d_* (Equation 2-13) and excess shear stress parameter $T*$ (Equation 3-43). The bed load is given as:

$$q_b = 0.053(s-1)^{0.5} g^{0.5} d_{50}^{1.5} T_*^{2.1} d_*^{-0.3} \quad for\, T_* < 3 \qquad 3\text{-}39$$

$$q_b = 0.053(s-1)^{0.5} g^{0.5} d_{50}^{1.5} T_*^{1.5} d_*^{-0.3} \quad for\, T_* \geq 3 \qquad 3\text{-}43$$

$$T_* = \frac{\theta}{\theta_c} - 1 \qquad 3\text{-}40$$

SISYPHE (2014) recommends using the Van Rijn (1984a) formula for fine sediments in the range $0.2 < d_{50} < 2.0$ mm

3.3 Coupling between sediment transport and hydrodynamic modules

In SISYPHE, the relevant hydrodynamic variables can be either imposed in the model (chaining method) or calculated by a hydrodynamic computation (internal coupling) by using one of the hydrodynamic modules of the TELEMAC system (modules TELEMAC-2D, TELEMAC-3D or TOMAWAC) or an external hydrodynamic model.

The SISYPHE and TELEMAC-3D codes were stored in separate libraries. An interface code had to be therefore activated to make a link between the hydrodynamic (TELEMAC-3D) and sediment transport module (SISYPHE). This study used internal coupling activating the codes by means of the hydrodynamic and the sediment transport parameter files (Appendix B).

Chapter 4. SCOUR MECHANICS OF A TSUNAMI-LIKE BORE AROUND A SQUARE STRUCTURE.

The article is in second review in Journal of Waterway, Port, Ocean, and Coastal Engineering (ASCE)

Abstract

This study presents a detailed analysis of the mechanics of scour around a square structure due to an inland-propagating tsunami-like bore using physical modelling. A series of hydraulic bores was simulated using the dam-break method in a flume at the University of Ottawa Hydraulics Laboratory. The dam-break bore was generated by releasing water from an impoundment through a rapidly opening swing gate. A novel video-recording system was used to record the evolution of the scour and vortex structure around the structure; image processing allowed tracking of the time and spatial evolution of the scour around the structure. In addition, different characteristics of a generated bore, final scour topography, and the relationship between scour depth and bore characteristics are assessed. The test program was designed such that propagation over dry bed, typical of the first tsunami-induced inundation, was investigated. It was found that the high velocity and relatively short duration of a tsunami-like bore can induce rapid scour around the structure. The deeper bore depth over dry bed conditions resulted in faster rates of infiltration and scour. Furthermore, it was found that the longer duration of a turbulent bore induced more scour depth compared to that produced by a height-equivalent solitary or long wave.

4.1 Introduction

Rapid submarine displacement of the ocean floor or large submarine landslides can generate, under certain conditions, a series of significantly long waves which are called tsunami. Such ocean or lake bottom displacements are usually generated by impulsive disturbances above or below the water surface such as the uplift or subsidence of the seafloor during submarine earthquakes, aerial or submerged landslides, underwater explosions, volcanic eruptions, or asteroid impacts. The energy of such extreme events is transmitted to the entire water column. The resulting waves propagate outward, in different directions, from the source. Their wavelength, amplitude and period vary, depending on the size of the source generating mechanism (U.S.NRC 2008).

Upon reaching the vicinity of the coastline, tsunami waves transform significantly and, depending on the nearshore bathymetry and coastal topography, a bore or a surge forms in shallow waters (FEMA 2012). A tsunami bore is characterized by a turbulent and steep foaming front which advances inland, often at high velocities. The breaking is predominant for leading elevation waves and occurs as a result of wave shoaling and non-linear transformations over the continental shelf (Yeh 2009).

Post-tsunami field survey evidence has indicated that destructive tsunamis cause substantial coastal sediment mobilization (Chen et al. 2013). Measurements collected from several tsunami events, such as the 1992 Nicaragua Tsunami, the 2004 Indian Ocean Tsunami, the 2011 Tohoku Tsunami have recorded substantial evidence of scour around damaged buildings and bridge foundations (Yeh and Li, 2008, Ghobarah et al. 2006, Saatcioglu et al. 2006a, Saatcioglu et al. 2006b, Chock et al. 2013). These forensic engineering field surveys noted that scour was one of the primary causes of coastal structural damage (Chen et al. 2016). Tsunami waves with inundation depths of 5–25 m have been measured following several major tsunami events during the last decade (particularly during the 2004 Indian Ocean and 2011 Tohoku Tsunami). Coastal inundation is accompanied by high overland flow velocities, both during the inland flow as well as during the drawdown phase. These high flow velocities produce high bed shear stresses and large amounts of sediment movement over large areas, resulting in substantial beach erosion and scour around many of the structures located in the inundation zone (Ghobarah et al. 2006, Saatcioglu et al. 2006a, Saatcioglu et al. 2006b, Chock et al. 2013, Li et al. 2012). Yeh and Li (2008) observed local scour at the seaward corner of a schoolhouse in Kalapakkom, India (Figure 4-1a). The inundation depth was 0.95 m above the building's floor and the run-up height was estimated at 4.1 m. Francis (2006) also reported local scour around the corner of the two-story pile supported hotel foundation in the Koh Khao Jomtien, Phangaa, Thailand (Figure 4-1b). The estimated run-up depth at that location was 10 m. The scour depth was approximately 1.5 m with a horizontal span of 5 m.


a) b)

Figure 4-1: Typical tsunami-induced scour holes at building foundations: a) approximately 1.5 m deep in India, from the 2004 Indian Ocean tsunami (Yeh and Li 2008); b) Koh Khao, Thailand. Case SS-4 (Francis 2006)

A vast amount of research exists on scour depth in waves, currents and combinations of waves and currents. However, in the case of tsunami-induced scour, forensic engineering post-tsunami surveys are the primary source of scour data and the literature is limited. Numerous studies have pointed out scour around structures as the main failure factor for many coastal structures during the 2011 Tohoku tsunami (Jayaratne et al. 2016). Researchers such as Van et al. (2007), Mazumder and Ojha (2007), Zhao et al. (2010), Yeh (2010), Kato et al. (2006, 2012), Yeganeh-Bakhtiary et al. (2012), Arikawa et al. (2012), and Arya and Shingan (2012) performed experimental studies which investigated scour mechanisms around vertical cylinders and breakwaters. Yoshii et al. (2017) and Yoshii et al. (2018) investigated tsunami inundation and associated sediment transport and deposition in the coastal hinterland using two large wave flume studies. However, experimental work related to scour around structures attempting to simulate the local scour induced by tsunamis inundation are limited to a few studies.

Two common approaches have been used in the past for experimentally investigating and generating tsunami waves: (1) the use of short solitary waves and (2) the use of long waves generated in a flume or wave basin. Tonkin et al. (2003) examined scour generated by a solitary wave to represent tsunami around a cylindrical structure located on a sloped sandy beach and with a blockage ratio (structure width to flume width) of 25%. The duration of measurements before the reversal of the flow was of approximately 6 s from the initial wave impact. Tonkin et al. (2003) observed scour effects caused by pore pressure gradients and concluded that the loss of sediment cohesion due to pore pressure gradients caused the sand to be scoured more easily and that pore pressure gradients were the main factor in the formation of the large scour hole behind the cylinder. Nakamura et al. (2008) conducted physical experiments around a square structure on a long-sloped beach leading to a steep revetment. The test runs were performed using solitary (short) and long-period waves (with a maximum T=14 s) and a blockage ratio of 20%. Both types of wave were generated using a piston-type wave maker. The durations of the long-period waves were approximately double those of the solitary waves. They concluded that the type of wave acting on a structure had a significant effect on the maximum and final scour depths around it. A solitary wave caused a maximum scour depth half that of the long wave, because of its shorter duration of action. The scour mechanism observed by Nakamura et al. (2008) differed from that of Tonkin et al. (2003) mainly because of the different geometries of the structures; also, no drawdown was used in Nakamura et al.'s (2008) experiments.

Tonkin et al. (2003)'s experiments have been numerically simulated and applied to model scour at bridge piers by Pan and Huang (2012); this methodology is cited in the ASCE7(2016) Chapter 6: ‘Tsunami Loads and Effects’ design standard. Madsen et al. (2008) noted that the solitary wave assumption does not allow for the period and length of the wave to be set independently, leading to unrealistic waveforms when scaled up to prototype. They also concluded that many of the solitary wave experimental studies failed to establish any realistic physically-based correlation to real tsunamis and showed also that the traditional solitary wave had, at the time, relative time- and space-scales on the order of several orders of magnitudes shorter and smaller, respectively, compared to those deduced from field surveys of the 2004 Indian Ocean Tsunami. Therefore, at present, scientific consensus indicates that, for most current experimental facilities solitary waves tend to be less representative of actual tsunamis due to their short period. This is particularly important for studies focusing on scour, where flow duration is a critical variable.

Moreover, lately, a combination of steady flows and waves have been combined numerically by Larsen et al. (2017) and, later, experimentally by Larsen et al. (2018) for tsunami-induced scour around offshore wind turbine monopiles. Foster et al. (2017) noted that, over shorter time scales, tsunamis are cyclic over their defined period T and can be assumed to exhibit quasi-steady currents. McGovern et al. (2019) also conducted a series of experiments using a Pneumatic Long Wave Generator to create tsunami-like oscillatory flows with wave periods of 25–147 s equivalent to 3–17.3 minutes at a 1:50 Froude scale. In their study, waves propagate over a slope before impinging over a flat wet sediment pit in which a square structure was placed. They used the Keulegan-Carpenter (KC) number which includes the period of the flow and its velocity which are the two key parameters in wave and current scour studies. McGovern et al. (2019) concluded that the instantaneous scour development is similar to that generated by a current or even a tidal current, due to the long period of the inundation by comparing the long wave scour with current and tidal current scour.

McGovern et al. (2019) concluded that the rate of onshore scour development varies with time due to the changes in flow velocity and depth and that the scour depths is more dependent upon inundation duration than velocity for their particular experimental conditions. They also reported that KC influence is not necessarily the same as observed for wind wave and current scour due to transition of tsunami from wave-like to current-like flows during inundation.

Over the past decade, a novel approach proposed to experimentally reproduce tsunami-induced hydraulic bores was to generate a dam-break wave by rapidly releasing water impounded behind a gate into a straight channel. Chanson (2006) analyzed visual images of an actual tsunami bore from the 2004 Indian Ocean Tsunami and concluded that the flow characteristics of tsunami-induced bores are similar to those of a dam-break wave. As a result, dam-break waves have been extensively used by numerous researchers to model wave-structure interaction (Nistor et al. (2009), Nouri et al. (2010), Shafiei et al. (2016a), Stolle et al. (2018), Wüthrich et al. (2018)), debris transport (Nandasena et al. (2011), Stolle et al. (2018b)) and debris impact (Ikeno et al. (2016), Shafiei et al. (2016b), Derschum et al. (2018)) in tsunami-like events.

A few experiments have investigated tsunami bore induced scour around coastal structures, such as those by Triatmadja et al. (2011), Shafiei et al. (2015) and Lavictoire et al. (2014). Triatmadja et al. (2011) investigated the scour around cylindrical and 0.045 m X 0.045 m square prism structures located on a sloped sand bed using a flume 20.4 m long and 0.60 m wide. They reported that, the ratio of the maximum scour depth around the structure to the flow depth was from 0.2 to 0.3, and that the maximum scour depth around the square prism structure was slightly larger than that around the cylindrical structure. However, no dynamic scouring process was measured in their experiment. Lavictoire et al. (2019) used dam-break waves to investigate tsunami-like bore-induced local scour around a cylindrical structure and found that the short duration and very turbulent nature of the bore resulted in a rapid scour process. Lavictoire et al. (2019) found that the ratio of scour depth to flow depth ranged between 0.6 and 1.8. This ratio is significantly larger than that reported by Triatmadja et al. (2011). In addition, Lavictoire et al. (2014) reported that the scour depth was highly dependent on the bore velocity. Similar toTriatmadja et al. (2011), they only measured the final scour depth. Shafiei et al. (2015) investigated the tsunami-like bore induced scour around inland structures placed on a wet sandy foundation using three model structures: a square prism, a diamond prism, and a cylinder. They observed that maximum scour depth during and after the bore impact increased with increasing bore strength and that the structure's shape had a significant influence on the maximum scour depth. However, none of these experiments presented a detailed description of scour process.

4.2 Research objectives

This study attempts to present a detailed analysis of the scour around a square structure induced by a hydraulic bore. Previous studies focused only on the observed final scour depth; however, in this study, a video-analysis system was used to record the temporal and spatial evolution of the scour around the structure and the associated vortex evolution. Image processing provided highly detailed information of the scouring process, yielding temporal and spatial evolution of the scour around the structure.

In this experimental program, the bore is generated using a rapid release of water impounded in a reservoir, which generates a dam-break wave. Importantly, for the first time, coherent structures occurring during the highly transient short duration bore are observed and related to the time progression of scour. The results of the present study can be generalized to local scour around buildings located in an initially dry, horizontal inland area located away from the shoreline, as is often the case for real world tsunami events. In post-tsunami forensic engineering surveys conducted in India and Thailand following the 2004 Great Sumatra Andaman tsunami, researchers were able to document local scour occurrences not only at buildings located close to shore, but also to structures located hundreds of meters inland (Ghobarah et al., 2006).

This paper is structured as follows: the "Experimental setup and test procedure" introduces the University of Ottawa Hydraulic Laboratory Dam Break Flume, the instrumentation used in this experimental program, the tracking method of scour evolution and geotechnical properties of the sediment used in this study. The "Validation of the model" section provides comparison of the experimentally-obtained bore profile and the dam-break analytical solution. The "Results" section presents the analysis performed on the bore hydrodynamics and scour process. The "Discussion" section presents some of the particularities of the results while the "Conclusion" section outlines the key findings, and the limitations of the current research are.

4.3 Experimental setup and test procedure

4.3.1 Flume and instrumentation

The hydrodynamic boundary conditions for this experimental program were simulated using the dam-break method in a hydraulic flume located in the Hydraulics Laboratory at the University of Ottawa (Canada). The flume is 30 m long, 1.5 m wide and 0.8 m deep. The dam-break bore was generated by the rapid release of water impounded behind a rapidly-opening swinging gate which was equipped with a lock and release mechanism. The sediment bed section, starting at 4.15 m downstream of the gate, was 3.30 m long and 1.5 m wide, delimited at each end by false floors, as shown in Figure 4-2a and b.

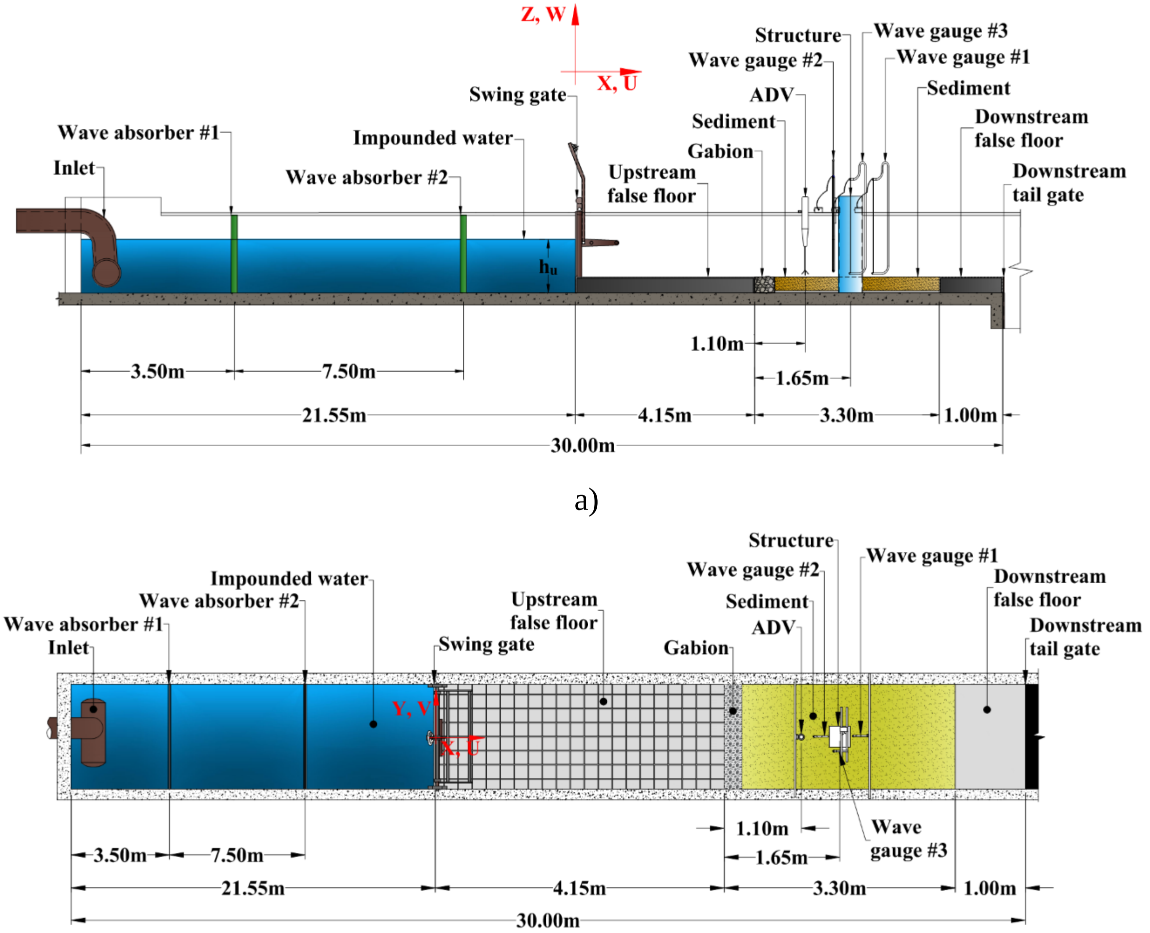

Figure 4-2: Experimental setup, a) side view (not to scale), b) plan view (not to scale)

Two aluminum false floors with a height of 0.2 m were installed (one before and one after the sediment bed section), downstream of the swinging gate, to ensure the formation of the fully developed dam break wave prior to its propagation over the sediment section. The upstream and downstream false floor sections had a length of 4.15 m and 1 m, respectively. The upstream false floor was covered with a layer of glued sand with a uniform grain size of 1 mm in order to provide surface roughness, limiting the influence of the transitional wave formation between the fixed and moveable bed sections. A grid with 20 cm x 20 cm spacing was painted on the top surface of the upstream false floor for flow tracking and measurement purposes. The base of the sediment bed was constructed of a layer of 1 cm thick coarse gravel covered by a geotextile sheet. The base layer drained any small amounts of water that infiltrated from below the false floor in order to prevent the water from influencing the level of saturation of the sediment bed. The sediment bed section with a thickness of 20 cm was filled with 1 mm uniform sand which is the most common sizes in coastal environment. Directly downstream of the false floor, a 15 cm-wide gabion was installed across the flume. The gabion was constructed in the form of a wire box filled with coarse, uniform gravel, with an average diameter of 30 mm and with a gabion thickness of approximately 3 cm. The gabion was used to minimize the local scour that would have occurred at the interface between the upstream false floor and the sediment sections. Two wave absorbers were installed upstream in the impounding reservoir in order to attenuate secondary waves within the reservoir to prevent water level fluctuations at the test section induced by the waves reflected by the inflow downstream structure.

Three calibrated WG-50 capacitances-type wave gauges manufactured by RBR Ltd. Canada with an accuracy of +/- 0.4% of measurement were used to record the time-history of the water surface elevation at different locations in the reservoir and flume, using a sampling rate of 30 Hz. Two video cameras, a GoPro HeroTM Black (1920 x 1440 at 60 fps) and an IO Industrial Flare™ high-speed video camera (2048 x 1088 at 60 fps) were used during the experimental investigations. The high-speed digital video camera had a dual purpose: a) to track the bore front as it propagated downstream over the false floor and b) to record the evolution the of scour and vortex structure. The GoPro HeroTM Black was used to estimate the average bore front celerity during its propagation over the sediment section. A 0.2 m x 0.2 m square cross section structure built of Plexiglas was used in the experiment. As shown in Figure 4-3a and b, the structure was installed in the center of the sediment section.

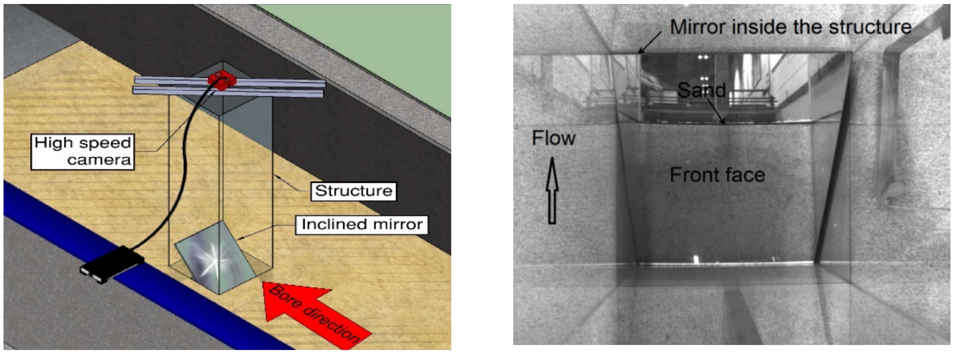

a) b)

Figure 4-3: a) Experimental setup to monitor the scour process; b) Reflected (looking down from the top of the structure to the mirror placed inside) view of the structure's front face

The structure was transparent in order to allow for monitoring (video-recording) of the scour process by means of the high-speed camera placed at the top of the structure in combination with a periscope system comprised of a mirror inclined at 45° and placed inside the structure, at its base. Measuring scales were attached onto the front, side, and back of the structure to help record real-time scour depth measurement; the time-development of the scour depth was obtained with an accuracy of ±0.005 m.

Velocity measurements were conducted using a Nortek Vectrino Acoustic Doppler Velocimeter (ADV) with a down-looking head equipped with four receivers set at a sampling rate of 30 Hz (installed with the sample volume in the flume centerline at x = 5.4 m downstream of the flap gate, which was 0.4 m upstream of the structure). Finally, a Disto TM laser altimeter with a precision of ± 1.00 mm was used to measure the final local scoured bathymetry around the structure at the end of each test, following the draining of all water.

4.3.2 Experimental procedure

Before each test, the sediment bed was levelled, and the reservoir was filled with water to the target depth. The swinging gate was then manually unlocked and rapidly opened. The bore then advanced over the false floor and finally over the dry sediment bed section, with all measuring instruments recording in a synchronized manner using the data acquisition system.

The Froude number deals with the relationship between gravity and inertial forces, whilst the Reynolds number deals with the relationship between frictional and inertial forces. For various reasons the similarity requirements posed by the Froude and Reynolds numbers can typically not be satisfied simultaneously. It is then necessary to decide which are the dominant force according to which the scaling must be done. The free surface flows are governed by gravity forces, although affected by frictional forces as well.

As shown in table 4-1 the Reynolds numbers are well above the critical value for transition to turbulence and that the flow is turbulent with relatively weak effects of drag on the process. Moreover, viscous effects are important only within boundary layers and have negligible effect on wave maker motion at the large Reynolds numbers encountered in both the laboratory and in field. Therefore, the Froude number based reduced scale modeling was selected.

Tests were conducted with initial impoundment depths of hu = 0.25 m, 0.20 m, and 0.15 m as Test 1, Test 2, and Test 3, respectively. For all three tests, the downstream bed was kept dry. A 1:40 Froude scaling ratio was used, resulting in hu = 0.25 m, 0.20 m, and 0.15 m corresponding to prototype inundation heights of 10 m, 8 m, and 6 m, respectively. Each test was repeated three times and the averaged results in terms of water surface elevation, scour and velocity are presented herein.

The opening time of the gate (t) was recorded to calculate the non-dimensional gate opening time $T_0 = t\ (g/h_u)$ 1/2, where g is the gravitational acceleration and hu is the water head behind the gate. The non-dimensional gate opening time should be less than the square root of two in order to achieve the ideal dam-break condition (Lauber and Hager, 1997). A previous experimental study conducted in the same flume and using the same gate by Stolle et al. (2018), shows that the non-dimensional gate opening time, depends on hu with an approximately linear relationship as

$$T_0 = 1.47–1.19\ h_u. \qquad (4\text{-}1)$$

For the range of impoundment depths tested in this study, the non-dimensional gate opening time was in the range of $1.17 < T_0 < 1.29$. Therefore, the range of T0 was less than square root of two (1.41) which is the acceptable non-dimensional gate opening time ($T_0 < 1.41$) defined by Lauber and Hager (1997). The main description of the experimental tests (hu and bed condition and prototype inundation heights), key results such hydrodynamic parameters (bore velocity, Froude number, Reynold number and critical velocity) are presented in Table 4-1. Key results will be discussed later in the results and discussion section.

Table 4-1**.** Experimental test program

Test #	**Initial impoundment depth (h_u), m**	**Bed condition**	**Prototype inundation heights, m**	***V (*m/s)**	$\frac{V}{V_{cr}}$	**Reynolds number**	**Froude number**
Test 1	0.25	dry	10	1. 58	5.64	3.16*10^5	1.45
Test 2	0.20	dry	8	1.44	5.14	2.88*10^5	1.38
Test 3	0.15	dry	6	1.10	3.92	2.20*10^5	1.31

4.3.3 Geotechnical characteristics of the sediment

Using a laboratory slump test, the dry angle of repose of the sand particles used in the sediment bed (ΦS) was determined to be 35 degrees. A sieve analysis was performed to measure the grain size distribution of the sediment. Its median particle diameter was determined to be d50 = 1.18 mm. The geometric standard deviation ($\sigma g = 1.33$) was calculated using Equation 4-2. The coefficient of uniformity (Cu) and the coefficient of curvature (Cc) for the soil were calculated as 1.59 and 0.96 using Equation 4-3 and Equation 4-4, respectively.

$$\sigma g = \sqrt{d_{84}/d_{16}} = 1.33 \qquad (4\text{-}2)$$

$$Cu = d60/d10 \qquad (4\text{-}3)$$

$$Cc = \frac{(d_{30})^2}{d_{10}d_{60}} \qquad (4\text{-}4)$$

The specific diameters of the sediment, d84, d16, d10 and d60 are the size of the particles for which 84, 16, 10 and 20 percentage of materials by weight are finer, respectively. The soil had low values of Cu and Cc, which shows that the soil was well sorted with a narrow range of particle sizes variation. The permeability test (Ks=0.675 m/s), maximum and minimum void ratios (emin=0.70; emax=0.91) and the specific gravity (S=2.64) of the soil were also measured.

4.3.4 Scale effects

The scour around a structure in the path of flow is influenced by various parameters such as ratio of the mean flow velocity to mean critical velocity, and the relative magnitudes of grain size, flow depth and structure size (Breusers et al., 1977). Scale effects in physical scour modeling occur due to the difficulty of simultaneously satisfying the three length scales of water depth, structure size and median sediment size. Sediment size cannot completely be scaled using the same method as the flow and structure's characteristics. In order to scale the sediment particles, the dimensionless shear stress (τ^*) has to be the same in the model and prototype by maintaining similarity between the particles according to the Shields diagram. Sediment particles smaller than about 0.1mm have a tendency to act cohesively and the particles finer than 0.6 mm tend to act as ripples which behave differently from those of the typically coarse bed materials in the field (Ettema et al. 1998). Consequently, modelled sediment is often coarser than required by geometric scaling. This scaling inaccuracy results in a distorted ratio of the structure size to sediment size, which may result in imperfect scaling of the modelled scour depth (Lee and Sturm, 2009).

Therefore, it is impossible to meet the similarity requirements that could relate scour through physical modeling to scour magnitude occurring in the field.

Melville and Chiew (1999) proposed that when $D/d50 < 50$, local scour depth is influenced by the sediment size (where D is a characteristic length of a structure's cross-section, such as diameter of a pier). For the present experiment, this ratio is 200, which suggests that grain size should not have influenced scour. Also, Raudkivi and Ettema (1983) concluded that local scour is not affected by channel blockage ratio when $D/b < 16\%$, where b= flume width. Zarrati et al. (2004) suggested a more restrictive ratio in which $D/b < 6.6\%$. In the present study, the structure size ($D = 0.20$ m) was selected to allow real-time monitoring of the time progression of scour using a video system inside the structure; thus, the blockage ratio was 13%. Still, as will be shown, scour did not extend near the wall, and the structure did not appear to influence near wall streamlines. In conclusion, scour and sidewall effects were deemed to be minimal.

4.3.5 Dam break wave hydrodynamics

A comparison between an analytical dam-break solution of Chanson (2009) and the experimentally generated bore profile is presented herein. Because of the limited number of wave gauges, a number of identical tests were repeated with the same experimental configuration by installing wave gauges at sequential steps in order to cover the entire length of the flume, downstream of the swinging gate. Repeated tests performed with the wave gauges at the same locations showed a high degree of reproducibility in terms of wave arrival time and spatial evolution of the water depth. Figure 4-4 presents the comparison between the dam-break analytical solution of Chanson (2009) and the experimentally obtained bore profile on the fixed floor, immediately upstream of the sediment bed section. The X-axis corresponds to the direction along the flume length and the Y-axis represents the bore height. Chanson's (2009) solution considers the bottom friction in the dominant wave-tip region, using the diffusive wave equation and Darcy-Weisbach friction factor (f). The value of f was taken as 0.03, corresponding to a hydraulically smooth surface. As shown in Figure 4, good agreement can be observed between the experimental bore profiles and Chanson's analytical solution. Duplicate values at the same location indicated good repeatability of the experimental tests.

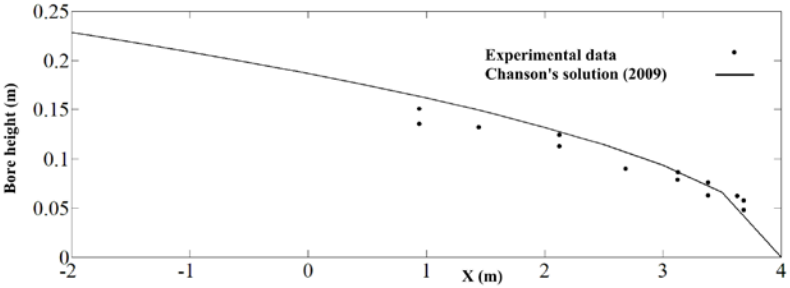

Figure 4-4.Comparison between Chanson's (2009b) dam-break analytical solution and the experimentally obtained bore profile for Test 1 at h_u = 2.48 s (0 point on X-axis presents the gate location).

4.4 Results

The first set of results that will be discussed in the subsequent sections deal with the analysis of observed scour process and bore propagation characteristics for Test 1, which corresponds to an impoundment depth, hu = 0.25 m. The second set of results to be discussed will compare the results of the three impoundment water depths (0.25 m, 0.20 m and 015 m). The set of results pertaining to the bore characteristics are the run-up tests, the stream-wise velocity, bore front velocities, and distribution of the flow field around the structure, as well as certain relationships derived from these, such as the Froude number. Further results include synchronized overlays of the bore scour depth and velocity, infiltration and scour rate, and the final bed elevations.

4.4.1 Scour processes – qualitative observations

Images from the video cameras located above (top view, Figure 4-5a) and at the side of the structure (side view, Figure 4-5b) provided a better understanding of how the bore propagated around the structure and of the local scour process. The flow in these images is propagating from right to left direction. The scour process was recorded directly using the video camera installed immediately above the structure with its view field focused onto the inclined periscopic mirror placed inside the structure and facing the incoming flow. As shown in Figure 4-5c, d and e, still images from these video recordings present the scour profiles at the front, side and back of the structure (named front face, side face and back face).

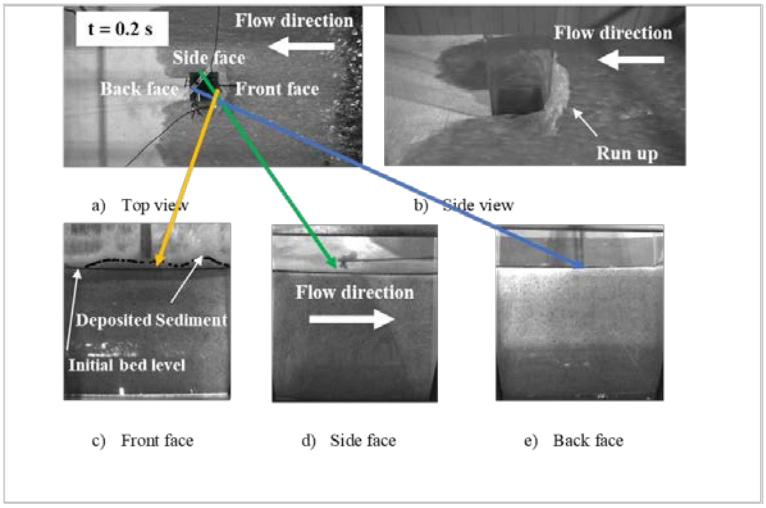

Figure 4-5**.** Incoming bore propagation and associated flow and scour pattern: a) top view of the incoming bore, b) side view of the incoming bore. Scour profiles around the structure; c) front face, d) side face, and e) back face, at t = 0.2 s for Test 1 (h_u = 0.25 m).

Figure 4-5 to Figure 4-10 show these images at four different time frames starting from the early scour stage after the initial bore impact at t = 0.2 s, at t = 1 s, t = 3.25 s, at the moment of the observed maximum scour at t =16.1 s, and at the time of the final scour profile at t = 24 s. As shown in Figure 4-5b, the initial impact of the bore with the structure pushed the flow vertically up onto the upstream face of the structure, forming an upward-directed flow called run-up. The upward flow fell back onto the incoming water surface a few centimeters upstream of the structure, forming a surface roller with very high turbulence and air bubble entertainment with significant fluctuations in its free surface. Figure 4-5a and b show the formation of a run-up on the upstream face of the structure as it is impacted by the bore propagating onto the dry bed. The initially small run-up depth increased rapidly immediately after the impact. As shown in Figure 4-5c with black dots, shortly after the initial impact, a small amount of sediment transported from upstream by the live bed was deposited at the front face of the structure. Also, as shown in Figure 4-5d and e, there was still no evidence of scour at the side or the back of the structure at t = 0.2 s; in fact, the back face of the structure was still dry at this time.

Figure 4-6a, b, e, d and e show the observed bore propagation and scour profile at t = 1 sec after bore arrival.

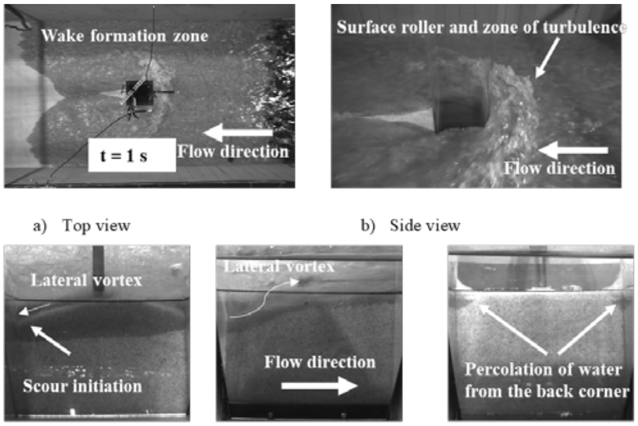

a) Top view b) Side view

c) Front face d) Side face e) Back face

Figure 4-6**.** Incoming bore propagation and associated flow and scour: a) top view of the incoming bore, b) side view of the incoming bore. Scour profiles around the structure; c) front face, d) side face, and e) back face, at t = 1 s for Test 1 (h_u = 0.25 m)

The flow run up onto the upstream face of the structure stretched laterally almost twice the side length of the structure and generated a surface roller, as shown in Figure 4-6b: below this area is where scour occurred. As the surface roller redirected alongside the structure, increased in elevation, and expanded laterally, the bore propagated in the wake of the structure. The redirected surface roller alongside the structure caused a rapid flow along its sides, indicative of the development of a lateral vortex at the front corners of the structure. At this stage, scour began to form at the corner of the structure moving gradually downstream along the structures edge, as shown in Figure 4-6c and d. This mechanism is in agreement with findings of Nakamura et al. 2008, Shafiei et al. 2015 and McGovern et al. 2019.

The separation of flow at the sides of the structure produced what is known in the literature as two wake vortices. The separated bore rejoined itself downstream of the structure at a distance about twice the side length of the structure in the downstream direction and formed a rooster-tail shape (Figure 4-6a and b). The rooster-tail enlarged, forming a conical shape at the back of the structure. Early stage of the wake development occurred at t = 0.9 s. However, the centre back face of the structure had yet to be inundated at this time (Figure 4-6a and b).

In the wake region, the flow started to percolate and move downwards through the soil from the back of the column corners, starting the development of local scour in this region, as shown in Figure 4-6e. Figure 4-7a, b, e, d and e shows the observed bore propagation and scour profile at t = 3.25 sec.

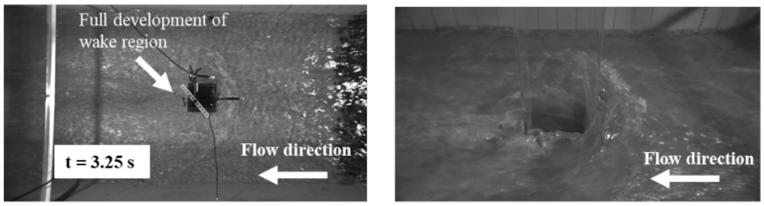

a) Top view b) Side view

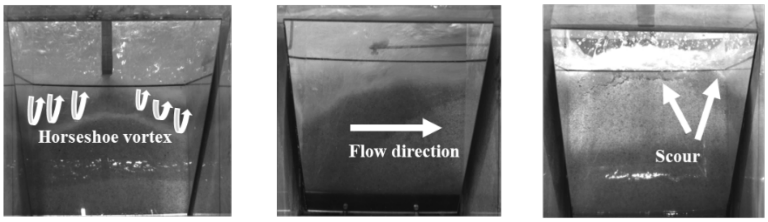

c) Front face d) Side face e) Back face

Figure 4-7**.** Incoming bore propagation and associated flow and scour: a) top view of the incoming bore, b) side view of the incoming bore. Scour profiles around the structure; c) front face, d) side face, and e) back face, at t = 3.25 s for Test 1 (h_u = 0.25 m)

Full development of the wake region did not occur until t = 3.25 s. This resulted in an oscillating vortex occurring in the leeside of the structure. At this time, the wake was highly turbulent and entrained significant air and the resulting vortex started to scour the soil from the center of the back side of the structure. As the scour hole enlarged, the downflow inside the front scour hole caused a strong upward flow (horseshoe vortex) within the scour hole. This upward flow increasingly suspended more bed sediment, which further accelerated the scour process. Also, along the sides, the flow became stronger and sediment was brought into suspension by the lateral vortex and transported downstream by the prevailing flow past the structure, as shown in Figure 4-7d.

As shown in Figure 4-7c, the scour depth at the front corner is deeper than that measured at the front centerline. Hjorth (1975) reported that the leading corner is the position of greatest bed shear stress amplification, while the centreline exhibits bed shear amplification 1. This would explain the delay in scour along the centreline. McGovern et al. (2019) also observed this delay and concluded that this delay is because the horseshoe vortex is likely not a strong influence in the early stages of the scouring process.

Finally, the zone of the surface roller upstream of the structure began to dissipate after approximately 10 to 15 seconds, as shown in Figure 4-8a and b.

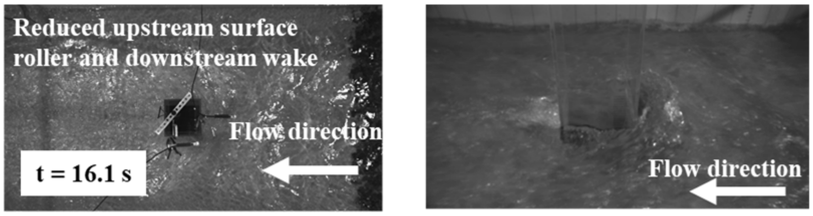

a) Top view b) Side view

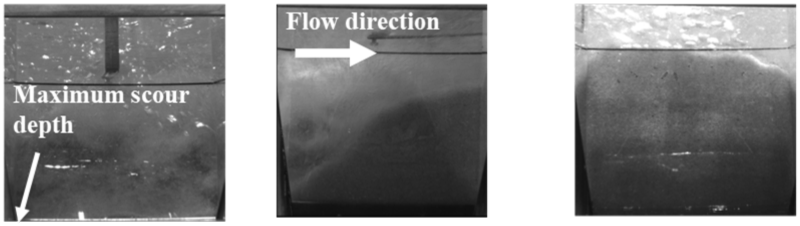

c) Front face d) Side face e) Back face

Figure 4-8**.**Incoming bore propagation and associated flow and scour: a) top view of the incoming bore, b) side view of the incoming bore. Scour profiles around the structure; c) front face, d) side face, and e) back face, at t =16.1 s for Test 1 (h_u = 0.25 m)

Following the emptying of the impoundment reservoir, as the flow velocity decreased and the zone of turbulence in front of the structure lost some of its turbulent energy, the scour hole reached its maximum depth. Figure 4-8c, d and e show the maximum scour depth at the front, side and back faces of the structure, respectively, at time t = 16.1 s, after which backfilling occurred at the front corners due to sediment slumping. The slumping is attributed exceeding the natural angles of repose and, additionally, to a drop in the flow velocity below the threshold of motion which led to eliminating its capability to artificially maintain slopes steeper than the natural angle of repose of the sediment. The scoured sediment on the sides of the structure also rolled down the steep slope formed during the initial uprush, and slowly filled the scour hole. This finding is also similar with the observation of McGovern et al. (2019. Both in current experiment and McGovern et al. (2019), only little scour occurred at the back of the structure.

Koken and Constantinescu (2008) investigated the spatial and temporal evolution of a turbulent horseshoe vortex system at the base of a spur using large eddy simulation (LES). They found that the horseshoe vortex system consisted of a larger primary horseshoe vortex and a smaller secondary horseshoe vortex. A main necklace vortex was observed to be constantly present; however, its intensity and coherence varied significantly with time. They reported that the main necklace vortex oscillated in chaotic fashion between two states: one where the vortex is closer to the spur dike and is more compact, and a second one located away from the spur dike. Analyzing the distribution of the bed shear stress, they concluded that the largest values were present in the strong acceleration region near the tip of the spur dike. Figure 4-9a, b and c show the evolution of the upstream scour hole geometry at different scour stages.

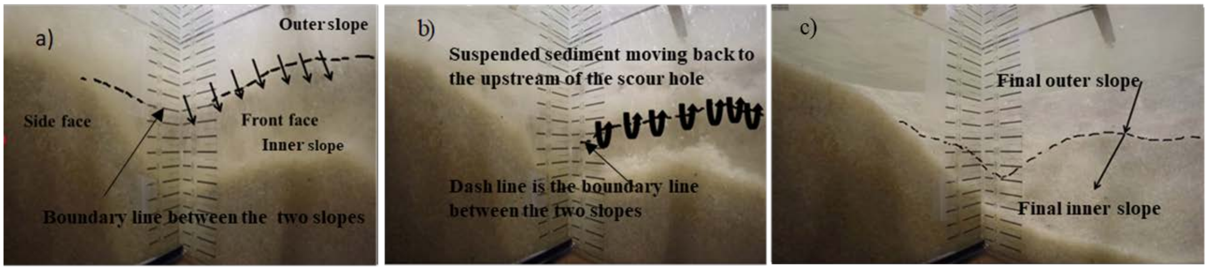

Figure 4-9**.**a) Suspended sediment movement from outer slope to inner slope at t = 6.41 s, b) Suspended sediment moving back to the upstream of scour hole and the oscillation of the boundary between two slopes at t = 7.06 s, c) Final scour hole geometry with outer and inner slopes at t = 24 s, for Test 1(h_u = 0.25 m)

The scour hole is characterized by a gradation of bed slope, an inner slope immediately adjacent to the structure and an outer slope, with a slope break in between them. The boundary between the two slopes within the front scour hole is shown with a dash line in Figure 4-9.

First, suspended sediment entrained from the outer scour hole entered the inner hole due to slope failure of outer slope (slumping), as shown with arrows in Figure 4-9a. Additionally the boundary between the two slopes moved toward the downstream of the inner slope (the latter shown with the dash line in Figure 4-9b). Furthermore, the suspended particles moved back to the upstream of the inner scour hole while still remaining suspended, shown with arrows in Figure 4-9b. As a result, the boundary moved back to the upstream part of the scour hole. Subsequently, the suspended sediment was carried out transversely, along the structure, and moved into the inner scour hole all over again. The oscillation of the boundary between the inner and outer slopes demonstrates the oscillation of the horseshoe vortex in terms of its location and magnitude over time in stream-wise direction. Following the contraction and retraction of the twisted horseshoe vortex at the corners of the structure, sediment particles were washed out toward the lateral sides of the column.

This finding was also generally confirmed by Kashyap (2012) in a 3-D numerical study of flow and coherent structures around submerged groynes in a channel bend, which described the oscillation of the boundary between two slopes and a deeper scour depth closer to the structure. It can be inferred that, due to the unsteadiness of a horseshoe vortex in a turbulent bore, sediment particles move irregularly in space and time.

This continued until equilibrium scour was reached. At this stage, the zone of turbulence lost most of its energy, as shown in Figure 4-10a and b.

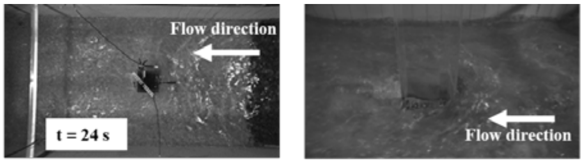

a) Top view b) Side view

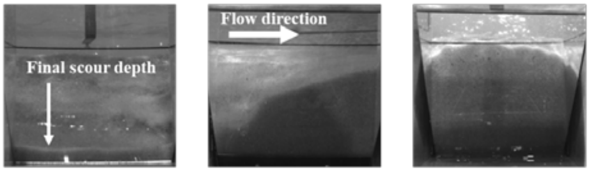

c) Front face d) Side face e) Back face

Figure 4-10**.**Incoming bore propagation and associated flow and scour: a) top view of the incoming bore, b) side view of the incoming bore. Scour profiles around the structure; c) front face, d) side face, and e) back face, at t = 24 s for Test 1 (h_u = 0.25 m)

Also, as is shown in Figure 4-10c and d, the final observed scour depth at t = 24 s was smaller than the maximum scour depth was recorded at t = 16.1 s, while the scour profile at the back of the structure (Figure 4-10e) remained almost unchanged after t = 16.1 s. The final scour hole, as a combination of the two different downward slopes, is shown in Figure 4-9c with arrows. The final outer slope was 35 degrees which is equal to the angle of repose of the sediment and had a lower slope compared to the inner slope.

4.4.2 Bore-scour and stream-wise velocity

Figure 4-11 shows the measured results for the initial condition of hu = 0.25 m (Test1). Bore duration was approximately 120 seconds and the first 25 seconds are shown in Fig. 10. The negative and positive values of the left axis represent scour and bore depth (m), respectively, whereas the right axis represents the stream-wise velocity (m/s). The black line represents the time-history of the horizontal flow velocity measured at X= 5.4 m from the longitudinal axis of the flume (40cm upstream of the structure). The red, light blue, and pink lines show the time-histories of the water surface elevation measured by the wave gauges located at the front, side and back face of the structure, respectively. Also, the red line with triangle pattern, light blue line with cross pattern and pink line with star pattern show the scour depth time-histories observed at the front, side and back of the structure, respectively.

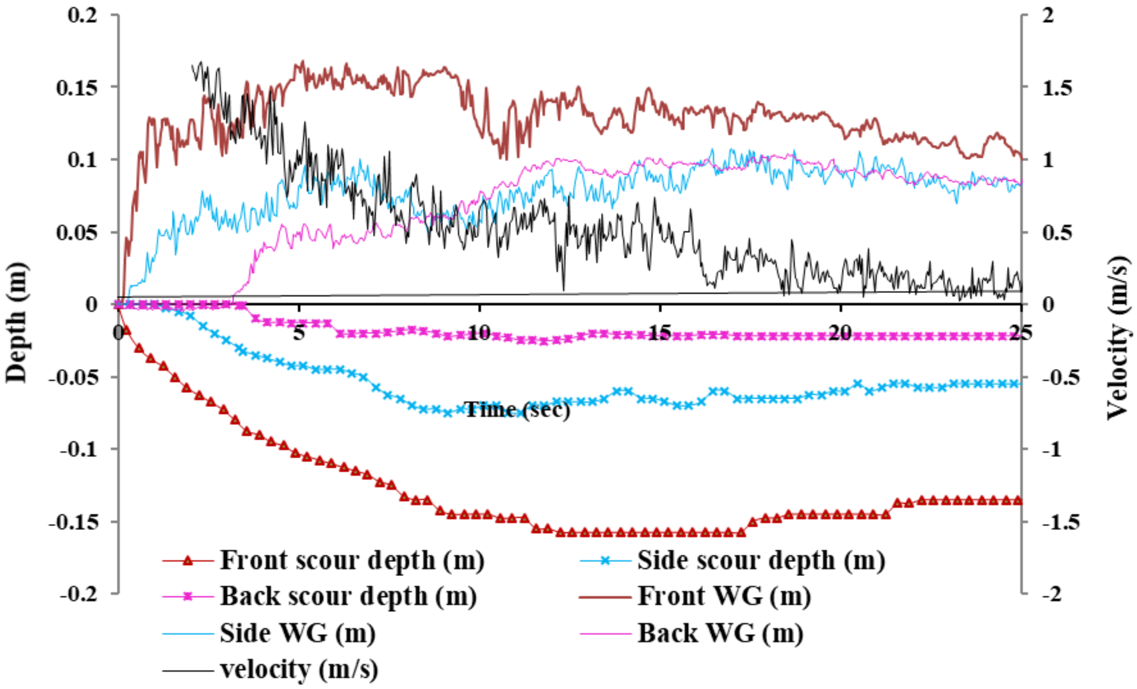

Figure 4-11**.**Time-history of the water surface elevations measured by the wave gauges located at the front (red line), side (light blue) and back (pink line) face of the structure, and scour depth measured at the front (red line with triangle pattern), side (light blue line with cross pattern) and back (pink line with star pattern) face of the structure, and horizontal velocity (black line) measured 50cm upstream of the structure for an impoundment depth, h_u = 0.25 m (Test 1)

It can be seen that stream-wise velocities were captured after 2 s from the passage of the bore front as the ADV measurements were noisy for the first 2 seconds after the arrival of the advancing bore due to air bubble entrainment and cavitation formed around the head of the ADV.

The time-history of the bore depth at the front of the structure suddenly increased moments after initial impact and continued to increase beyond the first sudden rise until a maximum value of 0.166 m was reached, after which a decrease was observed. The initial bore front (recorded by the front WG) had an almost vertical front profile, and the maximum bore depth was attained within 5 seconds after initial bore impact. When the separated bore rejoined exactly at the back of the structure, almost 3.25 s after the arrival of the bore, the back-wave gauge started to record the bore depth elevation. Therefore, there is a time delay between the initiation of recordings of the back-wave gauge and the measurements of the front and side wave gauges. The bore depths measured by the wave gauges installed on the side and back of the column show smaller bore height values compared to the bore depth measured by the front wave gauge. The maximum bore depths measured by the side and back wave gauges were 0.107 m and 0.10 m, respectively.

Figure 4-11also illustrates that the maximum bore depth (runup) measured on the upstream face was approximately 1.6 times greater than that recorded by the side and back wave gauges. It can be seen that the bore depths on the side and back faces reached a maximum almost 9.5 seconds after the maximum bore depth (runup) was measured on the front face. Scour at these three locations began shortly after the arrival of the bore at each face. Scour at the side of the structure started slightly later than the initiation of the scour at the front corner. The maximum scour depth of 0.16 m was measured at the front of the structure 13 seconds after the arrival of the bore. Maximum scour depths of 0.075 m and 0.025 m were observed at the side and back of the structure, respectively.

The critical velocity for the initiation of sediment motion was calculated using the Shields entrainment criterion. For the 1 mm grain size, the calculated critical velocity was 0.28 m/s. Figure 4-11 shows that the highest scour rate coincided with the largest flow velocities greater than the critical velocity Once the flow velocity decreased, the erosion rate slowed and the scour hole reached its maximum depth. As previously discussed, once the velocity decreased, slumping of the over-steep scour hole slopes towards the sediment's natural angle of repose was observed and filled the scour hole.

This was when the zone of turbulence began to weaken and dissipate, occurring almost 12 seconds after the bore arrival. Afterwards, the scour depth approached equilibrium (its depth no longer changed). The final maximum scour depth was therefore observed to be only 82% of the actual maximum scour depth during the event. This is also observed in McGovern at al. (2019); an approximate 30% reduction in the scour depth observed at the end of experiment was due to slumping.

4.4.3 Run-up and scour depth time history

To investigate further the scour process in the three tests, the corresponding run-up height time histories and scour depth time histories are shown on the same graph (Figure 4-12a and b).

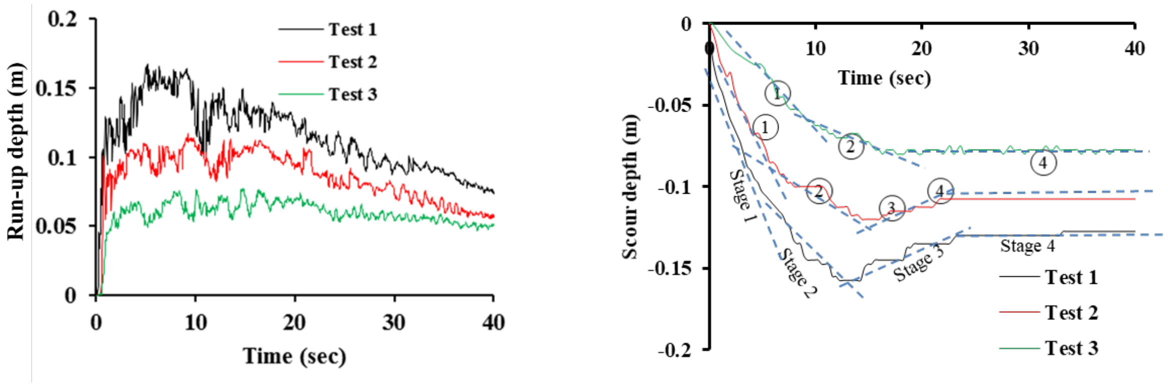

a) b)

Figure 4-12. a) Run-up depth time history; b) Scour depth time history

For better comparison of the tests, all plots commence from the initial impact at t = 0. Maximum run-up depths of 0.166 m, 0.115 m and 0.075 m were observed for Test 1 (hu = 0.25 m; black line), Test 2 (hu = 0.20 m; red line) and Test 3 (hu = 0.15 m; green line), respectively. Comparing the run-up depths, as expected, increasing the initial reservoir impoundment water depth resulted in a larger run-up depth with a steeper bore front. In all three tests, the initial bore fronts had an almost vertical profile. For Test 1, the maximum run-up depth was attained within 5 seconds of the arrival of the bore, after which the bore depth gradually decreased, whereas the maximum run-up depths for Test 2 and Test 3 occurred at t = 8.2 s and t = 9.4 s, respectively. Larger run-up depths exhibited a greater rate of decline due to higher initial reservoir impoundment water depths. As is illustrated in Figure 4-12a, after reaching to the maximum run-up value, no significant decrease was measured for the smallest bore depth, and it rapidly became a quasi-steady flow with a constant depth.

Figure 4-12b presents the time histories of the scour depth for the three experiments. Maximum scour depths of 0.16 m, 0.13 m and 0.85 m were observed at t = 12.2 s, 14.3 s and 16.3 s for Test 1, Test 2, and Test 3, respectively. It can be seen that maximum scour depth occurred, on average, 6.7 seconds after the maximum run-up depth had occurred. Also, the larger the bore depth, the earlier the maximum scour depth and maximum run-up depth occurred. The rate of decline of the scour depth was more significant for larger bore depths. As can be seen in Figure 4-12b, the evolution of the scour process evolved in four distinct stages. Stage 1: the rate of scour was greatest immediately after bore impact with the structure, leading to a steep slope in the plot of scour depth versus time. Also, on average, 65% of the maximum scour depth occurred at the end of this stage. Stage 2: the development of the scour depth decreased and the rate of scour became milder. At the end of this stage, the maximum scour depth was reached. Stage 3: Stage 3: due to slumping, the sediment started filling in the scour hole and its depth consequently decreased. Stage 4: the dimensions of the scour hole no longer changed significantly. The scour depth reached equilibrium as its variation was no longer noticeable. It can be seen that Stage 3 was not observed in Test 3, and that the final scour depth was the same as the maximum scour depth. This was probably because the velocities were not high enough to cause slumping. Comparing the times for the scour to reach equilibrium, the larger bore depth reached the equilibrium stage at t = 23.2 s, while Test 2 and Test 3 reached this phase at t =21.7 s and t = 16.3 s, respectively. This shows that the larger the bore depth, the later the equilibrium stage occurred.

4.4.4 Stream-wise velocity

The time-history of the stream-wise velocity was measured 0.4 m upstream of the structure face for all three tests is shown in Figure 4-13. The stream-wise velocity time histories appear to consist of four main segments. The first segment is characterized by a steady, steep decline which corresponded to the most significant rate of scour. The second segment had the appearance of a quasi-steady flow state where the development of the scour depth reduced comparing to the first segment. At the end of this segment, the maximum scour depth was reached. The third segment exhibited a sudden reduction in the bore velocity which caused slumping of the over-steep scour hole slopes towards their natural angle of repose. Finally, segment four corresponded to the transition to a quasi-steady flow state which resulted in a quasi-constant bore velocity during which the depth of the scour hole no longer changed and reached equilibrium. The maximum measured velocities for Test 1, Test 2 and Test 3 were 1.57 m/s, 1.44 m/s and 1.08 m/s, respectively. As expected, the deeper the impoundment depth, the larger the bore velocity.

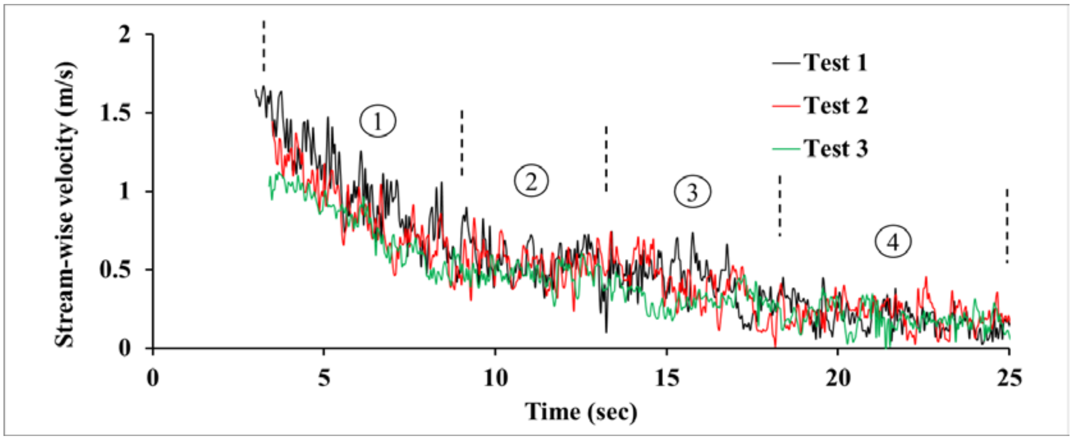

Figure 4-13. Comparison of the stream-wise velocity for Tests 1, 2 and 3

4.4.5 Characteristics of flow field around the structure

Comparing the arrival times of the bores, the initial impact of the bores with the structure for Tests 1, 2 and 3 occurred at 3.4 s, 4.3 s and 5.3 s after opening of the gate, respectively. Deeper reservoir depth produced a faster bore, so the bore arrived at the structure more quickly. The images in Figure 4-14a, b and c show comparisons between the distributions of the flow fields around the structure for Tests 1, 2 and 3.

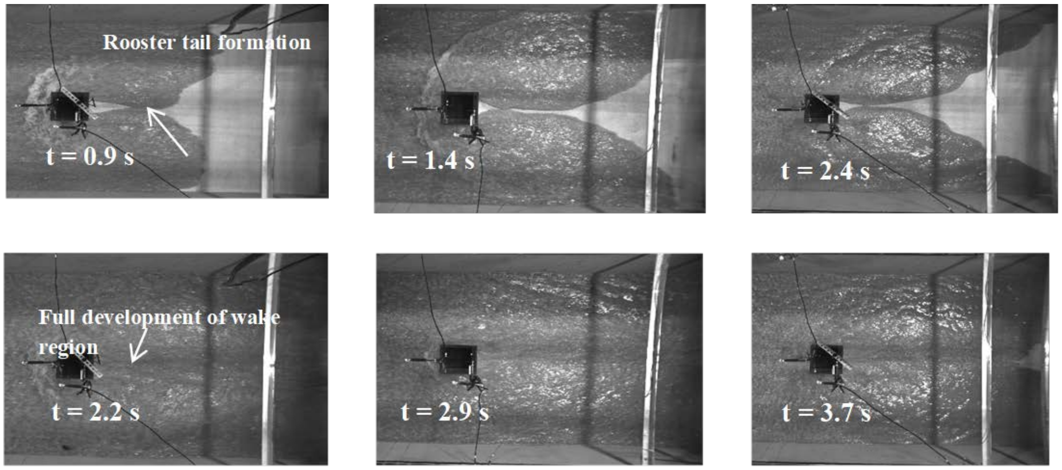

a) Test 1

b) Test 2

c) Test 3

Figure 4-14. Distribution of the flow field around structures for a) Test 1, b) Test 2 and c) Test 3

The images in the first row of Figure 4-14show the formation of a rooster tail. It can be seen that the separated bore streams rejoined 1 second after the initial impact for Test 1, while, for the smaller bores, they rejoined at t = 1.4 s and t = 2.4 s for Tests 2 and 3, respectively. For the larger bore, the separated flow around the structure had a tendency to converge toward the centerline of the flume at the back of the structure, while for smaller bore depths it diverged toward the side wall. Compared to the largest bore (in Test 1), the smallest bore (in Test 3) rejoined closer to the back of the structure. As shown in Figure 4-14c, at t= 2.4 s, reattachment right behind the structure occurred when the separated bores reached almost to the end of the sediment bed.

For the larger bore depth, the initial impact of the bore with the structure caused the water to form a surface roller with very high turbulence directly in front of the structure. For Test 1, the area of the surface roller is broader in the horizontal plane compared to those observed in Tests 2 and 3. The images in the bottom row of Figure 4-14show the duration recorded for each separated bore to completely fill up the wake region. Full development of the wake region occurred at 2.27 sec, 2.97 sec and 3.74 sec after the initial impact for Tests 1, 2 and 3, respectively. It can be concluded that the larger the bore depth, the sooner the wake region develops. The intense zone of turbulence for Tests 1 and 2 lasted for almost 5 and 3.6 seconds, respectively, while for the smallest bore depth (Test 3), initial turbulence caused by the bore impact did not occur and the bore behaved more like a sustained supercritical flow.

4.4.6 Bore front velocity

The propagation of the bore front along the flume's longitudinal axis was tracked using two high-speed video cameras, a GoPro HeroTM Black and an IO Industrial Flare™ high-speed video camera. As shown in Figure 4-15a and b, the velocity was calculated using selected time sequences of the video recordings in combination with the distance between the gridlines that were painted on the false floor and on the side wall in the sediment section.

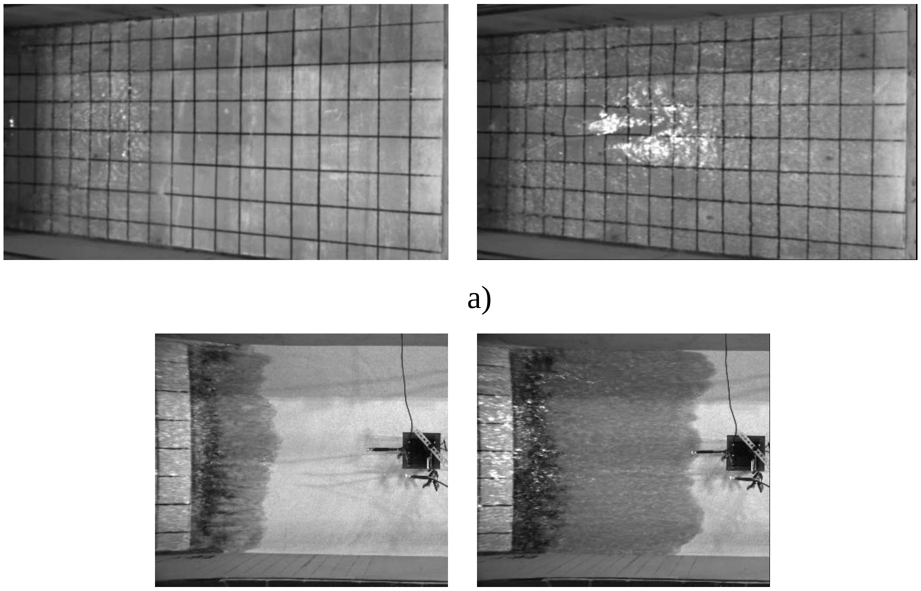

a)

b)

Figure 4-15**.** Video snapshot of the bore front tracking a) over the false floor and b) over the sediment section

The bore front velocity was calculated as the average velocity for each section between two gridlines spaced 20 cm and 10 cm apart on the false floor and on the side wall, respectively.

Figure 4-16a show the bore front velocity as it propagated over the false floor and the sediment sections. As expected, the highest flow velocities were recorded at locations closest to the gate and their magnitude decreased as they propagated downstream the flume as a result of the bed friction. As the bore propagated over the sediment section, the bore velocity decreased significantly. This was in part due to infiltration of the bore into the dry sand bed, as discussed below in the Infiltration and scour rate section. As the bore approached the structure, the bore front velocities remained almost constant as the bore had become fully developed. Maximum instantaneous velocities of 2.15 m/s, 1.58 m/s and 1.31 m/s were recorded at locations closest to the gate, while velocities of 1.14, 0.91 and 0.70 m/s were measured at the structure location for Tests 1, 2 and 3, respectively. The rate of flow velocity reduction over the false floor for Test 1 of 0.21 [m/s per s] was slightly larger than for the two other tests, which were 0.14 [m/s per s] for Test 2 and 0.13 [m/s per s] for Test 3.

The average bore front velocities are also plotted against the maximum bore depths in Figure 4-16b. In this case, the average bore front velocities were calculated as the flume-width-averaged velocity at the location of the interface between the false floor and the sediment bed. Using this value of the velocities ensures that the bore front velocity was not yet affected by the change in roughness at the sediment bed. As expected, the bore front velocities increased at a constant rate with increasing maximum bore depths. These results were also compared with the values proposed by FEMA- P646 (2012), and it appears that the results of the current tests resemble closely to those obtained from the equation proposed in FEMA- P646 (2012). This equation relates the bore velocity to the square root of twice the gravitational acceleration times the bore depth.

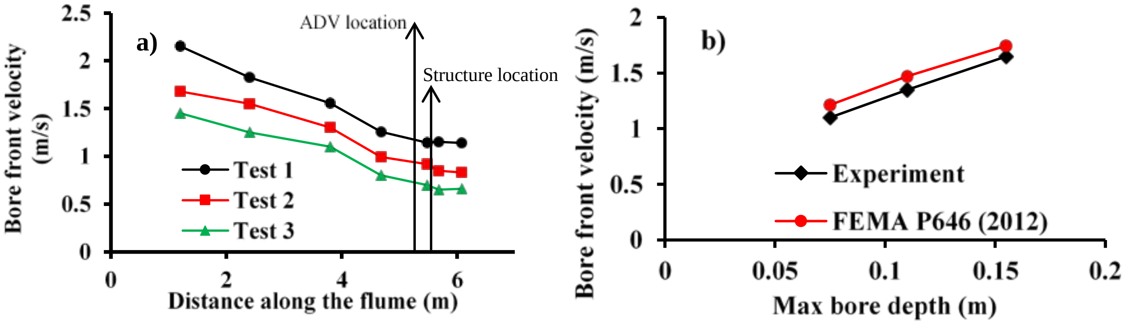

Figure 4-16. a) Bore front velocity along the flume; b) Relationship between maximum bore depth and bore front velocity

4.4.7 Froude number

Finally, the last set of results pertaining to the bore characteristics concerns the Froude number. Previous laboratory results such as those obtained by Favre (1935), Treske (1994), and Chanson (2009) have shown that the wave Froude number (Fr) controls the bore shape. They concluded that in the supercritical regime (Fr >≈ 1.4), the bore has a steep front, while undulations occur at the bore head in the near-critical state (Fr ≈ 1). Khezri and Chanson (2012) conducted experiments to study the inception of sediment motion beneath a tidal bore. They found that undular bores occurred when Froude numbers varied between 1 and 1.3, while fully broken bores occurred when the Froude number was above 1.3 to 1.4. No sediment motion was observed beneath undular bores. Robertson (ASCE, 2016) measured the depth of the bore for the case of the tsunami wave river bore travelling up the Natori River following the 2011 Tohoku Tsunami. Based on his calculations, a bore depth of 1.27 meters was measured and the Froude number was estimated to be approximately 1.95. This infers that the initial tsunami wave front advanced inland in the form of a broken bore. Therefore, in this study, the experiments were planned such that the bore front reached value of the Froude numbers above 1.3 upon initially reaching the structure. Table 4-2 provides the bore velocities and the corresponding bore depths and the calculated Froude numbers for each test. In all cases, the Froude numbers were greater than 1.3, thus indicating that they were fully broken bores. The bore characteristics were therefore adequately captured in the experimental tests.

Table 4-2. Calculated bore Froude numbers

Test#	Bore depth corresponding to the location where bore velocity was measured (m)	Bore velocity (m/s)	Froude number
Test 1	0.12	1. 58	1.45
Test 2	0.11	1.44	1.38
Test 3	0.07	1.10	1.31

4.4.8 Scour evolution

Figure 4-17provides a comparison of the scour depth time histories at different locations around the structure and also in order to investigate the similarity of the experimentally generated scour induced by bores. The green, blue, orange and gray lines represent the scour depth time histories at different locations labeled as A, B, C and D, respectively, as shown in Figure 4-17a. Line A and Line B correspond to the middle and corner of the front face whereas Lines C and D are located at the corner and middle of the side face. In this section, the comparison of different locations will be discussed in terms of maximum and minimum scour depth locations, times at which scour began and times at which maximum scour depth occurred.

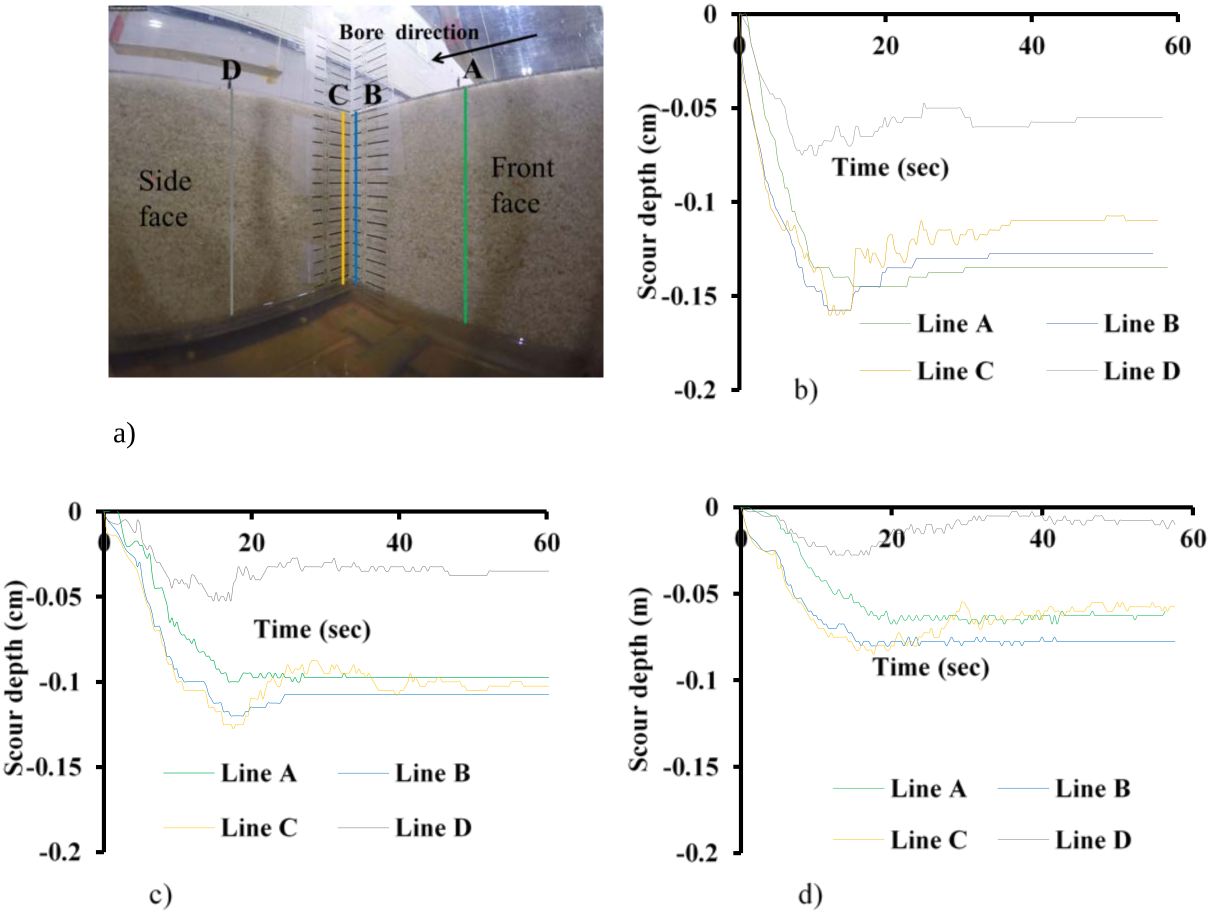

a) b) c) d)

Figure 4-17. a) Scour measurements location, Scour depth time history for b) Test1, c) Test 2 and d) Test 3

For all three tests, the maximum scour depth occurred at the corner of the side face (Line C) - this was slightly different compared to the scour depth observed at the corner of the front face (Line B). The middle of the side face (Line D) exhibited the least scour depth compared to all other locations. The ratios of maximum scour depth at the corner of the side face (Line C) divided by the maximum scour at Line D were 3.09, 2.42 and 2.13 for Tests 1, 2 and 3, respectively. The ratios decreased as the bore depth decreased, meaning that the higher the bore depth, the more intense the scour occurring at the corner of side face compared to the scour at the middle of side face. Also, the ratios of maximum scour depth at the corner of the front face (Line B) divided by the maximum scour depth at the middle of the front face (Line A) were 1.1, 1.2 and 1.1, for Tests 1, 2 and 3, respectively. It appears that this ratio was almost constant in all three tests for the front face.

Comparing the ratios of deposition after reaching the maximum scour depth, Line C exhibited the highest percentage of deposition. Therefore, the largest difference between the equilibrium scour depth and maximum scour depth occurred at Line C, whereas Line A showed the least difference compared to all other locations. As shown in Figure 4-17, scour at the middle of the front face (Line A) started, on average, 1.5 s later than the scour at the corner (Lines B and C), however, with the same rate. The visual observations with the aid of the video-camera and periscope system confirmed the formation of a horseshoe vortex developing from the front corners of the structure. Scour at Lines B and C started almost at the same time, while scour at Line D started on average 0.18 s after the scour at the corners. Scour at Line A started later than at Line D; however, the rate of scour for Line A was greater than that observed for Line D. For all three tests, Lines A, B and C have almost the same rate of scour, and, consistently, these were greater than the rate of scour observed for Line D. Also shown in Figure 4-17, the rate of scour decreased as the bore depth decreased from Test 1 to Test 3. The maximum scour depth for Tests 1, 2 and 3 occurred at t= 16.1 s, t = 18.5 s and t = 20.6 s, respectively. Therefore, it can be concluded that the greater the bore depth, the sooner the maximum scour depth occurs.

4.4.9 Infiltration and scour rate

The infiltration rate is the velocity or speed at which water drains through the soil while the scour rate is the speed at which the soil is being removed by the water. In this study, these two were calculated by using time sequence of the video recordings and the distance between the two adjacent gridlines on the scale attached onto the structure as shown in Figure 4-18 (the infiltration line of the water is shown with dash black lines).

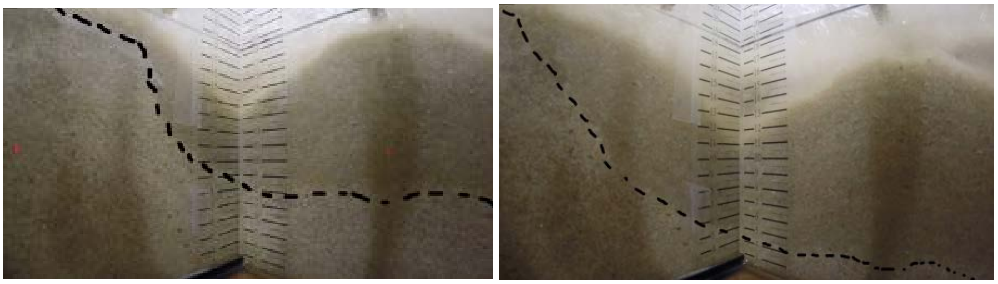

Figure 4-18**.** Video snapshots for tracking the infiltration and scour

In order to assess the infiltration and scour rates induced by a turbulent bore and to compare them for all three tests, graphs are provided in Figure 2-19a, b and c.

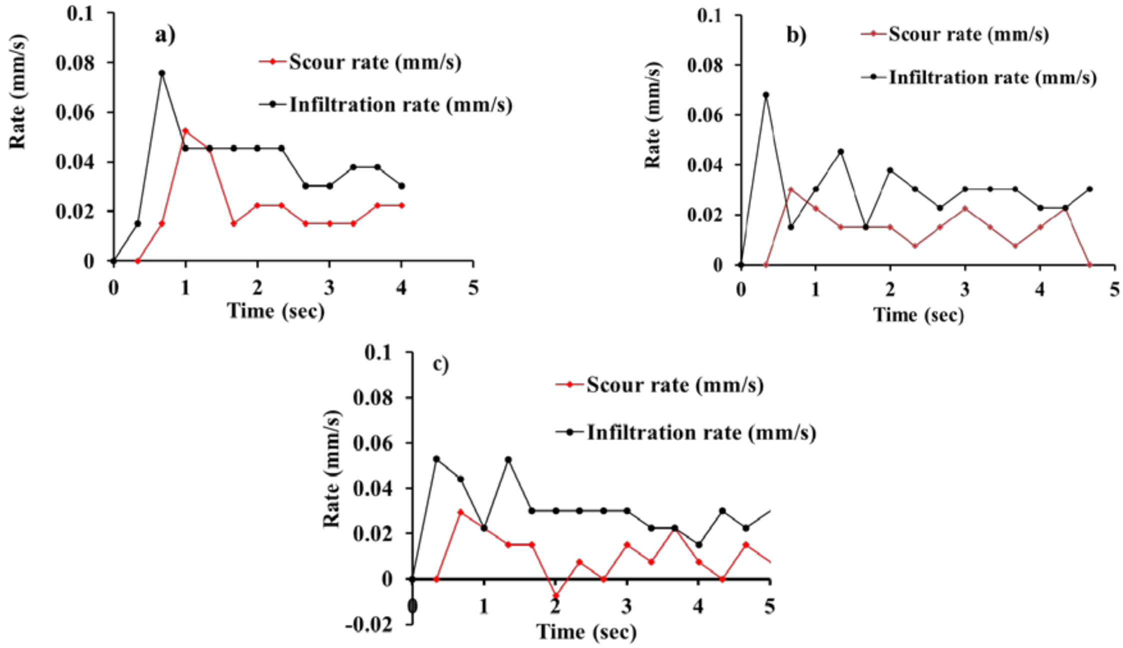

Figure 4-19**.** Scour rate (red line) and infiltration rate (black line) for: a) Test 1, b) Test 2 and c) Test 3

Black and red lines represent infiltration and scour rates, respectively. It can be seen that there is a sudden rise in both scour and infiltration rates, after which both parameters began to decrease. Moreover, there is a phase lag between the moment when the infiltration is observed and the moment when the soil starts to be scoured. For all three tests, scour started, on average, 0.28 sec after the water started infiltrating into the soil. For all three tests, the infiltration rates were higher than the scour rates. Comparing the scour and infiltration rates of the three tests, the higher initial reservoir impoundment depth and faster bore velocity in Test 1 resulted in higher rates of infiltration and scour. Tonkin et al. (2003) and Nakamura et al. (2008) concluded that the acceleration of sediment erosion due to changes in the pore pressure gradient caused the sand to be scoured more easily and represented an important factor in the formation of the large scour hole behind the cylinder. Investigating the effect of the pore pressure changes on the changes in scour requires further research.

4.4.10 Final scour topography

The final elevations of the scoured sediment bed were measured using a Disto TM laser. Based on the average elevation of the false floor on either side of the sediment bed, measurements were zeroed with respect to it as a reference level. In order to better capture sudden changes in bed elevation such as at the boundary of the main local scour hole, point measurements were taken at different grid spacings. Point measurements were set over the scour hole at grid spacings of 0.02

m and 0.05 m for the entire sediment bed, and then interpolated over the sediment bed area using Golden Software Surfer v.11.5. Figure 4-20 shows the final scour plots for each test.

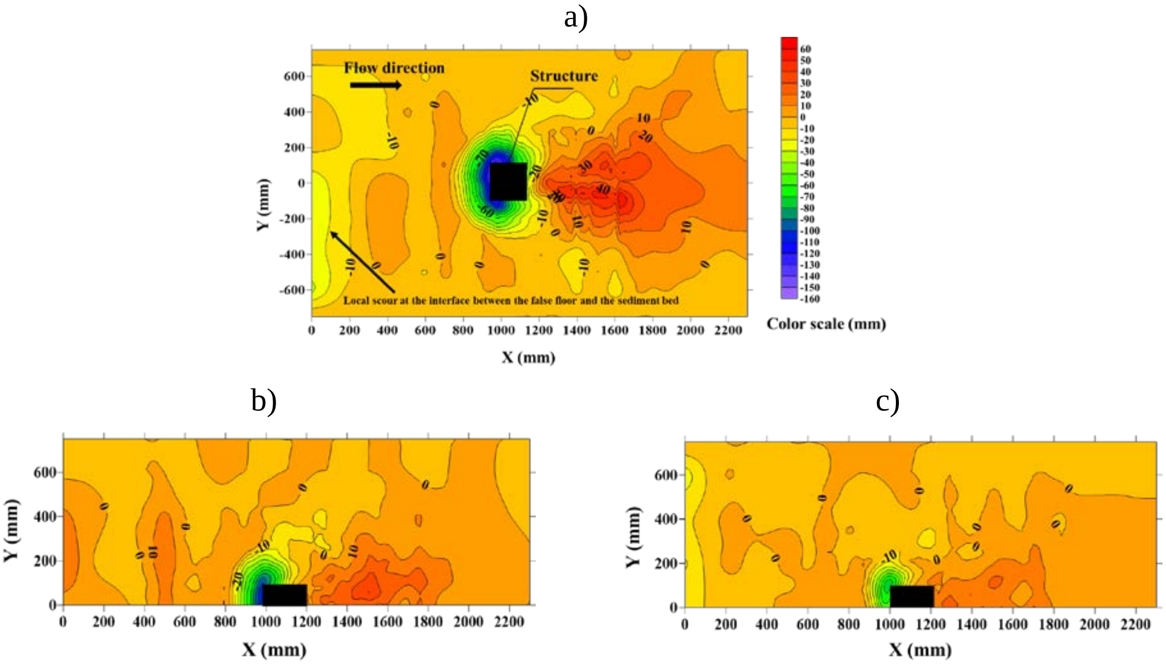
a)
b)
c)

Figure 4-20. Plan view of the bed scour depth for a) test 1, b) test 2 and C) test 3

Figure 4-20a provides the final scour bed elevation around the structure for Test 1. The positive and negative values on the scale represent deposition and erosion, respectively. As shown in these plots, the final plane local scour shape formed by the hydraulic bore was close to elliptical. The structure is shown as a black object, and, since the scour hole is symmetrical around the center of the structure, only one side of the final sediment bed was measured for Tests 2 and 3 as shown in Figure 4-20b and c.

As shown in Figure 4-20a, the scour hole extends less than half-way from the structure to the wall, confirming that the local scour was not affected by the wall. There was an area of local scour along the upstream boundaries of the sediment section at the interface between the false floor and the sediment bed which was caused by the transition between the two surfaces. As mentioned earlier, a 15cm wide gabion was used to minimize local scour along this interface. The maximum final scour was located at the upstream corner of the structure, and the scour depth further decreased linearly towards the structure’s downstream back face. The onshore side of the structure was not scoured to the same degree as the offshore side. There was also an area of deposition at the back of the structure which extended considerably in the plane area. All three tests were deemed live bed scour conditions as there was transport of bed material from upstream of the structure. In Tests 1 and 2, an area of mild surface local scour extending from the side of the structure to the walls of the flume was also observed. As shown in Figure 4-6a and b, the surface roller redirected alongside the structure, increased in elevation, and expanded toward the lateral wall of the flume. A rapid flow alongside the structure induced by the redirected surface roller caused an area of this mild surface local scour. For Test 1, the bore depth and velocity exhibited magnitudes such that a significant amount of the surrounding sand bed was scoured. Also, greater deposition depth was observed, which extended further downstream compared to the other two tests. As the scour hole was deeper, more sediment particles washed away from the scour hole and were deposited behind the structure. For Test 3, shown in Figure 4-20c, the scour process did not develop, and the dimensions of the scour hole did not grow to the same degree as in Tests 1 and 2.

4.5 Discussion

Post-tsunami field surveys of the Tohoku tsunami conducted by Chock et al. (2013) identified and documented various types of local scour at beaches, sea walls, roads, and building corners and other structures. There are numerous factors that influence scour depth such as soil type, location, flow velocity and depth, structure geometry and dimensions, and bed condition (wet vs dry). Moreover, as most of the field observations are based on post-tsunami surveys, the observed scour depth may be greatly influenced not only by multiple direct tsunami run-ups that advance overland, but also by episodes of vigorous tsunami backwash flow in reverse direction towards the coastline. Because of all the above factors, scour depths based on field observational are not easily comparable with the results of this study. However, the observed scour hole pattern is similar to field observations (as shown in Figure 4-1a and b). A distinct scour hole forms at the seaward corner of the structure in both experimental tests and field surveys. However, there is one field observation of local scour that could be considered a reasonable comparison to the current experimental results. A local scour of 4.2 m was measured around the viaduct pier in Miyako City, Japan following the 2011 Tohoku Tsunami and the flow depth of 6 m was reported for this location (Chock et al. 2013).

Figure 4-21provides a comparison between (scour depth/B) as a function of (h/B) observed in the current study, the Nakamura et al. (2008) results, Lavictoire et al. (2014) and Shafiei et al. (2015), McGovern et al. (2019), FEMA P646 (2012), ASCE (2016) and the observed local scour and flow depth around the viaduct pier in Miyako City.

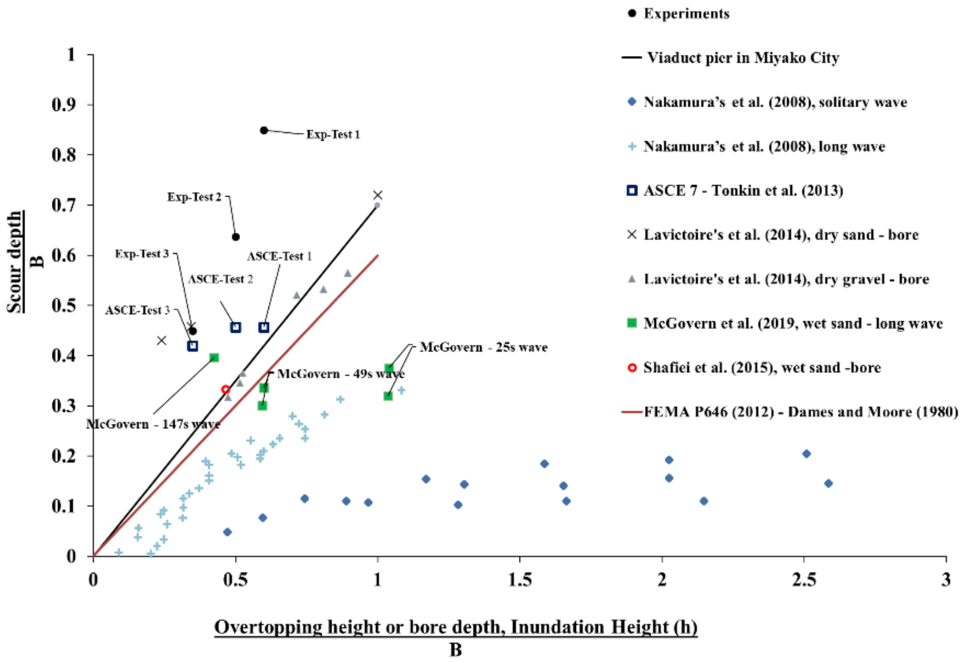

Figure 4-21. Relationship between scour depth and flow depth

By applying Froude number scaling the bore duration would scale as $(\frac{T_P}{T_M} = \sqrt{L})$, where TP and Tm are the bore durations in the prototype and the model and L is the length scale. Using a length scale of 40, the bore duration of 120 seconds in the model corresponded to 760 seconds (12 minutes) of the prototype bore duration. By comparing the experimental data with previous experimental data, the influence of bore height and duration on the scour depth can be studied. The scour depths induced by solitary and long waves of Nakamura et al. (2008) and the present dam break test are represented by the blue diamonds, light blue cross and solid black circles, respectively. Also, the experimental data of Lavictoire et al. (2014), Shafiei et al. (2015) and McGovern et al. (2019) are shown as gray triangle, "x" symbol, hollow red circle and sold green square, respectively. Moreover, the ratios obtained by FEMA P646 (2012), ASCE (2016) and Viaduct pier in Miyako city are shown using a red line, hollow navy-blue square and black line, respectively.

Experimental data of Nakamura et al. (2008), Lavictoire et al. (2014), Shafiei et al. (2015) and McGovern et al. (2019) are the most comparable studies to the current experiments. where h represents the over-topping height for the case of Nakamura et al. (2008), inundation depth for McGovern et al. (2019) and the bore depth for Lavictoire (2014), Shafiei et al. (2015) and current tests.

As described in the Introduction section, Nakamura et al. (2008) conducted tests using 'long waves' and solitary waves. The maximum period tested was 14 s. Lavictoire et al. (2014) studied the effect of dam-break bores flowing past a circular structure installed in sand and gravel beds. Shafiei et al. (2015) measured bore inundation and scour around square, diamond and circular structures placed in sand beds, while McGovern et al. (2019) investigated the scour development and spatio-temporal evolution around a square structure induced by tsunami-like long waves with three crest-led wave periods of 147 s and 25 s, and a trough-led one of 49 s wave.

Comparing the results of Test #1 and Test #2 from the current experimental work with those of Lavictoire et al. (2014), it can be seen that the scour magnitude of the current test differed from those tests, mainly because Lavictoire et al. (2014), measured only the final scour depth for different geometry size and shape. However, the scour depth for Test #1 exhibited similar magnitude of scour depths as the study of Lavictoire et al. (2014). For the case of Test#3, the velocity was not high enough to cause slumping and the final scour depth was the same as the maximum scour depth.

Comparing the results of the present study with those of Nakamura et al. (2008), it can be concluded that, for the same overtopping heights or flow depths, the scour depths due to long waves were always higher than those induced by solitary waves and lower than those generated by bores which was also previously reported by Lavictoire et al. (2014). The bores, due to their longer flow duration, were able to scour the bed more than the long waves. The longer duration of bores, compared to long waves used by Nakamura et al. (2008), induced more scour depth. Nakamura et al. (2008) and McGovern et al. (2019) also concluded that inundation duration had a greater influence than inundation height.

The results from the current experiment as well as the results of Lavictoire et al. (2014), of Shafiei et al. (2015) and of McGovern et al. (2019) have all differed from the Nakamura et al. (2008) 'long wave' study as they all used significantly longer inundation time than, further shows the importance of the inundation time on the amount of scour. The longer inundation times allowed the development of an equilibrium scour hole. Just as the case of McGovern et al. (2019), lateral vortex and horseshoe were observed to be the key scouring elements indicating that the scour mechanism is similar, despite the different inundation generation mechanisms. The current experimental employed a turbulent bore with a high initial velocity followed by a gradual reduction in inundation height and velocity – this was different that the unbroken long wave. However, comparing scour induced by the 147s long wave employed by McGovern et al. (2019) to that generated by the current turbulent bore which exhibited higher velocity, it can be seen that, in spite of a shorter flow duration, the turbulent bore induced more local scour than a cyclic long wave with longer duration and lower velocity. The two above comparisons indicate the importance of both the inundation velocity and flow duration on the amount of scour.

The ASCE/SEI 7 Chapter 6 - Tsunami Loads and Effects (ASCE, 2016) is the world's only design standard written in mandatory language. Section 6.12 provides conservative design guidance to assist with the estimation of tsunami-induced scour. Tonkin et al. (2013) presented a tsunami scour evaluation procedure which includes flow and soil characteristics. The envelope of local scour measurements indicates that scour can be calculated as 1.2 times the flow depth up to a maximum scour depth of 4 meters. This is maximum scour depth =1.2h for h< 3.05m and maximum scour depth = 3.66m for h > 3.05m. For Test 3, h is < 3.05m at 1:40 scale, the predicted scour depth is therefore 3.36m which at 1:40 scale is 0.084 m. For Test 1 and Test 2, h is >3.05m at 1:40 scale and the predicted scour depth at prototype scale is 3.66 m which, at 1:40 scale is 0.0915 m. For the Test 3, the guidance of ASCE (2016) performs almost well. However, for the Test 1 and Test 2, the ASCE (2016) provision on estimating scour underpredicts the maximum scour depth. The reason for this underprediction is these prescriptions are based on results from post-tsunami field surveys of observed scour around structures conducted by Tonkin et al. (2011). Thus, the use of the ASCE (2016) provisions, may lead to undesirable underestimations of maximum scour depth as shown in Figure 4-21.

The ratios of scour depth divided by flow depth obtained in the current tests, which were conducted using a loose sand bed, were 128%, 127% and 141% for Tests 1, 2 and 3, respectively, for an average of 132%. It can also be seen that calculated ratios for the experimental results are also higher than that of the field observation at the viaduct pier in Miyako City which is based on the post- tsunami field survey. FEMA P646 (2012) relies on the scour depth ratios proposed by Dames and Moore (1980). The ratio of scour depth divided by flow depth is given for structures located close to or far from a shoreline with different soil types. The value for loose sand suggested by Dames and Moore (1980) is 60%. When comparing these ratios to the ratio proposed by FEMA P646 (2012), the experimental ratios are all much higher, and the ratio given in the FEMA guideline underestimates the potential scour.

4.6 Conclusions

This study presents results of an experimental research program that focused on investigating scour and erosion around a square structure induced by tsunami-like bores. The physical experiments were based on the analogy between tsunami-induced bores and dam-break waves generated by the sudden release of an impounded volume of water. For all the tests, the calculated Froude numbers surpassed 1.3, thus indicating that bores were fully broken. Bore characteristics were therefore adequately captured in the experimental tests. The following conclusions can be drawn from the analysis of the recorded data.

Significant scour depths were reached at the front of structure while extensive sediment deposition was observed at the back of structure. Similar to the some of the post-tsunami field observations, the scour hole formed at the seaward corner of the structure while local scour at the shoreward corner was insignificant. The scour holes formed with a distinct break in the downward slope. Sand particles moved irregularly in space and time as a result of the oscillation of the horseshoe vortex in location and size over time along the stream-wise direction in the turbulent bore.

Four stages of scour process were distinguished: (1) intense erosion stage, (2) development stage, (3) stabilizing stage in which slumping occurs due to a drop-in velocity below the threshold of motion and (4) equilibrium stage. The occurrence of stage 3 depended on the height of bore: for the smallest bore investigated, the equilibrium stage appears instantly after the development stage. A higher bore depth resulted in higher rates of infiltration and scour. The measured bore front velocity and scour depth demonstrate that the larger bore depth resulted in greater bore front velocity and induced greater scour depth. Maximum scour depth occurred earlier for the larger bore depth than for the smaller bore depths.

Just as the case of McGovern et al. (2019), lateral vortices and the horseshoe vortex were observed to be key scouring element indicating that the scour mechanism is similar for both the bore type and long waves, despite their different generation mechanism. The short duration and very turbulent nature and higher bores velocity induced rapid scour more than that of that of long wave despite having lower inundation time (short lived bore), indicating the importance of both inundation height and time on the amount of scour.

The relationship between the maximum scour depths and bore heights was found to lead to less scour than the provisions of ASCE (2016); at the same time, the ASCE (2016) method underpredicts the maximum scour depth. When comparing these ratios to the value proposed by the older guidelines by FEMA P646 (2012), the latter underestimated the scour by more than 50%. Scour depth is significantly affected not only by multiple direct tsunami run-ups that travel inland, but also by the tsunami backwash flow. Larsen et al. (2018) observed that equilibrium in their cases was achieved only after approximately 50 waves, suggesting that it may take numerous waves to achieve equilibrium for the scour. McGovern et al. (2014) observed scour on the opposite side of the structure due to return flow in their study on scour around a cylinder in simulated tidal currents. Tonkin et al. (2003) showed that the most significant scour occurred due to a large vertical gradient in pore water pressure at the rear of the cylinder during the return flow. These, along with variation in sediment and structure size effects, should be investigated.

Chapter 5. EFFECT OF BED CONDITION (WET VERSUS DRY) ON LOCAL SCOUR DUE TO TSUNAMI-LIKE BORE

The article is in review in Coastal Engineering Journal

Abstract

In recent years, extreme natural phenomena such as large tsunamis events have affected coastal regions around the Indian and Pacific Oceans and caused significant loss of life and extensive damage to coastal communities. The lack of proper design documents to account for tsunami loads and effects across coastal communities has contributed to significant damage experienced by infrastructure in these regions. The extreme hydrodynamic characteristics of tsunami-induced coastal inundation lead to several negative effects: hydrodynamic loading on structures, flow-entrained debris loading as well as extreme erosion around structures. Forensic engineering post-tsunami surveys showed that various combinations of such loads can lead to failure of structures. While extensive research has been conducted in recent years on the hydrodynamic and debris loading, significantly less research focused on investigating erosion caused by tsunami inundation. This study investigates the effect of the bed condition (wet or dry) on the local scour induced by the impact of rapidly advancing tsunami-like hydraulic bores onto a freestanding structure. The experiments were conducted using hydraulic bores which have been shown to closely resemble tsunami-induced coastal inundation. The experimental program was conducted in the dam break Flume at the Hydraulic Laboratory of the University of Ottawa, Canada. The dam-break wave was generated by releasing water impounded behind a rapidly opening swing gate. The effect of the tsunami-like bore on the total local scour depth is presented and discussed. The results showed that the presence of an initial water layer downstream of the gate greatly influences the hydrodynamics of the hydraulic bore and the resulting local scour around the structure. The excessive scour depth may occur as a result of a second bore propagating on a previously scoured bed.

5.1 Introduction

It has been documented that tsunamis cause substantial surface (general) erosion as well as localized scour along shorelines affected by inundation (Nistor. 2012, Figure 5-1a). For example, the International Tsunami Survey Team (ITST, 2005) documented the existence of extensive scour damage around the foundation of a lighthouse tower located on the coast of Banda Aceh, Indonesia. In post-tsunami forensic engineering surveys of India and Thailand following the 2004 Great Sumatra Andaman Tsunami, researchers documented local scour occurrences not only at buildings located close to shore, but also hundreds of meters or kilometers inland. Yeh and Li (2008) discussed an undermined patio in Devanaanpattinam, India, where the observed run-up height was 3.0 m. The concluded that soil undermining resulted from the swift channelized flow during the drawdown of the tsunami wave (Figure 5-1b).

a) **b)**

Figure 5-1: Local scour due to tsunami bore around building foundations. a) Japan (courtesy of Dr. Ioan Nistor, 2012); b) 1.4 m deep in India, from the 2004 Indian Ocean tsunami (Yeh and Li 2008)

Several studies have been conducted to investigate scour around coastal structures due to tsunamis. Uda et al. (1987) performed an experimental investigation to study the scour and collapsing processes of a revetment caused by a tsunami wave. Noguchi et al. (1997) proposed an empirical equation for predicting maximum scour depth in front of a revetment due to an overtopping tsunami wave. Koyabashi and Lawrence [2004] examined tsunami-induced cross-shore sediment transport processes on a fine sand beach and revealed the importance of an incident tsunami profile in influencing breaker type, sediment suspension, wave run-up and downrush, net sediment transport, and the resulting profile change. Arya and Shingan (2012) performed experimental studies which investigated scour mechanisms around vertical cylinders and breakwaters. Wilson et al. (2012) studied sediment scour and deposition within harbours, while Chen et al. (2013) studied tsunami-induced scour at coastal roadways. Bricker et al. (2012) conducted a field survey of scour depths measured on the landward side of seawalls and floodwalls, as well as around a building foundation, following the 2011 Tohoku Tsunami.

However, experiments related to scour around structures caused by tsunamis are limited to only a few studies. Two common approaches used in the past for experimentally generating tsunami waves were solitary waves and long waves generated in a flume or wave basin.

Kato et al. (2000, 2001) and Tonkin et al. (2003), using solitary waves in a sediment tank, examined scour around a cylindrical structure located on a sloped sandy beach. Tonkin et al. (2003)'s experiments have been numerically simulated and applied to scour at bridge piers by Pan and Huang (2012) and this methodology is cited in the ASCE (2016) Chapter 6: ‘Tsunami Loads and Effects' design standards. However, solitary waves generated in the laboratory have a major limitation related to their period as it is difficult to ensure the proper time scale for the duration of such solitary waves. While the use of solitary waves is still acceptable for investigating initial wave impacts, in order to investigate scour occurring during a tsunami event, one needs more realistic scaling of the duration of the tsunami—induced bores. Madsen et al. (2008) noted that the solitary wave assumption does not allow for the period and length of the wave to be set independently, leading to unrealistic waveforms when scaled up to prototype. Many of the solitary wave studies failed to establish any correlation to geophysical tsunamis and showed that the traditional solitary wave had relative time- and space-scales on the order of several orders of magnitude smaller than field surveys of the 2004 Indian Ocean tsunami. Therefore, at present, general scientific consensus indicates that solitary waves tend to be less representative of actual tsunamis due to their short period. This is particularly important for studies focusing on scour, where flow duration is a critical variable.

Long waves have also been used in laboratory tsunami studies. However, while long waves may replicate tsunami periods, they are unlikely to produce the initial peak velocities of an advancing tsunami. Nakamura et al. (2008) used long waves to study scour around a square structure located on a horizontal sand bed. Most recently, combination of steady flows and waves have been corroborated numerically by Larsen et al. (2017) and experimentally by Larsen et al. (2018) for tsunami induced scour at scaled offshore wind turbine monopiles. Foster et al. (2017) noted that over shorter time scales, tsunamis are cyclic over their defined period T and can be assumed to exhibit quasi steady currents. McGovern et al. (2019) also conducted a series of experiments using a Pneumatic long wave generator to create tsunami wave periods of 25–147 s equating to 3–17.3 min at 1:50 Froude scale. In their study, waves propagated over a slope before impinging on a flat wet sediment pit in which a square structure was placed. They used KC number which includes the period of the inundation and the velocity, the two key scouring parameters in wave and current scour studies. McGovern et al. (2019) concluded that the instantaneous scour development is similar to a current or even a tidal current, due to the long period of the inundation by comparing the long wave scour with current and tidal current scour. McGovern et al. (2019) concluded that the rate of onshore scour development varies with time due to the changes in flow velocity and depth and that the scour depth is more dependent upon inundation duration than velocity. They also reported that KC influence is not necessarily the same as observed for wind wave and current scour due to transition of tsunami from wave-like to current-like flows during inundation.

All these studies underlined that a tsunami-induced scour hole due to a transient flow exhibits different mechanisms than from either a steady current or a consistent short-wave field. However, even when scaled, the use of solitary waves generated in a laboratory facility may be too short compared to real tsunamis, while long waves, such as those generated by pumps, may have insufficient initial velocity. As such, over the past decade, a new approach for experimentally reproducing tsunami-induced hydraulic bores is to generate a dam-break wave by rapidly releasing water impounded behind a gate into a straight channel. Chanson (2006) analyzed visual images of an actual tsunami bore from the 2004 Indian Ocean Tsunami and concluded that the flow characteristics of tsunami-induced bores are similar to those of a dam-break wave. Figure 5-2 shows the surge created by the first tsunami wave arriving at Rikuzentakata (roughly 1.5 km inland from the bay front) in Iwate Prefecture, Japan during the 2011 Tohoku tsunami (Hagen, 2014).

Figure 5-2: Surge created from the first tsunami wave arriving at Rikuzentakata (roughly 1.5 km inland from the bayfront) in Iwate Prefecture, Japan during the 2011 Tohoku tsunami (Hagen 2014).

A few experiments investigated tsunami bore induced scour around coastal structures using the dam break method, such as those by Triatmadja et al. (2011), Shafiei et al. (2015) and Lavictoire et al. (2015). Triatmadja et al. (2011) investigated the scour around cylindrical and 0.045 m X 0.045 m square prism structures on a sloped sand bed using a 20.4 m long and 0.60 m wide flume. They reported that the ratio of the maximum scour depth around the structure to the flow depth was from 0.2 to 0.3, and that the maximum scour depth around the square prism structure was slightly larger than that around the cylindrical structure. However, no dynamic scouring process was measured in their experiment. Lavictoire et al. (2015) observed tsunami bore induced local scour around a cylindrical structure and found that the short duration and very turbulent nature of the bore resulted in a rapid scour process. Lavictoire et al. (2015) found that the ratio of scour depth to flow depth ranged from 0.6 to 1.8. Shafiei et al. (2015) investigated tsunami bore induced scour around inland structures on a wet sandy foundation using three model structures a square prism, a diamond prism, and a cylinder. They observed that maximum scour depth during and after the bore impact increased with increasing bore strength and structure shape had a significant influence on the maximum scour depth. However, none of these experiments presented detail description of the scour process.

To the authors' knowledge, there has been no research on the effect of different bed conditions on local scour due to tsunami. However, several studies have investigated the effect of bed conditions on the *hydrodynamic characteristics* of a bore, which concluded that the presence of a still water layer can significantly influence bore propagation characteristics. Stansby et al. (1998) have conducted experiments to investigate dam-break flows over a fixed bed, where a thin plate separating water at different levels was withdrawn rapidly in an upwards direction. Leal (2006) conducted experimental tests to study the magnitude of dam-break bore front celerity for different downstream bed conditions (wet or dry) and different bottom frictions. Crespo et al. (2008) investigated a dam-break bore evolution over wet and dry beds using a two-dimensional SPH model. St-Germain et al. (2012) studied tsunami-like bore structure interactions propagating on wet and dry fixed bed conditions using the SPH method. The latter authors aimed to investigate the bore propagation characteristics such as velocity field and bore depth and the resulting hydrodynamic force for dry and wet beds. Douglas and Nistor (2014) used a three-dimensional multiphase numerical model (developed using OpenFOAM) to study the effect of bed conditions during the interaction of a tsunami-like bore with a square structure on a fixed bed. The results revealed a significant change in bore characteristics as the downstream water depth was increased.

5.2 Research objectives

The current study investigates the effect of bed condition on tsunami-induced erosion around an inland structure located on dry and wet horizontal beds. Depending on the nearshore bathymetry and topography, when the first tsunami wave reaches the shoreline it propagates in the form of either a surge or a turbulent hydraulic bore moving rapidly over mostly dry nearshore coastal areas. Depending on different factors such as the amplitude and period of the tsunami wave and the local topography, subsequent tsunami waves may advance over the previously inundated inland area before the water from the preceding wave has fully receded. Therefore, in addition to individual scour tests due to hydraulic bores propagating over wet or dry beds conditions, a number of tests were conducted to investigate any additional scour effects of a second tsunami bore propagating over an already inundated and scoured bed around a structure. It should be noted that wet and dry in the experimental tests simply mean if there is an initial water depth or not. It motivated by (1) changes in the hydrodynamics of the bore and (2) infiltration is very rapid in the soil near the beaches.

5.3 Experimental setup

Hydraulic bores were generated in the Dam-break Flume of the Hydraulics Laboratory at the University of Ottawa, Canada. The flume, as shown in Figure 5-3 and Figure 5-4, is 30 m long, 1.50 m wide and 1.0 m deep. The dam-break waves were generated by the sudden release of a given volume of water impounded behind a rapidly-opening swinging gate that was equipped with a lock and release mechanism. The same flume and gate were used in the experiments of Stolle et al. (2018) and Von Häfen et al (2018). The bore propagated over a sediment bed placed between two aluminum false floors sections, each with a height of 0.2 m above the concrete flume bed, which were installed located at a proper distance downstream of the gate to ensure the formation of the fully developed dam break wave prior to its propagation over the sediment bed section (Figure 5-3). The flume is equipped with a vertical gate was installed at its downstream in order to be able to create a wet bed initial condition (Figure 5-4a).

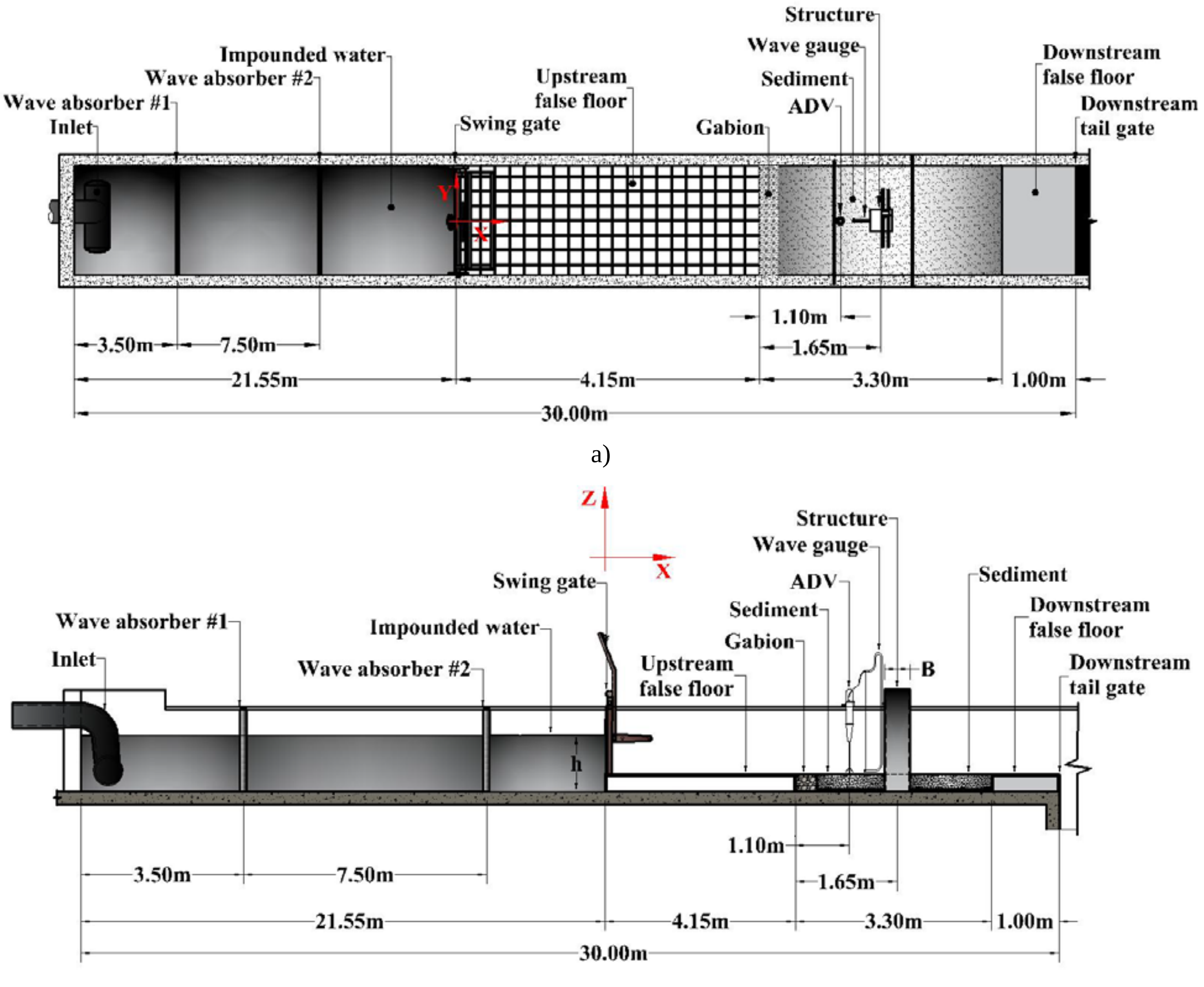

a)

b)

Figure 5-3: Experimental setup, a) side view (not to scale), b) plan view (not to scale))

The upstream false floor had a length of 4.15 m while the downstream false floor was 1 m long. The upstream false floor was covered with a layer of glued sand with a uniform grain size of 1 mm in order to ensure realistic roughness and a fully developed turbulent hydraulic bore. A grid with 20 x 20 cm spacing was painted on the top surface of the upstream false floor to allow for bore front velocity tracking and for flow measurement purposes (Figure 5-4a). The sediment bed section delimited by the upstream and downstream false floors was 3.30 m long by 1.50 m wide by 0.20 m deep, and was filled with uniform sand with D_{50} of 1 mm. Below the sand at the base of the sediment bed a drain in the form of a 1cm-thick layer of coarse gravel (D_{50} = 10 mm) covered by a geotextile sheet was installed. This allowed small amounts of water that infiltrated below the false floor to be drained and control thus the degree of saturation of the sediment bed above.

A 15cm-wide gabion mat was installed across the width of the flume between the upstream false floor and the sediment bed to ensure a smooth transition between the rough surface of the false floor and the sediment bed and to minimize the local scour that would have occurred at the interface of the false floor and sediment section (Figure 5-4a). The gabion was constructed in the form of a wire box filled with coarse, uniform gravel, with a D_{50} of 30 mm. Also, two wave absorbers were installed within the reservoir in order to attenuate the upstream-propagating secondary waves generated by the sudden opening of the gate and prevent any waves-induced water level fluctuations in the sediment test section. A calibrated WG-50 capacitance-type wave gauge manufactured by RBR Ltd with a measuring accuracy of 0.4% was used to record the time-history of the water surface elevation using a sampling rate of 30 Hz: The wave gauge was installed in the upstream face of the structure (Figure 5-4b).

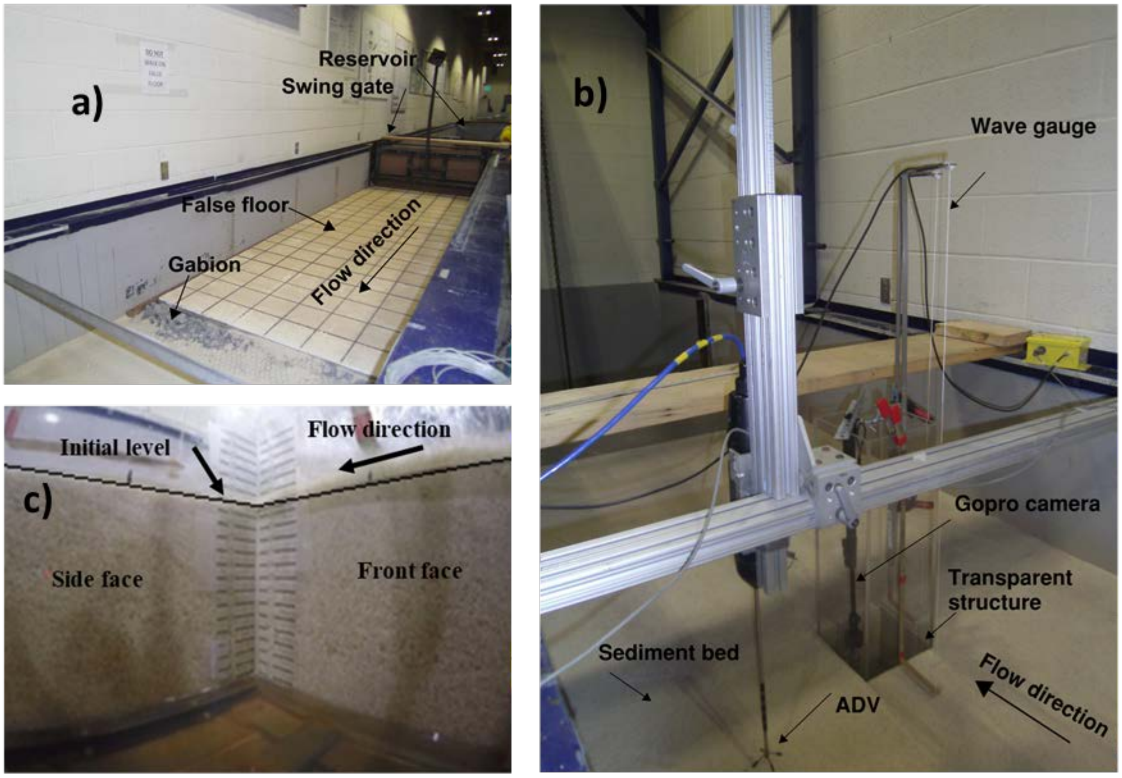

Figure 5-4: (a) Dam-break flume in the Hydraulics Laboratory at the University of Ottawa, Canada, b) Experiment setup for measuring the scour depths, velocity and water surface elevation and (c) View of the front and side faces from inside the structure shot with the GoPro video-camera

Two HD (high-definition) video cameras, a GoPro HeroTM Black (1920 x 1440 at 60 fps) and an IO Industrial Flare™ high-speed video camera (2048 x 1088 at 60 fps) were used during the experimental investigations to (1) estimate the bore-front velocity by tracking the bore front as it propagated downstream and (2) to conduct particle-tracking velocimetry (PTV) measurements, respectively.

Square model structures constructed from Plexiglas with square cross sections of either 0.30x30 m, 0.20x0.20 m and 0.10x0.10 m were installed in the centre of the sediment bed and attached to the flume bed. The model structures were transparent to allow time- and spatial-recording of the scour by means of the GoPro Hero Black, which was placed inside the structure (Figure 5-4b). Measuring scales were attached onto the front, side, and back of the structure model to record the time and spatial development of the scour depth induced by the hydraulic bore flow around it. Using this technique, the authors were able to record the time-development of the scour depth with an accuracy of ±0.005 m (Figure 5-4c).

Time history of the bore velocity was measured using a Nortek Vectrino Acoustic Doppler Velocimeter (ADV) with a down-looking head equipped with four receivers set at a sampling rate of 30 Hz (Figure 5-4b). The ADV was installed with the sample volume in the flume centerline at x = 5.40 m downstream of the swing gate, which was 0.40 m upstream of the structure. The flume was drained of water after each test and a Disto TM laser altimeter with a precision of ± 1.00 mm was used to measure the final local scour geometry around the model structure.

5.4 Experimental test program

The research program consisted of erosion tests around square model structures with three different cross sections using hydraulic bores generated using the rapid opening of the swing gate with various reservoir impoundment levels. Once the reservoir was filled to the desired level, the pump inflow was stopped. In order to investigate the effect of bed condition on bore velocity and scour depth, two initial conditions (wet and dry) were used for the sediment section downstream of the gate. A schematic illustration of the experiment is presented in Figure 5-5 , where h and d_1 are the initial water depths (m) upstream and downstream of the gate, respectively, d_2 is the flow depth (m) immediately behind the positive surge, and U is the bore front velocity (m/s). Also V_2 is the flow velocity (m/s) immediately behind the positive surge.

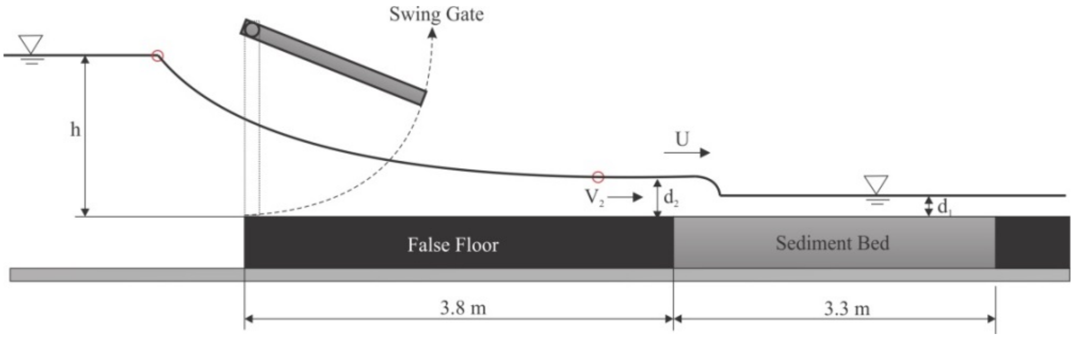

Figure 5-5: Dam-break wave propagation over the horizontal bed with a wet bed condition

In total, twenty-four (24) tests were conducted. The main description of the experimental tests is summarized in Table 5-1 . In this table, r is the ratio of d_1/h which is termed the *non-dimensional initial water depth*, D_{50} is the grain size and B is the structure width. A 1:40 Froude scaling ratio was used, with values for h varying between 0.15 m to 0.375 m corresponding to prototype wave heights of 6 m to 15 m.

Table 5-1: Experimental test program

Test #	**B (m)**	**h (m)**	**d_1 (m)**	**$r = d_1/h$**	**D_{50} (m)**	**Bed**	**Test #**	**B (m)**	**h (m)**	**d_1 (m)**	**$r = d_1/h$**	**D_{50} (m)**	**Bed**
1	0.20	0.25	0	0	0.001	Dry	**13**	0.20	0.15	0.02	0.13	0.001	Wet
2	0.20	0.20	0	0	0.001	Dry	**14**	0.20	0.30	0.125	0.41	0.001	Wet
3	0.20	0.15	0	0	0.001	Dry	**15**	0.10	0.25	0	0	0.001	Dry
4	0.20	0.25	0.025	0.10	0.001	Wet	**16**	0.10	0.20	0	0	0.001	Dry
5	0.20	0.25	0.05	0.20	0.001	Wet	**17**	0.10	0.15	0	0	0.001	Dry
6	0.20	0.25	0.125	0.50	0.001	Wet	**18**	0.30	0.25	0	0	0.001	Dry
7	0.20	0.30	0.05	0.16	0.001	Wet	**19**	0.30	0.20	0	0	0.001	Dry
8	0.20	0.375	0.150	0.33	0.001	Wet	**20**	0.30	0.15	0	0	0.001	Dry
9	0.20	0.15	0.03	0.20	0.001	Wet	**21**	0.20	0.25	0	0	0.01	Dry
10	0.20	0.15	0.075	0.50	0.001	Wet	**22**	0.20	0.25	0.01	0	0.01	Wet
11	0.20	0.225	0.075	0.33	0.001	Wet	**23**	0.20	0.25	0.05	0	0.01	Wet
12	0.20	0.18	0.03	0.16	0.001	Wet	**24**	0.20	0.030	0.05	0	0.01	Wet

According to the National Oceanic and Atmospheric Administration (NOAA), a tsunami is a series of waves, and the first wave may not be the largest. The time between the first tsunami wave and the next can vary between five minutes to an hour, and the threat can continue for many hours as multiple waves continue to arrive. If the first tsunami bore causes substantial erosion and scour along the coastal area, the second tsunami bore has the potential to generate more serious damage. Therefore, it is necessary to investigate the effect of a second tsunami bore on the local scour. For this purpose, in this section, three different tests are reported. Each set of tests consisted of two different runs. The first run was conducted in a dry bed condition while the second run was conducted as a second bore propagating over an already scoured sand bed in wet bed condition. Table 5-2 shows descriptions of the three tests. For the second run in each test, the area downstream of the gate was gradually filled with water so that the sediment bed and particularly the scoured hole from the previous run remained intact.

Table 5-2: Description of tests

	First run	**Second run**
Test 25	h = 0.25 m, d_1 = 0 m	h = 0.25 m, d_1 = 0.05 m
Test 26	h = 0.25 m, d_1 = 0 m	h = 0.25 m, d_1 = 0.125 m
Test 27	h = 0.15 m, d_1 = 0 m	h = 0.15 m, d_1 = 0.03 m

5.5 Test repeatability

All of the tests listed in were repeated at least twice and the average results in terms of water surface elevation, scour and velocity are presented herein. In order to check the repeatability of the experimental tests, repeated tests conducted for Test #1 are presented in Figure 5-6a, b and c. The graphs of water surface elevation, stream wise velocity and scour depth show that despite small differences, a good repeatability is obtained.

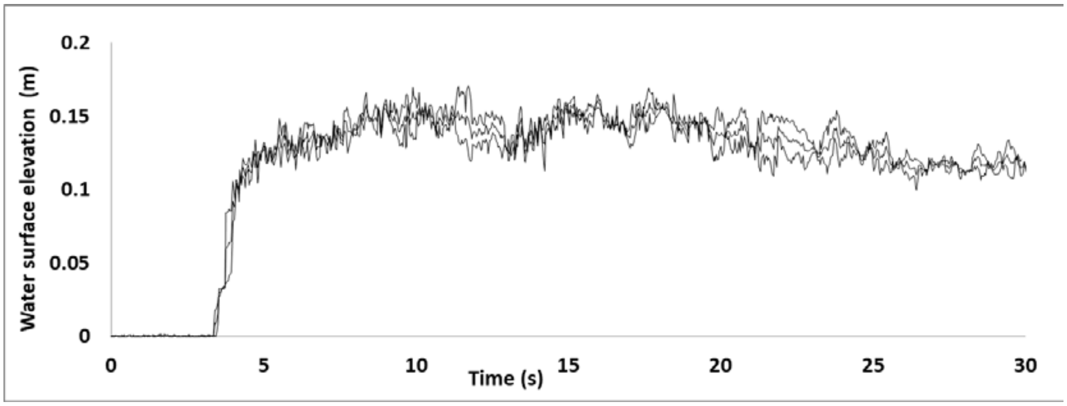

a)

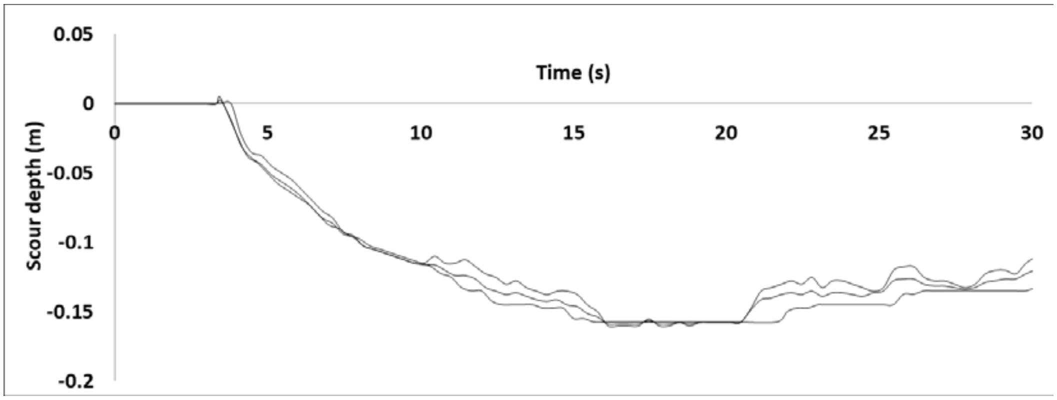

b)

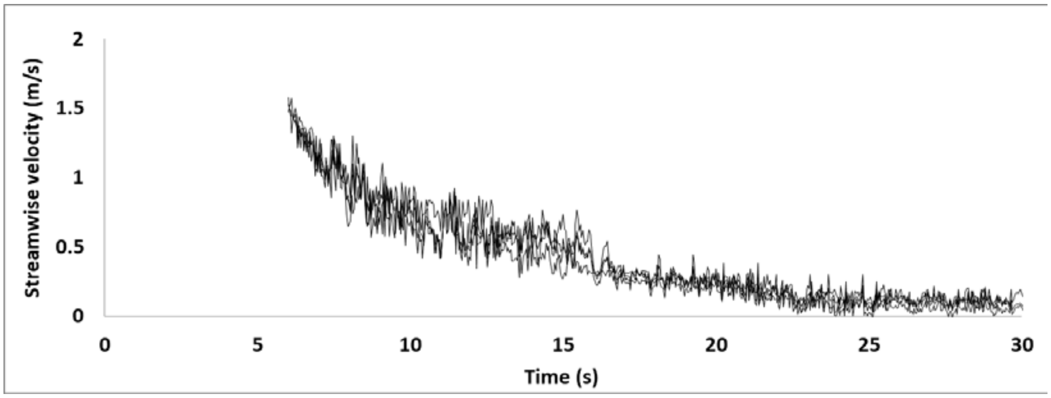

c)

Figure 5-6: Repeated tests conducted for Test #1, a) water surface elevation, b) scour depth and c) stream wise velocity

5.6 Results

In this section, the bore propagation characteristics and the resulting scour profiles for both wet and dry bed conditions are compared and discussed. in addition, the resulting scour induced by a second bore propagating over an already inundated and scoured bed is presented and discussed.

5.6.1 Effect of bed condition on bore characteristics

5.6.1.1 Sustained flow velocity (V_2)

Before initiating each test and prior to opening the swing gate, multiple small Styrofoam balls with a diameter of 4 mm and density of 0.035 kg/m^3 were placed on the surface of the water in the reservoir at approximately equal intervals from each other along the longitudinal reservoir axis as well as close to the swing gate. Figure 5-7 shows an image of the Styrofoam particle, circled in red, captured by the high-speed video camera.

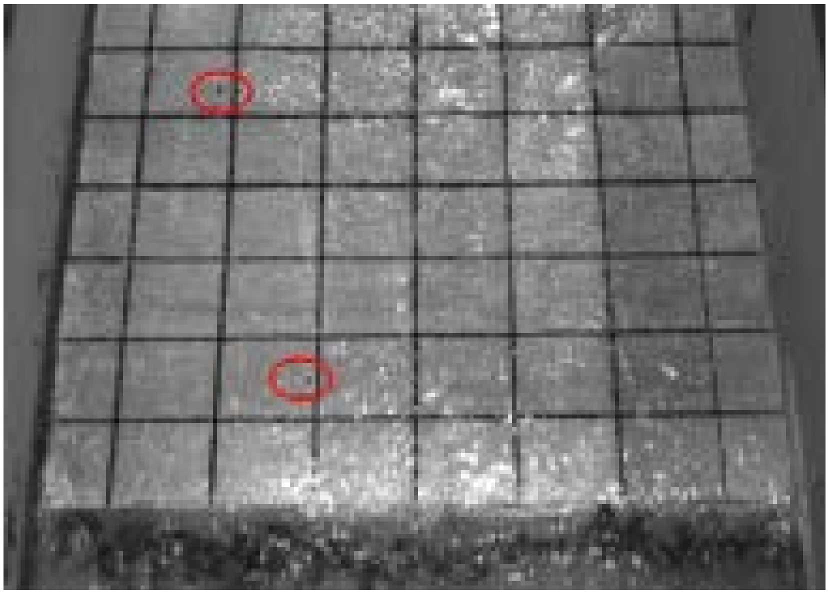

Figure 5-7: Image of the Styrofoam particle, circled in red, taken by the high-speed video camera

Once the gate was opened, frames of the moving Styrofoam balls were captured by the high-speed video camera as they travelled along the flume on the surface of the dam-break flow. The method used to calculate the flow velocity from these Styrofoam balls is known as particle tracking velocimetry and the authors have used it in the past in the same flume (Orendorff et al., 2011) in the analysis of flow velocity through an embankment dam breach. The first Styrofoam particles travelled with the bore right behind its front. The average flow velocity was measured between the two grid lines at X= 2.8 m and X=3.8 m, using the time sequence of the video recordings and the distance between the two grid lines. The particle velocity analysis provided estimates of the flow velocity, V_2, immediately following the passage of the bore front. Chanson (2004) presented an analytical solution for a dam-break wave moving over a frictionless horizontal channel initially filled with water; his analytical solution to calculate $V_2$is given by Equation (5-1):

$$V_2+2\sqrt{gd_2} = V_0+2\sqrt{gd_0} \qquad (5\text{-}1)$$

where V_0 is the initial reservoir velocity (m/s) which is equal to zero in the current experiments, and d_0 is the initial water depth (h) in the reservoir. Figure 5-8 shows the sustained flow velocity (V_2) measured by particle-tracking against the value calculated using Equation 5-1. Figure 5-9 compares the bore heights and Froude numbers calculated from Chanson's analytical solution

(2009b) and the current work. Both figures confirm that the measured values in this experiment are in good agreement with Chanson's analytical solution.

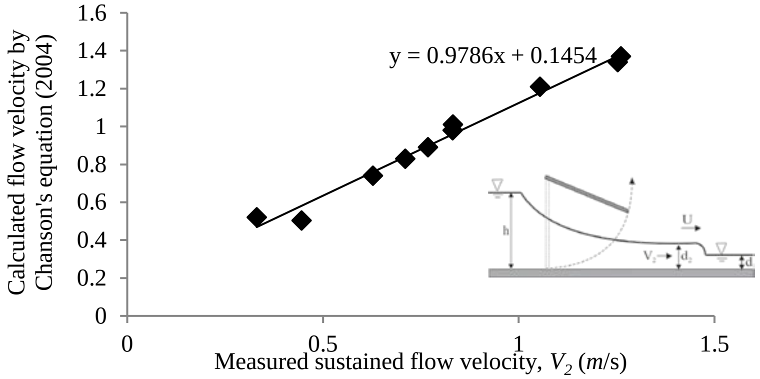

Figure 5-8: Comparison between the measured average sustained flow velocity (V_2) with the value calculated using Chanson's equation (2004) for Test # 4 to Test #14

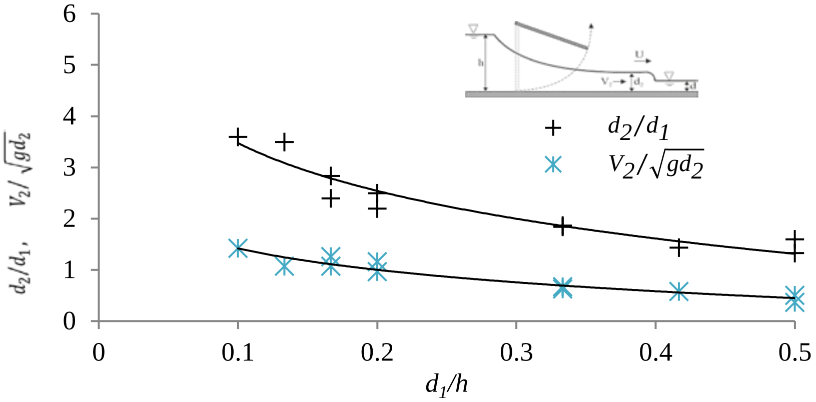

Figure 5-9: $V_2/\sqrt{gd_2}$ and $d_{2/}/d_1$ as a function of the d_1/h) for Test # 4 to Test #14

From Figure 5-9 it appears that the two parameters flow Froude number ($V_2/\sqrt{gd_2}$) and dimensionless depth $d_{2/}/d_1$ are a function of the non-dimensional initial water depth d_1/h. As the ratio of d_1/h increases, the two parameters decrease. Moreover, for d_1/h greater than 0.35, the rate of d_2/d_1 is no longer changed noticeably by further increases in d_1/h.

5.6.1.2 Bore front velocity (U)

Figure 5-10 presents the bore front velocity, averaged across the width of the flume, as a function of water depth ratio $r = d_1/h$. The propagation of the bore front along the upstream false floor of the flume was tracked using the high-speed video camera. The bore front velocity was calculated using a tracking method, similarly as the sustained flow velocities and at exactly the same locations on the false floor (between X= 2.8 m and X=3.8 m). A decrease in the bore front velocity was observed with an increase in the initial water depth ratio; therefore, the fastest bore front velocity over the fixed bed occurred in the dry bed condition.

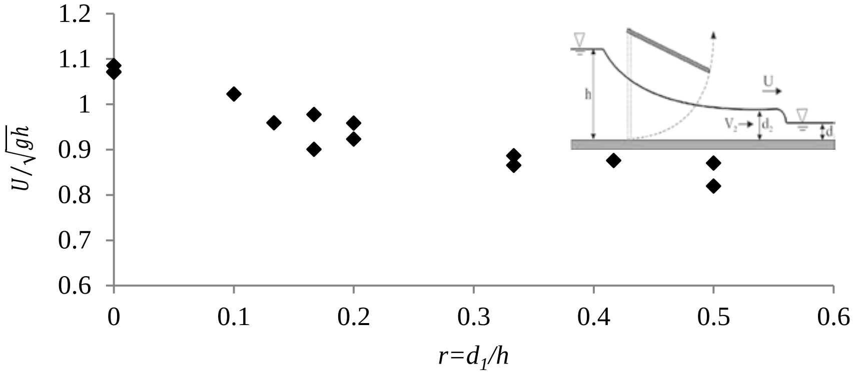

Figure 5-10: Average bore front velocity as a function of the water depth ratio (r=d_1/h) for Test # 1 to Test #14

To further investigate the effect of bed condition on bore front velocity, the velocities of the bore front as it propagated to the downstream end of the flume were calculated as shown in Figure 5-11.

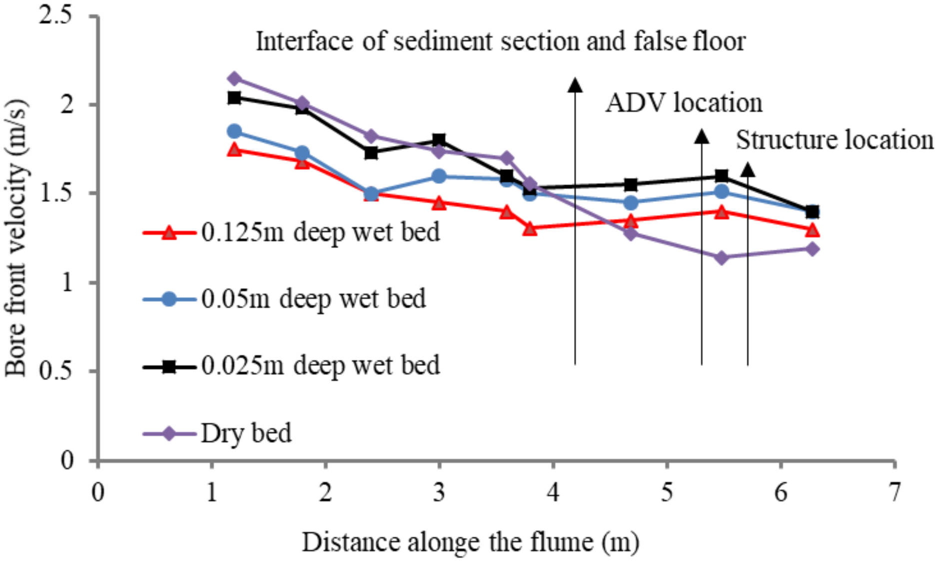

Figure 5-11: Bore-front velocity along the flume for Tests # 1,4,5,6 with h = 0.25 m and various downstream still water depths d_1.

The tests # (1, 4, 5 and 6) were conducted with an initial impoundment depth of h = 0.25 m, while downstream water depth d_1 for these tests varied between (0 m, 0.025 m, 0.05 m, or 0.125 m), respectively. Since the impoundment water depth was kept constant, the tests are identified according to downstream water depths as dry bed (purple line), 0.025 m wet bed (black line), 0.05

m wet bed (blue line), and 0.125 m wet bed (red line), respectively. For both dry and wet beds, the highest velocities were recorded at locations on the bed located closest to the gate. Due to bed friction and internal turbulent energy dissipation, the bore front velocity gradually decreased as the bore propagated downstream the flume.

On the fixed section of the bed, maximum instantaneous velocities reached as high as 2.15 m/s for the dry bed condition. The bore front velocities were 2.05 m/s, 1.84 m/s, and 1.75 m/s for the bore propagating over the 0.025 m wet bed, 0.05 m wet bed, and 0.125 m wet bed, respectively. The bore-front velocity decreased as the downstream still water depth increased. The presence of the still water layer created resistance to the propagation of the incoming bore, augmenting also energy dissipation in the bore front. Also, for the same impoundment depth, the higher downstream water depth with hence a lower total head subsequently resulted in lower kinetic energy and the observed reduction in the bore velocity.

The velocity measurement on the mobile bed showed a different trend from that observed for the case of the upstream located fixed bed. The bore-front velocity in wet bed conditions with a thin layer of water was faster than that measured for the bore propagating over a dry permeable bed. This was likely the result of water infiltrating into the bed under the dry condition, given the porosity and permeability of the bed sediment. In other words, energy and mass dissipation due to seepage is presumed to occur at the interface between the fluid flow and the sediment bed. The difference of bore velocity propagating over wet and dry beds was also mentioned in the previous studies by Stansby et al (1998), Chanson (2003), and Douglas and Nistor (2014), all of which found that, for the same generating conditions, the speed of a hydraulic bore on a dry (fixed) bed was higher than that on a wet bed. However, for all these experimental conditions, the bed was solid and hydraulically smooth, with no sediment (zero porosity). The present study results indicate that the higher bore-front velocity over a dry fixed bed cannot implicitly be extended to the case of a dry sediment bed.

5.6.1.3 Bore front free surface profile

The free surface profile of the bore front was obtained by using the high-speed camera and a grid painted on the sidewall of the flume. Figure 5-12a, b and c show the free surface profile for Tests #1, #5 and #6. Figure 5-13 also shows for these same tests the measured profile of the bore front at X= 5.6 m for both dry and wet bed conditions prior to the bore’s impact with the structure. It can be observed that the leading edge of the bore for the wet bed condition contains a larger volume of water. Comparing the dry bed condition with the wet bed condition, a distinctive difference in the bore-front profile was observed. The steep section at the bore front is shallower in the case of propagation over dry bed condition compared to that propagating over the wet bed. Undulation of the bore surface occurred prior to impact with the column for the case of the wet bed. The magnitude of the undulation increased as the initial downstream water depth increased. Furthermore, the slope of the leading edge was milder in the case of the dry bed condition compared to that of the wet bed one.

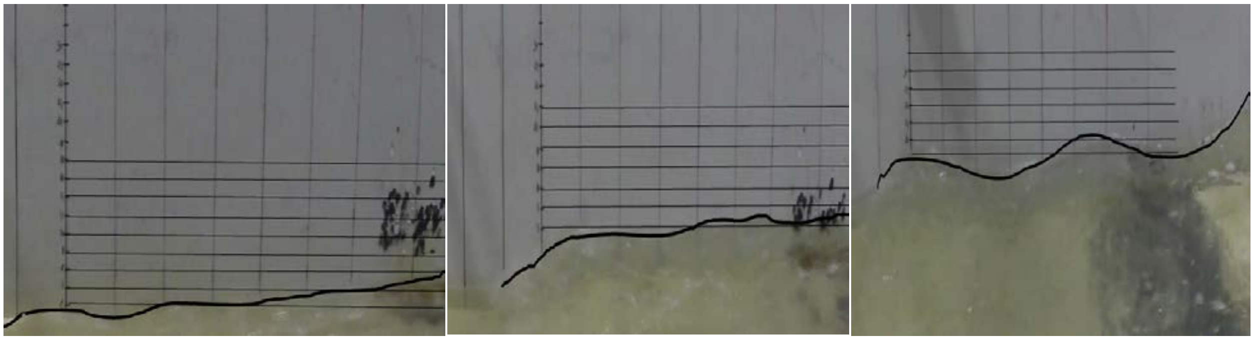

a) Test #1 b) Test #5 c) Test #6

Figure 5-12: Free surface profile measured at X= 5.6 m prior to the bore's impact with the structure a) Test #1 (h = 0.25 m, d_1= 0 m), b) Test# 5 (h = 0.25 m, d_1 = 0.05 m) and c) Test #6 (h = 0.25 m, d_1 = 0.125 m)

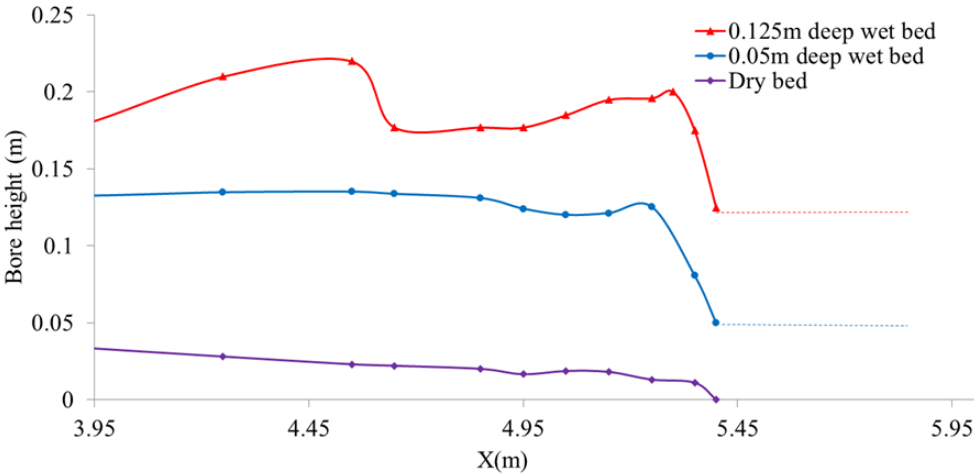

Figure 5-13: Comparison of bore front profiles for Test #1 (h = 0.25 m, d_1= 0 m; purple), Test# 5 (h = 0.25 m, d_1 = 0.05 m; blue) and Test #6 (h = 0.25 m, d_1 = 0.125 m; red)

Figure 5-14 clearly shows the differences between the bore fronts for the case of the a) dry bed and b) wet bed conditions. A significant amount of air entrainment and a deeper bore front were observed in the case of the wet bed condition, and this can be attributed to the passive resistance that the downstream still water imposes onto the propagation of the bore.

a) Dry bed, Test#1

b) 0.05 m deep wet bed, Test#5

Figure 5-14: Air-entrained bore front in the a) dry bed (Test#1) and b) wet bed (Test#5)

Figure 5-15 shows the top view of the bore front as it propagated along the fixed bed section. The shape of the bore front across the width of the channel is remarkably different between the dry and wet conditions. Air entertainment occurs significantly within the bore front in wet-bed conditions, and it was observed that air bubble entrainment decreased as the initial downstream water depth increased. Also, observations showed a steeper bore front with higher air entrainment for wet bed conditions compared to the dry bed one. Moreover, evidence of a distinct undulation pattern was observed for higher initial downstream water depths. In the case of the wet bed, the bore front propagated uniformly; however, in the case of a dry bed, the bore front propagated slightly faster towards the center of the flume. This likely occurred as a result of additional side friction due to the lateral walls. As the bore reached the sediment section in the case of the dry bed condition, the bore front entrained sand particles, and sand concentration was observed to rapidly increase in the bore front. However, for the bore propagating over the wet bed, sediment concentration immediately behind the bore front was substantially less, even for a relatively small initial still water depth. As the initial downstream water depth increased, the interaction of sediment particles with the flow reduced. Hence, another reason for the slower bore front velocity propagating over the dry movable bed than over the wet movable bed might be due to the added resistance caused by the significant entrainment of the sediment particles in the bore front in the case of the dry bed condition which may have reduced the energy of the flow.

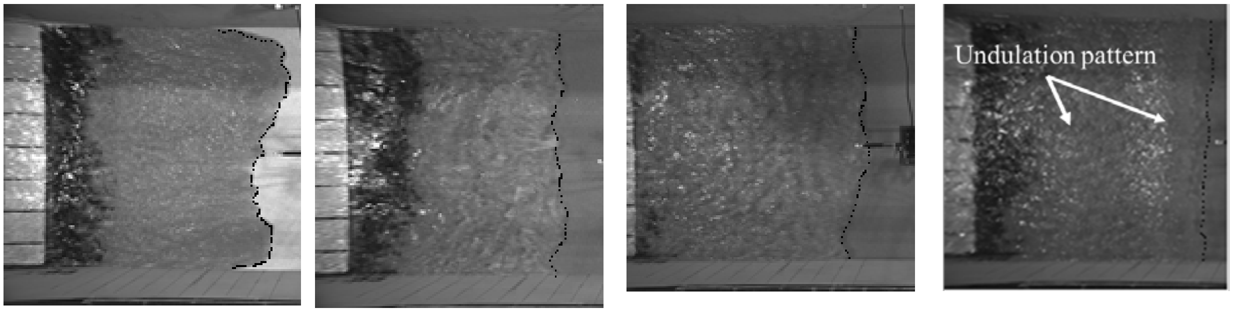

a) dry bed,Test#1 b) 0.025 deep wet bed, Test#4 c) 0.05 wet bed, Test#5 d) 0.125 wet bed, Test#6

Figure 5-15: Top views of bore front for: a) dry bed, Test#1 ; b) 0.025 m deep wet bed, Test#4; c) 0.05 m deep wet bed, Test#5; and d) 0.125 m deep wet bed conditions, Test#6. Flow from left to right.

Figure 5-16 shows the flow field around the structure as the bore propagated around the column. When the dam-break bore impacted the structure, the flow was pushed vertically onto the upstream face of the structure and formed an upward flow motion termed *run-up*. The upward flow fell back onto the incoming flow, causing a substantial increase in turbulence and air entrainment with fluctuations in its free surface leading to the formation of a surface roller. With an increase in the initial still water depth, the zone of turbulence decreased. As can be seen in Figure 5-16d, the initial turbulence caused by the bore impact did not occur at all for the 0.125 m deep wet bed, and the bore had the appearance of sustained supercritical flow. Furthermore, it can be observed that the zone of turbulence in the case of the dry bed condition (Figure 5-16a) was wider across the front face of the column and contained more air entrainment compared to that observed for the 0.025m deep wet bed condition (Figure 5-16b).

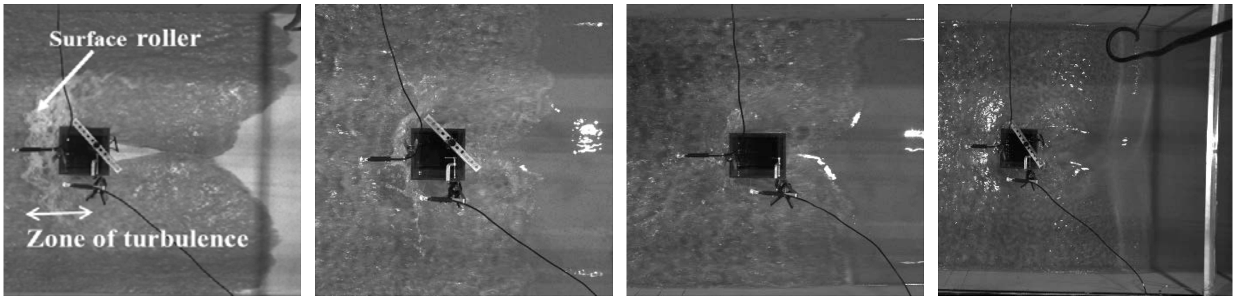

a) dry bed, Test#1 t = 0.9 sec b) 0.025 m deep wet bed, Test#4, t = 0.34 sec c) 0.05 m deep wet bed, Test#5, t = 0.42 sec d) 0.125 m deep wet bed, Test#6, t = 0.57sec

Figure 5-16: Top views of bore-front for: a) dry bed, Test#1, b) 0.025 m deep wet bed, Test#4 c) 0.05 m deep wet bed, Test#5 and d) 0.125 m deep wet bed conditions, Test#6. Flow from left to right.

Flow separation along the lateral the sides of the structure produced a wake vortex, and, past the column, the separated bore rejoined at the back of the structure. As shown in Figure 5-16a, the wake region in the dry bed condition started developing 0.9 seconds after the initial impact while the same was observed at 0.34 seconds, 0.42 seconds, and 0.57 seconds for the 0.025 m, 0.05 m, and 0.125 m deep wet bed conditions, respectively. For the wet bed condition, the separated bores rejoined closer to the back side of the structure, and the formation of the wake downstream of the column occurred earlier than in the case of the dry bed condition. Moreover, as a result of the slower bore front velocity for the 0.125 m deep wet bed, the wake region formed later than in the two other wet bed conditions.

5.6.1.4 Run-up and streamwise velocity of bore propagation

Comparisons of the time-history of the water surface elevation at the upstream face of the structure and the streamwise velocity at the ADV location are shown for different initial bed conditions in Figure 5-17.

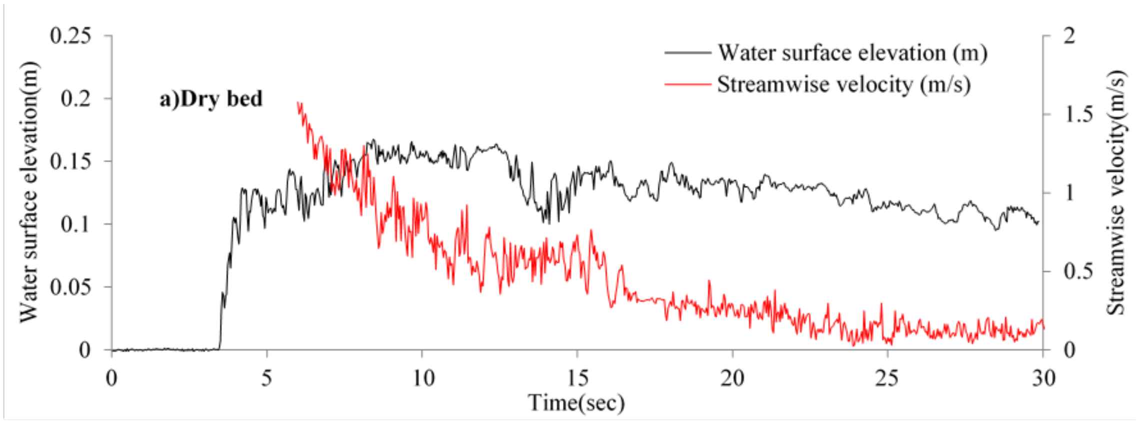

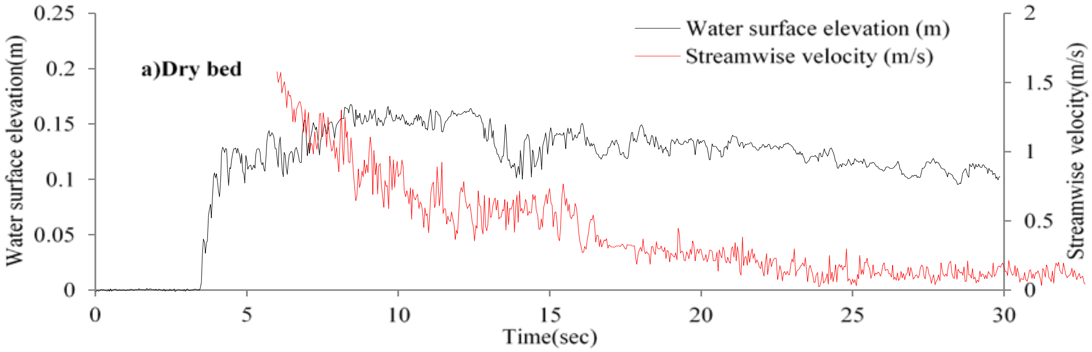

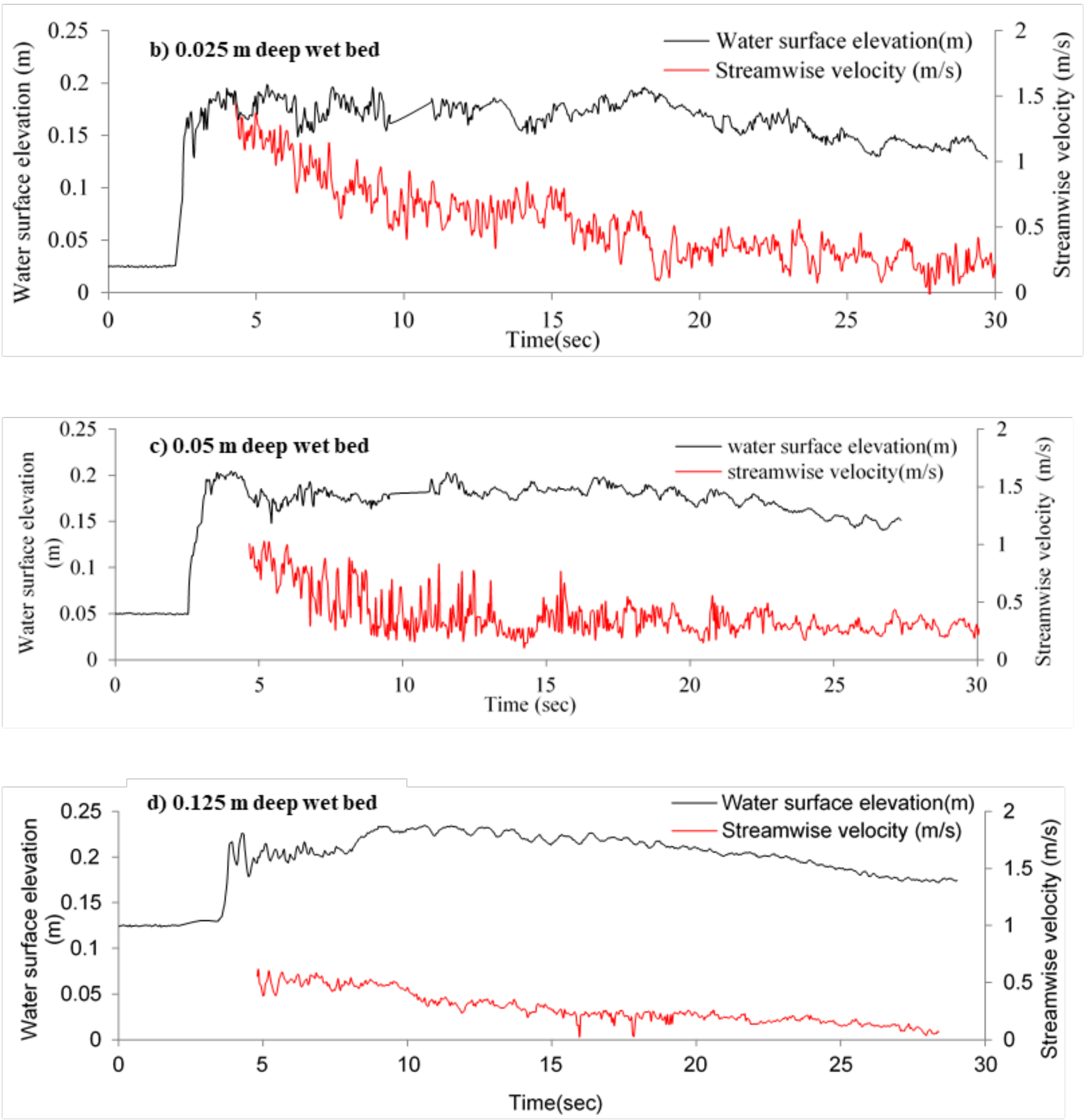

Figure 5-17: Measured water surface elevation (black line) and measured streamwise velocity (red line) for: a) dry bed (Test#1), b) 0.025 m deep wet bed (Test#4), c) 0.05 m deep wet bed (Test#5) and d) 0.125 m deep wet bed (Test#6)

For a better comparison of all the tests, time instant zero refers to the time of the sudden release of the water impounded in the upstream reservoir. As shown in the figures above, the run-up height resulting from the initial impact was influenced by the bed condition. The run-up height above initial water level reached its highest value (0.173 m) for the case of a bore propagating over a thin layer of water (0.025 m deep wet bed). The maximum run-up heights were 0.165 m for the dry bed, and 0.15 m and 0.11 m for the 0.05 m wet bed and 0.125 m wet bed, respectively. The increase in the run-up height is because (1) the bore front in the wet bed condition contains a larger volume compared to that occurring for the dry condition and (2) a loss of water due to a portion of the bore infiltrating into the bed affects run-up depth in a dry movable bed. Again, this is in contrast with results from other studies, such as Stansby et al. (1998) and Douglas and Nistor (2014), which observed greater run-up depths for bores propagating over dry smooth solid beds.

A consistent reduction in run-up height was observed with an increase in the still water depth for the wet bed condition. The maximum run-up height for the dry bed condition occurred 7.9 s after the arrival of the bore front, while maximum bore depth was attained within less than a second for the wet bed condition. Douglas and Nistor (2014) observed maximum bore heights within 0.5 s after the initial impact for bores propagating over dry smooth solid beds. A delay in maximum run-up height and in the arrival instant of the bore front can again be attributed to a loss of both volume of water and flow energy due to the infiltration of the water in the case of the dry bed condition. Consistent with Figure 5-13 and Figure 5-14, for the wet bed conditions, a relatively vertical bore front was observed when compared to the dry bed condition for which the bore was much thinner, and its slope was mild.

To further analyze the effects of bed condition on the bore propagation characteristics, the time-history of the streamwise velocity, measured 0.4m upstream of the structure, is shown in Figure 5-17 for all initial downstream still water depths. In all cases, the ADV sample volume was set such that it would be at or just below the bore surface. To avoid ADV measuring errors due to high flow front turbulence, streamwise velocity measurements began 2 s after the passage of the bore front. According to Figure 5-11, the bore front velocities at the location of the model structure were 1.14 m/s, 1.6 m/s, 1.51 m/s and 1.40 m/s, while from Figure 5-17 it can be seen that the maximum streamwise velocities were 1.57 m/s,1.45m/s, 1.005 m/s and 0.554 m/s for dry bed, 0.025 m deep wet bed, 0.05 m deep wet bed and 0.125 m deep wet bed, respectively. It appears that the lowest bore-front velocity occurred for the case of the dry bed condition, whereas the largest measured streamwise velocity occurred 2.53 seconds after the passage of the bore front in the dry bed condition. The authors hypothesize that the rapid hydraulic saturation of the initially dry bed allowed for an increase in the bore velocity once its front had passed. These results also show that the streamwise velocity decreased in magnitude as the downstream water depth increased.

5.6.2 Effect of bed condition on local scour

5.6.2.1 Scour depth time history

Figure 5-18 shows the time-history of the scour depths for the four primary comparison tests. The maximum recorded scour depth was 0.17 m during the 0.025 m deep wet bed case, and it should be noted that any further scour for this test would have been limited by the 0.17 m thickness of the sediment bed. The maximum measured scour depth for the dry bed test was 0.16 m. This would imply that a hydraulic bore propagating over a wet bed condition can be even more destructive than one advancing over dry land. The scour depths were respectively 0.12 m and 0.03 m for the 0.05 m and 0.125 m wet bed tests, indicating reductions of 40% and 140% compared to the 0.025 m deep wet bed test. Therefore, similar to the bore front velocity and stream-wise velocity, substantial reductions in scour depth were observed with an increase in the downstream initial still water depth.

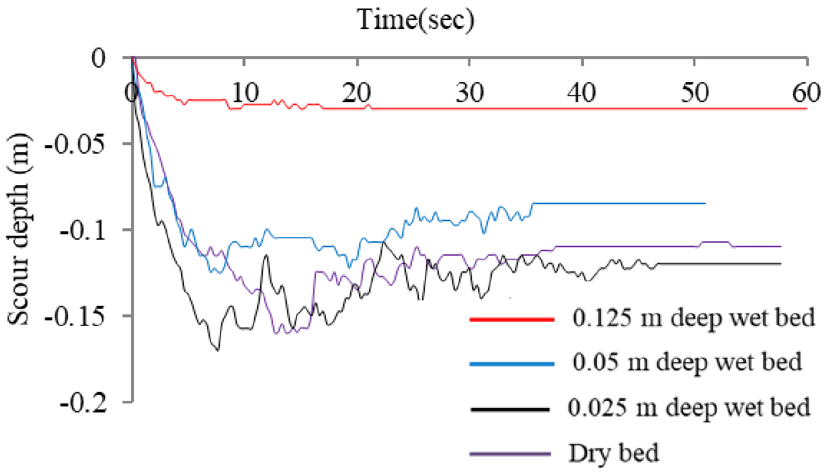

Figure 5-18: Time-history of the scour depth for dry bed (Test#1), 0.025 m deep wet bed (Test#4), 0.05 m deep wet bed (Test#5) and 0.125 m deep wet bed (Test#6)

There was also a noticeable difference between the time it took for the maximum scour depth to form for the dry bed condition compared to that observed for the case of any of the wet bed conditions. The maximum scour depth in the dry bed condition occurred 14.3 s after the bore front passage, while for the wet bed tests, this occurred within 7.6 s, 7.6 s and 4.6 s for the 0.025m, 0.05 m and 0.125 m still water depth cases, respectively. This was likely because for the dry bed condition, the bore reached the structure before the sand bed was fully saturated completely. Furthermore, it can be seen that the rate of scour decreased with an increase in initial downstream still water depth.

5.6.2.2 Final scour bathymetry

The final bathymetry of the scoured sediment bed was measured using a a Disto TM laser altimeter with a precision of ± 1.00 mm. The measurements were then referenced to the average elevation of the false floor on either side of the sediment bed section. Point measurements were taken over the entire sediment bed surface. Due to the sudden changes in sediment bed elevation, such as at the edge of the scour hole around the column model, point measurements were taken on a grid scale of 5 cm away from the edges of the scour hole, at 2 cm when close to the scour hole edge and 1cm over the entire scour hole area. Point measurements were interpolated over the sediment bed area using Golden Software Surfer v.11.5 in order to provide a better visualization of the final scour depth, scour magnitude and area. Figure 5-19a, b, c, and d show the final scour bed bathymetry around the structure for the 0.125 m deep wet bed, 0.05 m deep wet bed, and 0.025 m deep wet bed and dry bed cases, respectively. The positive and negative values on the scale represent deposition and erosion, respectively. The structure is shown as a black rectangle. As the scour hole is consistently observed to be symmetrical around the center of the structure, only one side was measured.

As shown, an area of local scour along the upstream boundaries of the sediment section at the interface of the false floor and sediment bed was observed. This was a result of the transition between the false floor and the sediment section. As mentioned previously, a short gabion mat was used to minimize the local scour at this upstream bed transition. The final scour holes formed by the hydraulic bores were, for the most part, elliptical in shape. For all cases, the maximum final scour depths were found at the upstream corners of the structure, and the scour depth decreased approximately linearly along the downstream sides of the structure.

For the cases of the (a) dry and (b) 0.025 m deep wet bed conditions, the bore depth and velocity had sufficiently high magnitudes that a substantial amount of the surrounding sand bed was scoured.

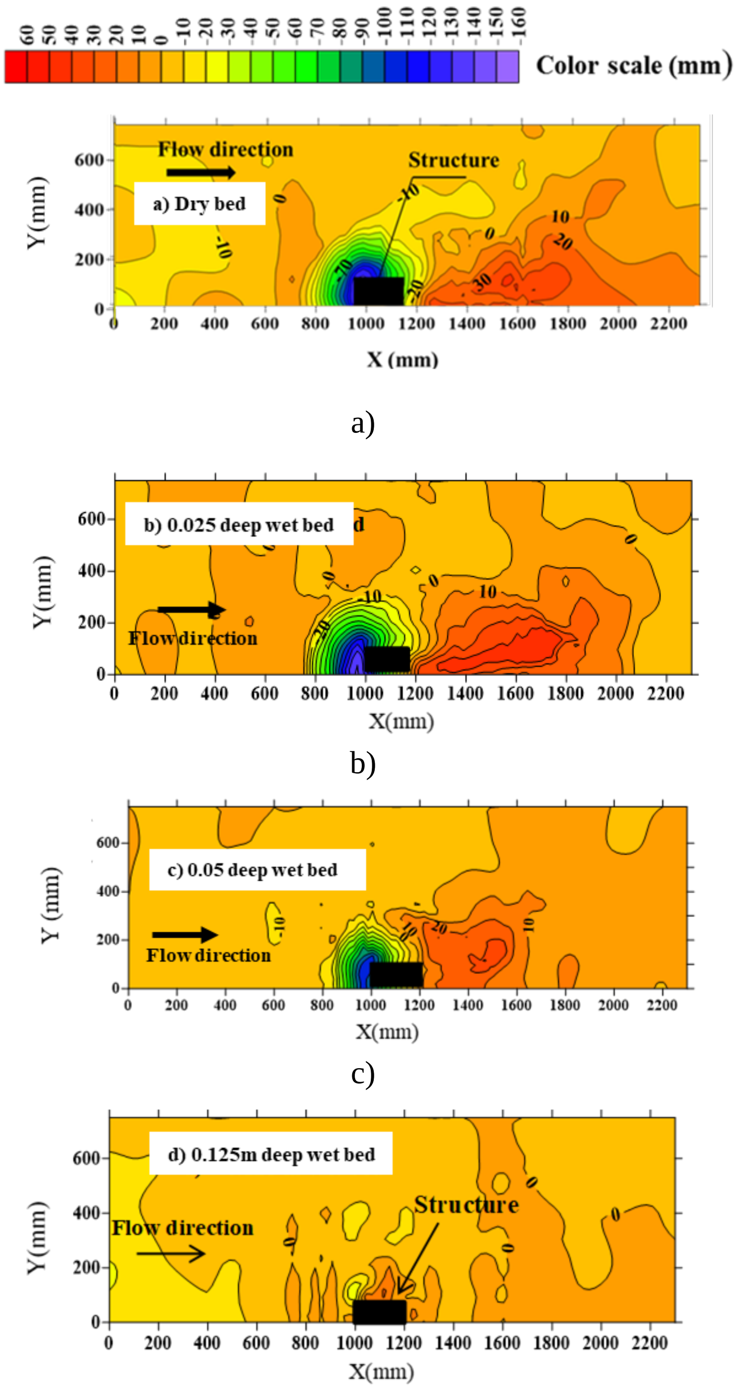

a)

b)

c)

d)

Figure 5-19: Final scour topography for a) dry bed (Test#1), b) 0.025 m deep wet bed (Test#4), c) 0.05 m deep wet bed (Test#5) and d) 0.125 m deep wet bed (Test#6)

For all tests, sediment particles carried away from the scour hole were deposited behind the structures. For the case of the 0.125 m deep wet bed, shown in Figure 5-19(d), the scour process did not develop and the dimension of the scour hole did not grow in size to the same extent as in the other wet bed tests, and, as a result, no downstream deposition was observed. Moreover, as the initial downstream still water depth increased, the scour hole decreased in depth and lateral extent and the downstream deposition area decreased. An angled area of scour extending from the side of the structure to the walls of the flume was observed only in the case of the dry bed. This scour pattern may have been related to the large plane area of the surface roller generated around the structure, as shown in Figure 5-16a. Comparing the deposition areas, for the wet bed conditions the deposition area extended more laterally towards the flume side walls than for the dry bed condition. This difference between the deposition shapes might be related to the bore separation patterns alongside the structure. As was shown in Figure 5-16 , the separated bores in the wet bed reattached at a location closer to the back of the structure, whereas they rejoined only further downstream in the case of the dry bed.

5.6.3 Effect of second tsunami wave

5.6.3.1 Time history of the scour depth

Figure 5-20(a) and (b) show the time history of the scour depth for Test #25 and Test #27. Black and red lines represent the results of the first and second runs, respectively. It can be seen that for Test #25, the maximum scour depth induced by the first bore was 0.16 m while the scour depth reached to 0.17 m after running the second bore (Figure 5-20a). The results show increases of 6% and 20% in the maximum and final scour depths, respectively. As mentioned before, the depth of the sediment bed was limited to 0.17 m, and after running the second bore the scour hole reached the bottom of the sediment bed before the test was completed. Hence, a further increase in scour depth could have occurred. For Test #26, the configuration of first run was the same as for Test #25, but the initial downstream water depth (d) was increased from 0.05m to 0.125m. After the second run, the scoured bed from the first run was unchanged, and therefore the results are not presented herein. Moreover, the result of Test #27 is shown in Figure 5-20b. It can be seen that the maximum scour depth after the second run increased by 27% and the final scour depth increased by 41%.

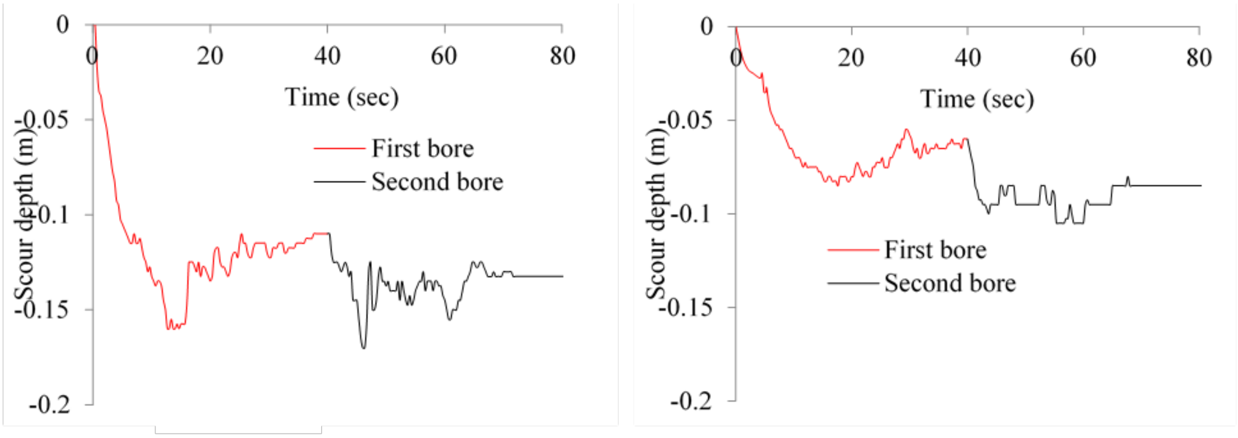

a)

b)

Figure 5-20: Scour depth time history for a) Test #25 and b) Test #27

5.6.3.2 Scour profile

Figure 5-21(a), (b), (c) and (d) show the scour profiles around the front and side face of the structure resulting from the first and second runs for Test #25 and Test #27. The figures show the moment when the maximum scour depth occurred for both runs. (Figure 5-21b) shows that the second run scoured to the flume floor; nonetheless, it is still evident that the scour depth was increased by the second bore. (Figure 5-21c) and (Figure 5-21d) present the scour profiles of Test #27 during the first and second runs. These figures also demonstrate the increased scour depth induced by the second bore. Comparing the increased scour depth at the middle of the front column side (Line A) and at the corner (Line B), the difference between the maximum scour depth generated by the first and second bores in Line A was 0.035m (an increase of 66% over the scour generated by the first bore). Also, the increase in scour depth at Line B at the corner of the structure was 0.025 m (an increase of 27%). The scour depth at the back of the structure did not undergo any changes after running the second bore.

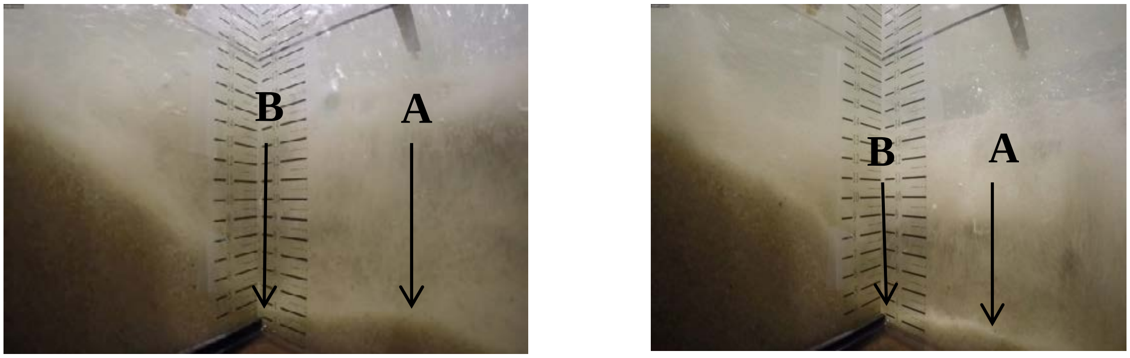

a)

b)

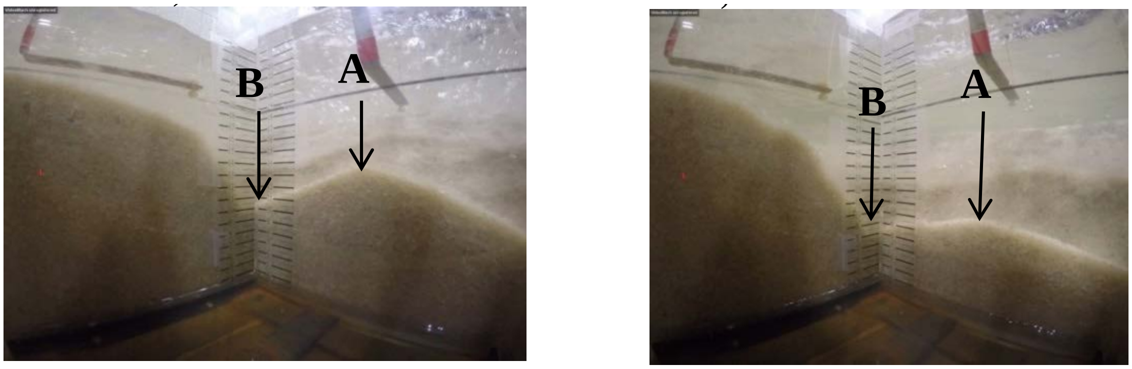

c) d)

Figure 5-21: Increased maximum scour depth due to the second bore, a) Test #25-first run, b) Test #25 – second run, c) Test #27 – first run, d) Test #27 – second run

5.6.3.3 Final scour topography

Figure 5-22a and b present the final scour topography after the first and second bores of Test #25, respectively. The scour hole increased in size after passage of the second bore. It can be seen that sand was eroded across most of the width of the sediment bed. During the tests it was observed that most of the sediment particles from the upstream of the sediment bed were washed away and were deposited in the area behind the structure.

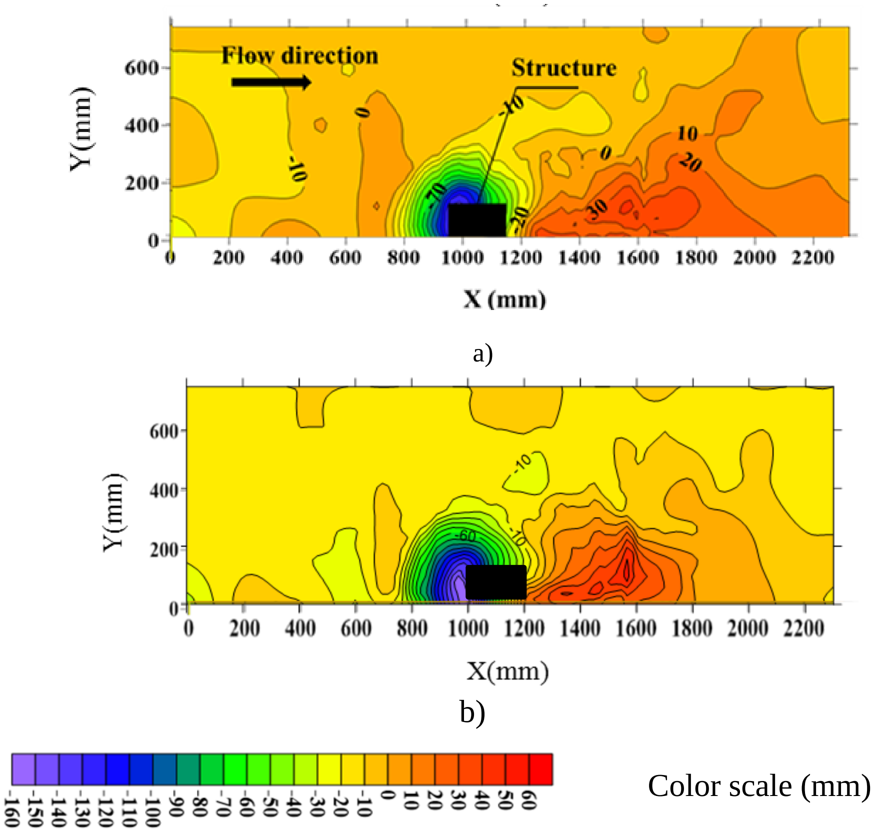
a)

b)

Figure 5-22: Final scour topography of Test #25 after: a) first run, b) second run

5.7 Discussion

There are various factors that affect scour depth during tsunami inundation, such as the soil type, the structure’s location, the flow velocity and depth, the structure’s shape and size, as well as the bed condition (Chock et al. 2013). Two field observations of local scour from the field surveys of the 2011 Tohoku Tsunami (Chock et al. 2013) are used to compare with the current test results. A local scour of 4.2 m was measured in the vicinity of the pier of a viaduct bridge built in sandy soil in Miyako City and a local scour of 1 m was observed around a bridge pier of Yogi port (Chock et al., 2013). The diameters of the piers were estimated using a reference object in the photographs provided by the authors (Chock et al. 2013). The diameters of the piers of the viaduct in Miyako City and the bridge pier at Yogi port were estimated to be approximately 3.75m and 1.7m, respectively. The maximum bore Froude number for this area affected by the 2011 Japan Tsunami varied from 1.14 to 1.5 (Nandasena et al. 2012).

Figure 5-23 shows the dimensionless scour depth $\mathrm{d_s/B}$ as a function of $\mathrm{V_2/\sqrt{gd_2}}$ which is the flow Froude number. Moreover, the results of experiments conducted by Lavictoire et al. (2014) in collaboration with the second and third authors of this study are also included in the plot. They used the same dam break wave generator to create tsunami-like bores moving around a circular structure placed onto a dry bed. The Chock et al. (2013) field results of the scour measured around the bridge pier of Yogi port and Viaduct bridge in Miyako City are also plotted using dash line and black line, respectively.

For the *Fr* values ranging from 0.3 to 0.5, the d_s/B is around 0.15, whereas for the *Fr* values between 0.6 and 1.6, the d_s/B varies between 0.3 to 1.3. In the dry bed condition, the sustained flow velocity (V_2) estimates the flow velocity immediately following the passage of the bore front over an already saturated bed, which can explain the larger *Fr* number in dry bed conditions compared to wet bed conditions. Moreover, it can be seen that the experimental data fall within the range of the field data.

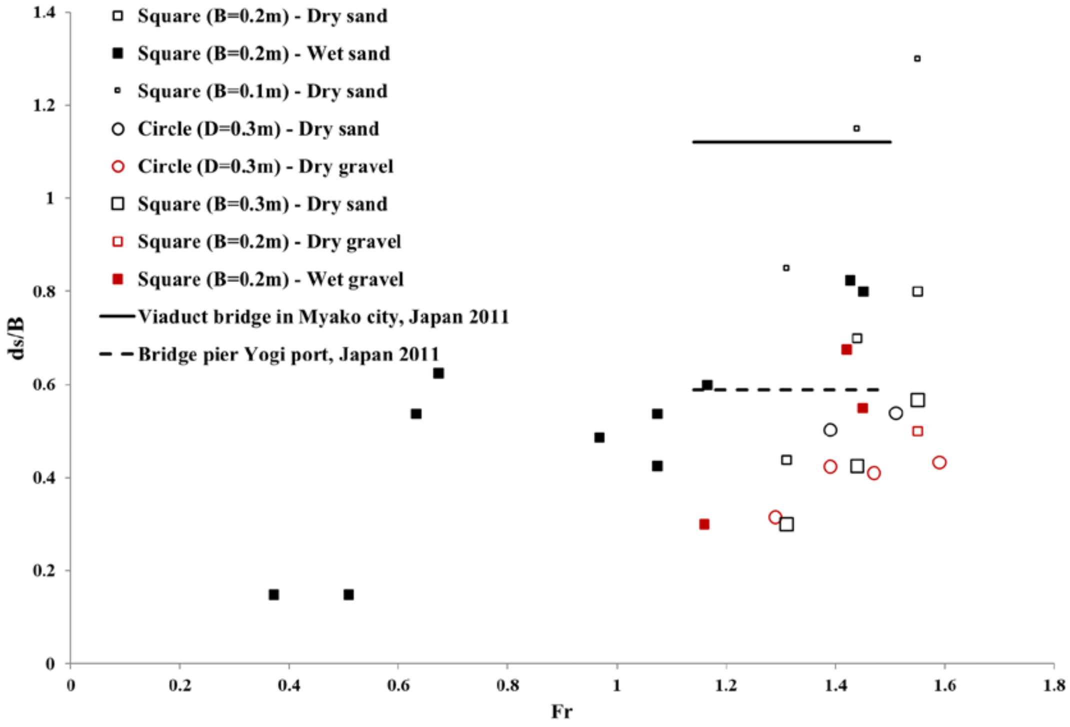

Figure 5-23: Scour depth ($\mathrm{d_s}$), for various structure shapes and sizes and bed sediment particle size and condition, as a function of the flow Froude number. Results for circular structures are from LaVictoire et al. (2014). The field data are described in Chock et al. (2013).

As already shown in Figure 5-18 , the presence of an initial still water depth reduced the magnitude of the scour depth. The presence of downstream water depth resulted in less kinetic energy which translates into lower flow velocity and, subsequently, less scour. In addition, the presence of an initial still water layer weakens the strength of the horseshoe vortex generated by the down-flow and surface roller. As a result, the bore becomes less effective at displacing the sediment grains around the structure with increasing the initial water depth. This hypothesis is demonstrated in the conceptual rendering shown in Figure 2-24a and b, which shows the main features of the flow field around the structure, and how the scour capacity of a turbulent bore reduces as the still water depth increases.

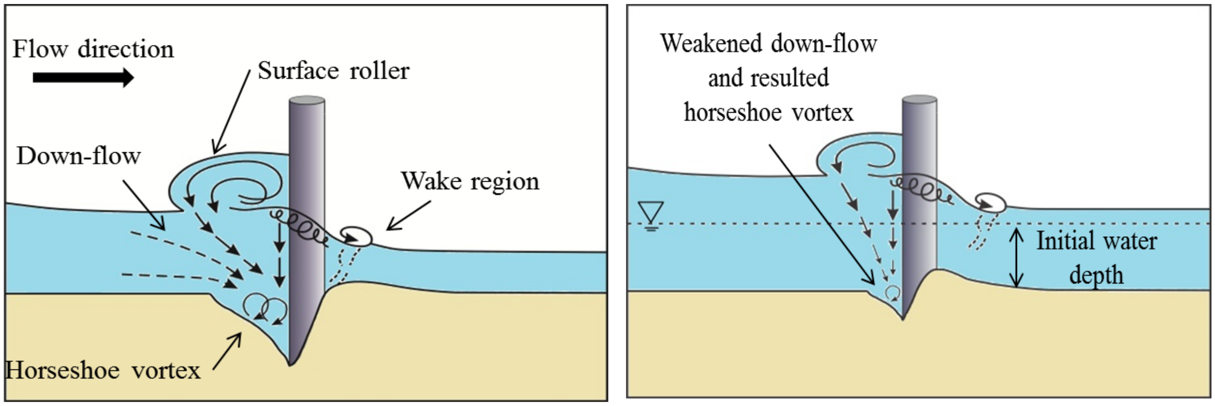

a) b)

Figure 5-24: main features of the flow field around the structure a) no initial water depth b) with initial water depth

In contrast to the current study, Arneson et al. (2012) reported that the scour capacity of a *steady* flow field decreases as the flow depth decreases. They hypothesized that the down-flow at the pier face becomes less well developed because it has a shorter distance over which to develop. The vorticity of the horseshoe vortex then weakens as the down-flow weakens, and the wake vortex also weakens due to the increased importance of bed friction at shallower depths. However, in the present *unsteady* flow conditions, the results of the present study show that the increase of the initial water depth reduced the scour potential of the transient turbulent bore.

In the case of the second bore advancing on a previously flooded and eroded bed, as shown in Figure 5-25, the down-flow weakens as it penetrates through the water column (d). The deeper initial water depth used in Test #26 (when compared to that of Test #25) weakened the generated downflow induced by the second bore in front of the column. As a result, the downflow is not strong enough to deepen the scour depth following the second bore. The same reasoning applies for the greater increase in scour depth for Line A compared to that of Line B in Test #27 (Figure 5-20d). Following the first bore, the scour depth induced by the first bore at Line A is deeper than that of Line B. Therefore, it can be concluded that the potential for excessive scour depth due to the second bore depends on not only the height of the second bore, but also on the scour and inundation flow depth resulting from the first bore passing the column.

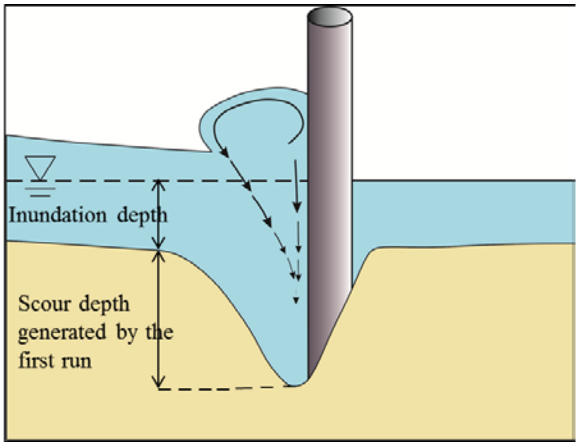

Figure 5-25: Second bore advancing on a previously eroded bed

5.8 Conclusions

This experimental program was directed at investigating the effect of wet versus dry bed conditions on bore characteristics and the resulting scour and deposition around a square structure model. The hydraulic bores were generated based on the similarity between dam-break waves and breaking tsunami waves advancing over relatively flat coastal plains (Chanson 2006). Good agreement between Chanson's analytical solution and the measured parameters from the current experiments was obtained. In general, it was found that the presence of an initial water depth can significantly influence both the hydraulic bore and the resulting local scour. Based on the described setup, the following conclusions are drawn:

- There is a distinctive difference in the bore front profiles when advancing over dry or wet bed conditions. A significant amount of air entrainment as well as a steeper a higher bore front was observed in the case of wet bed conditions. These are the result of the resistance that the downstream still water level imposes on the propagation of the bore.
- When the bore reached the dry sediment section, the bore front entrained the sediment, and sand particle concentration developed rapidly towards the bore front. However, for a bore propagating over a wet bed, sediment concentration developed behind the bore front, and the sediment load and concentration, were substantially reduced for even a relatively small

still water depths. As the initial downstream water depth increased, the entrainment of sediment particles within the flow decreased.

- Furthermore, results show that bed condition (wet vs. dry) as well as type of bed (movable or fixed) plays an important role in the hydrodynamic characteristics of a bore and its erosion potential. It was found that the bore behaves differently in the cases of wet and dry conditions on fixed versus mobile beds. In the case of a fixed bed, the higher downstream still water depth results in a lower total head and, subsequently, less kinetic energy and a lower velocity; therefore, the highest bore-front velocity occurs in the case of the dry bed condition. In contrast, in the case of a movable bed, the bore-front velocity in wet bed conditions with a thin layer of water was higher than that observed for the dry bed. For the case of the dry bed, this is likely a result of water infiltrating into the bed, and also the added resistance caused by concentration and entrainment of the sediment particles on the bore front. However, the results for the streamwise velocity measured by the ADV show that saturation of the initially dry bed allowed for increased velocity following passage of the bore front.
- The excessive scour depth that may occur as a result of a second bore propagating on a previously scoured bed depends on the height of the second bore, as well as on the inundation flow depth and the scour depth generated from the passage of the first bore.

Chapter 6. STRUCTURE WIDTH EFFECT ON LOCAL SCOUR INDUCED BY TURBULENT BORE

The article is in review in Canadian Journal of Civil Engineering (CSCE)

Abstract

In this study the effect of structure size on the scour depth induced by turbulent bores is presented and discussed. The hydraulic bores were generated based on the similarity between dam-break waves and tsunami-induced bores on relatively flat coastal plains. The experimental program was conducted in the dam break Flume at the Hydraulic Laboratory of the University of Ottawa, Canada. The dam-break wave was generated by releasing water impounded behind a rapidly opening swing gate. The results showed a consistent reduction in splash height as the structure size decreased. It was found that the scour process and how the final sediment bed topography is shaped are influenced by the variation of structure size. A strong surface roller propagating upstream of the widest structure caused an area of local scour extending from the side of the structure to the walls of the flume. As the structure size decreases, the size of the scour hole decreases in size and depth. Also, as the structure size decreased, the scour hole became more dominant at the back of the structure.

6.1 Introduction

Tsunamis are long waves induced by sudden motions of the seabed due to undersea earthquakes or landslides. They normally have periods the order of minutes to hours. According to the Federal Emergency Management Agency (FEMA) P-646 design guideline 2012, upon reaching shallow coastal areas, tsunamis break and can form, depending on the nearshore bathymetry and coastal topography, a bore or a surge in shallow waters. A tsunami bore is characterized by a turbulent and steep foaming front. The breaking is predominant for leading elevation waves and occurs as a result of wave shoaling and non-linear transformations over the continental shelf (Yeh 2009). The damage from historic tsunami events such as the 2004 Indian Ocean Tsunami and the 2011 Tohoku Japan Tsunami, and the storm surge associated with Hurricane Katrina in 2005 and Typhoon Haiyan in the Philippines (2014) can be categorized as: (1) direct hydrostatic and hydrodynamic loading from water inundation; (2) impact forces from water-borne debris; (3) fire spread by floating debris and combustible liquids; and (4) scour and slope/foundation failure (FEMA- P646).

Post-tsunami field surveys have recorded substantial evidence of scour around damaged buildings and bridge foundations (Yeh and Li 2008; Ghobarah et al. 2006; Saatcioglu et al. 2006a; Saatcioglu et al. 2006b; Chock et al. 2013). These field surveys noted that scour was one of the primary causes of coastal structural damage (Chen et al. 2016). There are two conditions for scour in a steady flow: clear-water and live-bed scour (Kothyari et al. 1992). Clear-water scour is the condition where there is no transport of bed material from upstream. In contrast, live-bed scour occurs when there is transport of bed material from upstream. The scour hole cyclically deepens during the rising stages of a flood and refills during the falling stages. Complex tsunami inundation flow patterns likely include both live-bed and clear-water conditions. This complicates the effort to explain field observations, since observed scour depths may not represent the maximum depth, or the conditions producing observed levels of damage (FEMA 2000).

Previous studies have mostly investigated the impacts of tsunami-induced forces on structures. Current design codes and guidelines provide only minimal information and recommendations for tsunami-induced scour around structures, and they are mostly based on a limited amount of field observations and a few lab tests. Studies investigating tsunami-induced scour around coastal and offshore structures are few. Wilson et al. (2012) studied sediment scour and deposition within harbors; Chen et al. (2013) conducted experiments to study tsunami-induced scour on coastal roadways; and Bricker et al. (2012) conducted a field study of scour depths measured on the landward side of seawalls and floodwalls and around building foundation footings from the 2011 Tohoku tsunami. As well, Tonkin et al. (2003) studied the scour promoted by incident solitary waves around a cylinder on a sloping beach, where the cylinder was mounted near the shoreline, and Nakamura et al. (2008) studied scour around a square pile induced by solitary and long waves. Two common approaches for experimentally generating tsunami waves are solitary waves and long waves inside a flume or wave basin. Chanson (2006) analyzed visual images of an actual tsunami bore resulting from the 2004 Indian Ocean tsunami and concluded that the flow characteristics of the bore were very similar to those of a dam-break wave. Moreover, recently Williams and Fuhrman (2016) simulated a series of tsunami-scale boundary layers, emphasizing that they may be both current-like due to their long durations but also wave-like in the sense that they are unsteady.

Due to the complex nature of scour in such a turbulent flow and to ensure proper design, different parameters should be considered in a tsunami scour estimation method, including the structure size, bore height, bed initial conditions (wet vs dry), median sediment size (d_{50}), and the effect of a second tsunami wave.

Structure size has a great influence on scour depth and geometry. Ettema et al. (2006) conducted experiments on local scour at vertical cylinders placed in a sand bed, and concluded that the frequency of vortex shedding and the amount of vorticity in the wake of a structure are directly related to the projected width of a structure.

Flow shallowness represents the effects of the depth of flow (y) in relation to the pier width (b), thus structure size directly influences flow shallowness. In steady flow, Melville (2008) explained that for deep flows compared to the pier width (narrow piers), the scour depth increases proportionately with pier width and is independent of y. Conversely, for shallow flows compared to the pier width, the scour depth increases proportionately with y and is independent of b, while for intermediate depth flows, d_s depends on both y and b. These trends are shown schematically in Figure 6-1.

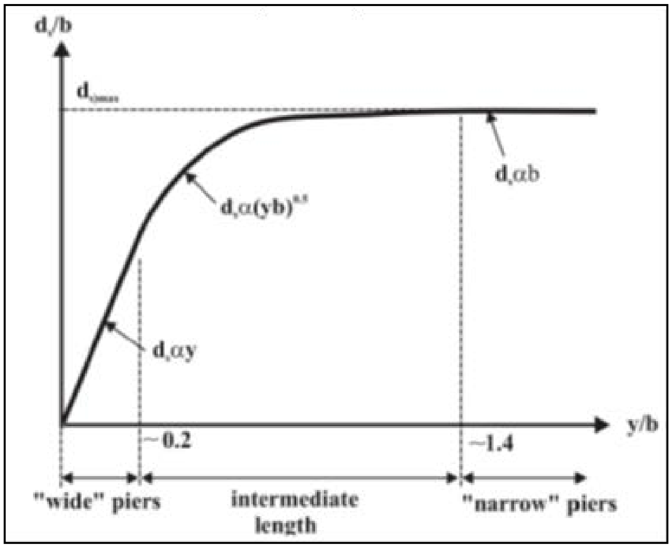

Figure 6-1: Local scour depth variation with flow shallowness in steady flow (Melville 2008)

In deeper flows, the strength of the horseshoe vortex and associated down-flow is related to the transverse size of the pier. Thus, the scour depth is dependent on the pier width. For intermediate size piers (or intermediate flow depths), flow depth influences local scour depth when the horseshoe vortex is affected by the formation of the surface roller. The two vortices have opposite directions of rotation. In principle, so long as they do not interfere with each other, the local scour depth is independent of flow depth, that is, the scour occurs at a narrow pier. With decreasing flow depth, the surface roller becomes more dominant and renders the base vortices less capable of entraining sediment. Thus, the local scour depth is reduced for shallower flows. Melville (2008) reported that this trend has been shown in the laboratory data of many researchers, including: Chabert and Engeldinger (1956), Laursen and Toch (1956), Laursen (1963), Hancu (1971), Bonasoundas (1973), Basak (1975), Breusers et al. (1977), Jain and Fischer (1979), Ettema (1980), Chee (1982), Chiew (1984), and Raudkivi (1986).

6.2 Research objectives

This study attempts to present the effect of structure size on the flow field and resulting scour depth. In this experimental program, the bore is generated using a rapid release of water impounded in a reservoir, which generates a dam-break flow. A video-analysis system was used to record the temporal and spatial evolution of the scour around the structure. The effect of structure size on the run up depth, scour profile, final scour topography

6.3 Experimental setup

The hydrodynamic boundary conditions for these experiments were simulated using a dam-break method in a flume located in the Hydraulics Laboratory at the University of Ottawa (Canada). The flume is 30 m long, 1.5 m wide and 0.8 m deep. The dam-break wave was generated by releasing water impounded behind a rapidly-opening swinging gate that was equipped with a lock and release mechanism. The sediment bed section was 3.30 m long and 1.5 m wide, starting at 4.15 m downstream of the gate, and delimited at each end by false floors, as shown in Figure 6-2.

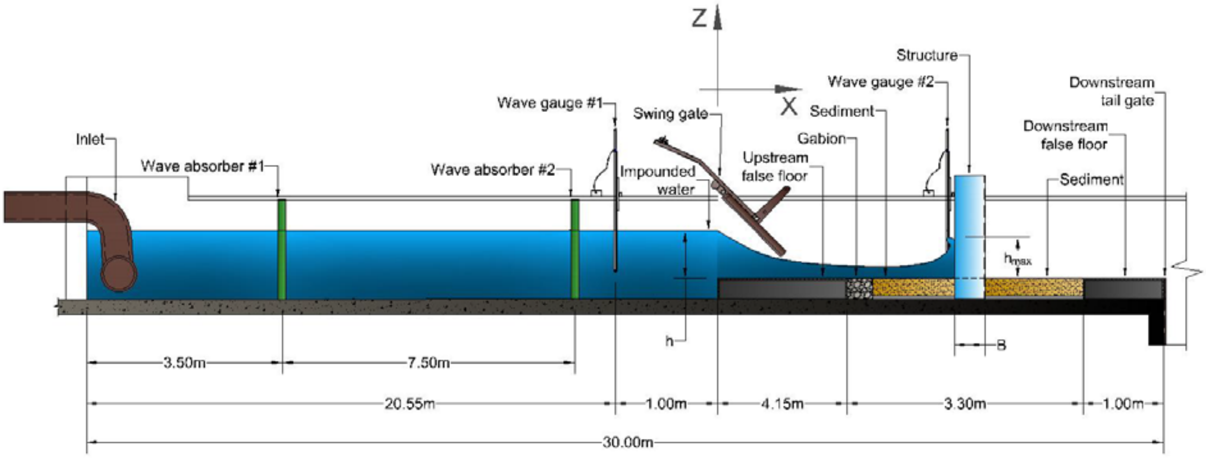

Figure 6-2: Experiment setup, side view, (not to scale)

Two aluminum false floors with a height of 0.2 m were installed before and after the sediment bed downstream of the swinging gate in order to ensure the formation of the fully developed dam break wave prior to its propagation over the sediment section. The upstream and downstream false floors had lengths of 4.15 m and 1 m, respectively. The upstream false floor was covered with a layer of glued sand with a uniform grain size of 1 mm in order to provide surface roughness, thus limiting the influence of the transition between the fixed and moveable beds.

The base of the sediment bed was composed of a layer of 1 cm thick coarse gravel covered by a geotextile sheet. The base layer drained water that infiltrated from below the false floor in order to prevent the water from influencing the level of saturation of the sediment bed. Directly downstream of the false floor, a 0.15 m-wide gabion was installed across the width of the flume. The gabion was constructed of a wire box filled with coarse gravel and was approximately 0.3 m thick. The gabion was used to minimize the inevitable local scour that would have occurred at the interface of the false floor and sediment section. Coarse sand was used, with a uniform grain size diameter of 0.001 m. Two wave absorbers were installed at the upstream end of the reservoir in order to attenuate secondary waves and prevent reflective wave-induced water level fluctuations in the test section.

WG-50 capacitance-type wave gauge manufactured by RBR Ltd, with an accuracy of 0.4% and time response of 2 ms, were used to record the time-history of the water surface elevation at different locations, in the reservoir and flume, using a sampling rate of 30 Hz. Two video cameras, a GoPro HeroTM Black (1920 x 1440 at 60 fps) and an IO Industrial

133 Flare™ high-speed video camera (2048 x 1088 at 60 fps), were used during the experimental investigations to record the flow field around the structure and the evolution of the scour. Three square structures built of Plexiglas with different cross-sections were used in the experiments. For each test, one of the structures was installed in the center of the sediment section. The square structures were transparent to allow for monitoring the scour process by means of the high-speed camera, which was placed at the top of the structure. Monitoring of the scour was achieved with the help of a mirror inclined at 45° inside the structure, as shown in Figure 6-3a and b. For this purpose, measuring scales were glued to the front, side, and back of the structure. In this way, scour depth with time could be obtained with an accuracy of ±0.005 m.

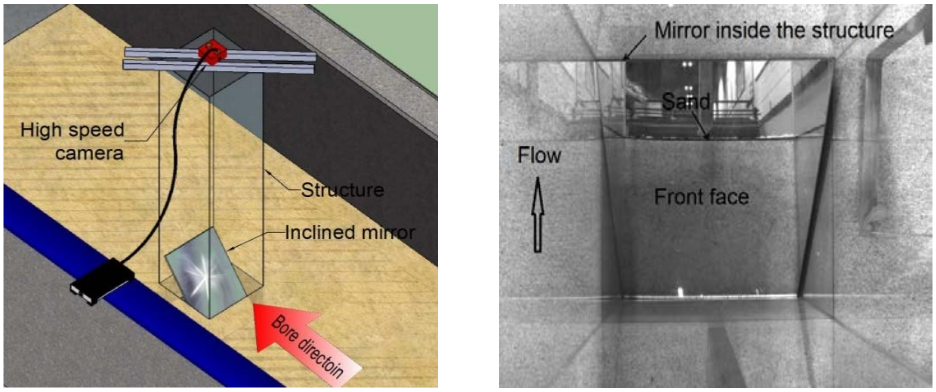

a) b)

Figure 6-3: (a) Experimental setup to monitor the scour process; (b) Reflected (looking from above-mirror inside) view of the structure's front face

Finally, a Disto TM laser altimeter with a precision of ± 1.00 mm was used to measure the final local scoured bathymetry around the structure at the end of each test, following the draining of all water.

In order to study the effect of variation in structure size (B) on maximum scour depth (d_s), nine tests were conducted using three different square structures of 0.1 m, 0.2 m and 0.3 m (Figure 6-4) and three different upstream initial water depths (h) of 0.25 m, 0.2 m and 0.15 m. For B = 0.1 m, the inclined mirror was very small to cover the whole depth. Therefore, the GoPro was placed inside the structure. The scour hole and the deepest point of scour depth at any time were easily identified and recorded by placing the GoPro at different heights from the base. The scour depth with elapsed time was obtained by reading the corresponding measurement on the scale. The main description of the experimental tests (B and h), hydrodynamic parameters (bore velocity and Froude number) and key results such as maximum scour depth (d_s), equilibrium scour depth (d_{se}), run up depth (H_{max}) and the times at which the maximum scour occurred (t_{max}) are presented in Table 6-1. Key results will be discussed later in the results and discussion section. Each test was repeated at least three times, and the average results are presented here.

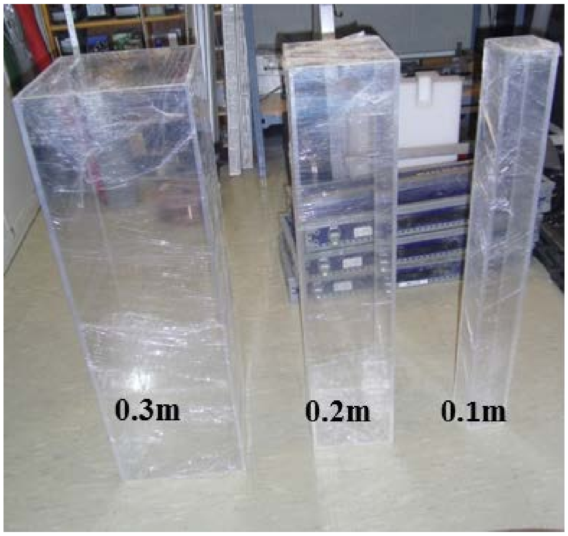

Figure 6-4: Three different square structure sizes

Table 6-1: Experimental test program

Test #	Test 1	Test 2	Test 3	Test 4	Test 5	Test 6	Test 7	Test 8	Test 9
***B* (m)**	0.3	0.2	0.1	0.3	0.2	0.1	0.3	0.2	0.1
***h* (m)**	0.25	0.25	0.25	0.2	0.2	0.2	0.15	0.15	0.15
Bore velocity (m/s)	1.58	1.44	1.10	1.58	1.44	1.10	1.58	1.44	1.10
Froude number	1.45	1.45	1.45	1.38	1.38	1.38	1.31	1.31	1.31
t_{max} (s)	11	12.24	7	11.76	14.33	9	13	16.3	10
d_s (m)	0.170	0.160	0.130	0.1275	0.125	0.115	0.085	0.087	0.085
d_{se}(m)	0.125	0.107	0.107	0.110	0.107	-110	0.675	0.775	0.675
H_{max} (m)	0.173	0.166	0.136	0.145	0.120	0.105	0.090	0.083	0.073

6.4 Results

6.4.1 Distribution of flow field around the structure

From the camera placed above the structure, images were captured to study the flow field around the structure. The images show the flow moving from left to right. Figure 6-5 compares the bore evolution around the column at several key moments for Test 2 and Test 3. It should be mentioned that the time origin considered in this paper corresponds to the initial impact of the bore with the structure. As the bore reaches the structure, the flow moves vertically over the front face of the structure and forms a so-called run-up flow. The run-up flows over the front face of each structure at t = 0.28 sec are given in the left column of Figure 6-5. The run-up flow collapses back onto the water surface, causing an area of very high turbulence with significant fluctuations called a surface roller, as shown in the middle column of Figure 6-5. Moreover, the bore splits along the sides of the structure into two streams. The separated bores reattach and develop on the lee side of the structure and produce a so-called wake vortex. The formation of the wake originating at the centerline of the structure is also shown in the middle column of Figure 6-5. In addition, full development of the wake region is given in the right column of Figure 6-5.

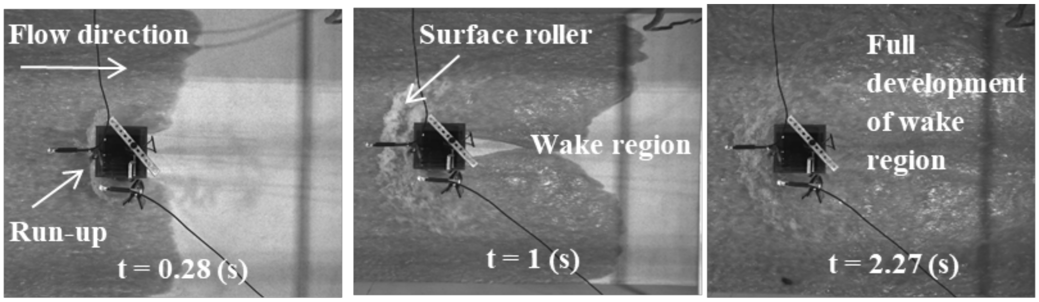

a) Test 2 (B = 0.2 m, h = 0.25 m)

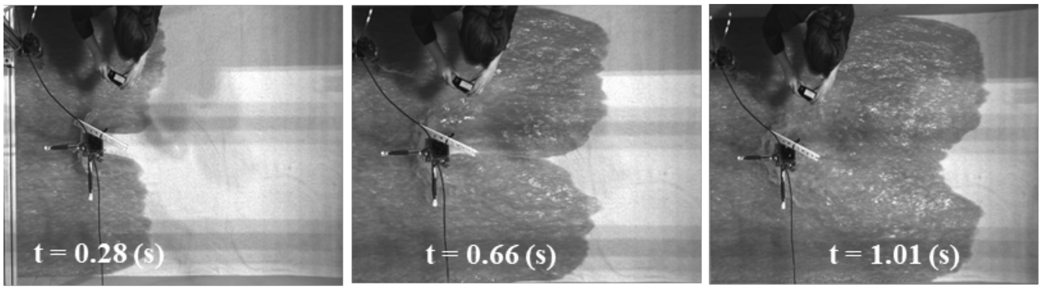

b) Test 3 (B = 0.1 m, h = 0.25 m)

Figure 6-5: flow field around structures, (left column: flow direction from left to right, run up over the front face), (middle and right columns: surface roller and wake development region) for a) Test 2 (B = 0.2 m, h = 0.25 m) and b) Test 3 (B = 0.1 m, h = 0.25 m)

The separated bores in the wake of B = 0.2 m merged at t = 1 sec, while for B = 0.1 m it occurred at t = 0.66 sec. The duration recorded for the separated bores to completely fill up the wake region was 2.27 sec and 1.01 sec for B = 0.2 m and B = 0.1 m, respectively. It can be concluded that the early stage of the wake development and full development of the wake region occurred sooner for the smaller structure size than for the larger structure. As displayed in the middle column of Figure 6-5, the separated bore merged at a closer distance to the structure for the smaller structure, and that the width of the surface roller is approximately equal to the structure size.

6.4.2 Run-up depth and scour depth time history

Figure 6-6 a and b respectively show the bore depths measured by the WGs installed at the front and side of the structure. Green, orange and purple lines represent the time history of the bore depths for B = 0. 3 m (Test 1), B = 0.2 m (Test 2) and B = 0.1 m (Test 3), respectively It is clear from the figure that the height of the splash following the initial impact is substantially influenced by the structure width. The splash reaches the highest elevation for the cases of a wider structure. A consistent reduction in splash height is observed as the structure size is decreased. Between B = 0.2 m and B = 0.1 m, a reduction of over 20% in peak splash height is observed. However, the difference between the run-up depths of B = 0.3 m and B = 0.2 m is only 1.73%. The increase in splash height was attributed to a greater volume of water being pushed onto the structure.

Moreover, comparing bore depth on the side of the structure, structure size appears to have no influence on bore depth. The maximum run-up depths on B = 0.3 m, B = 0.2 m and B = 0.1 m were 0.173 m, 0.170 m and 0.136 m, respectively, whereas the maximum bore depth on the side face for B = 0.3 m, B = 0.2 m and B = 0.1 m were 0.113 m, 0.106 m and 0.107 m, respectively. It is clear that the magnitude of the bore depth on the side face is less than the magnitude of the bore depth on the upstream face of the structure.

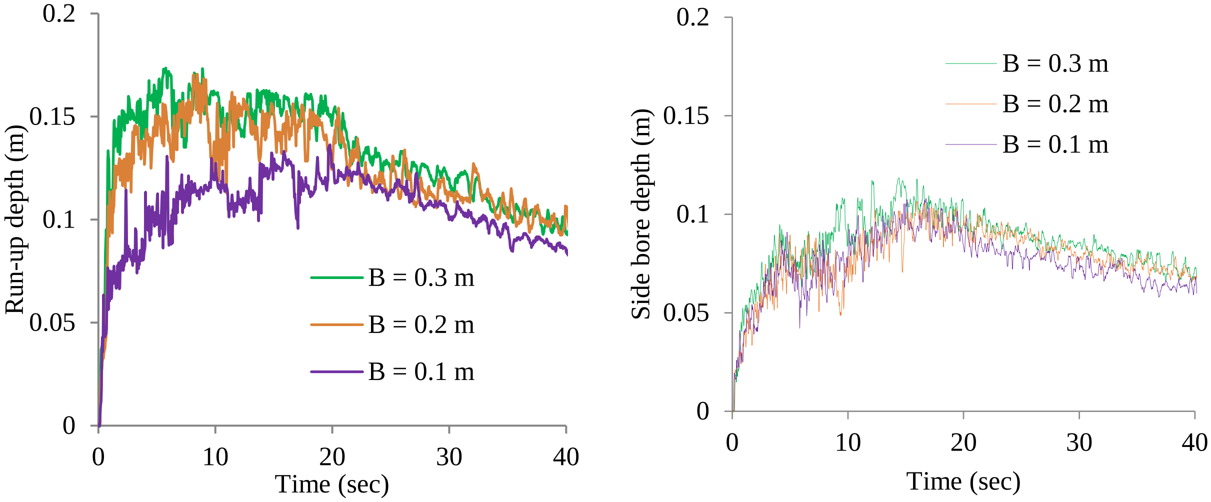

a) Bore depth at the front face (run-up)

b) Bore depth at the side face

Figure 6-6: Bore depth measured for Test 1 (B = 0.3 m, h = 0.25 m), Test 2 (B = 0.2 m, h = 0.25 m) and Test 3 (B = 0.1 m, h = 0.25 m) at a) the front face and b) the side face

6.4.3 Scour depth

Figure 6-7 compares scour development around three sizes of structure induced by 0.25 m upstream water depth (Test 1, Test 2 and Test 3). Purple, orange and green lines represent time history of scour depth for B = 0.1 m, B = 0.2 m and B = 0.3 m, respectively. The measurement shows the scour depth at the front corner of the structure where the maximum magnitude of scour depth occurred. It can be seen that for the same approach flow, the greatest scour occurred around the widest structure (B = 0.3m). The scour rate is almost constant for all three sizes of structure. The maximum magnitudes of the scour depth were 0.13 m, 0.16 m and 0.17 m, which occurred at t = 7 sec, 12.66 sec and 11 sec for B= 0.1 m, 0.2 m and 0.3 m, respectively. Equilibrium scour depth is defined as when the rate of sediment supply to the scour hole is equal to the rate of removal. For B = 0.1 m, the maximum and equilibrium scour depth developed earlier than in the two other cases. This is likely because the bore propagated and developed all along the smaller structure earlier than the two other wider structures, as was shown in Figure 6-5

Also, it can be see that for the smallest structure, the difference between the maximum scour depth and equilibrium scour depth is very small (0.0225 m), whereas for B = 0.2 m and B = 0.3 m, the difference was 0.050 m and 0.045, respectively.

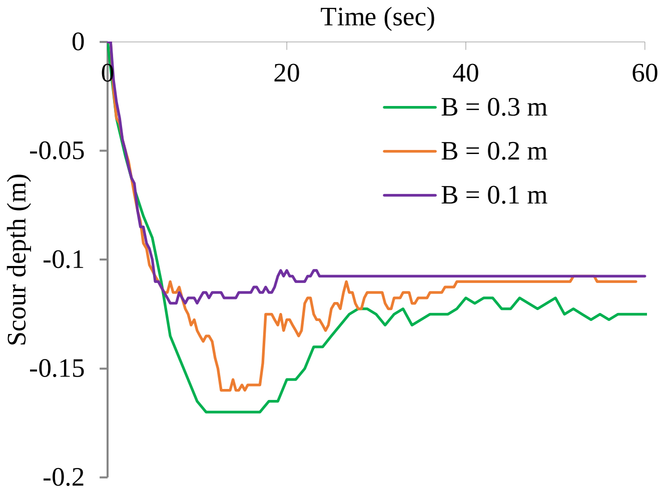

Figure 6-7: Scour development around the upstream corners of the structures for Test 1 (B = 0.3 m, h = 0.25 m), Test 2 (B = 0.2 m, h = 0.25 m) and Test 3 (B = 0.1 m, h = 0.25 m)

6.4.4 Scour profile

shows the final scour profile of the three structures for Test1, Test 2 and Test 3 indicated by dash lines. As it was impossible to capture the scour profile via a mirror from inside the smallest structure (B = 0.1 m), the scour profile was taken from outside of the structure.

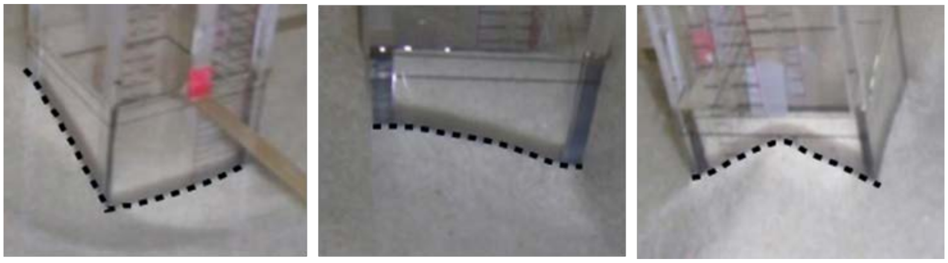

Test 3 (B = 0.1 m, h = 0.25 m)

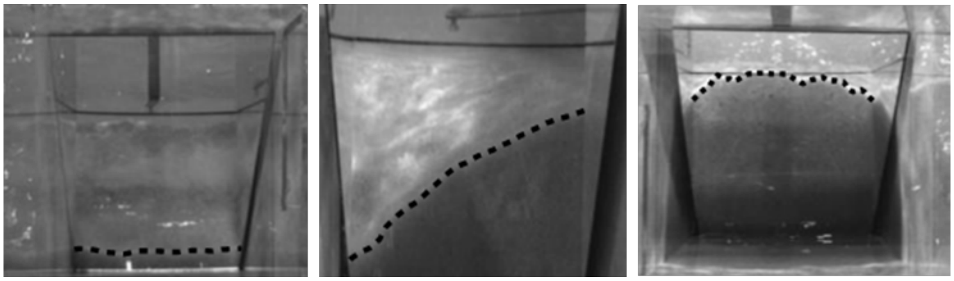

Test 2 (B = 0.2 m, h = 0.25 m)

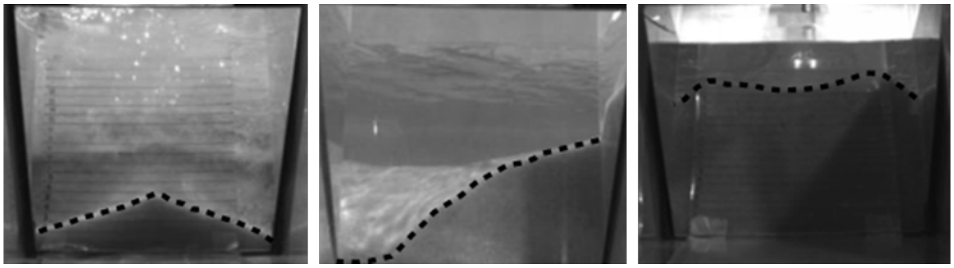

Test 1 (B = 0.3 m, h = 0.25 m)

Front face **Side face** **Back face**

Figure 6-8: Final scour profile indicated by dash lines for Test 1 (B = 0.3 m, h = 0.25 m), Test 2 (B = 0.2 m, h = 0.25 m) and Test 3 (B = 0.1 m, h = 0.25 m), left columns: front face, middle columns: side face and right columns: back face

Comparing the front-face scour profile from the images in the left column, the scour profile at the front of the structure is a straight line for both B = 0.1 m and B = 0.2 m. However, a triangle-shaped profile was observed for B = 0.3 m at the front face. The scour process at the front face of the wide structure features a slow-moving flow zone on the line of symmetry. In this region, scour activity is decreased and the central part of the width of the structure was not scoured to the same degree as the corner. The middle column in shows the side-face scour profiles. All three sizes of structure have a greater scour depth at the offshore corner. Also, the slope of the side scour profile for B = 0.3 m and 0.2 m is greater than that of B = 0.1 m. The right column in shows the scour profile at the back of each structure. The maximum scour depths measured at the back corner of B = 0.1 m, 0.2 m and 0.3 m are 0.040 m, 0.025 m and 0.025 m, respectively. As was mentioned previously, for the case of the smallest structure, the wake region formed faster, and closer to the structure. Also, the zone of wake development for the case of the smallest structure completed prior to the completion of the wake region behind the wider structures. This could explain the greater scour depth at the back of smallest structure. Ettema et al. (2006), by using the time-average structure of the wake vortices revealed from plots of instantaneous vorticity using LSPIV measurements taken immediately behind two cylinders in a steady flow, found that that the maximum vorticity of the wake flow behind the smaller cylinder was about twice that for the larger cylinder. The greater scour depth at the back of the smallest structure corroborates Ettema's (2006) results. This finding indicates that, for the same approach flow, the smaller structure is more likely to have sediment removal at the back compared to the larger structure because it produces stronger eddies.

6.4.5 Final scour topography

The final elevations of the scoured sediment bed were measured using a laser altimeter. The measurements were then referenced to the average elevation of the false floor on either side of the sediment bed. Point measurements were taken over the entire sediment bed surface, and due to the sudden changes in sediment bed elevation such as at the edge of the scour hole, the point measurements were taken at a grid scale of 0.05 m far from the scour hole, 0.02 m close to the scour hole and 0.01 m over the scour hole. The point measurements were interpolated over the sediment bed area using Surfer 11 in order to provide a better visualization of the final scour depths, magnitudes and locations. The interpolation method used was inverse distances weighted. a, b and c show the final scour plots for Test 1, Test 2 and Test 3 with the corresponding images of the final scour holes. The structure is shown as a black object, and since the scour hole is symmetrical around the center of the structure, only one side of the final sediment bed was measured. The positive and negative values on the scale represent deposition and erosion, respectively. As shown in the plots, the final local scour shape formed by the hydraulic bore was for the most part elliptical.

The maximum final scour was located at the upstream corner of the structure, and the scour depth then decreased linearly towards the back face. The onshore side of the structure was not scoured to the same degree as the offshore side. There was also an area of deposition at the back of the structure. The wake vortices weakened in intensity as they moved in the downstream direction. As a result, sediment particles dropped back to the bed and caused the formation of a dune-like mound on the lee side of the structures.

From the final scour topography, it can be seen that as the structure size decreases, the scour hole decreases in size and depth. The boundary shape of the scour hole around the smallest structure (B = 0.1 m) was circular, as is shown in the right column of c. For the wider structure (B = 0.3 m, c), the scour hole pattern become flatter and the scour hole splits into two symmetrical elliptical shapes. For the larger structure, an area of local scour extending from the side of the structure to the walls of the flume was also observed. This may have occurred due to the strong surface roller propagating upstream caused by the structural obstruction. Also, for the smaller structure, as the scour hole was smaller and less suspended sediment moved downstream, a lower downstream deposition height was observed. Furthermore, scour occurred behind the smallest structure compared to the lee sides of the two wider structures. Consequently, the zone of deposition was displaced downstream of the smallest structure, but as the structure size increased the deposition began immediately after the structure, and for the largest structure deposition occurred along the side wall.

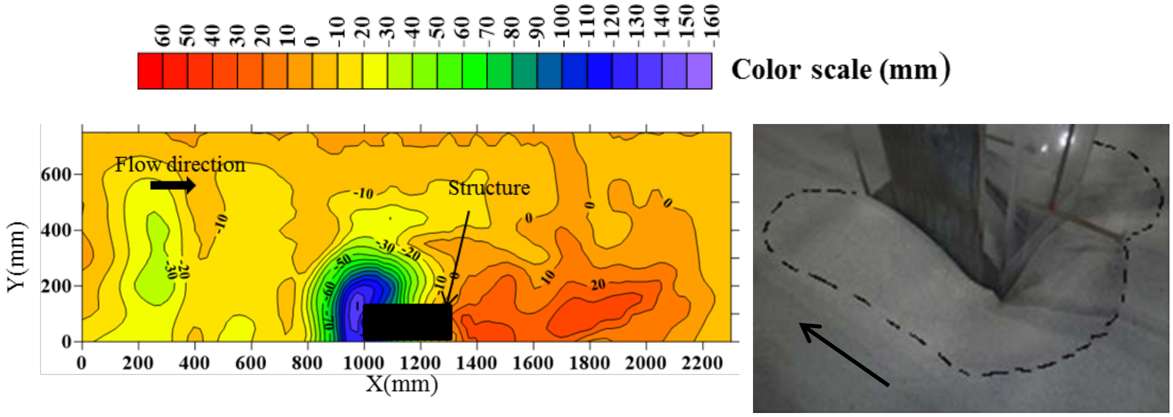

a) Test 1 (B = 0.3 m, h = 0.25 m)

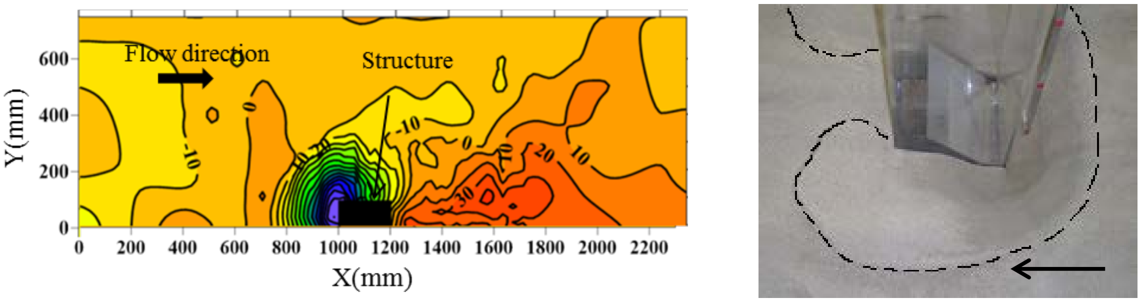

b) Test 2 (B = 0.2 m, h = 0.25 m)

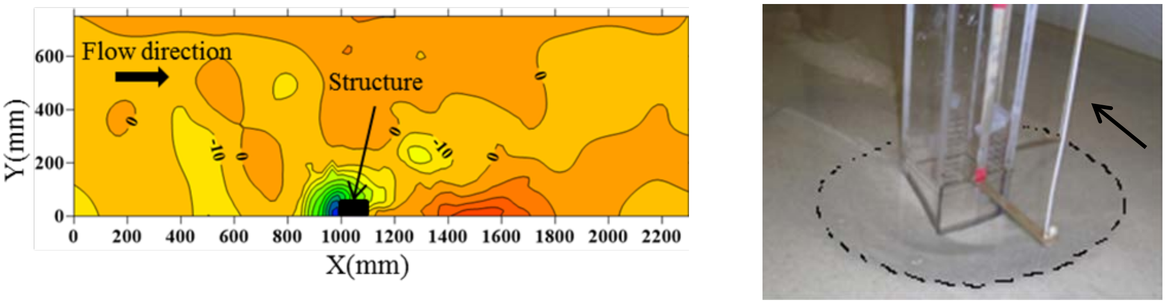

c) Test 3 (B = 0.1 m, h = 0.25 m)

Figure 6-9: left: final scour topography with black squares and arrows from left to right showing structures and flow direction, right: images of the final scour holes with arrows and dash lines showing flow direction and boundary of the final scour hole for a)Test 1 (B = 0.3 m, h = 0.25 m), b)Test 2 (B = 0.2 m, h = 0.25 m) and c) Test 3 (B = 0.1 m, h = 0.25 m)

6.4.6 Scour evolution around the structure

Figure 6-10a, b, c and d compares the scour depth time histories at different locations on the structure. The green, blue, orange and gray lines represent the scour depth time histories at the locations labeled as A, B, C and D, respectively, as shown in Figure 6-10a. Lines A and B are located in the middle and corner of the front face and lines C and D are located in the corner and middle of the side face. In this section, the comparison of different paths will be discussed in terms of maximum and minimum scour depth locations, the times at which scour began, and the times at which maximum scour depth occurred.

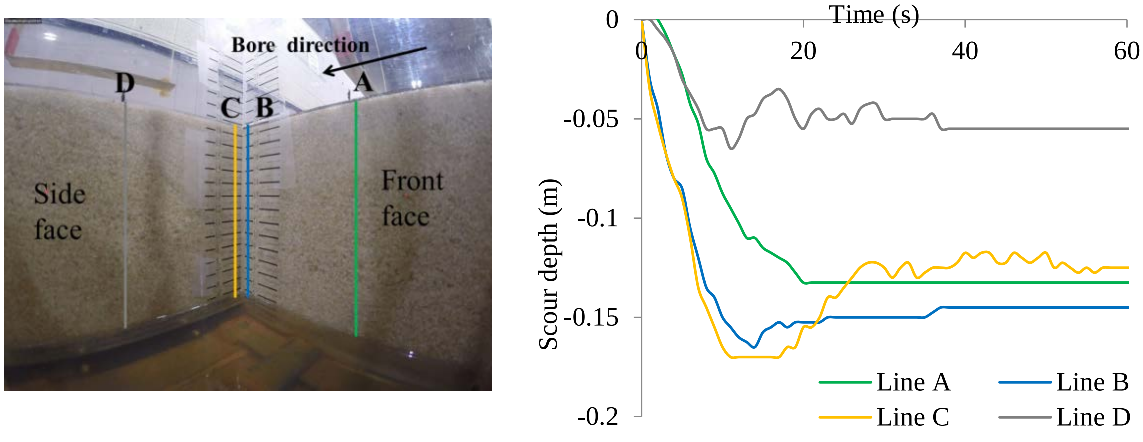

a) scour depth lines location

b) Test 1 (B = 0.3 m, h = 0.25 m)

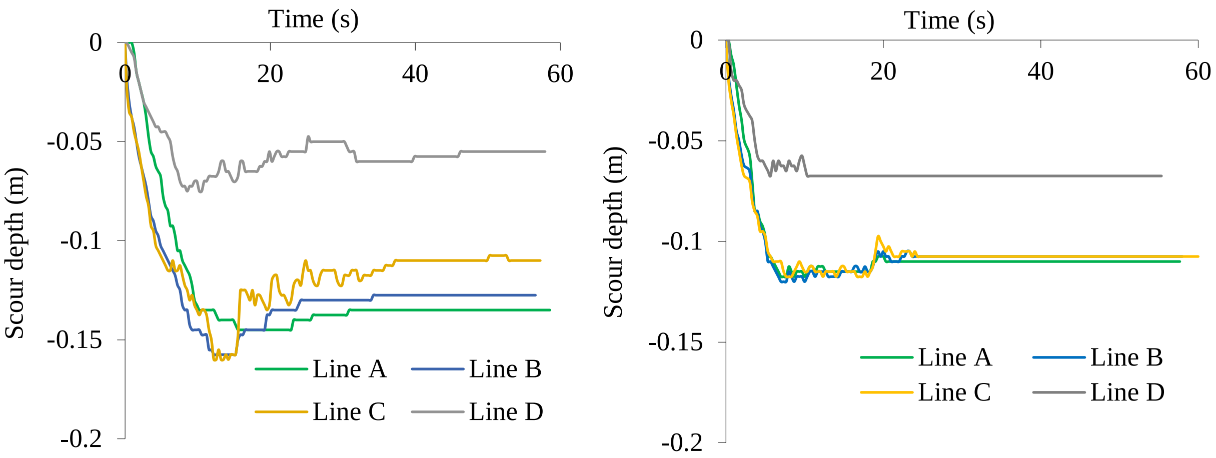

c) Test 2 (B = 0.2 m, h = 0.25 m)

d) Test 3 (B = 0.1 m, h = 0.25 m)

Figure 6-10: Scour evolution around the structures for b) Test 1 (B = 0.3 m, h = 0.25 m), c) Test 2 (B = 0.2 m, h = 0.25 m) and d) Test 3 (B = 0.1 m, h = 0.25 m). The different locations around each structure are shown in a.

For the two wider structures, B = 0.3 m and B = 0.2 m, the maximum scour depth occurred at the corner on the side face (Line C). As shown in Figure 6-10d, for B = 0.1 m, Lines A, B and C were all scoured at the same pace and had the same magnitude of scour depth. In all cases minimum scour depth was observed at the middle of the side face (Line D). Maximum scour depths at Line D were 0.065 m, 0.075 m and 0.068 m, and at Line C were 0.170 m, 0.160 m and 0.120 m for B = 0.3 m, B = 0.2 m and B = 0.1 m, respectively. The maximum scour depth at Line C decreased as the structure size decreased. However, the maximum scour depth at Line D was similar for all structure sizes. The stronger wake vortex for the smaller structure size could be the reason for the greater scour depth at Line D for the smaller structure.

As the structure size increased, the difference between the maximum scour depth at the front middle of the structure (Line A) versus at the front corner (Lines B and C) increased. As was mentioned previously, because of the slow-moving flow at the head of the wide structure (Line A), the central part of the structure was not scoured to the same degree as the corners. Also, as the structure size increased, the scour depth at Lines A and D started later than the scour at the corner (Lines B and C). Moreover, comparing the times for maximum scour depth occurrence, it can be seen that more time is needed to develop a scour hole for a wider structure.

Finally, it can be seen that for the all structures, the greatest difference between the maximum scour depth and final scour depth occurred at Line C. In other words, the scour hole had greater propensity for subsequent filling at the side corner than other locations. However, for the smallest structure the scour hole underwent less subsequent filling.

6.4.7 Structure width effect on scour depth and bore depth

The results of the run-up depth and scour depth for all 9 conducted tests are shown in Figure 6-11a and b. The graphs show the effect of structure size on scour depth and run-up depth as the upstream water impoundment depth is increased. As shown in Figure 6-11a, as the upstream water depth increased, the run-up depth also increased. For h = 0.15 m, the run-up depths were similar for all three structure sizes. However, the rate of increase in run-up depth with impoundment depth was greater for wider than narrower structures.

Furthermore, as is shown in Figure 6-11b for the tests conducted with h = 0.15 m, the scour depth did not change appreciably with an increase in structure size. As the reservoir impoundment depth increased, the scour depth increased, and the rate of increase in scour depth for B = 0.3 m and B = 0.2 m was greater than for B = 0.1 m. This suggests the effect of structure size on scour depth is more evident for higher energy flows generated with greater reservoir depths. The trend that was defined by Melville (2008) in steady flow as shown in Figure 6-1 might not applicable for these cases; however, it would be the same behavior for transient unsteady flow. For the case of h = 0.15

m, the three tests are probably in the range of wide piers category. As shown in Figure 6-1, for wide piers the scour depth depends more on the flow depth. Since the run-up depths resulting from *h* = 0.15 m over three size of structures have similar values, the generated scour depths are comparable. As *h* is increased, the range moves towards the intermediate level, where both the structure size and flow depth are effective. The results show similar trends and magnitudes for *B* = 0.2 m and *B* = 0.3 m. Comparing the maximum run-up depth resulting from *h* = 0.25 m as given in Figure 6-6a and Figure 6-11a, there is a noticeable difference between the run-up depths of *B* = 0.2 m and *B* = 0.1 m, which leads to the greater difference in their scour depths. But the difference between the run-up depth of *B* = 0.2 m and *B* = 0.3 m is small, which results in the closer values of the scour depths.

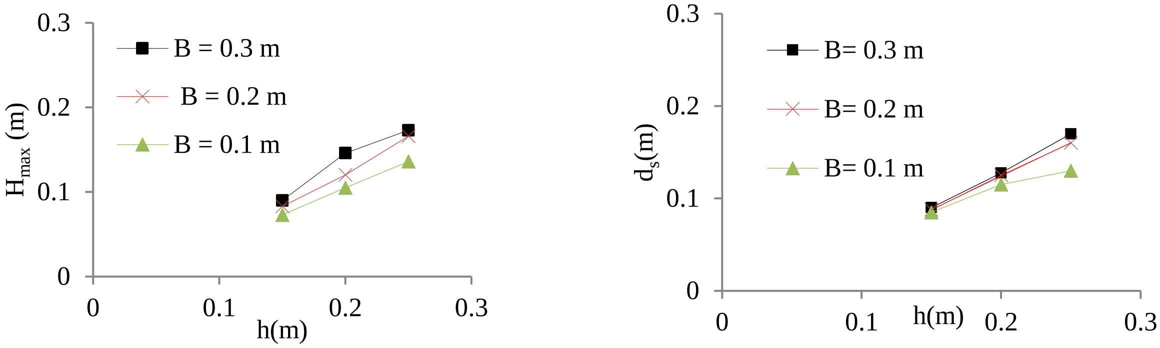

a) structure width effect on run-up depth

b) structure width effect on scour depth

Figure 6-11: Structure width effect on a) run-up depth and b) scour depth

In order to isolate the effects of different variables without the influence of structure diameter, non-dimensional bore height (H_{max}/B) is compared with non-dimensional reservoir water depth (h/B). Figure 6-12a demonstrates a positive linear relationship between the normalized maximum bore depths and the normalized reservoir water depths.

As was mentioned previously, structure size imposes influences in terms of flow shallowness. Flow shallowness represents the effects of depth of flow (H_{max}) in relation to structure width (*B*). In order to better investigate the effect of structure size and also to compare the obtained results with those of Melville (2008) in Figure 6-1, d_s /*B* is compared with H_{max}/B. Figure 6-12b demonstrates the relationship between bore depth, scour depth and structure size. In the current experiments H_{max}/B varied between 0.38 to 1.36. It can be seen that as the H_{max} / *B* increased, the ratio of d_s/B increased, with the consequence that d_s/B was greatest for the smallest structure. The linear positive trend shown in Figure 6-12b compares well with the wide pier linear portion of Figure 6-12 obtained by Melville (2008).

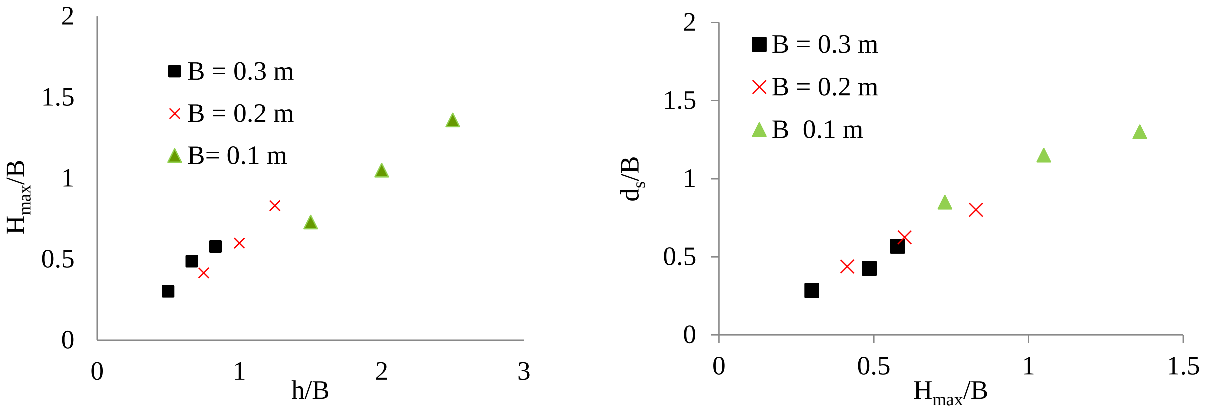

a) b)

Figure 6-12: a) h/ B variation with H_{max}/B, b) local scour depth variation with flow shallowness

6.5 Discussion

FEMA P646 (2012) used the scour depth ratios proposed by Dames and Moore (1980). The ratio of scour depth divided by flow depth is given for structures located close to or far from a shoreline with different soil types. The value for loose sand suggested By Dames and Moore (1980) is 60%. The ratios obtained in the current study were 80%, 72% and 45% for B = 0.3 m, B = 0.2 m and B = 0.1 m, respectively. The experimental results clearly show that these ratios depend on the structure size. However, the average value of these ratios is 65%, which is close to the value proposed by Dames and Moore (1980).

Figure 6-13 compare temporal development of scour depth for Test 1, Test 2 and Test 3 with the empirical equation of Gumgum and Guney (2019) for live-bed scour under flood waves. t_e is the time at which equilibrium scour depth occurred.

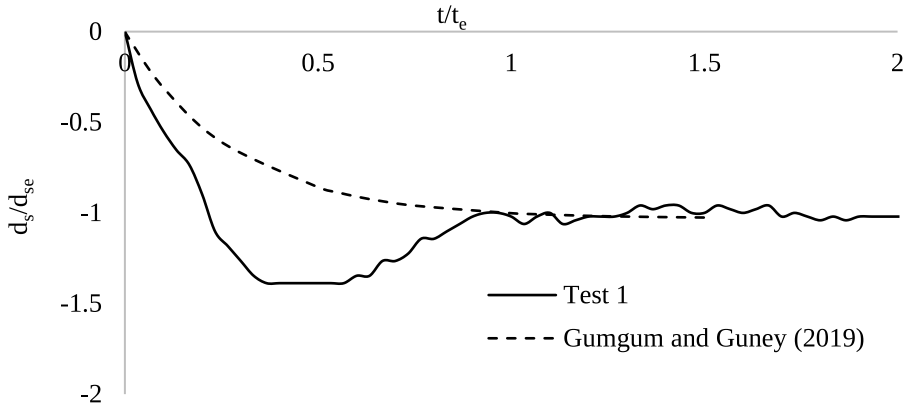

a) Test 1

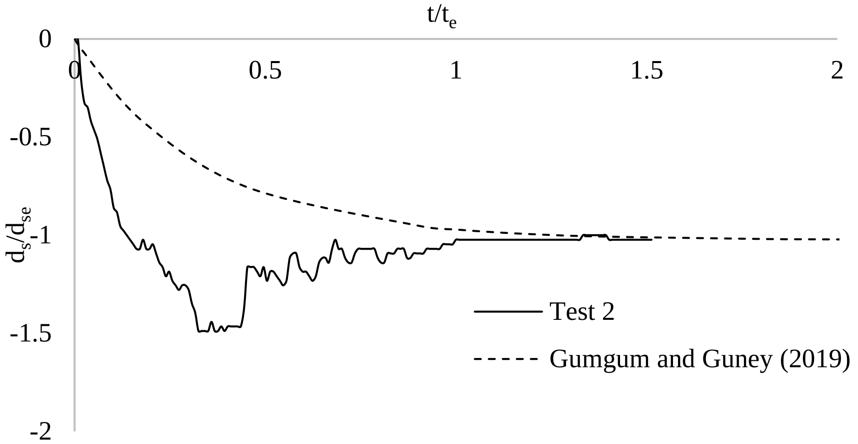

b) Test 2

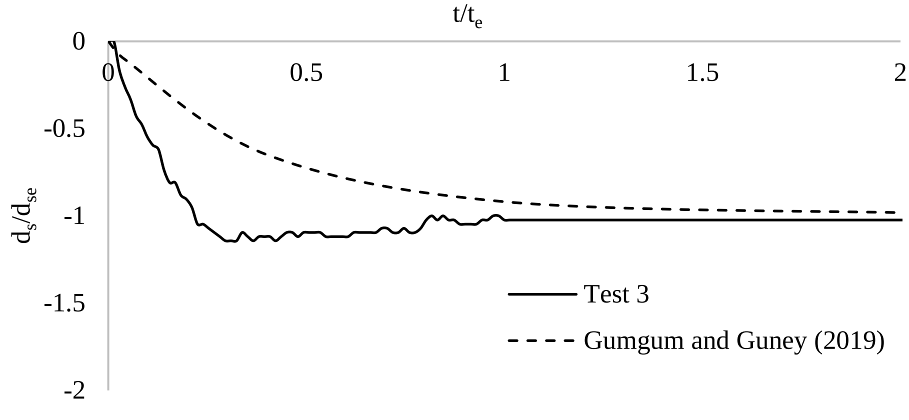

c) Test 3

Figure 6-13:comparison of temporal development of scour depth for Test 1, Test 2, Test 3 with the empirical equation of Gumgum and Guney (2019) for live-bed scour under flood waves

It can be seen that the scour rate is initially more rapid for tsunami scour compared to flood waves scour and reaches to the maximum scour more quickly than the flood wave time history equation. Also, deposition process starts much more quickly than the flood wave time history equation. This shows that in tsunami scour the short duration and very turbulent nature of the bores induced a rapid scouring process which is faster and higher than the flood wave scour. However, it can be seen that the equilibrium scour depth from the experimental tests equals the calculated scour depth from the equation. Previous studies on steady current concluded that maximum scour around square structure occurred at the front corner of structures, (Dey and Raikar, 2007), (Lončar et al. 2018) and (Du and Liang, 2019). However, in this study the central part of scour profile at the front face of 0.2 m and 0.1 m structures was scoured to the same degree as the corner. Comparing t_{max} for the three sizes of structure as shown in , it can be seen that proportionately more time is needed to develop the scour hole for a wider structure. For h = 0.25 m, time required to reach the maximum scour depth is 11(s), 12.24(s) and 7(s) for B = 0.3 m, B = 0.2 m and B = 0.1 m, respectively. Interestingly, it can be seen that t_{max} was greater for B = 0.2 m than for B = 0.3 m. Also, as shown in Figure 6-10b and c, greater scour depth was measured at line A for B = 0.2 m compared to that of B= 0.3m. All these may be related to the interference and merging of the vortices generated at the two front corners of the smaller B = 0.2 m structure, which produced stronger vortex that last longer than the individual separated vortices at the two front corners of the B = 0.3 m structure. Scour starts at the corners remains deepest at the corners, while scour at the centre middle of the front face depends upon the scale of the structure and amount of time available for the corner scour holes to expand and merge at the centre as they approach the equilibrium scour depth.

.

6.6 Conclusion

This experimental research was directed at investigating the effect of structure size on tsunami-like bore-induced local scour around square structures. The hydraulic bores were generated based on the similarity between dam-break waves and tsunami-induced bores on relatively flat coastal plains (Chanson 2006). Based on analysis of the recorded data, the authors have drawn the following conclusions.

A consistent reduction in splash height is observed as the structure size decreased. A greater volume of water being pushed onto the wider structure resulted in a higher elevation of splash height for that case. However, structure size appears to have no influence on bore depth at the side face.

It was found that the scour process and how the final sediment bed topography is shaped are influenced by the formation of the wake region. Early-stage and full development of the wake region around the smallest structure initiated earlier than around the wider structures. Since the smallest structure produces stronger eddies, it has more capacity to remove sediment at the back compared to the large structures.

A strong surface roller propagating upstream of the widest structure caused an area of local scour extending from the side of the structure to the walls of the flume. As the structure size decreases, the size of the scour hole decreases in size and depth. Also, as the structure size decreased, the scour hole became more dominant at the back of the structure.

The scour hole shape depends on the width of the structure. The scour hole boundary for the smaller structure is closer to a circular shape, while it become flatter for the wider structures. The scour hole was split into two symmetrical elliptical shapes for the largest structure.

For the same approach flow, the scour rate is almost constant for all three sizes of structure. As the initial reservoir depth increased, the scour depth increased. However, the rate of increase in scour depth was greater for the wider structures than for the smaller one.

The ratio of scour depth divided by flow depth depends on the structure size. However, the average value of these ratios is 65%, which is close to the value proposed by Dames and Moore (1980).

It was found that the scour rate is initially more rapid for tsunami scour compared to flood waves scour and reaches to the maximum scour more quickly than the flood wave time history equation and deposition process starts much more quickly than the flood wave time history equation.

In tsunami scour the short duration and very turbulent nature of the bores induced a rapid scouring process which is faster and higher than the flood wave scour.

For wide structure, scour starts at the corners remains deepest at the corners, while for smaller structure scour at the centre middle of the front face depends upon the scale of the structure and amount of time available for the corner scour holes to expand and merge at the centre as they approach the equilibrium scour depth.

Chapter 7. EXPERIMENTAL AND NUMERICAL MODELLING OF SCOUR AND EROSION INDUCED BY TURBULENT BORE

The article was published in the proceeding of The Canadian Society of Civil Engineering Conference (CSCE, 2020).

Abstract

This study presents new experimental and numerical results of bore-induced local scour around a square structure. A numerical model based on the three-dimensional-vertical Reynolds-averaged Navier–Stokes equations, with turbulence closure and a finite element method, was used. The hydrodynamic forcing conditions for the experimental program was due to a dam-break wave generated in a hydraulic flume located in the Hydraulics Laboratory at the University of Ottawa, Canada. This highly turbulent bore was generated by the rapid release of water impounded behind a rapidly-opening swing gate equipped with a lock and sudden release mechanism. A video system was used to record the evolution of the scour using video imaging obtained from inside of the structure model. The accuracy of the numerical model was assessed quantitatively and qualitatively by comparing its results with those obtained from the physical experiments. Comparisons made based on the scour evolution, velocity time history, final bed topography after the passage of the wave, as well as the run up due to the surface roller recorded at the front of structure. The computed surface roller run up elevation is accurately reproduced, especially for the wet bed condition. The location of maximum scour depth and sediment deposition pattern downstream of the structure are well captured by the numerical model, however; magnitude of scour depth is underpredicted by 50%.

7.1 Introduction

Post-tsunami reconnaissance missions have revealed that some structures previously understood to be invulnerable to tsunamis were heavily damaged or even destroyed during the events (Nistor et al., 2005; Ghobarah et al., 2006; Yeh et al., 2013). The field survey evidence indicates that destructive tsunamis cause substantial coastal sediment mobilization. Measurements collected following several tsunami events, such as the 1992 Nicaragua Tsunami, the 2004 Indian Ocean Tsunami, and the 2011 Tohoku Tsunami have provided substantial evidence of scour around damaged buildings and bridges. Tsunami-induced coastal inundation is characterized by high overland flow velocities, both during the inland flow phase as well as during the drawdown. These high flow velocities produce high bed shear stresses and large amounts of sediment movement over extensive areas, resulting in substantial beach erosion and significant scour around many of the structures located in the inundation zone.

Although most research and literature in the study of scour in supercritical flows is based on physical experimental work, some authors have combined these physical tests with simulations in numerical models. Tsunami sediment motion and scour were discussed by Yeh and Li (2008) using a hypothetical analytic solution. They demonstrated that a tsunami is capable of causing sediment motion even far offshore in both the runup and drawdown phases, and that the drawdown process is slightly stronger than the runup. They concluded that significant sediment motion in the form of bed load and suspension occur nearshore close to the maximum runup penetration. Another numerical model was developed by Nakamura et al. (2008) to simulate the scour around a square structure induced by the passing of a tsunami wave. The development of the numerical model was based on a principle introduced by Hur et al. (2007), in which two numerical sub models are coupled in order to better simulate the wave-seabed interactions. Nakamura et al. (2008) therefore decided to use a volume of fluid (VOF) sub model to simulate the wave field coupled with a finite element model (FEM) to simulate the sand foundation. In their simulation a continuity equation, modified Navier-Stokes equation and an advection equation of the VOF function were employed. The VOF model was able to compute velocity and pressure fields within the liquid flow. In conjunction with this, the wave-induced soil-water coupled FEM was used to calculate sand displacements and pore pressures within the sand bed. Although this type of coupled model had been previously used in other studies, Nakamura et al. (2008) attempted to improve the simulations of the model for the purposes of their own research. The results of the numerical model were in agreement with those of the experimental portion of the research. Nakamura et al. (2008) observed and concluded that the numerical model computed a propagation speed of the wave that was slightly higher than that experimentally measured. There was also a small phase lag between the experimental and numerical results. They also observed that in some cases, the numerical model underestimated wave runup, and in turn pore pressures, at the front of the structure. However, at other points, the excess pore water pressures were very well simulated by the numerical model for both solitary and long waves.

Fuji et al. (2009) carried out an experiment using a wide flume in order to clarify characteristic flow patterns and topography changes in harbors due to a tsunami. In their experiment, topography changes near an idealized harbor due to an isolated long wave were investigated. They also carried out numerical simulations on the tsunami induced topography changes using a vertically averaged model. Their model encountered difficulties in predicting deposition areas in the harbor. Although a significant local deposition area was observed at the center of the harbor in their experiment, a widespread deposition area was predicted by their numerical model. This inconsistency may have originated from the three-dimensional sediment transport in the deposition processes, which cannot be calculated by the vertically-averaged model. In the numerical simulation, to simultaneously calculate tsunami propagation in the long flume and the tsunami-induced sediment transport in the harbor in detail, a nested grid system with four domains of different resolutions was used. The velocity, water level and topography changes in the harbor predicted by their numerical model agreed with experimental data. The deposition at the center of the harbor could be predicted by their numerical model, although it could not be well predicted by the vertically averaged numerical model.

7.2 Research objectives

This paper aims to present physical and numerical modelling of the scour around a square structure due to an inland-propagating tsunami-like bore. The accuracy of the numerical model was assessed quantitatively and qualitatively by comparing its results with those obtained from the physical experiments. Comparisons made based on the scour evolution, final bed topography after the passage of the wave together with the run up on the structure associated with the surface roller, and scour evolution. Furthermore, this study aims to investigate the effect of grain size on local scour in both dry and wet bed conditions induced by a turbulent bore.

7.3 Laboratory experiment

The hydrodynamic boundary conditions for these experiments were simulated using a dam-break method in a flume located in the Hydraulics Laboratory at the University of Ottawa (Canada). The flume was 30 m long, 1.5 m wide and 0.8 m deep. The dam-break wave was generated by releasing water impounded behind a rapidly opening swinging gate which was equipped with a lock and release mechanism. The sediment bed section was 3.30 m long and 1.5 m wide, delimited at each end by false floors installed as shown in Figure 7-1. Two aluminum false floors with a height of 0.2 m were installed before and after the sediment bed, downstream of the gate, to provide formwork for the sediment section. A tail gate was installed at the end of the downstream false floor to be able to create a wet bed initial condition. The upstream and downstream false floors had lengths of 4.15 m and 1 m, respectively. A grid system of 20 cm x 20 cm was painted on the top surface of the upstream false floor for measurement purposes.

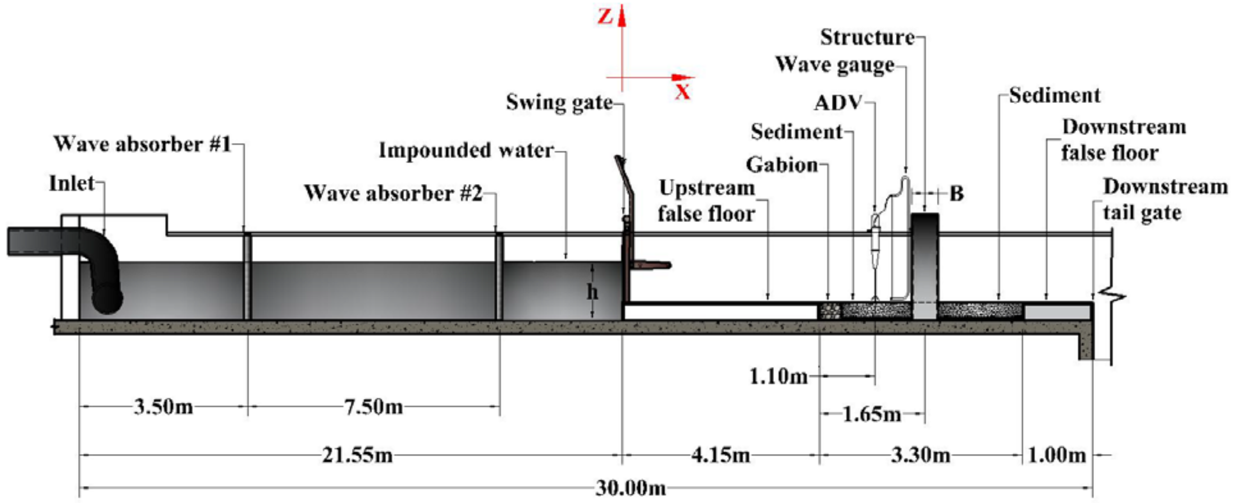

Figure 7-1: Experimental setup side view (not to scale)

The base of the sediment bed was composed of a layer of 1 cm thick coarse gravel covered by a geotextile sheet. The base layer drained water that infiltrated from below the false floor, to prevent the water from influencing the sediment bed. Directly downstream of the false floor, a 15-cm wide gabion was installed across the entire width of the flume. The gabion was constructed with a wire box filled with coarse gravel, approximately 3 cm thick. The gabion was used to minimize the inevitable local scour that would occur at the interface of false floor and sediment section. Both coarse sand and pea gravel were used, with uniform grain size diameters of 0.001 m and 0.01 cm, respectively, shown in Figure 7-2. 1mm sand is the most common size in coastal environment and gravel is being used for filling around the structure. Two wave absorbers were installed at the upstream end of the reservoir in order to attenuate secondary waves and prevent reflective waves-induced water level fluctuation at the test section.

Figure 7-2: Sediment section: Left: Sand bed, Right: Gravel bed

WG-50 capacitance type manufactured by RBR Ltd wave gauges with an accuracy of 0.4% and time response of 2 ms were used to record the time-history of the water surface elevation installed at the front of structure, using a sampling rate of 30 Hz. A 0.2 m x 0.2 m square cross section structure built of Plexiglas was installed in the center of the sediment section. The square structure was transparent to allow for monitoring the scouring process by means of, a GoPro HeroTM Black (1920 x 1440 at 60 fps) which was placed inside the structure. Experiments were performed with 0.25 m upstream water depth and two different downstream water depths of 0 m and 0.05 m. Table Table 7-1 present the summary of experimental tests. The measurements for local scour depth with time were achieved utilizing visual techniques. For this purpose, measuring scales were glued to the front of the structure. In this way, scour depth with elapsed time could be obtained up to an accuracy of ±0.005 m. Velocity measurements were conducted using a Nortek Vectrino Acoustic Doppler Velocimeter (ADV) with a down-looking head equipped with four receivers set at a sampling rate of 30 Hz (installed with the sample volume in the flume centerline at x = 5.4 m downstream of the flap gate, which was 0.4 m upstream of the structure). Finally, a Disto TM laser altimeter with a precision of ± 1.00 mm was used to measure the final local scoured bathymetry around the structure at the end of each test, following the draining of all water. Finally, a Disto TM laser altimeter with a precision of ± 1.00 mm was used to measure the final local scour around the structure at the end of each test.

Table 7-1: Summary of experimental tests

Test #	Upstream depth (m)	Initial condition (m)	Sediment size (m)	Bed condition
1	0.25	0.00	0.001 (Sand)	Dry
2	0.25	0.05	0.001 (Sand)	Wet
3	0.25	0.00	0.01 (Gravel)	Dry
4	0.25	0.05	0.01 (Gravel)	Wet

7.4 3D numerical model

In this study an open source Telemac-Mascaret modeling system was used to simulate local scour due to a turbulent bore. Telemac is a property of electricite de france (EDF) and was initially created at laboratoire national d'hydraulique et environment, LNHE of EDF R&D. TELEMAC is a set of modelling tools capable of simulating several aspects of natural free surface hydraulics: currents, waves, transport of tracers and sedimentology. The 3D hydrodynamics module (Telemac-3D) is based on the solution of the 3D continuity and Reynolds Averaged Navier-Stokes (RANS) equations with non-hydrostatic pressure approximation. 3D RANS equations are solved using a finite element discretization. The 3D hydrodynamic model is coupled internally with the sediment transport module SISYPHE. The bed topographic evolution due to erosion or deposition is computed from a sediment mass balance equation (Villaret and Tassi, 2014).

An unstructured triangular mesh was used to discretize the geometry of the model with 47438 elements (Figure 3a and b). The mesh size varied between 0.05 m upstream and downstream of the structure and 0.01 m in the vicinity of structure. In order to prepare the mesh of the 3D flow domain, a two-dimensional mesh comprising triangles that covered the computational domain (the bottom) in a plane was first constructed. The mesh along the vertical direction was duplicated in a number of curved surfaces known as "planes". Between two such planes, the links between the meshed triangles make up prisms. For the simulations six superimposed planes were used in the vertical direction. Sensitivity tests conducted on increasing the number of planes showed no perceptible differences on the results.

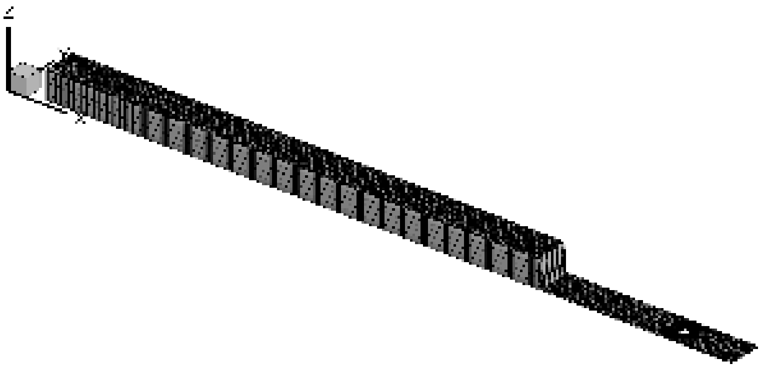

a)

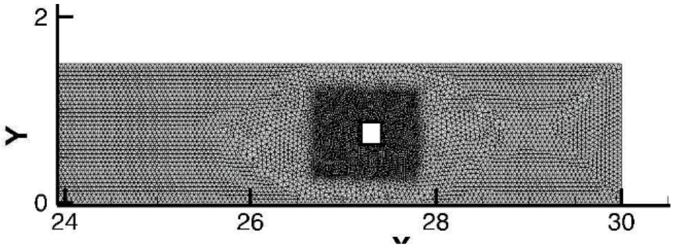

b)

Figure 7-3: a) 3D mesh isometric view (not to scale), b) 2D mesh over the sediment section and around the structure

Sensitivity analysis of the numerical results to several parameters, such as the mesh size, turbulence model for RANS (k-e, constant viscosity and mixing length) or LES (Smagorinsky) formulations, bed roughness, settling velocity, critical dimensionless shear stress as well as the sediment transport formula were conducted (see Figure 1, 2, 3, 4, 5, 6, 7 and 8 in Appendix C). The bed evolution equation was solved using four different sediment transport formulae: Meyer-Peter & Muller (1948), Einstein - Brown (1950), Engelund - Hansen (1967), and Van Rijn (1984a). The Engelund - Hansen (1967) for tests with sand and Meyer-Peter & Müller formula for tests with gravel were found to better reproduce the experimental results. The sensitivity results revealed that LES is a more appropriate approach for scour models induced by bores that are turbulent with high Reynolds numbers.

The time step was 0.02 s. Critical dimensionless shear stress values of 0.022 and 0.04 were used for sand and gravel, respectively. The roughness Manning coefficient was considered on the basis of the bed material diameter and thus set at 0.028 and 0.035 for sand and gravel bed, respectively. The upstream boundary condition was a closed wall. Settling velocity of 0.1 m/s and 0.4 m/s were also used for sand and gravel, respectively. A Neumann-type boundary condition (i.e. free height and velocity) was imposed on the downstream end. A zero velocity field was imposed as an initial condition. All four tests presented in Table 7-1 were replicated in the numerical simulation. The numerical predictions were then compared to measurements from laboratory experiments.

7.5 Results and discussion

7.5.1 Time-history of water surface

Figure 7-4a, b, c and d show the measured and computed run up depth on the structure due to the surface roller. Time 0 refers to the time that turbulent bore reaches to the structure. For the tests conducted on dry sand, the maximum measured and computed run up depths were 0.17 m and 0.19 m, respectively, while these values were 0.15 m and 0.16 m for the tests carried out on dry gravel. Moreover, for the tests performed on wet sand, the maximum measured and computed run up depths were similar values around 0.15 m. Whereas, in wet gravel, these values were 0.13 m and 0.12 m, respectively. Both experiments and the 3D model show higher run up depth in dry bed condition compared to that of wet bed condition. Moreover, both models show that the run-up depth is higher in the case of sand compared to that of gravel. As shown in Figure 7-4c and d, the 3D model reproduces the run-up depth accurately for both sediment sizes in case of wet bed condition. However, there are discrepancies at the first few seconds in the case of dry bed condition. This discrepancy is caused by the fact that in the 3D model loss of water due to infiltration in dry bed condition is not considered.

The maximum measured run-up height occurred 7.9 s after the arrival of the bore in case of dry bed conditions, while maximum measured run up depth were attained within less than a second for the tests conducted on wet bed conditions. Nevertheless, the maximum run up depth for both wet and dry beds is attained within the first second in the numerical model. The delay in maximum measured run-up height in the experiment is likely a result of water infiltrating into the bed given the porosity and permeability of the sediment bed under dry bed conditions.

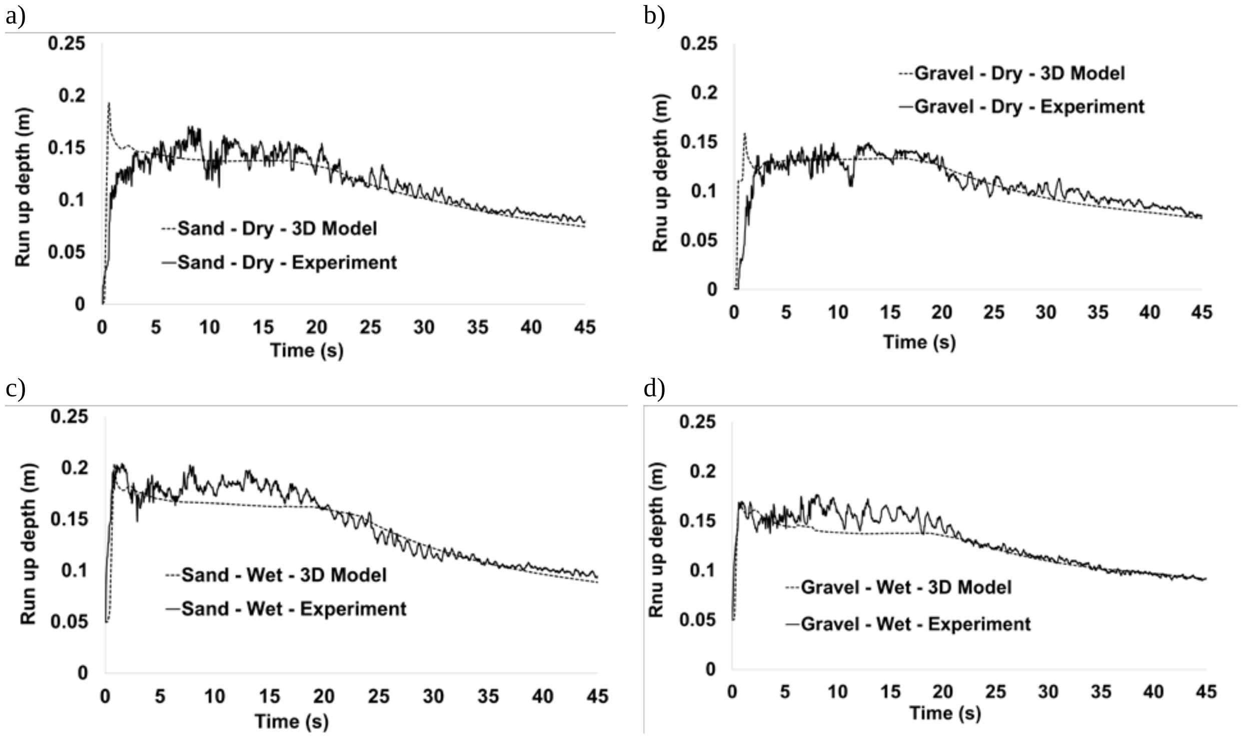

Figure 7-4: Measured and computed run up depth: a) sand - dry bed, b) gravel - dry bed, c) sand – wet bed, d) gravel- wet bed

7.5.2 Velocity time history

Figure 7-5 shows the measured and computed steamwise velocity 0.4m upstream of the structure at the elevation of 0.02 m above the bed. To avoid ADV measuring errors due to high flow front turbulence, streamwise velocity measurements began 2 s after the passage of the bore front.

The stream-wise velocity time histories interestingly appear to consist of four main segments in both computed and measured streamwise velocity. The first segment is characterized by a very steady and steep decline. The second segment has the appearance of a quasi-steady state. The third segment follows with a sudden reduction in bore velocity, and, finally, segment four is a transition to the quasi-steady state which results in a quasi-constant bore velocity. The maximum measured and computed velocities are 1.57 m/s, 1.7 m/s, respectively. The authors hypothesize that due to ADV measuring error the maximum streamwise velocity could not be measured right after the passage of the bore front.

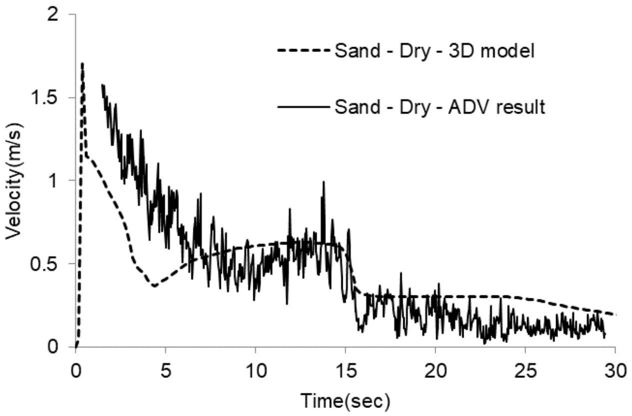

Figure 7-5: measured streamwise velocity at 2cm depth above the bed

To further analyze the effects of bed condition and sediment size on the characteristics of the bore, the computed depth averaged velocity, 0.4m upstream of the structure, is shown in Figure 7-6a and b. It can be seen that the maximum streamwise velocities were 1.74 m/s for dry sand and 0.91 m/s for wet sand, respectively. Moreover, the computer streamwise velocity for dry gravel and wet gravel are 1.55 and 0.89 m/s. Comparing wet and dry bed conditions, the numerical models show that the presence of downstream still water depth resulted in a lower total head and less kinetic energy and subsequently results lower velocity. Both experimental and numerical models show the reduction of streamwise velocity as the sediment size increases from 0.001 m to 0.01 m.

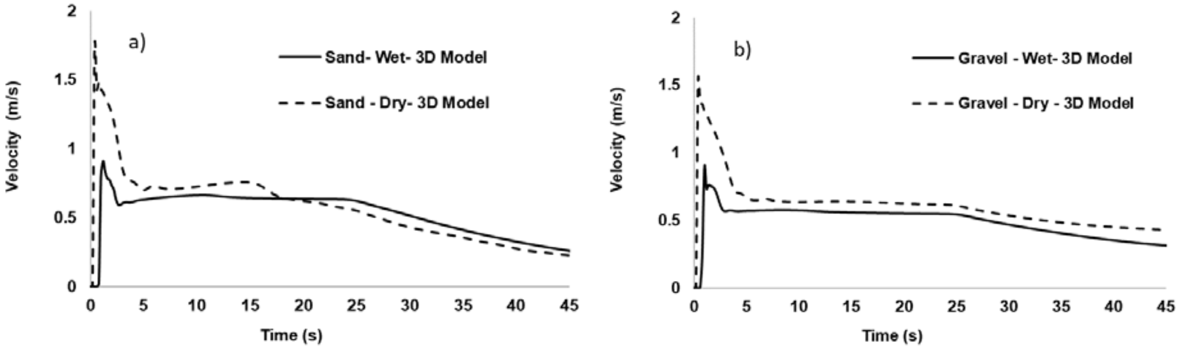

Figure 7-6: Computed depth average velocity: a) sand, b) gravel

7.5.3 Time history of scour depth

Figure 7-7a, b, c and d compare the time history of the scour depth for the sediment bed filled with sand and gravel for two different hydrodynamic conditions. The maximum measured and computed scour depth for dry sand were 0.17 m and 0.075 m (Figure 7-7a). Also, as shown in

Figure 7-7c, these values were 0.125 m and 0.05 m for the tests conducted on wet sand. The measured and computed scour depths for the dry gravel bed case were 0.095 m and 0.04 m (Figure 7-7b), while these values were 0.055 m and 0.03 m for the wet bed gravel condition (Figure 7-7d). Both experimental and numerical models show the reduction of scour depth as the size of the sediment increases from 0.001m to 0.01m. Comparing wet and dry bed conditions, both experimental and numerical models show that the presence of downstream still water depth resulted in a lower total head and less kinetic energy and subsequently results less scour depth. The results illustrate that the 3D model under predicts the maximum scour depth.

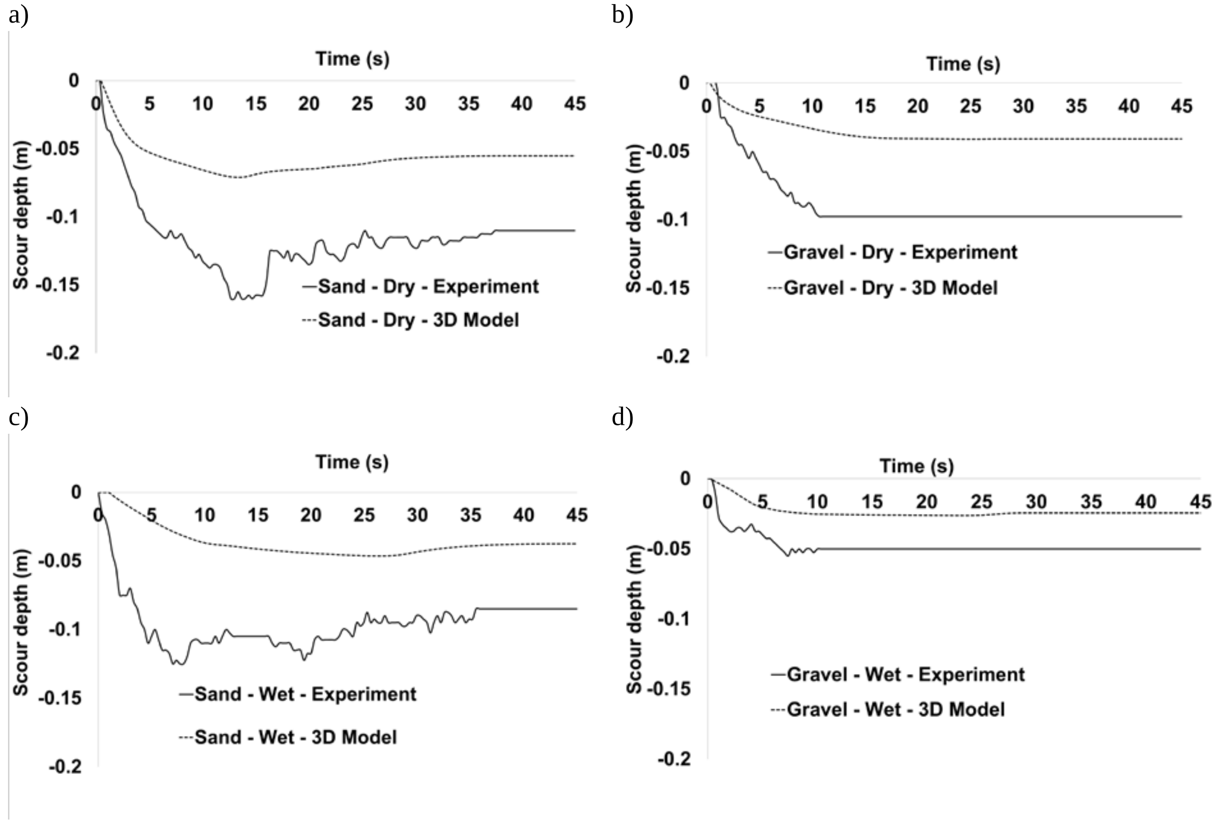

Figure 7-7: Measured and computed scour depth time history: a) sand - dry bed, b) gravel - dry bed, c) sand – wet bed, d) gravel- wet bed

7.5.4 Bathymetry

Based on observations during the experiment, the motion of the gravel particles differs from that of sand. Sand particles were entrained and displaced away from the structure by the bore, whereas gravel particles moved as bedload like a sheet flow and were deposited further downstream of the structure. Figure 7-8a and b show the measured final bathymetry. It can be seen that deposition extended further downstream for the sand bed than for the gravel bed.

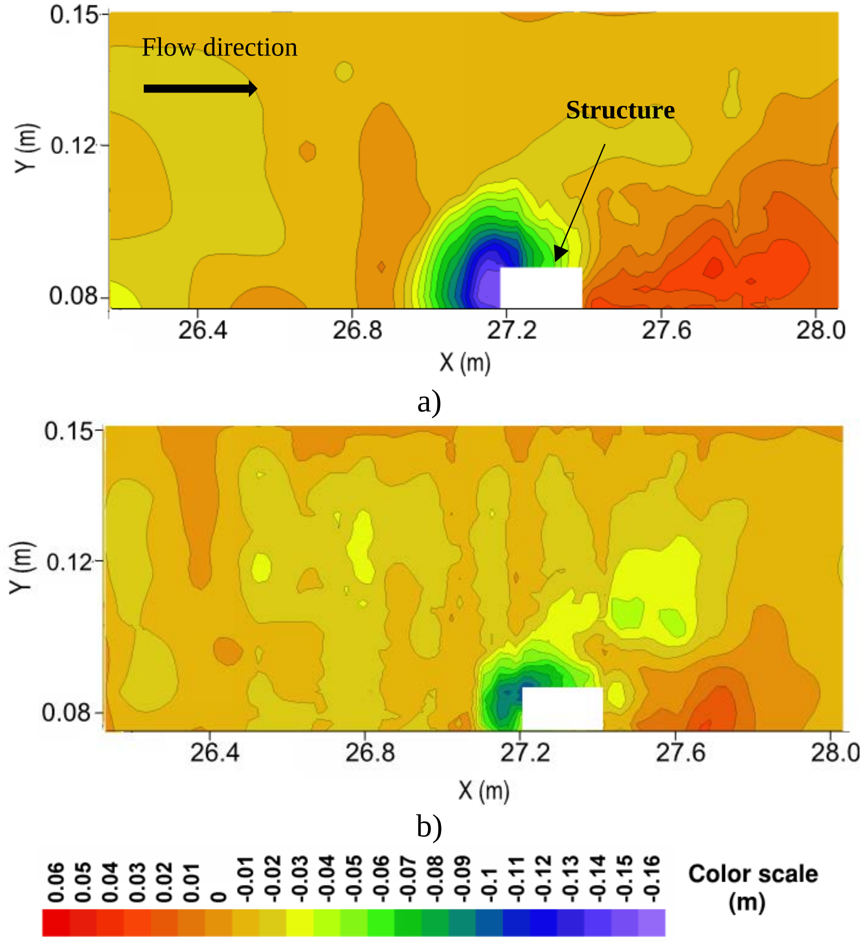

Figure 7-8: Measured final bathymetry a) sand-dry, b) gravel-dry

The final bathymetry is only presented for the dry bed condition as they were measured only for the dry bed during the experimental work. The structure is shown as a white object, and, since the scour hole is symmetrical around the center of the structure, only one side of the final sediment bed was measured. Comparing Figure 7-8a and b, the sand bed and gravel bed had very similar final scour patterns. One important difference is that the scour process is even more inhibited by the gravel over the short duration of the bore. This indicates that the scour of the entire sediment bed occurred in addition to the local scour around the structure. As shown also in Figure 7-9a and b the maximum scour depth occurred at the corner of the structure for both size of sediments.

Figure 7-9: Final scour profile from the inside video camera a) sand - dry condition, b) gravel – dry condition

In addition, as shown in Figure 7-10a and b, the numerical model produces similar scour and deposition pattern as experimental work. The location of maximum scour depth and sediment deposition pattern downstream of the structure are well captured by the numerical model. The numerical model also simulates the local scour at the intersection of false floor and sediments section. However, magnitude of scour depth computed by the 3D model is underpredicted by approximately 50% and the 3D model could not reproduce the scour observed at the front of the structure as shown in Figure 7-8a and b. The discrepancy is likely due to incapability of existing sediment transport models to more realistically account for the effects of turbulent flow field. As the influence of the turbulence fluctuation and the lifting force are not considered in the traditional sediment model used in this study.

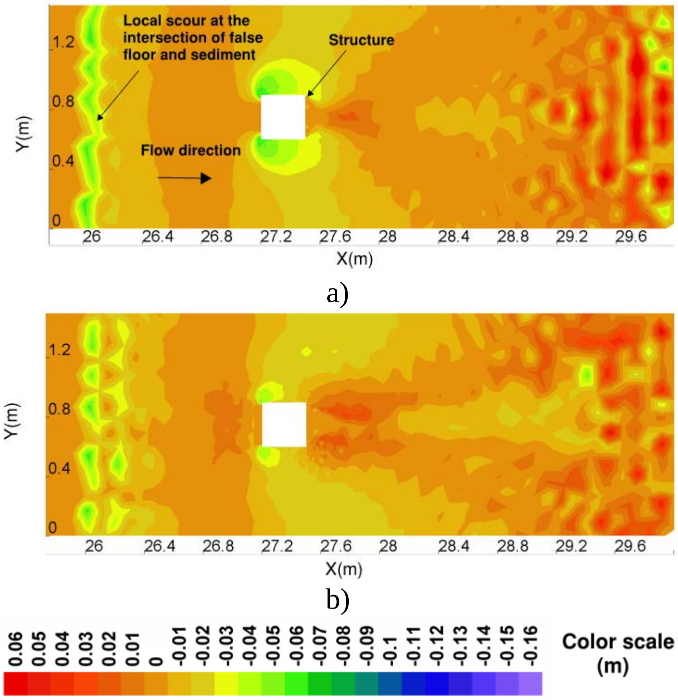

a)

b)

Figure 7-10: Computed final bathymetry a) sand-dry, b) gravel-dry

7.5.5 **Flow field induced by turbulent horseshoe vortex**

Figure 7-11 shows contours of instantaneous streamwise velocity and streamtracers in the plane of Y = 0.75 m simulated with LES approach at the upstream of the structure at various time steps. It demonstrates that the highest streamwise velocity occurred at the time of impact and its magnitude is around 1.6 m/s. The magnitude of the streamwise velocity decreases as the bore propagated to the downstream end of the flume and it is higher at the surface above the generated horseshoe vortices. The results show that the numerical simulation developed captures the main features of the scour process, a downward flow from the upper flow zone at the upstream face of the structure resulted in a strong backward flow close to the bed, leading to the creation of the horseshoe vortex. However, the 3D model does not simulate the surface roller at the upper body of the water at the front of the structure as observed in the experiment.

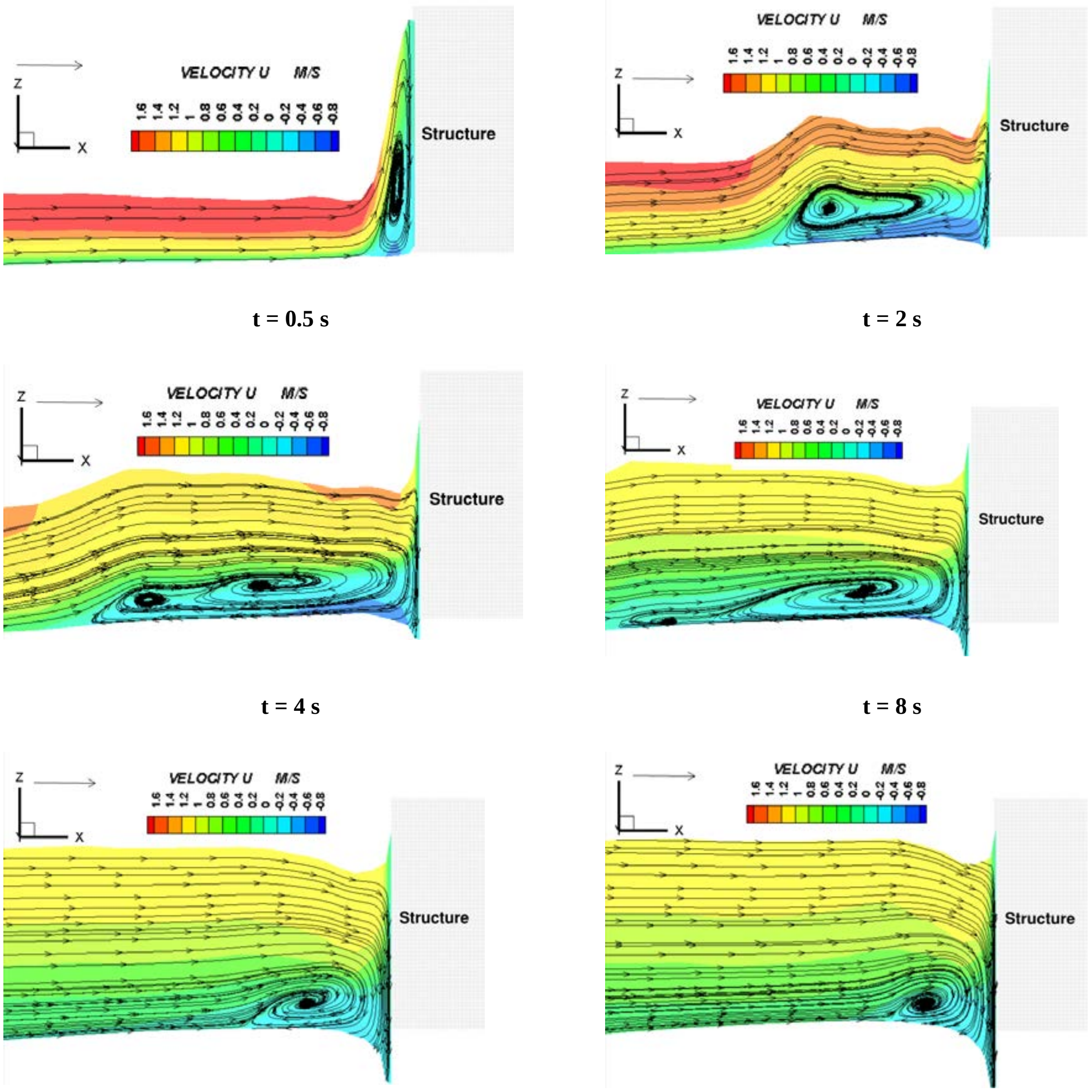

t = 0.5 s

t = 2 s

t = 4 s

t = 8 s

t = 15 s

t = 35 s

Figure 7-11: contours of instantaneous streamwise velocity and streamtracers in the plane of Y = 0.75 m

7.6 Conclusions

In this study, turbulent bore-induced local scour around a square structure was simulated experimentally and numerically. The physical and numerical model were based on the analogy between tsunami-induced bores and dam-break waves generated by the sudden release of an impounded volume of water. The following conclusions can be drawn from the analysis of both models.

- Computed water surface elevation is accurately reproduced, especially on wet bed condition. Both experimental and numerical results show the higher run up and scour depths in case of dry condition compared to those of wet bed condition.
- Comparing wet and dry bed conditions, both experimental and numerical models show that the presence of downstream still water depth resulted in a lower total head and less kinetic energy and subsequently results lower velocity and less scour depth.
- Comparing the results on sand bed versus gravel bed, both models show the reduction of streamwise velocity as the sediment size increases from 0.001 m to 0.01 m. Both models show the reduction in both scour and run up depths with increasing the sediment size from 0.001 m to 0.01 m.
- The location of maximum scour depth and sediment deposition pattern downstream of the structure are well captured by the numerical model. The main features of the scour process, a downward flow and the horseshoe vortex were well captured. However, the 3D model was not able to simulate the surface roller at the upper body of the water at the front of the structure.
- The results of the hydrodynamic model were in agreement with those of the experimental portion of the research. However, the scour results from the morphodynamic model are underpredicted by approximately 50% and the 3D model could not reproduce the scour observed at the front of the structure.
- The actual limitations of the morphodynamic model are due to the high degree of empiricism of the sediment transport formula and incapability of existing sediment transport models to more realistically account for the effects of turbulent flow field. As the influence of the turbulence fluctuation and the lifting force are not considered in the traditional sediment model used in this study.
- The numerical model developed here was a very useful and powerful tool in investigating water-structure interactions. However, Further research should therefore be paid to improve the applicability of the morphodynamic model.

Chapter 8. CONCLUSIONS AND RECOMMENDATION FOR FUTURE WORK

8.1 Conclusion

The thesis presented herein examined the unique scouring process of a tsunami-like bore and the formation of local scour around a square structure. This study aimed to improve the understanding of scour mechanisms due to inland propagating tsunami-like bore. The influence of different parameters on the bore propagation characteristics and how they affect the scouring process was investigated. Based on the results of this study, the following general conclusions can be drawn:

- The short duration and very turbulent nature of the bores induced rapid scour process while a longer duration of a turbulent bore induced more scour depth compared to that generated by solitary or long waves.
- Similar to some of the post-tsunami field observations, the scour hole formed at the seaward corner of the structure while local scour at the shoreward corner was insignificant. The scour holes formed with a distinct break in the downward slope. Sand particles moved irregularly in space and time as a result of the oscillation of the horseshoe vortex in location and size over time along the stream-wise direction in the turbulent bore.
- The measured bore front velocity and scour depth demonstrate that the larger bore depth resulted in greater bore front velocity and induced greater scour depth.
- A distinctive difference in bore front profiles advancing over dry or wet bed conditions was identified. A significant amount of air entrainment and a higher and steeper bore front was observed in the case of wet bed condition. However, in case of bore advancing over dry bed, the bore front entrained with the sediment, and sand particle concentration developed rapidly towards the bore front.
- It was found that the bed condition (wet vs dry) as well as the type of bed (movable or fixed bed) plays an important role in the changes of the hydrodynamic features of a bore. The bore behaves differently in the cases of wet and dry conditions on fixed vs mobile beds. A particularly notable finding is that the bore characteristics over a dry sand bed are influenced by infiltration.

- It was found that the ASCE (2016) prescriptions on estimating scour underpredicts the maximum scour depth and thus, the use of the ASCE (2016) provisions, may lead to undesirable underestimations of maximum scour depth.
- Additional scour depth formed as a result of a second bore propagating over a previously scoured bed
- For the same approach flow conditions, the scour rate was almost constant for all of three sizes of structures used. As the initial impoundment reservoir depth increased, the scour depth increased. However, the rate of increase in scour depth for a wider structure was greater than that observed in the case of a smaller one.
- The ratio of scour depth divided by flow depth depends on the structure size. However, the average value of these ratios is 65%, which is close to the value proposed by Dames and Moore (1980).
- Based on the experimental observation, the motion of the gravel particles differs from that of sand. Sand particles were entrained and displaced away from the structure by the bore, whereas gravel particles moved as bedload like a sheet flow and were deposited further downstream of the structure. One important difference is that the scour process was even more inhibited by the gravel over the short duration of the bore. This indicates that the scour of the entire sediment bed occurred in addition to the local scour around the structure.
- In the numerical modelling, the computed water surface elevation was accurately reproduced, especially on wet bed condition. The location of maximum scour depth and sediment deposition pattern downstream of the structure are well captured by the numerical model. However, the magnitude of scour was underpredicted.
- The actual limitations of the morphodynamic model are due to the high degree of empiricism of the sediment transport formula and incapability of existing sediment transport models to more realistically account for the effects of turbulent flow field. As the influence of the turbulence fluctuation and the lifting force are not considered in the traditional sediment model used in this study.
- Both experimental and numerical results showed higher run up and scour depths in case of dry condition compared to those of wet bed condition. Both models showed a reduction in both scour and run up depths when increasing the sediment size from 0.001 m to 0.01 m.

- Both experimental and numerical models show the reduction of scour depth as the size of the sediment increases from 0.001m to 0.01m. Comparing wet and dry bed conditions, both experimental and numerical models show that the presence of downstream water depth resulted in a lower total head and less kinetic energy. Therefore, the lower kinetic energy generates lower velocity and subsequently results in less scour depth.
- The numerical model developed here was a very useful and powerful tool in investigating water-structure interactions. However, Further research should therefore be paid to improve the applicability of the morphodynamic model.

This research encompassed a comprehensive experimental and numerical investigation and analysis for the scour mechanism and vortex structures due to inland-propagating tsunami-like bores on a dry or flooded horizontal mobile bed. This study yielded highly detailed measurements of the local scour, leading to a better understanding of this unique scouring process. The research results will help improve methods of estimating local scour for future application in design codes. These findings can be used in establishing new design guidelines for tsunami loading or as a preliminary design recommendation for infrastructure in tsunami-prone areas. It is worth noting that the experimental results of this thesis have been incorporated into the most recent version of the ASCE7 Chapter 6 - Tsunami Loads and Effects design and were voted favourably by the ASCE Main Balloting Committee. The newly revised ASCE7 Chapter 6 is due to be published in 2022 guideline.

8.2 Recommendations for future work

The potential for future work in this field of study is significant. The following recommendations mostly pertain to the results of the current study that would greatly help to improve the accuracy of the methodology.

- The experiments were performed at a relatively small-scale (1:40 or smaller). The flume dimensions and reservoir size represent a major challenge which limited the size of the structural model and the maximum depth of the flow. Therefore, the availability of larger flumes (deeper and longer) will help researchers perform experimental tests with larger structural models and to investigate a wider range of flow depths and velocities. Therefore, larger-scale experimental testing is desirable to allow for larger structure size and larger flow depth and velocity.
- Because of time restrictions, only columns with square cross-sections were investigated in this study. Further investigation using different structural geometry is recommended.
- This study was investigated over a flat bed with uniform sediment size and flow advancing over a sloped bed as well as flow drawdown was not considered in this study. Further study on influence of complex topographies with mixed or layered sediments and bores propagating on sloped bed is recommended.
- The experimental work only conducted on two types of non-cohesive sediments and scour induced by turbulent bore in a cohesive sediment bed was not studied.
- Tonkin et al. (2003) showed the most significant scour occurred due to a large vertical gradient in pore water pressure at the rear of the cylinder during the return flow. If the mechanism is similar to tidal scour (e.g., McGovern et al., 2014) but on a shorter time-scale then the return flow is likely to cause scour on the back of the structure. Future studies should consider the return flow phase during draw-down.
- Further investigation into the vortex formation when a bore impacts a structure is warranted. Evidence that the turbulent characteristics of the flow surrounding the structure are different for large bore depths than for small bore depths was observed in this study. Additional analysis of these flow patterns could shed light on the scouring process induced by the bores.
- It is recommended that a better sediment transport formula, which would more accurately predict the effect of the downflow, horseshoe vortex and wake, needs to be developed.

- A similar study can be performed for the use of the other incipient motion criteria except the Shields parameter.
- The 3-D numerical model did not simulate the surface roller at the upper body of the water at the front of the structure. It is recommended to develop another numerical model that would more accurately simulate the surface roller.

REFERENCES

Al-Faesly, T., Palermo, D., Nistor, I., Cornett, A., (2012). Experimental modeling of extreme hydrodynamic forces on structural models. International Journal of Protective Structures 3, 477–506.

Amicarelli, A., Albano, R., Mirauda, D., Agate, G., Sole, A., Guandalini, R., (2015). A Smoothed Particle Hydrodynamics model for 3D solid body transport in free surface flows. Computers & Fluids 116, 205–228.

Armitage N & McGahey C, (2003), "A unit stream power model for the prediction of local scour in rivers", Report No 1098/1/03, Water Research Commission, South Africa

Arnason, H., Petroff, C., Yeh, H., (2009). Tsunami bore impingement onto a vertical column. Journal of Disaster Research 4, 391–403.

Arneson, L.A Zevenbergen, L.W. Lagasse P.F Clopper P.E. (2012). “Evaluating Scour at Bridges” Hydraulic Engineering Circular 18, Fifth Edition, FHWA HIF 12 003 HEC-18, Federal Highway Administration, U.S. Department of Transportation, Washington, D.C

Arikawa, T., (2011). Experimental study on tsunami disaster, in: Proc., 7th Int.Workshop Coastal Disaster Prevention

Arikawa, T., Sato, M., Shimosako, K., Hasegawa, I., Yeom, G. & Tomita, T, (2012), “Failure mechanism of Kamaishi breakwaters due to the Great East Japan earthquake tsunami” In Proc. of33rd Int. Conf. on Coastal Engineering, ASCE, Santander, pp. 1–13.

Arya, A. and Shingan, B, (2012), “Scour mechanism detection and mitigation for subsea pipeline integrity” Int J Eng Res Technol 1(3)

ASCE, (2010) , “Minimum Design Loads for Buildings and Other Structures” ASCE/SEI Standard 7-10, American Society of Civil Engineers, Reston, Virginia, USA.

Bagnold RA (1966), "An approach to the sediment transport problem from general physics", US Geological Survey Professional Paper 422-J

Bricker, J. Francis, M. & Nakayama, A. (2012), “Scour depths of coastal structures due to the 2011 Tohoku Tsunami” Jrnl of Hydraulic Rsrch, 50:6, 637-641

Bailard J., (1981). An energetics total load transport model for a plane sloping beach. Journal of Geophysical Research, 86, C11, 10938-10954.

Basak, V. (1975). “Scour at square piles”, Report No. 583, Devlet Su isteri genel mudurlugu, Ankara, Turkey, Bijker E.W., (1968). Mechanics of sediment transport by the combination of waves and current. In Design and Reliability of Coastal Structures, 23rd Int. Conf. on Coastal Engineering, 147-173. Bonasoundas, M.: Strömungsvorgang und kolkproblem, Report No. 28, Oskar v. Miller Institu, Tech. Univ. Munich, Germany, 1973.

Bruce W, Melville 1 and Yee-Meng Chiew, (1999) "Time scale for local scour at bridge piers" J. Hydraul Eng. 125(1): 59-65

Breusers، H. N. C. and Raudkivi، A. J. (1991) "Scouring Hydraulic structures design manual" volume2, Balkema, Rotterdam،

Breusers, H.N.C. (1966). "Conformity and time scale in two-dimensional local scour" Proceedings symposium on model and prototype conformity. Hydraulic Research Laboratory Poona, p. 1-8.

Breusers, H.N.C, Nicollet, G. and Shen, H.W. (1977) "Local Scour Around Cylindrical Piers", J. Hydraulic Research, 15(3), 211-252.

Canelas, R.B., Ferreira, R.M., Crespo, A., Domιnguez, J., (2013). A generalized SPH-DEM discretization for the modelling of complex multiphasic free surface flows, in: 8thinternationalSPHERICworkshop.

Capart, H., and Young, D. L. (1998) "Formation of a jump by the dam break wave over a granular bed" J. Fluid Mech., 372, 165–18

Carrier, G., Greenspan, H., (1958). Water waves of finite amplitude on a sloping beach. Journal of Fluid Mechanics 4, 97–109.

Carrier, G., Wu, T., Yeh, H., (2003). Tsunami run-up and draw-down on a plane beach. Journal of Fluid Mechanics 475, 79–99.

Chanson, H., Aoki, S.-I., Maruyama, M., (2003) "An experimental study of tsunami run-up on dry and wet horizontal coastlines" Science of Tsunami Hazards 20 (5), 278–293

Chanson, H. (2004a). "The hydraulics of open channel flow".An introduction. Butterworth-Heinemann, Oxford, UK, 2nd edn, 630.

Chanson, H. (2004b) "Environmental Hydraulics of Open Channel Flows. Elsevier Butterworth Heinemann,Oxford, UK, 483 pages (ISBN 0 7506 6165 8).

Chanson, H. (2006) "Tsunami surges on dry coastal plains: application of dam break wave equations". Coastal Eng. J. 48 (04), 355–370.

Chanson, H. (2009a). "An Experimental Study of Tidal Bore Propagation: The Impact of Bridge Piers and Channel Constriction." Hydraulic Model Report No. CH74/08, School of Civil Engineering, The University of Queensland, Brisbane, Australia.

Chanson, H. (2009b). "Application of the method of characteristics to the dam break wave problem." Journal of Hydraulic Research Vol. 47, No. 1 (2009), pp. 41–49

Chabert, J. and Engeldinger, P. (1956): Etude des affouillements autour des piles des ponts, Laboratoire d'Hydraulique, Chatou, France (in French)

Chen, Y.H. & Simons, D.B. (1979) “An Experimental Study of Hydraulic and Geomorphic Changes in an Alluvial Channel Induced by Failure of a Dam” Water Resources Research. 15 (5): 1183-1188.

Chen, J., Huang, Z., Jiang, C., Deng, B., Long, Y., (2013). Tsunami-induced scour at coastal roadways: a laboratory study. Nat. Hazards 69 (1), 655–674. http://dx.doi.org/ 10.1007/s11069-013-0727-6.

Chen, J., Jiang, C., Yang, W. (2016). “Laboratory study on protection of tsunami-induced scour by offshore breakwaters” Nat Hazards, **81**: 1229. Doi: 10.1007/s11069-015-2131-

Chen, Y.H. & Simons, D.B, (1979). “An Experimental Study of Hydraulic and Geomorphic Changes in an Alluvial Channel Induced by Failure of a Dam” Water Resources Research 15 (5): 1183-1188

Cheng NS (1997), "Simplified settling velocity formula for sediment particle" J. Hydr. Engrg. ASCE, Vol. 123, Issue 2, pp 149-152

Chiew, Y.M. (1984): Local scour at bridge piers, Report No. 355, School of Engineering, The University of Auckland, Auckland, New Zealand, 200pp,.

Chien N & Wan Z (1999), Mechanics of sediment transport, ASCE Press

Chinnarasri, C., Thanasisathit, N., Ruangrassamee, A., Weesakul, S., Lukkunaprasit, P., (2013). The impact of tsunami-induced bores on buildings. Proceedings of the Institution of Civil Engineers: Maritime Engineering 166, 14–24.

Chock, G., Roberson I., Kriebel D., Francis M., Nistor, I. (2013). Tohoku Japan tsunami of March 11, 2011 – Performance of structures under tsunami loads, ASCE/SEI Report, 359 p

City and County of Honolulu Building Code (CCH), (2000)“Department of Planning and Permitting of Honolulu Hawaii” Chapter 16 Article 11. Honolulu, Hawaii

Clague JJ, Munro A, Murty T (2003) Tsunami hazard and risk in Canada. Nat Hazards 28(2):435–461.

Colebrook CF & White CM. (1937), "Experiments with fluid friction in roughened pipes" Proc. Roy. Soc. London, Vol A161, pp 367-381

Crespo, A. J. C. Gómez-Gesteira M, and Dalrymple, R. A (2008) “Modeling dam break behavior over a wet bed by a SPH technique” J. Waterway, Port, Coastal, Ocean Eng., 134(6), 313–320

Dames & Moore. (1980) “Design and Construction Standards for Residential Construction in Tsunami-Prone Areas in Hawaii" prepared by Dames & Moore for the Federal Emergency Management Agency, Washington D.C.

Dey, S and Raikar, R. V. (2007), “Characteristics of Horseshoe Vortex in Developing Scour Holes at Piers”, Journal of Hydraulic Engineering © ASCE

Dibajnia M., Watanabe A., (1992). Sheet flow under non-linear waves and currents. Proc. of the Intl. Conf. on Coast Eng., 2015-2029.

Douglas, S, Nistor, I. (2015). "On the effect of bed condition on the development of tsunami-induced loading on structures using OpenFOAM" Natural Hazards, 76(2), 1335-1356.

Du, S and Liang, B. (2019) “Comparisons of Local Scouring for Submerged Square and Circular Cross-Section Piles in Steady Currents”, Water 2019, 11(9), 1820

Einstein H.A. (1950). The bed load function for sediment transportation in open channel flow. US Dep. Of Agriculture, Techn. Bull.

Engelund F. and Hansen E., (1967). A monograph on sediment transport in alluvial streams. Techn. Univers. Of Denmark, Copenhagen, Denmark.

Ettema, R. (1980): Scour at bridge piers, Report No. 216, School of Engineering, The University of Auckland, Auckland, New Zealand, 527pp.

Ettema, R., Melville, B.W. and Barkdoll, B. (1998) “Scale Effects in Pier-Scour Experiments”, J. Hydraulic Eng, 124(6), 639-642.

Ettema, R., Kirkil, G. and Muste, M. (2006): Similitude of large-scale turbulence in experiments on local scour at cylinders, Journal of Hydraulic Engineering, A.S.C.E., Vol.132(1), pp.33 40

Fahlbusch, F.E. (1994). “Scour in rock riverbeds downstream of large dams”. The International Journal of Hydropower and Dams, IAHR, 1, pp. 30-32

Favre, H. (1935). "Etude Théorique et Expérimentale des Ondes de Translation dans les Canaux Découverts." ('Theoretical and Experimental Study of Travelling Surges in Open Channels.') Dunod, Paris, France (in French).

Federal Emergency Management Agency (2008, 2012) Guidelines for Design of Structures for Vertical Evacuation from Tsunami Washington D.C., USA

Feldens P, Schwarzer K, Szczucinski W, Stattegger K, Sakuna D, Somgpongchaiykul P. (2009) “Impact of the 2004 Indian Ocean tsunami on seafloor morphology and sediments offshore Pakarang Cape”, Thailand. Pol J Environ Stud. 18(1):63–68

Foster, A.S.J., Rossetto, T., Allsop, W., (2017). An experimentally validated approach for evaluating tsunami inundation forces on rectangular buildings. Coast Eng. 128, 44–57. Fritz, H.M.,

Francis M. (2006). “Tsunami Inundation Scour of Roadways, Bridges and Foundations: Observations and Technical Guidance from the Great Sumatra Andaman Tsunami”. EERI/FEMA NEHRP Professional Fellowship Report

Fujii, N, M. Ikeno, T. Sakakiyama, M. Matsuyama, M. Takao, and. T. “Mukouhara, (2009). Hydraulic experiment on flow and topography change in harbor due to tsunami and its numerical simulation” Ann. J. Coast Eng., 56, 291–295, (in Japanese)

Gessler J (1970), "Self-stabilising tendencies of alluvial channels" loumal of the Waters and

Harbours Division. ASCE, Vol. 96, No. WW2, pp 235-249

Ghobarah, A, Saatcioglu, M., Nistor, I (2006) “The impact of 26 December 2004 earthquake and tsunami on structures and infrastructure”, Engineering Structures, Elsevier, 28(2), 312-326

Goseberg. N, A. Wurpts, T. Schlurmann. (2013) “Laboratory-scale generation of tsunami and long waves” Coastal Engineering, 79, pp 57-74

Goseberg, N., (2013). Reduction of maximum tsunami run-up due to the interaction with beachfront development - application of single sinusoidal waves. Nat Hazards Earth Syst Sci Disc 1, 1119–1171.

Gumgum, F and Guney, M. S., (2020), “Time Dependent live bed scour around circular piers under flood waves” Periodica Polytechnic Civil Engineering, 64(1), pp. 65-72,2020

Hagen, M. (2014). Detailed Analysis of the 2011 Japan Tsunami – Video Footage, Wave Heights and Damage Imagery. Available at: www.extremeplanet.me. Hancu, S.: Sur le calcul des affouillements locaux dams la zone des piles des ponts, Proc., 14th. I.A.H.R. Congress, Paris, France, Vol. 3, pp.299-313, 1971.

Henderson, F.M. (1966). “Open channel flow” Macmillan Publishing Co, New York

Hoffmans, (1993) “A hydraulic and morphological criterion for upstream slopes in local-scour holes” Report W-DWW-93-255 G.J.CM. Hoffmans Road and Hydraulic Engineering Division P.O. Box 5044 2600 GA Delft

Hoffmans, G.J.CM, (1990), Concentration and flow velocity measurements in a local scour hole. Report No.4-90, Faculty of Civil Engineering, Hydraulic and Geotechnical Engineering Division, Delft University of Technology, Delft.

Hoffmans, G. J. C. M, and H. J. Verheij, (1997), “Scour Manual” 205 pp, A. A. Balkema, Brookfield, Vt.

Hoffman J & Jhonson C (2003), "Adaptive DNSILES: a new agenda in CFD." CIMS, New York University, USA

Hunziker R.P., (1995). Fraktionsweiser Geschuebetransport, Ph.D. thesis, Mitteeilungen Nr 138 deer Versuchanstalt fur Wasserbau, Hydrologie und Glaziologie, ETH Zurich, Switzerland. Hung-Chu Hsu, Alec Torres-Freyermuth, Tian-Jian Hsu, Hwung-Hweng Hwung & Ping-Chiao

Idelchik, I.E. (1969). Mémento des pertes de charge. Eyrolles Editor, Collection de la direction des études et recherches d’Electricité de France, Paris, France (in French).

Idelchik, I.E. (1994). Handbook of Hydraulic Resistance. CRC Press, 3rd edn. Boca Raton, USA, 790.

Imamura, F., Goto, K., Ohkubo, S., (2008). “A numerical model for the transport of a boulder by tsunami. Journal of Geophysical Research: Oceans (1978–2012) 113.

International Tsunami Survey Team (ITST) (2005) “The 26 December 2004 Indian Ocean tsunami: Initial findings from Sumatra,” Western Coastal and Marine Geology, U.S. Geological Survey, Internet Resource, http://walrus.wr.usgs.gov/tsunami/sumatra05/

Jayaratne, R., Premaratne, B, Abimbola, A., Mikami, T., Matsuba, Sh., Shibayama, T, Esteban, M, Shibayama, T, Nistor, I, (2016), “Failure Mechanisms and Local Scour at Coastal Structures Induced by Tsunami”, Coastal Engineering Journal, Vol. 58, No. 4 1640017

Jain, S.C. and Fischer, E.E. (1979): Scour around bridge piers at high Froude numbers, Report No. FH-WA-RD-79-104, Federal Highway Administration, U.S. Department of Transportation, Washington, D.C., U.S.A.

K. El Kadi Abderrezzak, Paquier A· and Gay B. (2008) “One-dimensional numerical modelling of dam-break waves over movable beds: application to experimental and field cases”, Environ Fluid Mech 8:169–198

Kabir. A, (2005), Modelling Local Scour Around Bridge Piers Using Telemac, University of Cape Town

Kato, F. Inagaki, S. & Fukuhama, M, (2006) “Wave force on coastal dike due to tsunami” in Proc.30th Int. Conf. Coastal Engineering, ASCE, San Diego, pp. 5150–5161.

Kato, F., Suwa, Y., Watanabe, K. & Hatogai, S. (2012) “Mechanism of coastal dike failure induced by the Great East Japan Earthquake Tsunami,” in Proc. 33rd Int. Conf. Coastal Engineering,ASCE, Santander, pp. 1–8.

Kashyap, S. (2012). A 3-D Numerical Study of Flow, Coherent Structures, and Mechanisms Leading to Scour in a High Curvature 135° Channel Bend With and Without Submerged Groynes, Ph.D. Thesis, University of Ottawa.

Khan, A. A., Steffler, P. M., and Gerard, R. (2000), “Dam-break surges with floating debris” J. Hydraul. Eng., 126_5_, 375–379

Khezri, N., & Chanson, H. (2012). Inception of Bed Load Motion beneath a Bore. Geomorphology (153-154), 39-47.

Koken, M., and Constantinescu, G. (2008). “An investigation of the flow and scour mechanisms around isolated spur dikes in a shallow open channel: 1. Conditions corresponding to the initiation of the erosion and deposition process.” Water Resources Res., 44, W08406, doi: 10.1029/2007WR006489

Kobayashi, N. & Lawrence, A. R. (2004) “Cross-shore sediment transport under breaking solitary waves,” J. Geophys. R. 109, C03047.

Kothyari‹ U. C. & R. J. Garde‹ & K. G. Ranga raju (1992) “Temporal variation of scour around circular bridge piers ‹ Journal of Hydraulic Engineering‹ ASCE‹ Vol. 118‹ No. 8‹ pp. 1091-1106

Kuo (2014). On dam-break wave propagation and its implication to sediment erosion, Journal of Hydraulic Research, 52:2, 205-218

Lavictoire A., Nistor, I., Rennie C. (2014). Local scour around structures due to hydraulic bores, Annual Conf. of the Canadian Society for Civil Eng., CSCE, Halifax, Canada, 10p

Lauber, G., & Hager, W. H. (1997). Experiments to dam break wave: Horizontal channel. Journal of Hydraulic Research, 36(3), 291-307

Larsen, B.E., Fuhrman, D.R., Baykal, C., Sumer, B.M., (2017). Tsunami-induced scour around monopile foundations. Coast Eng. 129, 36–49.

Larsen, B.E., Arboll, L.K., Kristoffersen, S.F., Carstensen, S., Fuhrman, D.R., (2018). Experimental study of tsunami-induced scour around a monopile foundation. Coast Eng. 129, 36–49.

Laursen, E.M. and Toch, A. (1956): Scour around bridge piers and abutments, Bulletin No.4, Iowa Highways Research Board, Ames, Iowa, U.S.A,.

Laursen, E.M. (1963): Analysis of relief bridge scour, Journal of the Hydraulics Division, A.S.C.E., Vol.89(3), pp.93-118,

Li L, Huang Z, Qui Q, Natawidjaja DH, Sieh K. (2012). Tsunami-induced coastal change: scenario studies for Painan, West Sumatra, Indonesia. Earth Planets Space 64:799–816

Leal, J. G. A. B., Ferreira, R. M. L., and Cardoso, A. H. (2002) “Dambreak waves on movable bed” Proc., River Flow 2002, D. Bousmar and Y. Zech, eds., Balkema, Rotterdam, The Netherlands, 2, 981–990.

Leal, J. G. A. B, Ferreira, R. M. L, and Cardoso, A. H. (2006) “Dam-break wave-front celerity” J Hydraul Eng., 132(1), 69–76

Lin, P., Liu, P., (2000). “A numerical study of breaking waves in the surf zone”. Journal of Fluid Mechanics 259, 239–264.

Liu PL-F, Woo SB, Cho YS (1998). “Computer programs for tsunami propagation and inundation” Technical report, Cornell University

Leonard LJ, Rogers GC, Mazzotti S (2014). “Tsunami hazard assessment of Canada”. Nat Hazards 70(1):237–274

Lončar1, G., Andročec2, V., Klapčić3, S., Mišura,4 I. (2018), “Scour around the Circular and Square Profile Piers”, Jubilee Annual 2017-2018 of the Croatian Academy of Engineering

McGoverna, D.J., Toddb, D., Rossettod, T., Whitehouseb., R.J.S., Monaghana, J., Gomesc E. (2019), “Experimental observations of tsunami induced scour at onshore structures”, Coastal Engineering Journal, pp 378-383/

Madsen, P.A., Fuhrman, D.R., Schäffer, H.A. (2008). “On the solitary wave paradigm for tsunamis” Journal of Geophysical Research C: Oceans 113 (12), 1–22.

Madsen, P.A., Schaeffer, H.A., (2010). Analytical solutions for tsunami runup on a plane beach: single waves, N-waves and transient waves. Journal of Fluid Mechanics 645, 27–57.

Madsen, P.A., (2010). On the evolution and run-up of tsunamis. Journal of Hydrodynamics, Ser. B 22, 1–6.

Mazumder, B. S. & Ojha, S. P. (2007) “Turbulence statistics of flow due to wave current interaction” Flow Meas Instrum 18, 129–138

Melville BW (1997), "Pier and abutment scour: integrated approach." J. Hydr. Ellgrg. ASCE,Vol. 123, Issue 2, pp 125-136

Melville, B.W. and Chiew, Y.M. (1999) “Time Scale for Local Scour at Bridge Piers”, J. Hydraulic Eng, ASCE, 125(1): 59-65.

Melville, B. W (2008). The physics of local scour at bridge piers. Fourth international conference on scour and erosion. ISCE-4. 5-7th November 2008. Tokyo, Japan

Meyer-Peter PE & Muller R (1948), "Formulas for bed load transport" Proc. 3rd International Association for Hydraulic Research, Stockholm, Sweden, pp 39-64

Moronkeji A. (2007). “Physical Modelling of Tsunami Induced Sediment Transport and Scour” Earthquake Engineering Symposium for Young Researchers. Seattle

Nakamura T., Yasuki M. and Mizutani N**.** (2008) “Tsunami Scour Around a Square Structure” Coastal Engineering Journal 2: Vol. 50. - pp. 206-246.

Nandasena NAK, Paris R, Tanaka N. (2011) “Numerical assessment of boulder transport by 2004 Indian Ocean tsunami in Lhok Nga, West Banda Aceh (Sumatra, Indonesia)” Comput Geosci 37:1391–1399

Nandasena, N., Sasaki, Y., Tanaka, N., (2012). Modeling field observations of the 2011 great east Japan tsunami: efficacy of artificial and natural structures on tsunami mitigation. Coast. Eng. 67, 1–13.

Nistor, I., Saatcioglu, M. & Ghobarah, A. (2005) “The 26 December 2004 earthquake and tsunami — Hydrodynamic forces on physical infrastructure in Thailand and Indonesia,” in Proc. 2005 Canadian Coastal Eng. Conf., Halifax, Canada (CD-ROM), pp. 15.

Nistor, I., Palermo, D., al Faesly, T., Cornett, A., (2009). “Modelling of tsunami-induced hydrodynamic forces on buildings” 33rd IAHR Congress: Water Engineering for a Sustainable Environment

Noguchi, K., Sato, S. & Tanaka, S. (1997) “Large-scale experiments on tsunami overtopping and bed scour around coastal revetment,” Proc. Coastal Eng. 44, 296–300 (in Japanese).

Ontowirjo, B., Paris, R., and Akira Mano, A., (2013) “Modeling of coastal erosion and sediment deposition during the 2004 Indian Ocean tsunami in Lhok Nga, Sumatra, Indonesia”. Natural Hazards, vol. 65, issue 3, pages 1967-1979

Orendorff, B., Rennie, C., & Nistor, I (2011) “Using PTV through an embankment breach channel” Journal of Hydro-environment Research, 5, 277-287

Pan. C, and Huang. W, (2012) “Numerical Modeling of Tsunami Wave Run-Up and Effects on Sediment Scour around a Cylindrical Pier” J. Eng. Mech., 138(10), 1224–1235.

Peterson, C.D., B.E. Jaffe, and B. Peters, (2006), “Estimating uncertainty and frequency of high-velocity paleotsunami inundation from geologic records in back barrier settings, test locality Cannon Beach” Oregon (abs.). Eos, Transactions American Geophysical Union, 85(47), Supplement, F1038

Pilarczyk K, (1998). “Dikes and Revetments: Design, Maintenance and Safety Assessment”. Hydraulic engineering division, Delft

PRITCHARD A, HOGG A.J. (2002) “On sediment transport under dam-break” flow, J. Fluid Mech. vol. 473, pp. 265{274. c Cambridge University Press

Przedwojski R Blazejewski R & Pilarczyk KW (1995). River training techniques jimdamenla/s. design and applications, A.A. Balkem. Rotterdam, Brookfield, Netherlands

Pope SB (2000). Turbulent Flows, Cambridge University Press. Cambridge. CK

Raudkivi, AJ & Ettema, R. (1983), 'Clear-water scour at cylindrical piers', Journal of Hydraulic Engineering, vol. 109, no. 3, pp. 338-50.

Raudkivi, A.J. (1986) : Functional trends of scour at bridge piers, Journal of Hydraulic Engineering, A.S.C.E., Vol.112(1), pp.1-13,.

Raudkivi AJ (1998). Loose boundary hydra1llics. AA Balkema. Rotterdam. Netherland

Chien N, Wan Z H. (1999), Mechanics of sediment transport. American Society of Civil Engineers, Virginia: ASCE Press

Ritter, A. (1982). “Die Fortpflanzung de Wasserwellen.” Zeitschrift Verein Deutscher Ingenieure”, 3633, 947–954 in German.

Rossetto, T., Allsop, W, Charvet, I, Robinson, D.I, (2011) “Physical modelling of tsunami using a new pneumatic wave generator” Coastal Engineering 58 (6), 517–527

Saatcioglu, M., Ghobarah, A., Nistor, I. (2006a). Performance of structures in Indonesia during the December 2004 Great Sumatra earthquake and Indian Ocean tsunami, Earthquake Spectra, Earthquake Engineering Research Institute, ASCE, 22(S3), 295-320 http://earthquakespectra.org/doi/pdf/10.1193/1.2209171

Saatcioglu, M., Ghobarah, A., Nistor, I. (2006b). Performance of structures in Thailand during the

2004 Great Sumatra earthquake and Indian Ocean tsunami, Earthquake Spectra, Earthquake Engineering Research Institute, ASCE, 22(S3), 355-376 http://earthquakespectra.org/doi/pdf/10.1193/1.2209175

Seiffert, B., Hayatdavoodi, M., Ertekin, R.C., (2014). Experiments and computations of solitary-wave forces on a coastal-bridge deck. Part I: Flat Plate. Coastal Engineering 88, 194209.

Shields A (1936); 'Application of similarity principles and turbulence research to bed load movement'". California Institute of Technology. Pasadena (translated from German)

Simon BD & Richardson EV (1966), "Resistance to flow in alluvial channels" US Geology Survey Professional Paper 422-.1

SISYPHE (2014). "User Manual" Sediment transport. SISYPHE V8.P0, TELEMAC Modelling System.

Soulsby R., (1997). Dynamics of marine sands. Thomas Thelford Edition

Sriram, V., Didenkulova, I., Sergeeva, A., Schimmels, S., (2016). Tsunami evolution and run-up in a large scale experimental facility. Coastal Engineering 111, 1–12.

Stansby, P. K., Chegini, A., and Barnes, T. C. D. (1998) “The initial stages of dam-break flow.” J. Fluid Mech., 370, 203–220

St-Germain P, Nistor I, Townsend R (2012) Numerical modeling of the impact with structures of tsunami bores propagating on dry and beds using the SPH method. International Journal of Protective Structures 3(2), 221–255.

Stoker, J. J. (1957). “Water waves: The mathematical theory with applications” Wiley Interscience, New York

Stolle, J., Takabatake T., Takahito M., Shibayama T., Goseberg, N., Nistor, I., Petriu E., (2017). “Laboratory Study of Debris Damming Loads and Effects in Flood Events” Geoscience, MDPI, 7(3), 74,

Stolle, J., Ghodoosipour, B., Derschum, C., Nistor, I., Petriu, E., Goseberg, N. (2018) Swing gate generated dam-break waves. J.Hydraul. Res., 1–13.

Stolle. J, (2019). Debris Hazard Assessment in Extreme Flooding Events. University of Ottawa. Canada.

Synolakis, C.E., Deb, M.K., Skjelbreia, J.E., (1988). The anomalous behavior of the runup of cnoidal waves. Physics of Fluids (1958-1988) 31, 3–5.

Tadepalli, S., Synolakis, C.E., (1994). The run-up of N-waves on sloping beaches, in: Proceedings Royal SocietyLondonAMathematical,Physical Engineering Sciences. The Royal Society, pp. 99–112.

Takahashi, S., Kuriyama, Y., Tomita, T., Kawai, Y., Arikawa, T., Tatsumi, D., (2011). Urgent survey for 2011 Great East Japan Earthquake and Tsunami disaster in ports and coasts—Part I (tsunami). Port and Air Port Research Institute.

Thanh Ca.V., Yamamoto, Y., Charusrojthanadech, N. (2012) Proceedings of the Twentieth International Offshore and Polar Engineering Conference Beijing, China, June 20-25

TELEMAC-3D (2018). "User Manual" TELEMAC-3D V8.P0. TELEMAC Modelling System.

TELEMAC-3D (2018), "Theory Guide" TELEMAC-2D V8.P0. TELEMAC Modelling System,

Tonkin, S., Yeh, H., Fuminori, K., & Shinji, S. (2003). “Tsunami scour around a cylinder”. Journal of Fluid Mechanics, 496, 165-192.

Tonkin, S.P, Francis, M., and Bricker, J.D. (2013) “Limits on Coastal Scour Depths due to Tsunami” In: Proceedings of the 14 Sixth China-Japan-US Trilateral Symposium on Lifeline Earthquake Engineering Davis, C., Du X., Miyajima, M., and Yan, 15 L., eds. TCLEE Monographs TCLEE 38, ASCE

Toro-Escobar, C, Voigt Jr, R, Melville, B, Chiew, M & Parker, G (1998), 'Riprap performance at bridge piers under mobile-bed conditions', Transportation Research Record, no. 1647, pp. 27-33

Treske, A. (1994). “Undular Bores (Favre-Waves) in Open Channels - Experimental Studies”. J of Hyd. Res., IAHR, Vol. 32, No. 3, pp. 355-370. Discussion: Vol. 33, No. 3, pp. 274-278.

Uda, T., Omata, A. & Yokoyama, Y. (1987) “Experimental study on tsunami run-up – the effects of coastal topography and structures against tsunami run-up,” Technical Note of Public Works Research Institute 2486 (in Japanese).

Van, M. C., Geldar, V. P. H. A & Vrijling, J. K. (2007) “Failure mechanisms of sea dikes Inventory and sensitivity analysis,” in Proc. of the Coastal Structures

van Rijn L.C., (1984). Sediment transport - Part I : bed load - Part II : suspended load, J. of Hydraulic Division, Proc. ASCE, 110, HY10, 1431-56, HY11, 1613-41.

van Rijn L.C., (1987). Mathematical modelling of morphological processes in the case of suspended sediment transport, Doctoral Thesis, Faculty of civil engineering, Delft University of technology).

van Rijn L.C., (1993). Principles of Sediment Transport in Rivers, Estuaries and Coastal Seas. Aqua Publications.

Vanoni VA (1975)-editor, Sedimentation Engineering. ASCE Press

Versteeg. HK & Malalasekera. W (1995), An introdllcliol1 10 Complltational Fluid Dynamics. mAddison Wesley Longman Limited. J-Iarlo\v, Essex. UK

Villaret C. and Tassi P., (2014). “Sisyphe 6.3 Reference manual”, Report EDF R&D H-P74-2012-02004-EN.

Von Häfen H., Stolle J., Goseberg N., Nistor I., (2018). Gate-Opening Criteria for Generating Dam-break Waves, J. of Hydraulic Eng., ASCE, (accepted, in press)

Wilcox DC (2000). Turhulence modellingfor CFD. DCW Industries. California, USA

Williams, I.A., Fuhrman, D.R., (2016). Numerical simulation of tsunami-scale wave boundary layers.Coast Eng. 110, 17–31

Wilson, R., Davenport, C., Jaffe, B., (2012). Sediment scour and deposition within harbors in California (USA), caused by the March 11, 2011 Tohoku-Oki tsunami. Sediment. Geol. 282, 228–240.

Wüthrich, D., Pfister M., Nistor I., Schleiss A.J. (2018). Experimental study on the hydrodynamic impact of tsunami-like waves against impervious free-standing buildings, Coastal Engineering Journal, JSCE, Taylor and Francis, (published online, https://doi.org/10.1080/21664250.2018.1466676)

Wüthrich, D., Pfister M., Nistor I., Schleiss A.J. (2020). Effect of overtopping on wave-induced loads on impervious free-standing buildings, J. of Hydraulic Res., IAHR 58:2, 289-304, https://www.tandfonline.com/doi/full/10.1080/00221686.2019.1573764

Yao, Y., Huang, Z., Lo, E.Y.M., Shen, H.-T., (2014). A preliminary laboratory study of motion of floating debris generated by solitary waves running up a beach. Journal of Earthquake and Tsunami 8.

Yang CT (1973). "Incipient motion and sediment transport" J Hydt. Dil'. ASCE. Vol. 99. Issue HYlO. pp 1679-1704

Yang CT (1996), Sediment transport. thec) JY ({nd practice, McGraw-Hili Inc. New York, USA

Yu-Hai Wang, Wei-Guo Jiang, and Yan-Hong Wang, (2013) “Scale Effect in Scour Physical Model Tests: Cause and Alleviation” Journal of Marine Science and Technology, Vol. 21, No. 5, pp. 532-537 DOI: 10.6119/JMST-012-0718-2

Yeganeh-Bakhtiary, A., Ghorbani, M. & Pourzangbar, A. (2012) “Determination of the most important parameters on scour at coastal structures,” J. Civil Eng. Urbanism **2**(2), 68–72.

Yeh, H., Kato, F., and Sato, S. (2001). Tsunami scour mechanisms around a cylinder. Tsunami Research at the End of a Critical Decade (Ed: G.T. Hebenstreit), Kluwer Academic Publishers. 33−46.

Yeh, H., Robertson, I., and Preuss, J., (2005), Development of Design Guidelines for Structures that Serve as Tsunami Vertical Evacuation Sites, Open File Report 2005-4, Washington Division of Geology and Earth Resources, State of Washington (contract 52-AB-NR-200051), Olympia, Washington

Yeh, H., Tonkin, S., Heller, E., Arduino, P., Kato, F., and Sato, S. (2004). “Mechanisms of scour induced by tsunami runup” Proceedings of Seccond International Conference on SCOUR and EROSION, Singapore Vol 2, 464−471

Yeh, H. (2006) Maximum Fluid Forces in the Tsunami Runup Zone, Journal of Waterway Port and Coastal Engineering, November/December, ASCE, Reston, VA.

Yeh, H and Li, W (2008) “Tsunami Scour and Sedimentation”, Fourth International Conference on Scour and Erosion, pp. 95-106.

Yeh, H., (2009). In: Bernard, E.N., Robinson, A.R. (Eds.), “The Sea – Tsunamis”. Harvard University Press, pp. 333–369

Yeh, H. (2010) “Tsunami effects on coastal infrastructures and how to evaluate them,” Northwest Transportation Conf., USA, 1–39.

Yeh, H., Sato, S. & Tajima, Y. (2013). The 11 March 2011 East Japan earthquake and tsunami: tsunami effects on coastal infrastructure and buildings. Pure and Applied Geophysics 170(6-8), 1019–1031.

Yeh, H. & Mason, H. B. (2014). Sediment response to tsunami loading: mechanisms and estimates, Géotechnique 64, No. 2, 131–143 [http://dx.doi.org/10.1680/geot.13.P.033]

Young, Y.L. Xiao. H, Maddux.T. (2010) “Hydro- and morpho-dynamic modeling of breaking solitary waves over a fine sand beach” Part I: Experimental study.Marine Geology. .269(3-4):107-118

Young DF. Bruce RM & Theodore HO (1997). A brief introduction of fluid mechanic, John Wiley & Sons. Inc. Ne\v York

Yoshii, T, Ikeno. M, Matsuyama. M and Fujii N. (2010) “Pick-up Rate of Suspended Sand Due to Tsunami” Conference on Coastal Engineering” Shanghai [s.n.], - Vol. 32

Zarrati, A.R., Gholami, H, Mashahir, M.B. (2004) “Application of Collar to Control Scour Around Rectangular Bridge Pier”, J. Hydraulic Research, IAHR, 42(1), 97-103.

Zyserman J.A. and Fredsoe J. (1994). Data analysis of bed concentration of suspended sediment, Journal of Hydraulic Engineering, ASCE, Vol. 120, N_9, pp 1021-1042.

Zhao, M., Cheng, L. & Zang, Z. (2010) “Experimental and numerical investigation of local scour around a submerged vertical circular cylinder in steady currents” Coastal Eng. 57, 709 772.

APPENDIX A

APPENDIX A - HYDRODYNAMIC AND SEDIMENT TRANSPORT NUMERICAL PARAMETERS

HYDRODYNAMIC PARAMETERS FILES

```
/----------------------------------------------------------------------
/ TELEMAC3D VERSION V7P1 NOV 29, 2016
/ NOM INCONNU
/----------------------------------------------------------------------
/----------------------------------------------------------------------
/ EQUATIONS
/----------------------------------------------------------------------
LAW OF BOTTOM FRICTION             =4
FRICTION COEFFICIENT FOR THE BOTTOM =0.028
/----------------------------------------------------------------------
/ EQUATIONS, INITIAL CONDITIONS
/----------------------------------------------------------------------
INITIAL CONDITIONS ='CONSTANT ELEVATION'
INITIAL ELEVATION  = 0.05
VARIABLES FOR 2D GRAPHIC PRINTOUTS = 'U,V,H,S,B'
VARIABLES FOR 3D GRAPHIC PRINTOUTS = 'Z,U,V,H,B'
/----------------------------------------------------------------------
/ INPUT-OUTPUT, FILES
/----------------------------------------------------------------------
STEERING FILE           ='CASE1.CAS'
GEOMETRY FILE             ='PIERSCOUR.SLF'
COUPLING WITH             ='SISYPHE'
3D RESULT FILE          ='RESULTWITHSIS3DDRYCV.SLF'
SISYPHE STEERING FILE    ='SIS.CAS'
2D RESULT FILE          ='RESULTWITHSIS2DDRYCV.SLF'
FORTRAN FILE            ='SIM3D.F'
BOUNDARY CONDITIONS FILE ='BOTTOM_BC.CLI'
/----------------------------------------------------------------------
```

```
/ INPUT-OUTPUT, GRAPHICS AND LISTING
/----------------------------------------------------------------------
GRAPHIC PRINTOUT PERIOD =10
/----------------------------------------------------------------------
/ NUMERIC PARAMETERS
/----------------------------------------------------------------------
NUMBER OF HORIZONTAL LEVELS =6
NUMBER OF TIME STEPS        =800
/----------------------------------------------------------------------
/ NUMERICAL PARAMETERS
/----------------------------------------------------------------------
PRESCRIBED ELEVATIONS =0
/DEBUGGER              =1
TIME STEP            =0.02
DURATION             =60
/----------------------------------------------------------------------
/ NON-HYDROSTATIC
/----------------------------------------------------------------------
NON-HYDROSTATIC VERSION =    YES
/DYNAMIC PRESSURE IN WAVE EQUATION =NO
/NUMBER OF SUB ITERATIONS FOR NON LINEARITIES =10
/VARIABLES FOR 2D GRAPHIC PRINTOUTS = 'U, V, H, B'
/VARIABLES FOR 3D GRAPHIC PRINTOUTS = 'H, U, V, B'
GRAPHIC PRINTOUT PERIOD = 100
NUMBER OF FIRST TIME STEP FOR GRAPHIC PRINTOUTS = 4
LISTING PRINTOUT PERIOD=60
MASS-BALANCE = YES
/----------------------------------------------------------------------
/ TURBULENCE
/----------------------------------------------------------------------
COEFFICIENT FOR HORIZONTAL DIFFUSION OF VELOCITIES = 1.0D-6
COEFFICIENT FOR VERTICAL DIFFUSION OF VELOCITIES = 1.0D-6
HORIZONTAL TURBULENCE MODEL =4
/ 1: CONSTANT VISCOSITY,
/ 3: K-E MODEL,
/ 4: SMAGORINSKI,
/ 7: K-W MODEL.
VERTICAL TURBULENCE MODEL=4 / 1. CST VISCO 2. MIXING LENGTH 3. K-EPS
/MIXING LENGTH MODEL = 1  / 1. PRANTL 3. NEZU AND NAKAGAWA
/DAMPING FUNCTION = 3 / 2. VIOLLET 3. MUNK AND ANDERSON
/OPTION FOR THE BOUNDARY CONDITIONS OF K-EPSILON=1
/MIXING LENGTH MODEL  (VERTICAL TURBULENCE)
/TURBULENCE REGIME FOR LATERAL SOLID BOUNDARIES
/TURBULENCE REGIME FOR THE BOTTOM
/ACCURACY FOR DIFFUSION OF TRACERS = 1.E-6
/MAXIMUM NUMBER OF ITERATIONS FOR DIFFUSION OF TRACERS = 200
/----------------------------------------------------------------------
/ NUMERICAL PAREMETERS
/----------------------------------------------------------------------
/TREATMENT OF THE LINEAR SYSTEM =2 /WAVE EQUATION
MASS-LUMPING FOR DEPTH =1
/MASS-LUMPING FOR DIFFUSION=0
MASS-LUMPING FOR VELOCITIES=1
FREE SURFACE GRADIENT COMPATIBILITY =0.9
/TYPE OF ADVECTION =1;5;14  /14;5;14 AUSSI RECOMMANDE AVEC TIDAL FLATS
/SUPG OPTION =0;0;0
/SOLVER =1 /CONJUGATE GRADIENT METHOD
SOLVER FOR DIFFUSION OF TRACERS =1 /CONJUGATE GRADIENT METHOD
/SOLVER FOR K-EPSILON MODEL
/CONTINUITY CORRECTION =YES
/VARIABLE TIME STEPS = YES
```

```
/DESIRED COURANT NUMBER =1
/-----ADVECTION--------
SUPG OPTION =0;0;0
SCHEME FOR ADVECTION OF VELOCITIES=14
SCHEME OPTION FOR ADVECTION OF VELOCITIES=1
SCHEME FOR ADVECTION OF DEPTH=5
/SCHEME FOR ADVECTION OF K-EPSILON=14
/SCHEME OPTION FOR ADVECTION OF K-EPSILON=1
/SCHEME FOR ADVECTION OF TRACERS=5
NUMBER OF SUB ITERATIONS FOR NON LINEARITIES=1
NUMBER OF CORRECTIONS OF DISTRIBUTIVE SCHEMES=0
NUMBER OF SUB-STEPS OF DISTRIBUTIVE SCHEMES=2
/-------DIFFUSION--------
SCHEME FOR DIFFUSION OF VELOCITIES=1
SCHEME FOR DIFFUSION OF TRACERS=1
SCHEME FOR DIFFUSION OF K-EPSILON=1
/OPTION FOR THE DIFFUSION=
/-------IMPLICITATION--------
IMPLICITATION FOR VELOCITIES=1
IMPLICITATION FOR DEPTH=1
/IMPLICITATION FOR DIFFUSION=1
/-------SOLVERS---------
/ DEFAUT: CONJUGATE GRADIENT METHOD
SOLVER FOR DIFFUSION OF TRACERS =1 /CONJUGATE GRADIENT METHOD
/SOLVER FOR DIFFUSION OF K-EPSILON
/SOLVER FOR DIFFUSION OF VELOCITIES
/SOLVER FOR PROPAGATION
/SOLVER FOR VERTICAL VELOCITY
/-------PRECONDITIONING------
/PRECONDITIONING FOR DIFFUSION OF VELOCITIES=2
/PRECONDITIONING FOR PROPAGATION=2
/PRECONDITIONING FOR PPE=2
/PRECONDITIONING FOR VERTICAL VELOCITY=2
/PRECONDITIONING FOR DIFFUSION OF TRACERS=2;2
/PRECONDITIONING FOR DIFFUSION OF K-EPSILON=2
OPTION FOR LIQUID BOUNDARIES    = 2
/-------MASS LUMPING---------
MASS-LUMPING FOR DEPTH =1
/MASS-LUMPING FOR DIFFUSION=1
MASS-LUMPING FOR VELOCITIES=1
/-------OTHER---------
TIDAL FLATS = YES
OPTION FOR THE TREATMENT OF TIDAL FLATS =1
TREATMENT OF NEGATIVE DEPTHS =2
/HYDROSTATIC INCONSISTENCY FILTER = YES
FREE SURFACE GRADIENT COMPATIBILITY =0.9
NON-HYDROSTATIC VERSION = NO
```

SISYPHE PARAMETERS FILES

```
/---------------------------------------------------------------------
/ SISYPHE VERSION V7P1 NOV 29, 2016
/ NOM INCONNU
/---------------------------------------------------------------------
/---------------------------------------------------------------------
/ BED MATERIAL
/---------------------------------------------------------------------
SEDIMENT DIAMETERS =0.01
D90                =.01
BED-LOAD TRANSPORT FORMULA =1
/---------------------------------------------------------------------
/ DATA FILES
/---------------------------------------------------------------------
BOUNDARY CONDITIONS FILE ='BOTTOM_BC.CLI'
/---------------------------------------------------------------------
/ FRICTION
/---------------------------------------------------------------------
/LAW OF BOTTOM FRICTION =4
/FRICTION COEFFICIENT   =0.012
/---------------------------------------------------------------------
SHIELDS PARAMETERS =0.022
/---------------------------------------------------------------------
/ INPUT-OUTPUT, FILES
/---------------------------------------------------------------------
GEOMETRY FILE ='PIERSCOUR.SLF'
/---------------------------------------------------------------------
/ MISCELLANEOUS
/---------------------------------------------------------------------
DEBUGGER =1
/---------------------------------------------------------------------
/ NUMERICAL PARAMETERS
/---------------------------------------------------------------------
SOLVER FOR SUSPENSION =7
/---------------------------------------------------------------------
/ RESULTS
/---------------------------------------------------------------------
GRAPHIC PRINTOUT PERIOD =10
RESULTS FILE           ='R2SIS.SLF'
/---------------------------------------------------------------------
/ SLOPE EFFECT
/---------------------------------------------------------------------
SEDIMENT SLIDE               =TRUE
FRICTION ANGLE OF THE SEDIMENT =35
/---------------------------------------------------------------------
```

```
/ SOLVER
/---------------------------------------------------------------------
/SOLVER OPTION FOR SUSPENSION =3
/---------------------------------------------------------------------
/ SUSPENSION
/---------------------------------------------------------------------
/SUSPENSION          =TRUE
SETTLING VELOCITIES =0.1
/TETA SUSPENSION     =0.5
/---------------------------------------------------------------------
/ TIME
/----------------------------------------------------------------------
STEERING FILE                ='SIS.CAS'
MEAN DIAMETER OF THE SEDIMENT =.01
```

MODIFIED FORTRAN CODES DEVELOPED FOR THE NUMERICAL WORK

```
!                    ********************
                     SUBROUTINE CONDI3DH
!                    ********************
!***********************************************************************
! TELEMAC3D   V7P3
!***********************************************************************
!
!BRIEF    INITIALISES DEPTH
!
!HISTORY  C.-T. PHAM (LNHE)
!+        24/03/2017
!+        V7P3
!+   CREATION FROM NOT SPLITTED CONDIM
!+   CALLED BY CONDIM
!
!HISTORY  C.-T. PHAM (EDF, LNHE)
!+        01/08/2017
!+        V7P3
!+   CHANGE IN THE NUMBER OF ARGUMENTS WHEN CALLING CONDI_TPXO
!
!~~~~~~~~~~~~~~~~~~~~~~~~~~~~~~~~~~~~~~~~~~~~~~~~~~~~~~~~~~~~~~~~~~~~~~~
!~~~~~~~~~~~~~~~~~~~~~~~~~~~~~~~~~~~~~~~~~~~~~~~~~~~~~~~~~~~~~~~~~~~~~~~
!
      USE BIEF
      USE INTERFACE_TELEMAC3D, EX_CONDI3DH => CONDI3DH
      USE DECLARATIONS_TELEMAC
      USE DECLARATIONS_TELEMAC3D
      USE TPXO
!
      USE DECLARATIONS_SPECIAL
      IMPLICIT NONE
!
!-----------------------------------------------------------------------
!
      INTEGER I
!
!-----------------------------------------------------------------------
!
!     INITIALISES H, THE WATER DEPTH
```

```
!
      IF(.NOT.SUIT2) THEN
!
      IF(CDTINI(1:10).EQ.'COTE NULLE'.OR.
     &   CDTINI(1:14).EQ.'ZERO ELEVATION') THEN
        CALL OS('X=C     ', X=H, C=0.D0)
        CALL OV('X=X-Y   ', X=H%R, Y=Z, DIM1=NPOIN2)
      ELSEIF(CDTINI(1:14).EQ.'COTE CONSTANTE'.OR.
     &       CDTINI(1:18).EQ.'CONSTANT ELEVATION') THEN
        CALL OS('X=C     ', X=H, C=COTINI)
        CALL OV('X=X-Y   ', X=H%R, Y=Z, DIM1=NPOIN2)
      ELSEIF(CDTINI(1:13).EQ.'HAUTEUR NULLE'.OR.
     &       CDTINI(1:10).EQ.'ZERO DEPTH') THEN
        CALL OS('X=C     ', X=H, C=0.D0)
      ELSEIF(CDTINI(1:17).EQ.'HAUTEUR CONSTANTE'.OR.
     &       CDTINI(1:14).EQ.'CONSTANT DEPTH') THEN
        CALL OS('X=C     ', X=H, C=HAUTIN)
      ELSEIF(CDTINI(1:25).EQ.'ALTIMETRIE SATELLITE TPXO'.OR.
     &       CDTINI(1:24).EQ.'TPXO SATELLITE ALTIMETRY') THEN
        CALL OS('X=-Y    ', X=H, Y=ZF)
        CALL CONDI_TPXO(NPOIN2,MESH2D%NPTFR,MESH2D%NBOR%I,
     &                  X2%R,Y2%R,H%R,U2D%R,V2D%R,
     &                  LIHBOR%I,LIUBOL%I,KENT,KENTU,
     &                  GEOSYST,NUMZONE,T3DL93,LATIT,LONGIT,
     &                  T3D_FILES,T3DBB1,T3DBB2,
     &                  MARDAT,MARTIM,INTMICON,MSL,
     &                  TIDALTYPE,BOUNDARY_COLOUR,ICALHWG)
      ELSEIF(CDTINI(1:13).EQ.'PARTICULIERES'.OR.
     &       CDTINI(1:10).EQ.'PARTICULAR'.OR.
     &       CDTINI(1:07).EQ.'SPECIAL') THEN
!     USER INPUT :
!     PROGRAM HERE SPECIAL INITIAL CONDITIONS ON DEPTH
        WRITE(LU,11)
11      FORMAT(1X,'CONDI3DH: WITH SPECIAL INITIAL CONDITIONS'
     &      ,/,1X,'          YOU HAVE TO MODIFY CONDI3DH')
        CALL PLANTE(1)
        STOP
!     END OF SPECIAL INITIAL CONDITIONS
!     END OF USER INPUT
      ELSE
        WRITE(LU,*) 'CONDI3DH: INITIAL CONDITION UNKNOWN: ',CDTINI
        CALL PLANTE(1)
        STOP
      ENDIF
      ELSE
        WRITE(LU,*) 'DEPTH IS READ IN THE BINARY FILE 1'
      ENDIF
              CALL CORSUI(H%R,Z,X,Y,NPOIN2)
!
!     CLIPS H
!
      DO I=1,NPOIN2
        H%R(I)=MAX(H%R(I),0.D0)
      ENDDO
!
```

```
      CALL OS('X=Y     ', X=HN, Y=H)
!
!-----------------------------------------------------------------------
!
      RETURN
      END
 !              ***************************************************
              DOUBLE PRECISION FUNCTION DISTAN(X1,Y1,X2,Y2,X3,Y3)
!              ***************************************************
!
!***********************************************************************
! PROGICIEL : TELEMAC           23/07/91
!
!***********************************************************************
!
!   FONCTION : CETE FONCTION CALCULE LA DISTANCE ENTRE UNE DROITE
! ET UN POINT SUR LE MAILLAGE
!-----------------------------------------------------------------------
!                         ARGUMENTS
! .________________.____.______________________________________________.
! |      NOM       |MODE|                   ROLE                       |
! |________________|____|______________________________________________|
! |    X1          | -->  ABSCISSE DU PREMIER POINT SUR LA DROITE
! |    Y1          | -->| COORDONNEE DU PREMIER POINT SUR LA DROITE
! |    X2          | -->  ABSCISSE DU DEUXIEME POINT SUR LA DROITE
! |    Y2          | -->| COORDONNEE DU DEUXIEME POINT SUR LA DROITE
! |    X           | -->| ABSCISSE DU POINT POUR LEQUEL ON CHERCHE DIST1
! |    Y           | -->| COORDONNEE DU POINT POUR LEQUEL ON CHERCHE DIS
! |    DISTAN      |<-- |  DISTANCE ENTRE LA DROITE ET LE POINT
! |________________|____|_______________________________________________
! MODE : -->(DONNEE NON MODIFIEE), <--(RESULTAT), <-->(DONNEE MODIFIEE)
!***********************************************************************
!
!
      USE DECLARATIONS_SPECIAL
      IMPLICIT NONE
      DOUBLE PRECISION X1,X2,X3,Y1,Y2,Y3
      DOUBLE PRECISION A1,B1,C1,DET
      INTRINSIC SQRT
      A1=Y1-Y2
      B1=-X1+X2
      C1=X1*Y2-X2*Y1
      DET=SQRT((A1**2)+(B1**2))
      DISTAN=((A1*X3)+(B1*Y3)+C1)/DET
      RETURN
      END
!                    *****************
                     SUBROUTINE CORSUI
!                    *****************
!
!
     &(H,ZF,X,Y,NPOIN2)
!
!***********************************************************************
! PROGICIEL : TELEMAC           01/03/90    J-M HERVOUET
```

```
!***********************************************************************
!
!  FONCTION  : FONCTION DE CORRECTION DES FONDS RELEVES
!
!            CE SOUS-PROGRAMME UTILITAIRE NE FAIT RIEN DANS LA
!            VERSION STANDARD. IL EST A LA DISPOSITION DES
!            UTILISATEURS, POUR LISSER OU CORRIGER DES FONDS SAISIS
!            PAR EXEMPLE.
!
!-----------------------------------------------------------------------
!                        ARGUMENTS
! .________________.____.______________________________________________
! |      NOM       |MODE|                   ROLE
! |________________|____|_______________________________________________
! |      ZF        |<-->| FOND A MODIFIER.
! |      X,Y,(Z)   | -->| COORDONNEES DU MAILLAGE (Z N'EST PAS EMPLOYE).
! |      NPOIN     | -->| NOMBRE DE POINTS DU MAILLAGE.
! |________________|____|______________________________________________
! MODE : -->(DONNEE NON MODIFIEE), <--(RESULTAT), <-->(DONNEE MODIFIEE)
!-----------------------------------------------------------------------
!
! PROGRAMME APPELANT : TELMAC
! PROGRAMMES APPELES : RIEN EN STANDARD
!
!***********************************************************************
!
      USE DECLARATIONS_SPECIAL
      IMPLICIT NONE
!
      INTEGER NPOIN2,I
!
      DOUBLE PRECISION H(*),X(*),Y(*),ZF(*)
!
      DOUBLE PRECISION DISTAN,X1,X2,Y1,Y2,HD
      EXTERNAL DISTAN
!
!-----------------------------------------------------------------------
!
!   INITIALISATION DES VARIABLES POUR LE CALCUL DE LA SITUATION DU POINT
!   X1,Y1,X2,Y2 POINT DEFINISANT LA DROITE DE LIMITE DE BARRAGE
!   X3,Y3 POINT DEFINISANT LES COORDONNEES D POINT A DROITE DE LIMITE DE
!
      X1= 21.55D0
      Y1= 0.00D0
      X2= 21.55D0
      Y2= 1.5D0
!
      DO I=1,NPOIN2
        HD=DISTAN(X1,Y1,X2,Y2,X(I),Y(I))
        IF(HD.GT.0.001D0) THEN
          H(I) = 0.250D0
        ENDIF
!
!  ZONE DERRIERE LE BARRAGE MAIS QUI N'EST PAS DANS
!  LA RETENUE.
```

```
!
!       IF((X(I)-4500.D0)**2+(Y(I)-5350.D0)**2.LT.200.D0**2) THEN
!         H(I)=0.D0
!       ENDIF
!
!       H(I)=MAX(0.D0,H(I))
!
      ENDDO
!
!-----------------------------------------------------------------------
!
      RETURN
      END
!                    *****************
                     SUBROUTINE NOEROD
!                    *****************
!
     &(H , ZF , ZR , Z , X , Y , NPOIN2 , CHOIX , NLISS )
!
!***********************************************************************
! SISYPHE   V6P3                                   21/07/2011
!***********************************************************************
!
!BRIEF    FIXES THE NON-ERODABLE BED ELEVATION ZR.
!
!NOTE     METHODS OF TREATMENT OF NON-ERODABLE BEDS CAN LEAD TO ZF.
!NOTE  CHOOSE TO SMOOTH THE SOLUTION WITH NLISS > 0.
!
!HISTORY  C. LENORMANT
!+
!+        V5P1
!+
!
!HISTORY  N.DURAND (HRW), S.E.BOURBAN (HRW)
!+        13/07/2010
!+        V6P0
!+   TRANSLATION OF FRENCH COMMENTS WITHIN THE FORTRAN SOURCES INTO
!+   ENGLISH COMMENTS
!
!HISTORY  N.DURAND (HRW), S.E.BOURBAN (HRW)
!+        21/08/2010
!+        V6P0
!+   CREATION OF DOXYGEN TAGS FOR AUTOMATED DOCUMENTATION AND
!+   CROSS-REFERENCING OF THE FORTRAN SOURCES
!
!HISTORY  J-M HERVOUET (EDF R&D, LNHE)
!+        21/06/2013
!+        V6P3
!+   NOW ZR=ZF-100.D0 BY DEFAULT
!+   PREVIOUS VERSIONS WAS ERRONNEOUSLY ZR=-100.D0
!
!~~~~~~~~~~~~~~~~~~~~~~~~~~~~~~~~~~~~~~~~~~~~~~~~~~~~~~~~~~~~~~~~~~~~~~~
!| CHOIX          |-->| SELECTED METHOD FOR THE TREATMENT OF RIGID BEDS
!| H              |-->| WATER DEPTH
!| NLISS          |<->| NUMBER OF SMOOTHINGS
```

```
!| NPOIN          |-->| NUMBER OF 2D POINTS
!| X,Y            |-->| 2D COORDINATES
!| Z              |-->| FREE SURFACE
!| ZF             |-->| BED LEVEL
!| ZR             |<--| RIGID BED LEVEL
!~~~~~~~~~~~~~~~~~~~~~~~~~~~~~~~~~~~~~~~~~~~~~~~~~~~~~~~~~~~~~~~~~~~~~~~~~~~~~~~~~~~~~~~~~~
!
      USE BIEF
!
      USE DECLARATIONS_SPECIAL
      IMPLICIT NONE
!
!+-+-+-+-+-+-+-+-+-+-+-+-+-+-+-+-+-+-+-+-+-+-+-+-+-+-+-+-+-+-+-+-+-+-+-+-+-+-+-+-+
!
      INTEGER, INTENT(IN):: NPOIN2 , CHOIX
      INTEGER, INTENT(INOUT):: NLISS
!
      DOUBLE PRECISION, INTENT(IN)::  Z(NPOIN2) , ZF(NPOIN2)
      DOUBLE PRECISION , INTENT(IN)::  X(NPOIN2) , Y(NPOIN2), H(NPOIN2)
      DOUBLE PRECISION , INTENT(INOUT)::  ZR(NPOIN2)
!
!+-+-+-+-+-+-+-+-+-+-+-+-+-+-+-+-+-+-+-+-+-+-+-+-+-+-+-+-+-+-+-+-+-+-+-+-+-+-+-+-+
!
!     INTEGER I
      DOUBLE PRECISION   PI,XMAX,XMIN,ZEMAX
            INTEGER I
!---------------------
! RIGID BEDS POSITION
!---------------------
!
!     DEFAULT VALUE: ZR=ZF-100.D0
!
        ZEMAX=0.8D0
        CALL OV( 'X=Y+C     ',ZR,ZF,ZF,-ZEMAX,NPOIN2)
              XMAX=26.D0
        DO I=1,NPOIN2
           IF(X(I).LE.XMAX) THEN
            ZR(I)=ZF(I)
          ENDIF
        ENDDO
!
!------------------
! SMOOTHING OPTION
!------------------
!
!     NLISS : NUMBER OF SMOOTHING IF  (ZF - ZR ) NEGATIVE
!             DEFAULT VALUE : NLISS = 0 (NO SMOOTHING)
!
      NLISS = 0
!
!--------------------------------------------------
! CONTROL (CAN BE ACTIVATED IF ZR USER DEFINED...)
!--------------------------------------------------
!
!     DO I=1,NPOIN
```

```
!       IF(ZR(I).GT.ZF(I)) THEN
!         WRITE(LU,*) 'POINT ',I,' NON ERODABLE BED HIGHER THAN BED'
!         CALL PLANTE(1)
!         STOP
!       ENDIF
!     ENDDO
!
!-----------------------------------------------------------------------
!
      RETURN
      END
```

APPENDIX B

APPENDIX B – PUBLISHED CONFERENCE PAPERS

EXPERIENTAL MODELLING OF SUPERCRITICAL FLOWS-INDUCED EROSION AROUND STRUCTURES

Published in the proceeding of the 6th international conference on the application of physical modelling in coastal and port engineering and science (coastlab16), Ottawa, Canada, (2016).

Abstract: In recent years, extreme natural phenomena such as extreme tsunamis have affected populated coastal regions around the Indian and Pacific Oceans and caused significant loss of life and extensive damage to coastal communities. The present study investigates scour mechanisms around a square structure due to an inland-propagating tsunami-like bore using physical modelling. A series of hydraulic bores was simulated using the dam-break method in a flume at the University of Ottawa Hydraulics Laboratory. The dam-break wave was generated by releasing water impounded behind a rapidly-opening swing gate. A video-recording system was used to record the evolution the of scour and vortex structure. Image processing allowed tracking the time and spatial evolution of the scour around the structure. Additionally, characteristics of the bore, including bore depth-time history and bore front velocity for different initial downstream conditions (dry bed vs wet bed) will be presented. Also, the parameters affecting local scour will be presented and discussed.

KEWORDS: Tsunami scour, Physical modeling, Square structure, Sediment.

Introduction

It is well documented that the tsunamis cause substantial erosion and scour along the shoreline affected by inundation. The international Tsunami Survey Team (ITST, 2005) documented the existence of scour damage around the foundation of a lighthouse tower near the coast of Banda Aceh, Indonesia. Many research have so far been conducted about scour around coastal structures in a marine environment. In post-tsunami forensic engineering surveys of India and Thailand following the 2004 Great Sumatra Andaman tsunami, researchers were able to document local scour occurrences not only at buildings located close to shore, but also hundreds of meters inland (Nistor (2012); Tonkin (2013)) as shown in Fig. 1

a) **b)**

Figure.1: Local scour due to tsunami bore around building foundation a) Japan (courtesy of Dr. Ioan Nistor, 2012); b) Local scour, Koh Khao, Thailand. Case SS-4. Tonkin (2013)

Laboratory experiments related to scour around structures caused by tsunamis are limited. Two studies that are the most related to the research are Tonkin (2003) and Nakamura (2008). The first one, by Tonkin (2003), examines scour around a cylindrical structure located on a sloped sandy beach, whereas the other study of Nakamura (2008), focuses on scour around a square structure located on a horizontal sand bed. Both studies underline that such a tsunami-induced scour hole occurs in a transient flow which exhibits different mechanisms from a steady current and a consistent short-wave field. They demonstrated that a transient flow condition such as the one generated by solitary waves creates pore pressure gradients inside the seabed, probably resulting in the acceleration of local scour. In this study the scouring mechanism around the square structure due to inland-propagating tsunami bores using experimental modeling has been investigated. Since a tsunami is composed in fact of a series of waves, the bore front of the first wave reaching the shoreline will generally propagate onshore over dry land. Subsequent waves will then advance overland which was previously flooded by the first wave. Therefore, the current study focuses on inland structures located on both dry and flooded horizontal land (bed).

Experimental setup

Hydraulic bores were simulated using the dam-break method in a flume located in Hydraulics Laboratory at the University of Ottawa. The flume is 30 *m* long, 1.5 *m* wide and 1 *m* deep. The dam-break wave was generated by releasing water impounded behind a rapidly-opening swinging gate which was equipped with a lock and release mechanism. Two aluminum false floors with a height of 0.2 *m* were installed before and after the sediment bed in downstream of the gate to provide a formwork for the sediment section as shown in Fig. 2.

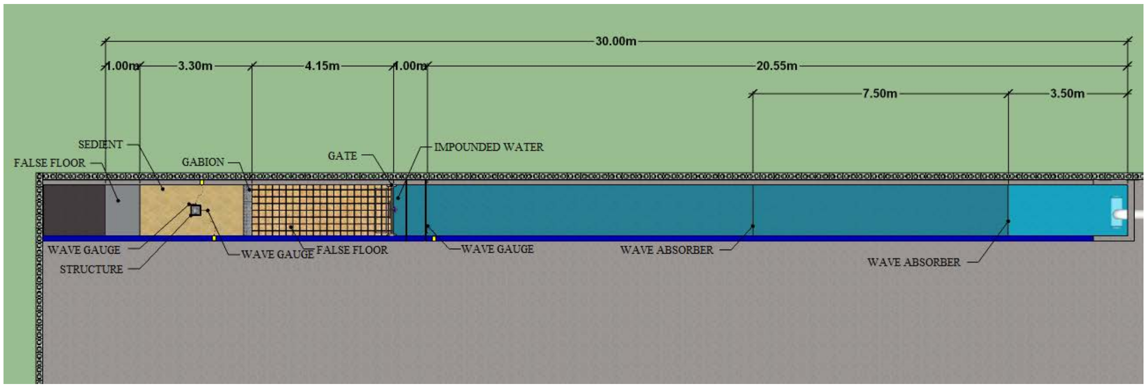

Figure.2: Experimental setup - plan view

The upstream false floor had a length of 4.15 *m* and the downstream had a length of 1 *m*. The upstream false floor was covered with a layer of glued sand with a uniform grain size of 1 mm, in order to provide roughness. A grid system of 20 x 20 *cm* spacing was also painted on the top surface of the upstream false floor for measurement purposes. The sediment bed section was 3.30 *m* long and 1.5 *m* wide, delimited at each end by the false floors. The base of the sediment bed was composed of a layer of 1cm thick course gravel covered by a geotextile sheet. This drained water that infiltrated below the false floor and eventually reached the sediment bed. Right after the upstream false floor, a 15 *cm* wide gabion was installed across the flume. The gabion was constructed with wire box filled with coarse gravel of approximately 3cm thick. The gabion used to minimize the inevitable local scour that would occur at the interface of false floor and sediment section. Three structures made of Plexiglas with different square cross section size of 0.3 *m*, 0.2 *m* and 0.1*m* wide were used in the experiment. The structures were installed in the center of sediment section which was filled with 1 *mm* uniform sand. Also, three wave absorbers were installed in order to attenuate secondary waves within the reservoir and prevent reflective waves-induced in water level fluctuation at the test section. Three WG-50 capacitance type wave gauges with an accuracy of 0.4% were used to record the time-history of the water surface elevation at different locations of the experimental setup using a sampling rate of 30 Hz. Two wave gauges were positioned as follows: one on the front face and the other one on the side face of the structure. The third wave gauge was placed at a distance of 1.0 *m* behind the swing gate, inside the reservoir. This wave gauge was used to record the time-history of the water surface elevation within the reservoir over the duration of the test. Two video cameras, the GoPro Hero Black and the IO Industrial Flare™ high speed video camera, were also used during the experimental investigations for different purposes. Firstly, it was used to track the bore front as it propagated downstream, towards the structure, in order to estimate bore front velocities. The second was used for particle tracking velocimetry (PTV) measurements. The three-square structures were transparent to allow for monitoring the scouring process by means of the high speed camera which was placed at the top of the structure. The monitoring was achieved with the help of a mirror inclined at 45° inside the structure as shown in Fig. 3 (*a*), (*b*). Finally, a Disto TM laser altimeter with a precision of ± 1.00 *mm* were used to measure the final local scour around the structure at the end of each test.

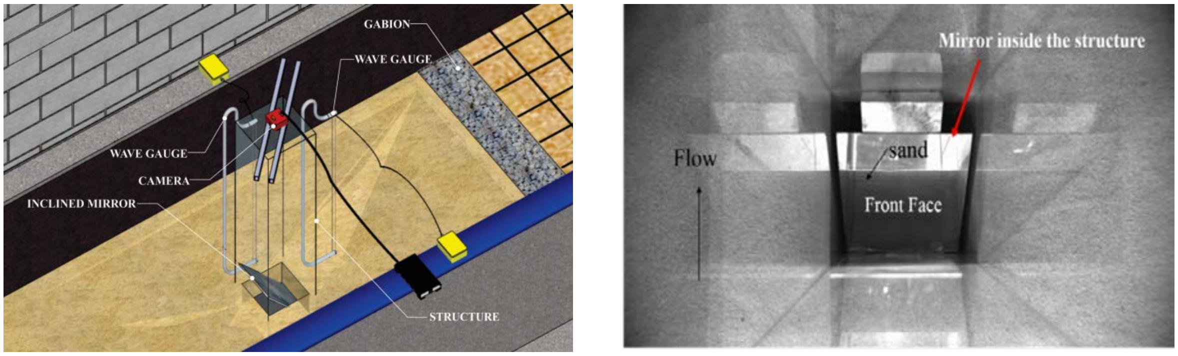

a) b)

Figure. 3: Experiment setup to monitor the scour process (a); Reflected (looking from above-mirror inside) view of the structure's front face (b)

Experimental test program

The research program employed different impounded depths with the purpose of generating different initial downstream water depths. Once the reservoir was filled to the desired level, initial inflow was stopped. In order to investigate effect of bed condition on bore velocity and scour depth, two initial conditions (wet versus dry condition) were considered for downstream of the gate. Schematic illustration of the experiment is presented in Fig. 4, where h and d_1 are the initial water depth (*m*) in upstream and downstream of the gate respectively. d_2 is a flow depth (*m*) immediately behind the positive surge, U is a bore front velocity (*m/s*), also V_2 is a flow velocity (*m/s*) immediately behind the positive surge.

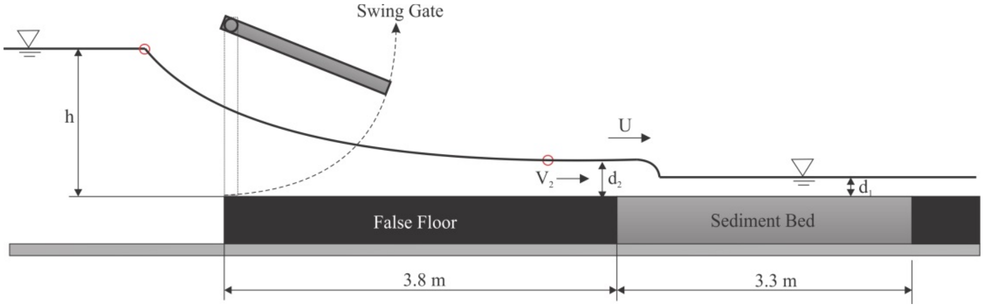

Figure. 4: Dam break wave propagation over the horizontal bed with wet bed condition

A total of twenty tests were conducted. Each test was repeated at least twice, and the synchronous time-averaged magnitudes of the results are presented herein. The main description of the experimental tests is summarized in Table 1. In this table, *r* is the ratio of h/d_1 which is the non-dimensional initial water depth.

Table 1: Experimental test program

Test #	***B(cm)***	***h(cm)***	***d_1(cm)***	***$r = d_1/h$***	***Bed condition***	**Test #**	***B(cm)***	***h(cm)***	***d_1(cm)***	***$r = d_1/h$***	***Bed condition***
1	30	25	0	0	dry	**11**	20	25	5	0.2	wet
2	30	20	0	0	dry	**12**	20	25	12.5	0.5	wet
3	30	15	0	0	dry	**13**	20	30	5	0.16	wet
4	20	25	0	0	dry	**14**	20	37.5	12.5	0.33	wet
5	20	20	0	0	dry	**15**	20	15	3	0.2	wet
6	20	15	0	0	dry	**16**	20	15	7.5	0.5	wet
7	10	25	0	0	dry	**17**	20	22.5	7.5	0.33	wet
8	10	20	0	0	dry	**18**	20	18	3	0.16	wet
9	10	15	0	0	dry	**19**	20	15	2	0.13	wet
10	20	25	2.5	0.1	wet	**20**	20	30	12.5	0.41	wet

Results and discussion

Sustained flow velocity (V_2)

Before starting each test, three small Styrofoam balls were placed on the surface of the water in the reservoir at approximately equal intervals from each other along the longitudinal reservoir axis as well as close to the swing gate. Once the gate opened, the images of the moving Styrofoam balls were easily captured by the high-speed video camera as they travelled along the flume on the surface of the dam-break wave. The first Styrofoam particles travelled right behind the initial bore front. The average velocity was measured along the first 1.3 *m* of the sediment bed section located downstream of the swing gate using the time sequence of the video recordings and the distance between the two grid lines. Results of the particle velocity analysis provided estimates of the flow velocity, V_2, immediately following the passage of the bore front. Chanson (2009b) presented an analytical solution for a dam break wave moving over a frictionless horizontal channel initially filled with water. His results showed that three non-dimensional parameters $U/\sqrt{gd_1}$, $V_2/\sqrt{gd_2}$ and $d_{2/}/d_1$ are a function of the h/d_1. V_2 is the flow velocity (*m/s*) immediately behind the positive surge which can be calculated by equation (1).

$$V_2+2\sqrt{gd_2} = V_0+2\sqrt{gd_0} \tag{1}$$

where, V_0 is the initial reservoir velocity (*m/s*) which is equal to zero in current experiments and d_0 is the initial water depth h(*m*) in the reservoir. Fig. 5 shows the measured sustained flow velocity by particle tracking against the calculated V_2 by equation.1 and Fig. 6 compares different parameters calculated from Chanson's analytical solution (2009b) and current experimental work. Both figures confirm that the measured values in this experiment are in good agreement with Chanson's analytical solution.

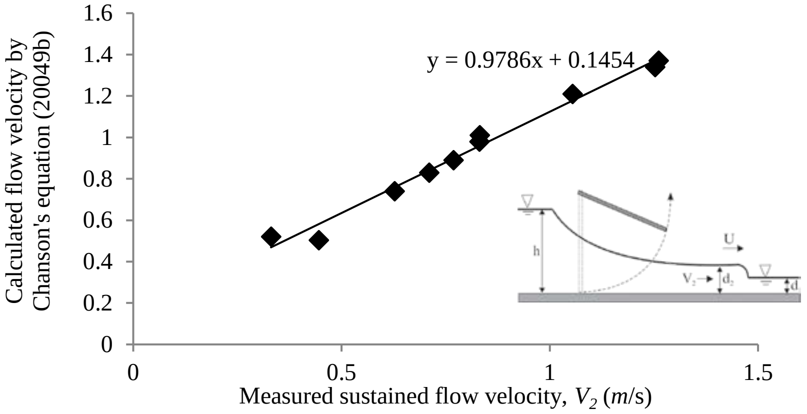

Figure. 5: Comparison between measured average sustained flow velocity V_2 with the calculated V_2 by Chanson's equation (2009b) in wet bed condition

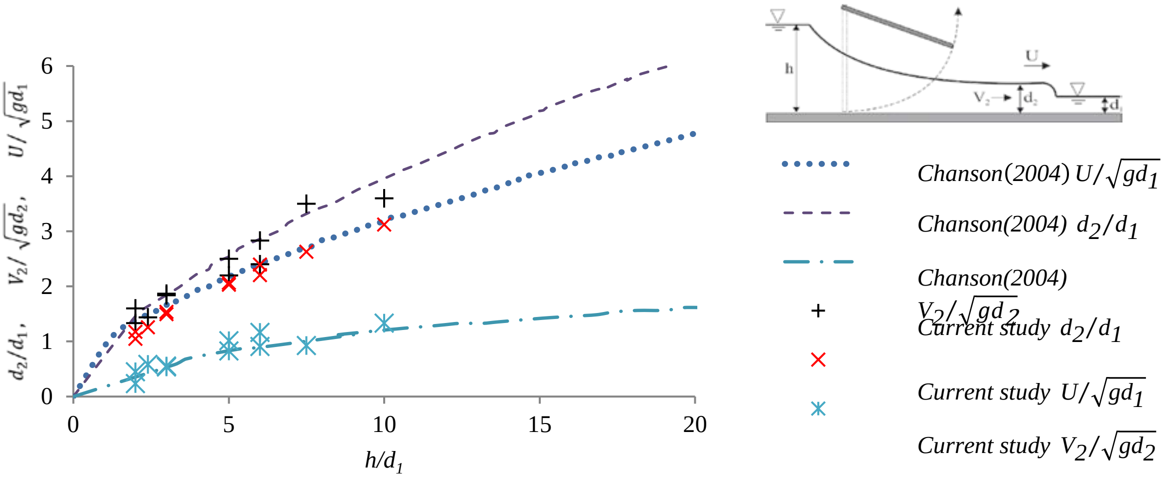

Figure. 6: Comparisons of different parameters calculated from Chanson's analytical solution (2009b) and current experimental data in wet bed condition

Scour mechanism

The scouring process was recorded using the video camera installed above the structure and the inclined periscopic mirror placed inside the structure. Fig. 7 (*a*) presents still images from the video recordings in the form of scour profile at three different time frames starting from initial sediment profile before scouring at *t* =0 *sec*, early scouring stage at *t* = 1 *sec* and final scour profile at t = 20 *sec*. These images provided a good evolution and understanding of the local scouring processes.

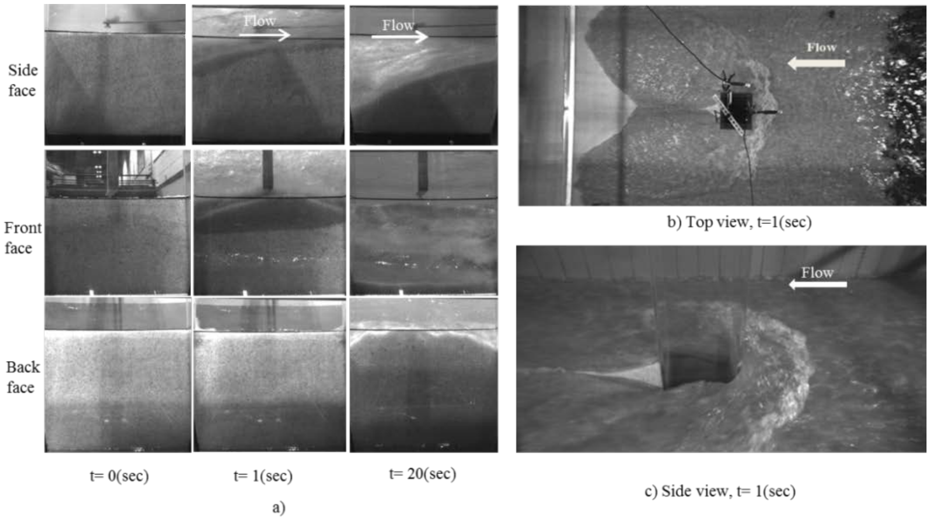

Figure. 7: a) Scour profiles around the structure; side (top), front (middle) and back face (bottom), b) Top view of the initial bore impact, c) Side view of the initial bore impact for (B=20cm, h=25cm, d_1=0 cm)

Fig. 7 (*b*) and (*c*) shows top and side view of the massive run-up and the initial bore impact at t = 1 *sec*. Bore depth initially is very small and immediately after the first impact, the bore depth increases rapidly and causes scouring along the structure. A large horseshoe vortex originating from the reversed flow and the formation of the scour hole causes a strong upward flow inside the hole at the corner of the model. This upward flow suspends the sediment which accelerates the scouring process and causes the maximum scour depth at the front corner of the structure. However, the scour at the back of the structure is negligible. Later on, as the flow velocity reduces, the suspended sediment starts to settle and fill the scour hole. This continues until the final scour depth, which is reduced compared to than the maximum scour depth, occurs. Therefore, using the observed final scour depth as a design criterion for the foundation of coastal structures is not recommended. Also, the suspended sediment moves towards the back of the square model and forms a distinct deposition pattern at the back of the structure. Fig. 8 presents the result of bore and scour depth time histories for the test number 4 (*B*= 20 *cm*, *h*= 25 *cm*, d_1=0 *cm*). The negative and positive values represent bore and scour depth time history, respectively. The bore-scour depth graph shows that significant scour depth occurs over a short period of time after the first impact of the bore. The initial bore front has a vertical front profile and with maximum bore depth being attained within 6 seconds. The maximum scour depth occurs after the first 13 seconds following the arrival of the bore front at the structure.

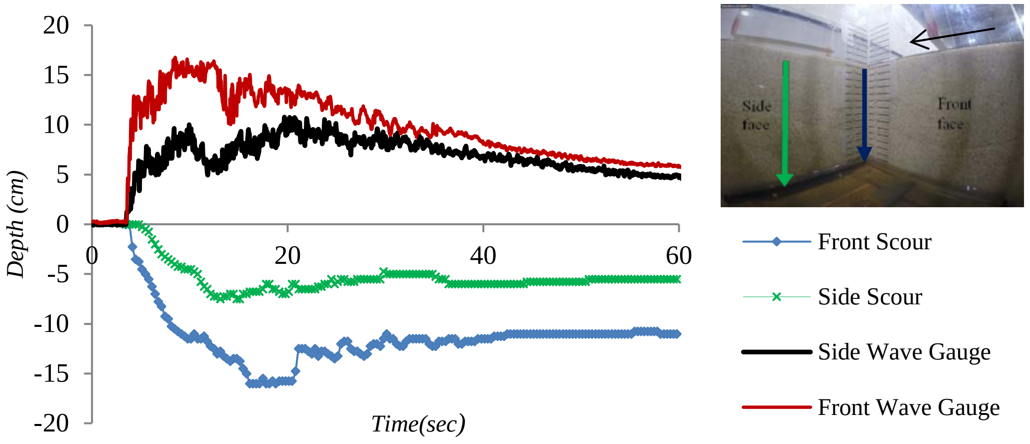

Figure. 8: Time history of the: (a) scour depth (blue and green line) and (b) bore depth (black and red) for test# 4

Fig. 9 (a) and (b) provides a 3-D scour profile and final scour bed elevation around the structure for the test number 4 (B = 20 *cm*, d_1 = 0 *cm)*. The positive and negative values on the scale represent deposition and erosion, respectively. As shown in the plots, the local scour holes formed by the hydraulic bore were for the most part elliptical in shape, with the maximum final scour was located at the upstream corner of the structure. The scour depth then decreased linearly towards the downstream back face of the structure. This time-limited scouring process was observed for all tests and can be attributed to the natural short duration of the generated bores. The two angled areas of scour extending from the back of the structure to the walls of the flume were also observed in all tests. These scour patterns may have been caused by the secondary waves reflected of the structure and bouncing back from the flume walls. The local scour along the upstream boundaries of the sediment section were caused by the transition between the sediment bed and the false floor.

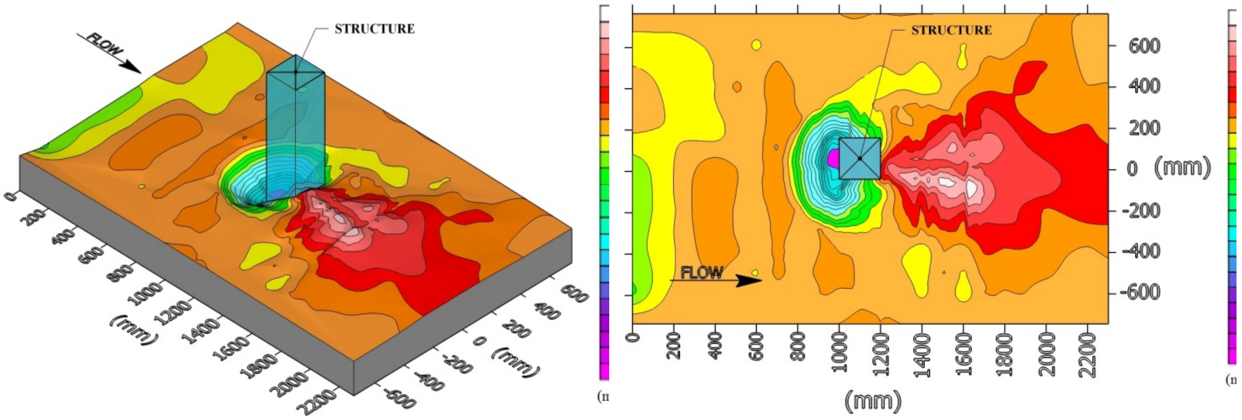

a) b)

Figure. 9: a) 3D scour profile; b) 2D bed scour elevation for (B=20cm, d_1=0 cm, h=25 cm)

Effect of bed condition

Fig. 10 presents bore front average velocity as a function of water depth ratio $r = d_1/h$. These velocities were calculated much in the same way as the sustained flow velocities. This velocity was assumed to represent the average velocity of the flow for the bed section. The result shows a decrease in the bore front velocity with an increase in the initial water depth ratio; therefore, the fastest bore front velocity occurs for the condition of (r = 0.1) when there is an initial thin layer of water depth downstream of the gate. Zero initial water depth (d_1 = 0 *cm*, r = 0) defines dry bed condition in which case the sediment bed is completely dry. Also, it can be seen that, the bore front velocity in wet condition is faster than that occurring in dry permeable bed condition. That is probably due to loss of water which infiltrates in the bed under dry condition; give the porosity and permeability of the sediment bed. In other words, energy dissipation due to seepage is presumed to originate from the interface between the fluid and the sediment bed. In contrast, the other studies in the literature review Chanson (2003) and Stansby et al. (1998) observed that the speed of the bore on a dry bed (fixed bed) is higher than that on wet bed. However, for both of their experimental conditions, the bed was solid and hydraulically smooth, with no sediment (zero porosity). Therefore, present results indicate that Chanson's and Stansy et al conclusions were drawn for a bore front moving over a fixed, dry bed cannot be expanded to the case with sediment bed.

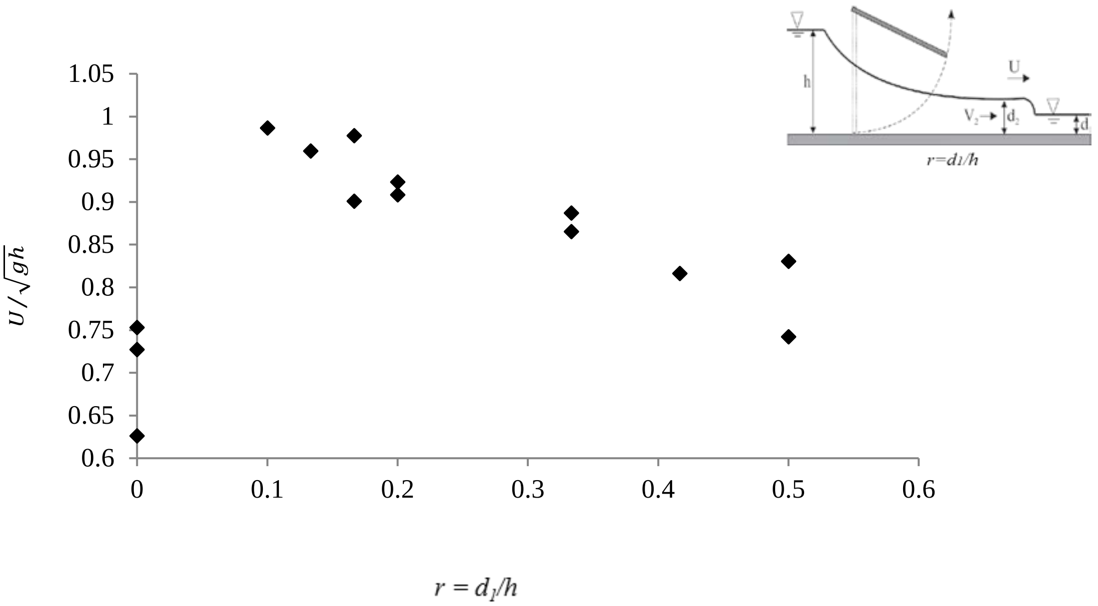

Figure. 10: Average bore front velocity as a function of the water depth ratio (r=d_1/h)

The plot in Fig. 11, shows the dimensionless scour depth d_s / B (cm) for 20 cm square structure based on $V_2/\sqrt{gd_2}$ which is the flow Froude number.

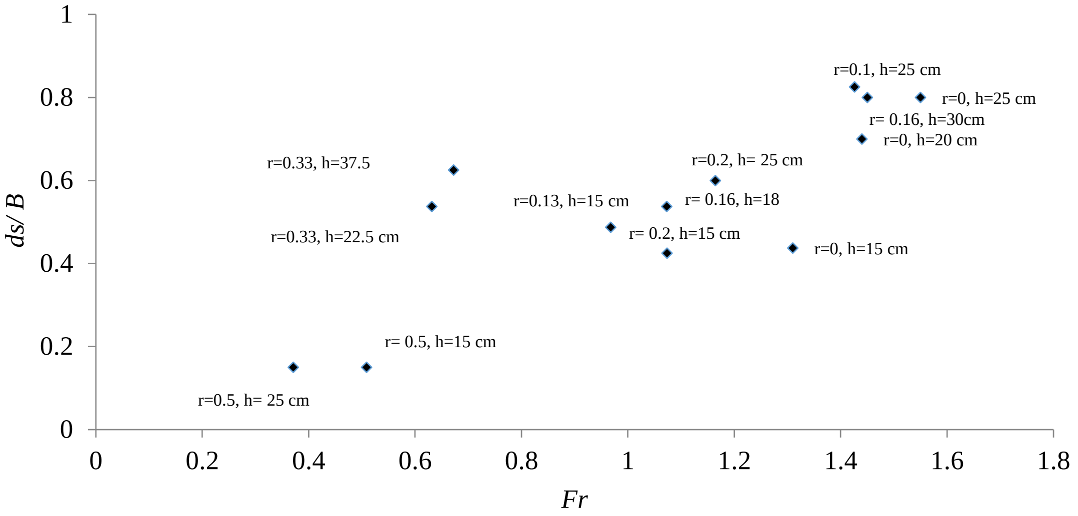

Figure. 11: d_s / B as a function of Froude number of flows in wet and dry bed condition for B = 20 cm

It can be concluded that, for the values of *Fr* ranges from 0.3 to 0.6, the d_s/B is around 0.2 whereas for the *Fr* values between 0.6 and 1.4 d_s/B increases from 0.4 to 0.7. Also, for the larger values of the *Fr* from 1.4 to 1.8 d_s/B is between 0.7 and 0.8. As it can be seen in Fig. 11, the higher values of $V_2/\sqrt{gd_2}$ are attributed to the smaller ratio of initial water depth $r = d_1/h$. Therefore, it can be concluded that the higher scour depth occurs when for initial condition there is a thin layer of water above the sediment bed. As the value of *r* increases, the bore becomes less effective at displacing the sediment grains around the structure. Comparing the scour depths in wet and dry bed conditions, for small initial water depth ratios the scour depths are slightly larger than those generated for the dry bed test for the same reservoir initial water levels (same bore characteristics). Since the depth of the sediment bed was limited to 17 *cm*, the scour for the test with *h*= 25 *cm* and *r* = 0.1 reached the bottom of the sediment bed before the end of the test. Hence, greater scour depth may have occurred for this case, something which could not be measured. As previously discussed, the dry sediment bed reduced the bore font velocity. Therefore, it could be concluded that for the case of the permeable bed, wet condition with thin layer of water - in other words, saturated condition - results in higher scour depths compared to those occurring under dry bed condition. This would imply that the second tsunami wave can be even more destructive than the first wave which propagates on dry land. `However it is still required to conduct more experiments to prove the conclusion made above with higher level of certainty. In dry bed condition, the suspended flow velocity (V_2) estimates the flow velocity immediately following the passage of the bore front over an already saturated bed which can explain the larger *Fr* number in dry bed condition compared to wet bed condition

Pier width effect on scour depth

In order to study effect of variation in pier width, *B*, on scour depth, d_s, nine tests were conducted using three different square structures of 10 *cm*, 20 *cm*, and 30 *cm* wide at various upstream initial water depths *h*(*cm*) in dry condition. Results of scour depth as a function of the structure's width for the nine tests are presented in fig. 12

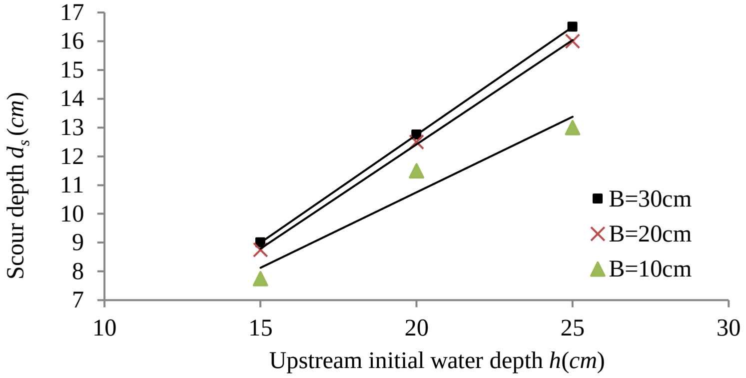

Figure. 12: Pier width effect on scour depth in dry bed condition

The tests showed that, for the same bore depth, more scour occurred at the front corner of the structure with an increase in pier width. However, there is not a noticeable difference when comparing the scour results observed for the tests with the 20 *cm* wide pier versus the 30 *cm* pier. Excessive scour depth for 20cm wide pier probably could be as a result of the interference of the two vortexes at two corners of the square structure. Fig. 13 shows final scour profile around the structure (top) and front face final scour profile (bottom) for two square structures *(a)* triangle shape profile for *B =30 cm* and *(b)* straight line profile for *B =20 cm*. These patterns could possibly confirm interference of the two vortexes for the smaller structure.

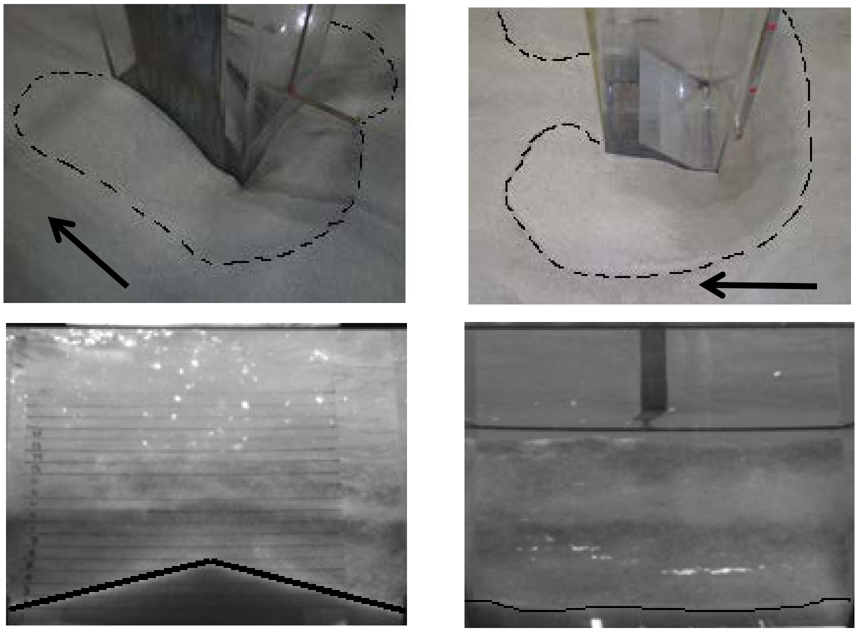

a) B=30cm *b) B=20 cm*

Figure. 13: Final scour pattern around the structure (top) and front face scour profile (Bottom) for a) B = 30cm, b) B=20cm

Conclusions

In this study, the scouring mechanism around a square structure due to a tsunami-like, inland-propagating bore has been investigated experimentally. Based on the analysis of the data obtained from laboratory experiments, the following conclusions are drawn.

❑ With an increase in the initial water depth ratio ($r=d_1/h$) the velocity of the bore front decreases. Therefore, the fastest bore front velocity was recorded at (r = 0.1), when there is a thin layer of water.

❑ Bore front velocity over dry bed is lower when compared to the bore front velocity in wet bed condition. This phenomenon is probably due to added flow resistance of the dry sediment bed.

❑ Maximum scour depth is slightly larger for bores propagating over wet bed condition with a thin layer of water compared to those generated by the same bore in dry bed condition. This implies that tsunami waves subsequent to the initial one can induce larger scour than the latter.

❑ For a constant bore depth, larger scour at the front corner of the structure was observed with an increase in pier width

- The short duration and very turbulent nature of the bores induced a rapid scouring process. Significant scour depths were reached over a short period of time at the front of structure while repetitive sediment deposition pattern has been observed at the back of structure.

MODELLING SUPERCRITICAL FLOW-INDUCED SCOUR AROUND STRUCTURES

Published in the proceeding of the CSCE2017, Vancouver, Canada, (2017).

Abstract: The present study investigates the scour mechanism and vortex structure around a square structure due to inland-propagating tsunami-like bores on a dry or flooded horizontal mobile bed. A series of hydraulic bores were simulated using a dam-break wave generated by the release of water impounded behind a rapidly opening swing gate. A novel video-recording system was used to monitor the evolution of the scour and vortex structure. Image processing allowed tracking the time and spatial evolution of the scour and the observation of sediment movement around the structure. It was found that the scour mechanism associated with dam break waves differs from that of a steady flow. The influence of bed condition (fixed versus mobile) and (dry versus wet) on bore characteristics, and how they might affect the scouring process will be presented and discussed.

Introduction and research needs

Field evidence indicates that destructive tsunamis cause substantial coastal sediment mobilization (Chen et al. 2016). Measurements collected from multiple tsunami events, such as the 1992 Nicaragua Tsunami and the 2004 Indian Ocean Tsunami, have recorded substantial evidence of scour around damaged buildings and bridge foundations (Yeh and Li, 2008). The field surveys noted that scouring was one of the primary causes of coastal structural damage (Chen et al. 2016). Tsunami waves have been observed with wave heights of 5–10 m. The inundating waves will be inevitably accompanied by very high flow velocities when they penetrate inland. The high flow velocities produce high bed shear stresses and large amounts of sediment movement over large areas, resulting in substantial beach erosion and scouring around a large number of structures (Li et al. 2012). Yeh and Li, (2008) observed local scour at the seaward corner of a schoolhouse in Kalapakkom, India. The inundation depth was 0.95 m above the building's floor and the run-up height was 4.1 m. The scour depth was approximately 1.5 m with a horizontal span of 5 m. They also observed an undermined patio in Devanaanpattinam, India, where the observed runup height was 3.0 m. The undermining resulted from swift channelized flows during the drawdown of the tsunami wave. During the 1993 Okushiri Tsunami attack, at the entrance of Okushiri Port, Japan, a scour depth of 4 m was created between breakwaters, causing the breakwater to overturn as a result of foundation failure. Generally, the first tsunami wave propagates over dry lands (dry bed condition) while the subsequent waves may intrude on the flooded coastline (wet bed condition) before full recession of the first wave. Previous research has shown that the water layer presence on the bed could influence the tsunami bore characteristics (Stansby et al. 1998; Douglas and Nistor, 2014). Laboratory experiments related to scour around structures caused by tsunamis are limited. Tonkin et al. (2003) examined scour around a cylindrical structure located on a sloped wet sandy beach. Nakamura et al. (2008) focused on scour around a square structure located on a horizontal wet sand bed. Both studies underline that such a tsunami-induced scour hole, occurring in such transient flow conditions, exhibited significantly different mechanisms than observed in steady current and consistent short-wave field studies. Laboratory waves employed in these studies were either solitary waves or long waves. At present, general scientific consensus indicates that solitary waves tend to be less representative of actual tsunamis due to their short period. This is particularly important for studies focusing on scour, where flow duration is a critical variable. The use of hydraulic bores generated from dam break waves have been shown to better replicate the temporal features of tsunami-induced flooding (Chanson. 2006). Using dam-break flow conditions, this study investigated the scour mechanism and vortex structure around the square structure due to inland-propagating tsunami bores on a dry and flooded horizontal bed. Additionally, characteristics of the bore, including run up, stream-wise velocity and bore front velocity for different initial downstream conditions (dry bed vs wet bed) will be presented.

Experimental set up

Flume and instrumentation

The hydrodynamic boundary conditions for these experiments were simulated using a dam-break method in a flume located in Hydraulics Laboratory at the University of Ottawa (Canada). The flume was 30 m long, 1.5 m wide and 0.8 m deep. The dam-break wave was generated by releasing water impounded behind a rapidly-opening swinging gate which was equipped with a lock and release mechanism. The sediment bed section was 3.30 m long and 1.5 m wide, delimited at each end by false floors as shown in Figure 1.

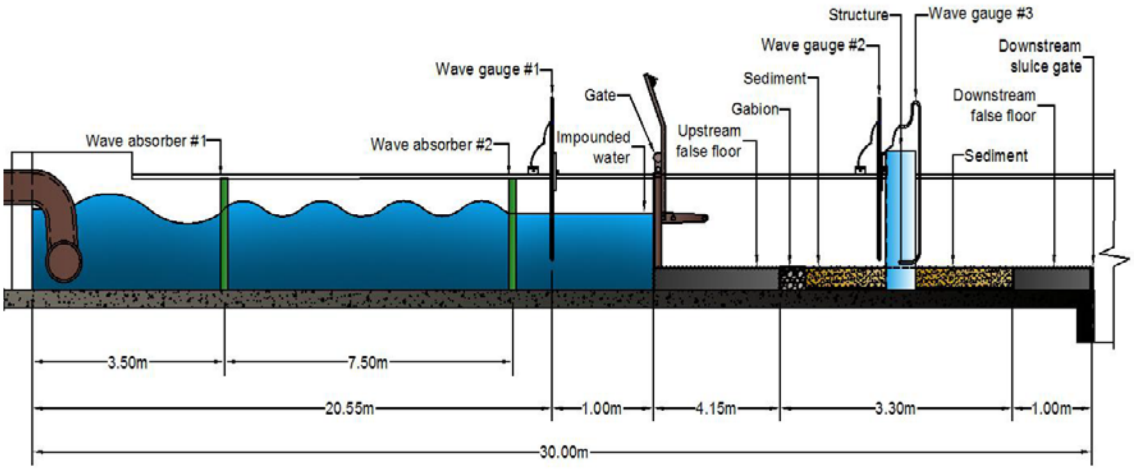

Figure 1: (a) Experiment setup, side view, (not to scale)

Two aluminum false floors with a height of 0.2 m were installed before and after the sediment bed, downstream of the gate, to provide formwork for the sediment section. A sluice gate was installed at the end of the downstream false floor to be able to create a wet bed initial condition. The upstream and downstream false floor had a length of 4.15 m and 1 m, respectively. The upstream false floor was covered with a layer of glued sand with a uniform grain size of 1 mm, in order to provide surface roughness, limiting the influence of the transition between the fixed and moveable bed. A grid system of 20 x 20 cm spacing was also painted on the top surface of the upstream false floor for measurement purposes.

The base of the sediment bed was composed of a layer of 1 cm thick coarse gravel covered by a geotextile sheet. The base layer drained water that infiltrated from below the false floor, to prevent the water from influencing the sediment bed. The sediment section was filled with 1 mm uniform sand. Directly downstream of the false floor, a 15 cm wide gabion was installed across the flume. The gabion was constructed with a wire box filled with coarse gravel, approximately 3 cm thick. The gabion was used to minimize the inevitable local scour that would occur at the interface of false floor and sediment section. Three wave absorbers were installed in order to attenuate secondary waves within the reservoir and prevent reflective waves-induced in water level fluctuation at the test section.

Three WG-50 capacitance type wave gauges with an accuracy of 0.4% were used to record the time-history of the water surface elevation at different locations, using a sampling rate of 30 Hz.

Two wave gauges were positioned as follows: one on the front face and the other one on the side face of the structure. The third wave gauge was placed at a distance of 1.0 m behind the swing gate, inside the reservoir. This wave gauge was used to record the time-history of the water surface elevation within the reservoir over the duration of the test. Two video cameras, a GoPro Hero^{TM} Black and an IO Industrial Flare™ high speed video camera, were used during the experimental investigations a) to track the bore front as it propagated downstream towards the structure, and b) to record the evolution the of scour and vortex structure. A 0.2 m x 0.2 m square structure built of Plexiglas was used in the experiment. The structure was installed in the center of the sediment section. The square structure was transparent to allow for monitoring the scouring process by means of the high speed camera which was placed at the top of the structure. The monitoring of the scour was achieved with the help of a mirror inclined at 45° inside the structure as shown in Figure 2.

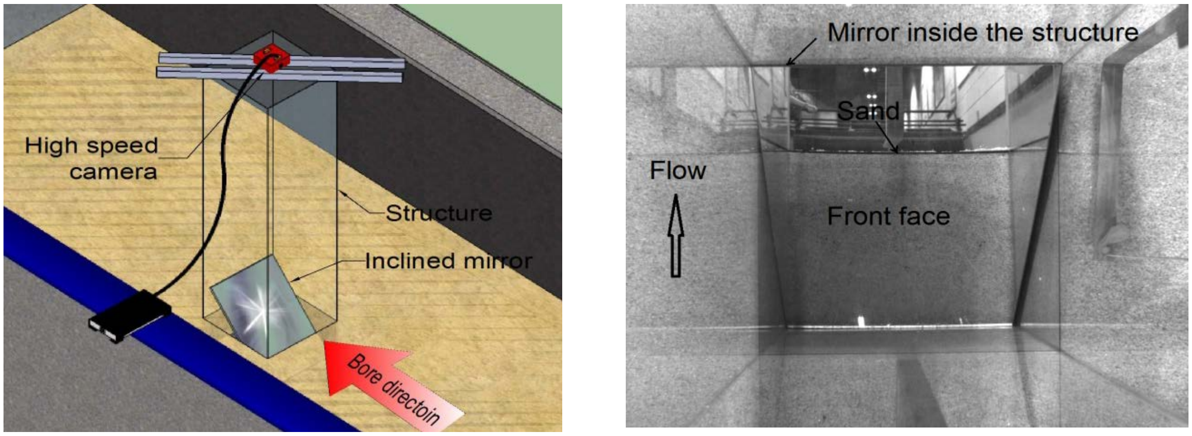

a) b)

Figure 2: (a) Experiment setup to monitor the scour process; (b) Reflected (looking from above-mirror inside) view of the structure’s front face.

Turbulent velocity measurements were conducted with an Acoustic Doppler Velocimetry (ADV) using the Nortek Vectrino with a down-looking head equipped with four receivers using a sampling rate of 25 Hz (installed at x = 5.15 m from the gate).

Experimental procedure

Before each experiment, the sediment bed was levelled, and the reservoir was filled with water to the desired impounded water depth. The swinging gate was then manually unlocked and rapidly opened. The bore then advanced over the false floor and finally over the sediment bed section, while all measuring instruments were recording. The opening time of the gate was recorded to calculate the non-dimensional removal period $t\ (g/h)^{1/2}$. The expression should be less than the square root of two to achieve the ideal dam-break condition (Lauber and Hager, 1997). To investigate the effect of bed condition on bore velocity and scour depth, two initial conditions (wet versus dry conditions) were considered downstream of the gate. A schematic illustration of the experiment is presented in Figure 3, where h_u and h_d are the initial water depths (m) upstream and downstream of the gate, respectively. All the tests were conducted with an initial impoundment depth of h_u = 0.25 m, while downstream water depth h_d varied between tests (0 m, 0.025 m, 0.05 m, or 0.125 m). Since the impoundment water depths were kept constant, tests are named according to downstream water depths as dry bed, 0.025 m wet bed, 0.05 m wet bed and 0.125 m wet bed, respectively. For the experiment, a 1:40 Froude scaling ratio was used, resulting in h_u = 0.25 m corresponding to a prototype height of 10 m.

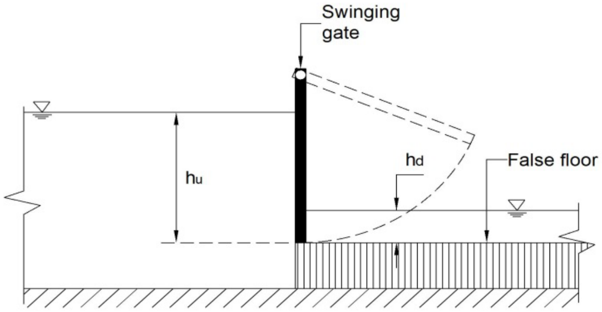

Figure 3: Schematic illustration of the experiment

Validation of the model

A comparison between a dam-break analytical solution and the experimentally obtained bore profile is presented here. Because of the limited number of wave gauges, a number of identical tests were repeated with the same experimental configuration by installing wave gauges in sequential steps of 1 m to cover the entire flume. Repeated tests performed with the wave gauges at the same location showed a high degree of reproducibility in terms of wave arrival time and evolution of water depth. Figure 4 presents the comparison between the dam-break analytical solution and the experimentally obtained bore profile on the fixed floor before arrival of the bore on the sediment section. The x-axis corresponds to the direction along the flume length and h represents the water surface elevation. Chanson's (2009b) solution considers the bottom friction in the dominant wave tip region, using the diffusive wave equation and Darcy-Weisbach friction factor (*f*). The value of *f* was taken as 0.03, described as a smooth surface. As shown in Figure 4, a good agreement can be observed between the experimental bore profiles and Chanson's solution.

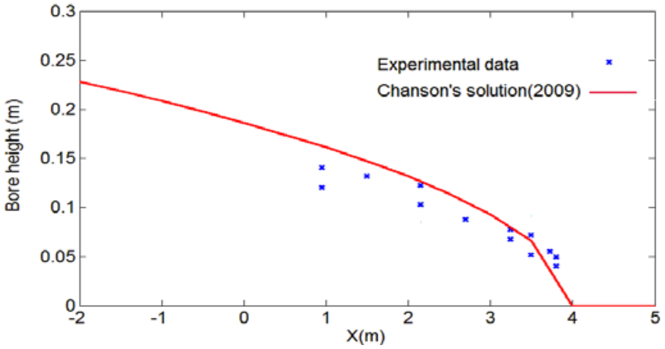

Figure 4: Comparison between dam-break analytical solution and the experimentally obtained bore profile for h_u = 0.25 m, h_d = 0 m at t = 2.48 sec

Result and discussion

Scour mechanism

Figure 5 shows the measured results for the initial condition of h_u = 25 cm and h_d = 0 cm (dry bed condition). The black line represents the horizontal velocity measured 50cm upstream of the structure. The green and red lines show the scour depth and water surface elevation time-histories, respectively, measured at the front face of the structure. It can be seen that stream-wise velocities were captured after 2 s. The ADV measurements were noisy for the first 2 seconds of advancing bore as a result of air bubble entrainment and cavitation during the first few seconds after the bore arrival. The graph shows that significant scour depth occurs over a short period of time after the initial impact of the bore.

The short duration and turbulent nature of the bore induced a rapid scouring process. The initial bore front had a vertical front profile, and the maximum bore depth was attained within 8 seconds. The maximum scour depth occurred 13 seconds after the arrival of the bore front.

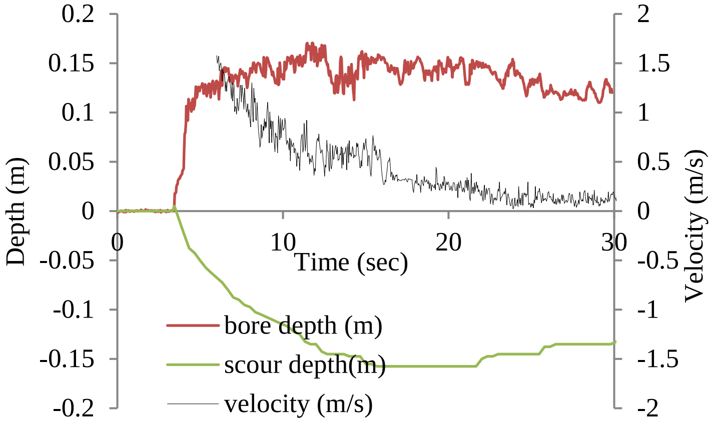

Figure 5: Water surface elevation (red line) and scour depth time history (green line) measured at the front face of the structure and horizontal velocity (black line) measured 50cm upstream of the structure for $h_u = 0.25$ m, $h_d = 0$ m

The critical shear stress for initiation of sediment motion was calculated from the Shields diagram in order to compute critical shear velocity. For the 1 mm grain size, the calculated critical velocity was 0.28 m/s. Figure 5 shows that the highest scour rate coincided with the largest flow velocities greater than the critical velocity. As the flow velocity decreased, the scouring pace slowed and the suspended sediment started to settle, filling the scour hole.

Effect of bed condition

Generally, the first tsunami wave propagates in a form of turbulent hydraulic bore over coastal areas that are in a dry bed condition, while the second or third tsunami waves may advance into the previously inundated inland area, which is referred to as the “wet bed condition”. It is reported that the presence of a still water layer (h_d) can significantly influence the bore propagation characteristics. In this section, the bore propagation characteristics and the resulting scour profile on both wet and dry bed conditions are compared and discussed.

Bore front velocity (U)

Figure 6 presents bore front average velocity as it propagated to the downstream end of the flume. The propagation of the bore front along the flume was tracked using the high-speed video camera. The velocity was calculated using the time sequence of the video recordings and the distance between the two gridlines. This velocity was assumed to represent the average velocity for that section. In general, for both fixed and movable beds, the highest velocities were recorded at locations closest to the gate, as a result of the bed friction. The bore front velocity gradually decreased as the bore propagated to the downstream end of the flume.

On the fixed bed, maximum instantaneous velocities reached as high as 2.26 m/s for the dry bed. The bore front velocities were 2.15 m/s, 1.84 m/s and 1.75 m/s for the 0.025 m wet bed, 0.05 m wet bed and 0.125 m wet bed, respectively. The bore front velocity decreased as the downstream water depth increased. The presence of the still water layer caused a resistance to the propagation of the incoming bore, inducing energy dissipation in the bore front. The higher downstream water depth resulted in lower total head and subsequent less kinetic energy and lower velocity. Therefore, the fastest bore front velocity occurred in the dry bed condition.

Conversely, the velocity measurement on the mobile bed showed different trends from that of a fixed bed. The bore front velocity in wet bed conditions with a thin layer of water was faster than observed in dry permeable bed. This was likely a result of water infiltrating into the bed under the dry condition, given the porosity and permeability of the sediment bed. In other words, energy dissipation due to seepage is presumed to originate from the interface between the fluid and the sediment bed. This counter some previous results in other studies discussed in Section 1. Chanson, (2003) and Stansby et al. (1998) observed that the speed of the bore on a dry (fixed) bed is higher than that on a wet bed. However, for both of their experimental conditions, the bed was solid and hydraulically smooth, with no sediment (zero porosity). Therefore, the present results indicate that the conclusion of higher bore front velocity moving over a dry fixed bed cannot be expanded to the case with a sediment bed.

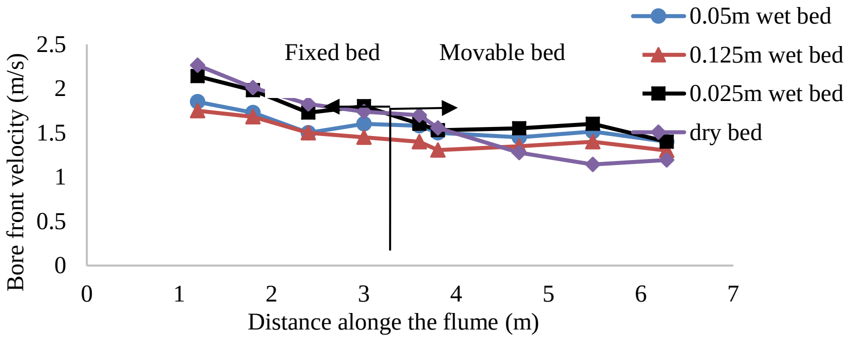

Figure 6: Bore front velocity along the flume for all initial conditions

Run up and stream-wise velocity of bore propagation

Comparisons of the time-history of water surface elevation at the upstream face of the structure and stream-wise velocity are shown for different initial conditions in Figure 7. It can be seen that the run-up height resulting from the initial impact was influenced by the bed condition. The run-up height reached the highest elevation (0.175 m) for the case of bore propagating over a thin layer of water (h_d =0. 025 m). The maximum run up heights were 0.17 m, 0.15 m and 0.11 m for h_d =0 m, h_d =0.05 m and h_d =0.125 m, respectively. Therefore, it can be seen that splash height in wet bed condition with thin layer of water was slightly greater than that of the dry bed condition.

Comparing the results in wet bed condition, a consistent reduction in the run-up height was observed with increasing downstream water depths. The maximum run up height for the dry condition was 0.17 m which occurred 7.9 s after the arrival of the bore front, while maximum bore depth was attained within less than a second for wet bed conditions. This also contrasted other studies, such as Stansby et al. (1998) and Douglas and Nistor, (2014), which observed that maximum bore heights occurred within 0.5 s after the initial impact for bores propagating over dry smooth solid beds. This delay in maximum run up height again could be caused by permeability of the mobile bed under dry conditions. Moreover, a delay in the arrival of the bore front was observed as the downstream depth increased, which shows a similar trend as the bore front velocity. For the wet bed conditions, a relatively vertical bore front was measured with respect to the dry bed condition. Observations showed steeper and deeper bore front with higher air entrainment in the bore front for wet bed conditions as the downstream water depth increased. To further analyze the effects of bed condition on propagation characteristics, a time-history of stream-wise velocity, measured upstream of the structure, is also given in Figure 7 for all initial downstream water depths. In all cases, the ADV sample volume was set such that it would be at or just below the bore water surface. As noted above, the stream-wise velocity measurements began 2 s after arrival of the bore. According to Figure 6, the bore front velocities at the location of the model structure were 1.14 m/s, 1.6 m/s, 1.51 m/s and 1.4 m/s, while from Figure 7 the maximum stream-wise velocities were 1.57 m/s,1.45m/s, 1.005 m/s and 0.554 for h_d=0 m, h_d=0.025 m, h_d=0.05 m and h_d=0.125 m, respectively. It appears that the lowest bore front velocity occurred in the dry bed condition, whereas the dry bed run had the highest measured stream-wise velocity 2.53 seconds after bore arrival. It appears that saturation of the initially dry bed allowed for increased velocity following passage of the bore front. Moreover, these results show reductions in the stream-wise velocity for increasing initial downstream depths, similar to the trend for bore front velocity.

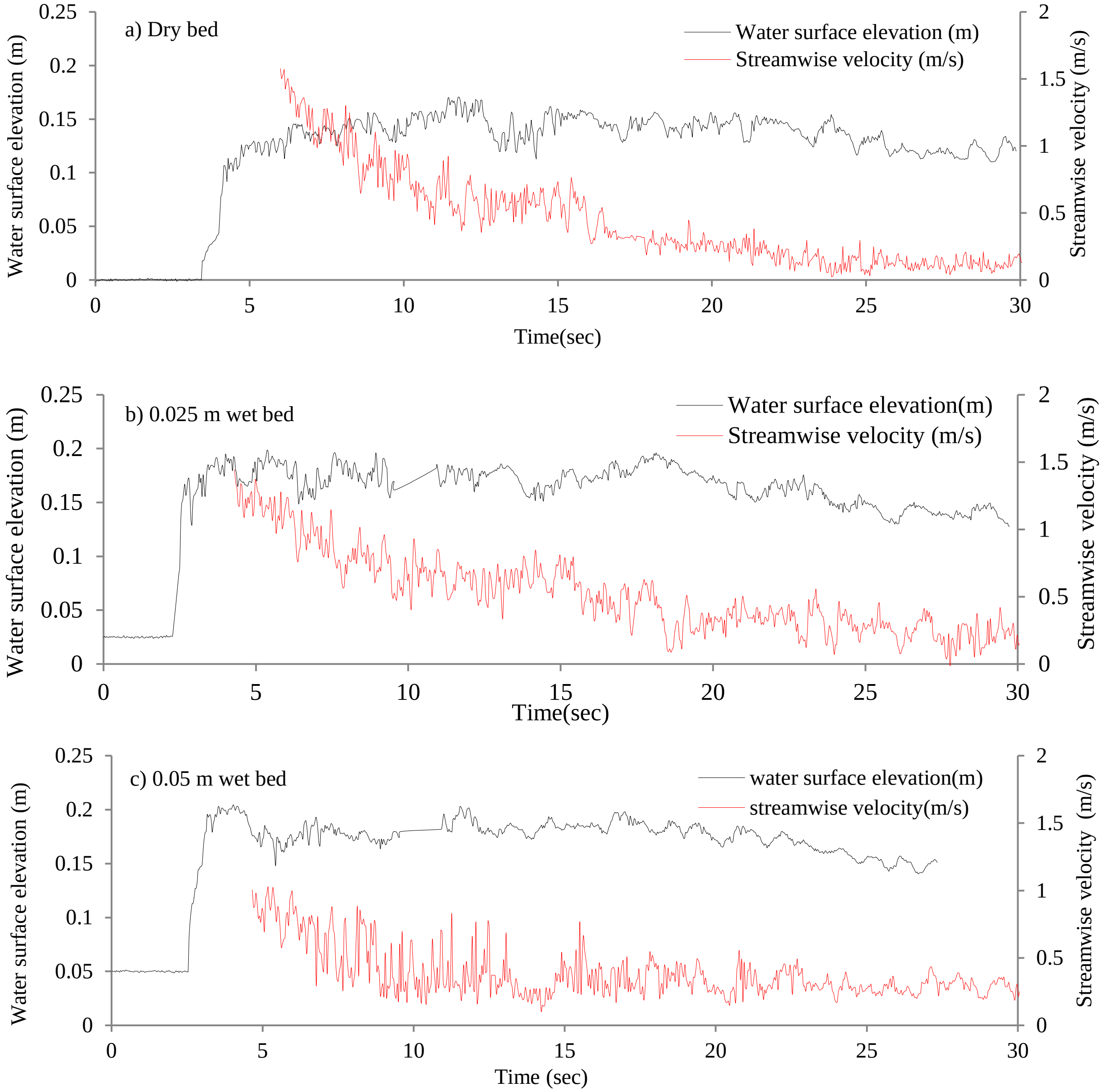

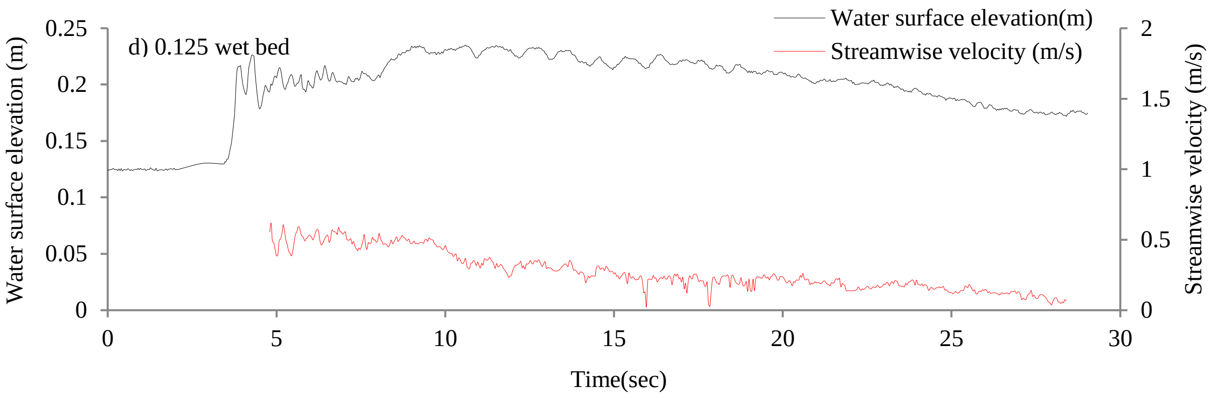

Figure 7: measured water surface elevation (black line) and measured streamwise velocity (red line) for a) h_d = 0 m, b) h_d = 0.025 m , c) h_d= 0.05 m and d) h_d = 0.125 m

Scour depth

Figure 8 demonstrates time-history of scour depth for all the experimental tests. For better comparison of all the tests, time zero refers to the bore arrival time at the structure, i.e., when the scouring process would be initiated. The magnitude of the scour depth for the 0.025 m wet bed was 0.16 m, which was slightly larger than that generated for the dry bed test (0.15 m scour depth). This would imply that the second tsunami wave can be even more destructive than the first wave propagating on dry land. The scour depths were respectively 0.12 m and 0.03 m for the 5 cm and 12.5 initial water depths, reductions of 40% and 140% compared to the 2.5 cm initial water depth case. Therefore, similar to bore front velocity and stream-wise velocity, a substantial reduction in scour depth was observed with increasing the downstream initial water depth. The presence of the initial still water depth weakened strength of the down-flow at the structure face and the bore became less effective at displacing the sediment grains around the structure. In contrast, Arneson et al. (2012) reported that the scour capacity of a steady flow field reduces as the flow depth decreases. The down-flow at the pier face becomes less well developed because it has a shortened length over which to develop. The vorticity of the horseshoe vortex weakens as the down-flow weakens, and the wake vortex also weakens due to the increased importance of bed friction in a shallower depth. There is a noticeable difference between the time that it takes for the maximum scour depth to form in a dry bed compared to that of wet bed conditions The maximum scour depth in the dry bed condition was attained 14 s following the bore arrival, while for the wet bed tests it was attained within 7, 7 and 4.6 s. This was likely because under the dry bed condition the bore reached the structure before the bed was saturated completely.

Lastly, it can be seen that the final scour depth was less than the maximum scour depth. Therefore, using the observed final scour depth as a design criterion for the foundation of coastal structures is not recommended.

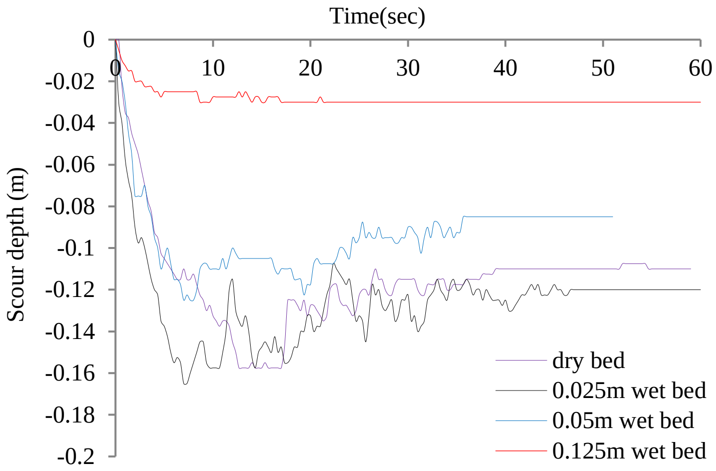

APPENDIX C

APPENDIX C- SENSITIVITY ANALYSIS

Sensitivity analyses have been performed to achieve a desirable combination of numerical parameters. Initially, the influence of mesh variation is tested using different mesh resolutions.

Figure. 1 compares the experimentally monitored and simulated runup on the structure face for uniformly distributed 0.01x0.01 m cells, uniformly distributed 0.05x0.05 m cells which was refined to 0.01x0.01 m in the near structure region and a mesh generated with an initially uniform distribution of 0.1x0.1 m grid cell which was refined to 0.01x0.01 m in the vicinity of the structure. The initial peak in the time-history of surface elevation represents the run up that occurs following impact of the rapidly advancing bore. As evidenced by Figure1 the mesh resolution has an influence at this stage. In moving from the refined 0.1x0.1 m to the refined 0.05x0.05x1.5 mesh, a 0.04 m increase in the computed surface elevation and 0.011 m increase in the computed scour depth is observed, bringing about better agreement with the experimental data. However, the uniform mesh with 0.01x0.01 m cells does not appear to have any additional influence on the run-up height and scour depth. The delay in maximum measured run-up height in the experiment is likely a result of water infiltrating into the bed given the porosity and permeability of the sediment bed under dry bed conditions and inability of the 3D model to capture the surface roller.

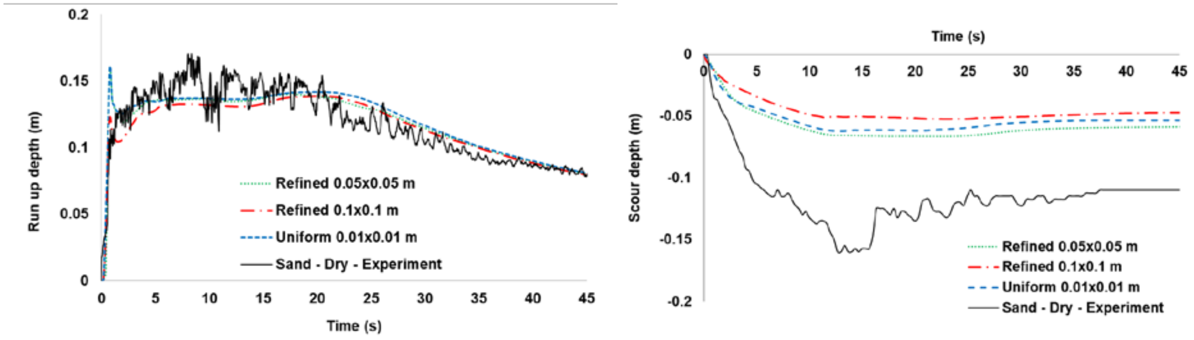

Figure 1: Sensitivity analysis of mesh size Run-up depth b) Scour depth

Moreover, a comprehensive sensitivity analysis was conducted (Figure 2, 3, 4, 5, 6, 7 and 8). By changing one variable at a time, and keeping all other variables fixed to their baseline values. Baseline model was conducted with 0.05X 0.05 m mesh size, Smagorinsky turbulent model, sediment transport formula of Engelund – Hansen for sand and Mayer-Peter&Muller for gravel, manning roughness coefficient of 0.018 for sand and 0.025 for gravel and the shield parameter of 0.022 for sand and 0.044 for gravel. Selected parameters and values for the final modelling are shown with green color.

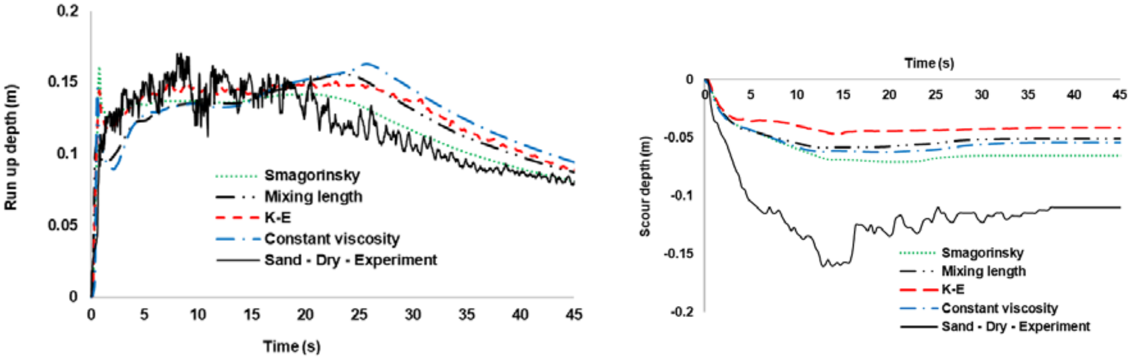

Figure 2: Sensitivity analysis of turbulent model a) Run-up depth b) Scour depth

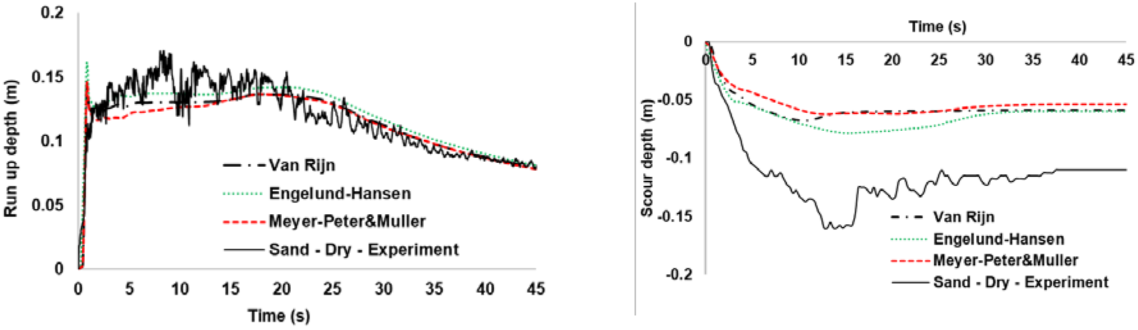

Figure 3: Sensitivity analysis of sediment transport formula for sand a) Run-up depth b) Scour depth

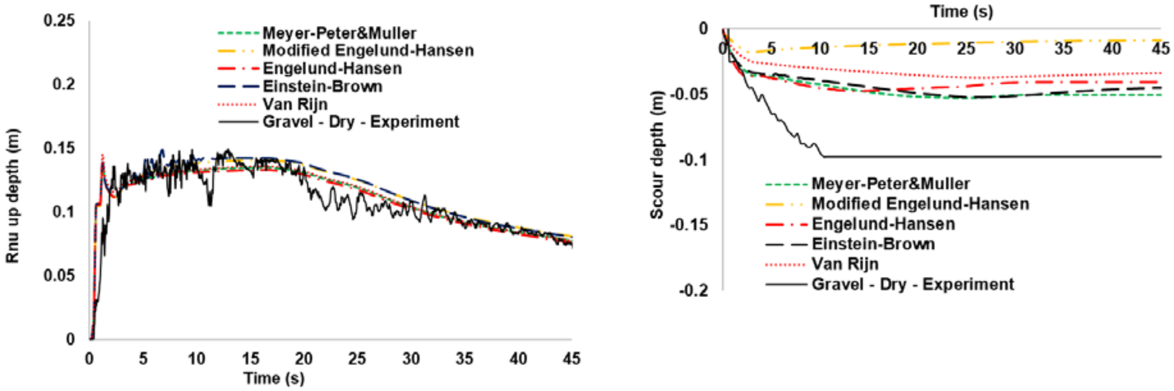

Figure 4-: Sensitivity analysis of sediment transport formula for gravel a) Run-up depth b) Scour depth

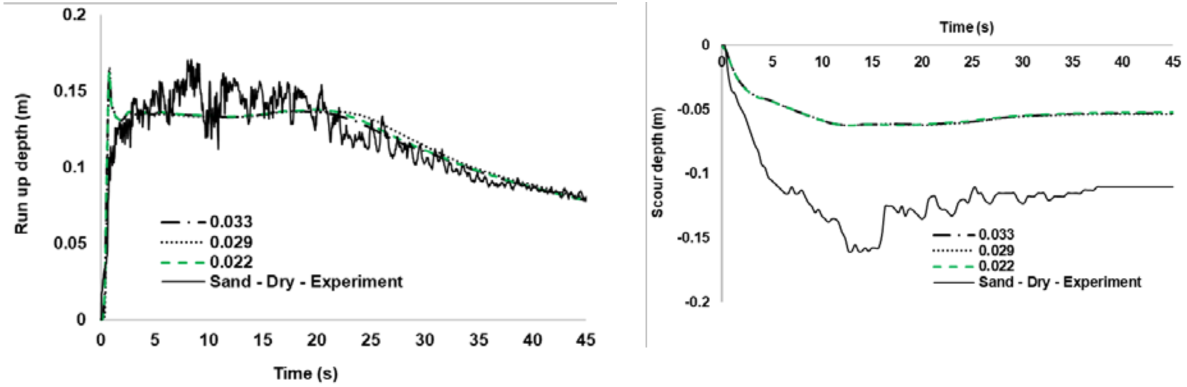

Figure 5: Sensitivity analysis of shield parameter for sand a) Run-up depth b) Scour depth

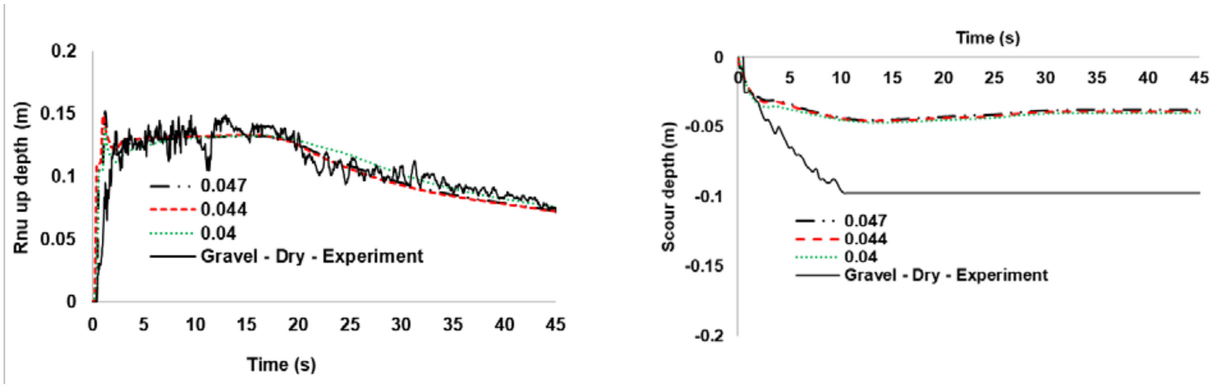

Figure 6: Sensitivity analysis of shield parameter for gravel a) Run-up depth b) Scour depth

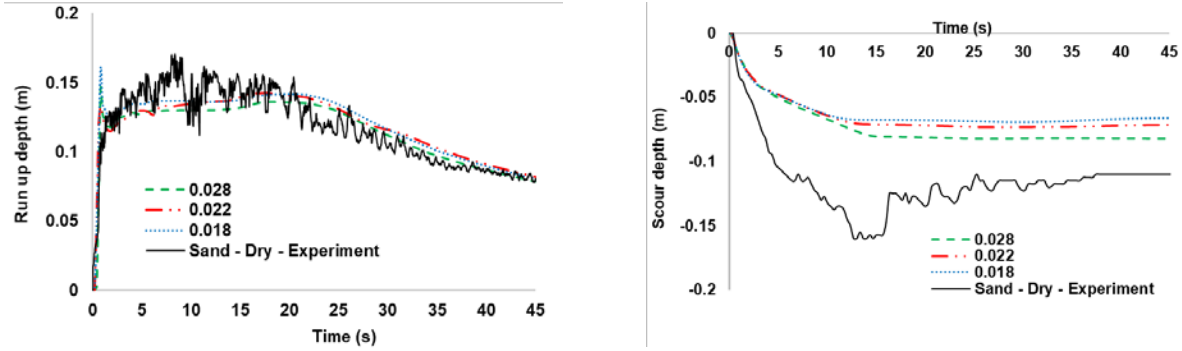

Figure 7: Sensitivity analysis of manning roughness coefficient for sand a) Run-up depth b) Scour depth

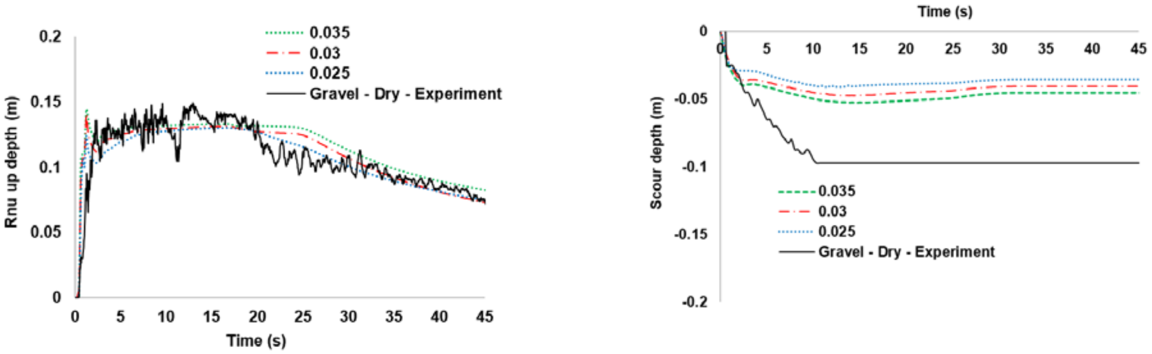

Figure 8: Sensitivity analysis of manning roughness coefficient for gravel a) Run-up depth b) Scour depth